

JOHAN FABIAN TRIANA GALVIS

**NON-ADIABATIC PHOTOFRAGMENTATION OF SIMPLE MOLECULES
SUBJECT TO ULTRASHORT LASER PULSES AND CONFINED IN
QUANTUM OPTICAL CAVITIES USING THE MULTICONFIGURATIONAL
TIME DEPENDENT HARTREE METHOD**

**NON-ADIABATIC PHOTOFRAGMENTATION OF SIMPLE MOLECULES
SUBJECT TO ULTRASHORT LASER PULSES AND CONFINED IN
QUANTUM OPTICAL CAVITIES USING THE MULTICONFIGURATIONAL
TIME DEPENDENT HARTREE METHOD**

JOHAN FABIAN TRIANA GALVIS



1 8 0 3

Instituto de Física
Facultad de Ciencias Exactas y Naturales
Universidad de Antioquia - UdeA -

July 20, 2018

Johan Fabian Triana Galvis:

Non-adiabatic photofragmentation of simple molecules subject to ultrashort laser pulses and confined in quantum optical cavities using the multiconfigurational time dependent Hartree method,

© July 20, 2018

SUPERVISOR:

Prof. Dr. José Luis Sanz-Vicario

LOCATION:

Medellín, Colombia

Ohana means family.
Family means nobody gets left behind, or forgotten.
— Lilo & Stitch

God doesn't play dice with the world.
— Albert Einstein

*Dedicated to my grandparents, Gabriel and Flor
and all whom I love.*

PUBLICATIONS

Some ideas and figures have appeared previously in the following publications:

1. Johan F. Triana, Daniel Pelaez, José Luis Sanz-Vicario, "Entangled Photonic-Nuclear Molecular Dynamics of LiF in Quantum Optical Cavities", *J. Phys. Chem. A*, vol. 122, 2266, 2018.

OTHER PUBLICATIONS DURING THE DEVELOPMENT OF THIS THESIS

1. Johan F. Triana, Andrés F. Estrada and Leonardo A. Pachón, "Ultrafast Optimal Sideband Cooling under Non-Markovian Evolution", *Phys. Rev. Lett.*, vol. 116, 183602, 2016.

*We keep moving forward, opening up new doors and
doing new things, because we are curious...
and curiosity keeps leading us down new paths.*

— Walt Disney

ACKNOWLEDGMENTS

First of all, I want to thank my family for trusting and supporting me in all the decisions I have made in my life. Specially to my grandparents, Gabriel and Flor, for educating me when I was just a child. There are no words for thanking them. Similarly, to my mother Marlen for her support, aid and understanding.

Second, I thank to my advisor, Prof. Dr. José Luis Sanz-Vicario, who I have shared with the best moments in my academic and professional life and who taught me a great passion for science, specially how the micro-world or molecules work. Additionally, I appreciate all the support and dedication, without this and our long longgggg discussions, the developments of this work could not be concluded. Likewise, I consider him as an example both form the personal and professional point of view in the academic life. I also have to thank him for his quick administrative aids with -CODI-, COLCIENCIAS and GFAM group at Universidad de Antioquia, to receive the support for events, scholarship and interships during the time of my PhD work.

Third, I thank the other professors of GFAM group, Leonardo Pachón, Boris A. Rodríguez and the former GFAM member Alvaro Valdés de Luxán (now at Universidad Nacional), with whom I have shared academic discussions and great coffee breaks.

Similarly, I thank other members, fellow students and colleagues in the GFAM group for the social activities, discussions, shared moments and the working atmosphere at SIU. All this interactions made me grow up both personally and professionally.

Finally, I thank to the professors Majdi Hochlaf at Université Paris-Est Marne-la-Vallée and Daniel Peláez-Ruiz at Université de Lille for receiving me in their groups to perform my compulsory PhD interships abroad. They were places were I could learn a lot about the subject treated in this PhD thesis and allow me to share a great time with people coming from different parts of the world.

CONTENTS

INTRODUCTION	1
i ELECTRONIC STRUCTURE	3
1 ADIABATIC APPROXIMATIONS	5
1.1 Crude diabatic approximation	7
1.2 Born-Oppenheimer Adiabatic Approximation	8
1.3 Born-Huang Adiabatic Approximation	9
2 HARTREE-FOCK MOLECULAR ORBITAL THEORY	11
2.1 Hartree-Fock Method: Basic Principles of ab initio calculations	11
2.2 Gaussian Basis Sets Functions	13
3 POST HARTREE-FOCK <i>ab initio</i> METHODS	15
3.1 Multi-Configurational Self-consistent Field (MCSCF) Method	15
3.2 Multireference Configuration Interaction (MRCI) Method	16
3.3 Coupled Cluster Singles and Doubles (CCSD)	16
ii MOLECULAR QUANTUM DYNAMICS	19
4 TIME-DEPENDENT METHODS	21
4.1 Spectral Methods using basis expansions	22
4.2 Time-Dependent Hartree (TDH)	24
4.3 Multiconfigurational Time-Dependent Hartree Method (MCTDH)	26
5 MOLECULAR DYNAMICS	31
5.1 Adiabatic vs. Non-Adiabatic Dynamics	31
5.2 Diabatic Dynamics	33
iii THE NATURE OF RADIATION	37
6 CLASSICAL APPROACH	39
6.1 Mathematical Definition of ultrashort pulses	39
6.2 Coherent Control Theory	44
7 QUANTUM APPROACH FOR LIGHT	49
7.1 Quantization of electromagnetic field	49
7.2 Quantum States of Light	50
8 LIGHT-MATTER INTERACTION	57
8.1 Light-matter interaction with a classical field	57
8.2 Light-matter interaction with a quantized field	58
8.3 Dressed States Basis	60
iv POTENTIAL ENERGY SURFACES AND PHOTODYNAMICS	63
9 DIATOMIC MOLECULES	65
9.1 H ₂ and H ₂ ⁺ (Hydrogen Molecule)	65
9.2 LiF (Lithium Fluoride)	70
10 TRIATOMIC MOLECULES	77
10.1 H ₂ O (Water) and HOD (Semiheavy Water)	77
10.2 CO ₂ (Carbon Dioxide)	89
11 TETRATOMIC MOLECULES	105
11.1 CH ₃ (Methyl Radical)	105
12 CAVITY FEMTOCHEMISTRY: CONTROLLING MOLECULES WITH QUANTIZED FIELDS	113
12.1 Revealing non-adiabatic effects in lithium fluoride induced by quantized fields	113
12.2 Uncovering light induced crossings in molecules immersed in optical cavities using pump-probe laser schemes	125
CONCLUSIONS	135
v APPENDIX	137
BIBLIOGRAPHY	141

LIST OF FIGURES

Figure 1.1	Breaking of the Born-Oppenheimer approximation.	9
Figure 4.1	Schematic representation of two electronic states A and B in the Born-Oppenheimer (BO) approximation for a diatomic molecule.	23
Figure 5.1	Schematic representation of a Conical intersection in its branching space.	33
Figure 5.2	Avoided crossing between states ${}^1\Sigma_1$ and ${}^2\Sigma_1$ in LiF molecule.	34
Figure 6.1	Schematic representation of electric field vector and its sine carrier-envelope function.	40
Figure 6.2	Schematic representation of electric field vector for two different frequencies.	41
Figure 6.3	Schematic representation of the Fourier transform for pulses with different pulse time duration.	44
Figure 6.4	Schematic representation of the Brumer-Shapiro control theory.	45
Figure 6.5	Schematic representation of the Tannor-Rice control theory.	46
Figure 6.6	Schematic representation of the pump-probe pulse.	47
Figure 7.1	Phase space representation for a coherent and squeezed coherent states.	53
Figure 7.2	Evolution of a coherent and squeezed state.	55
Figure 8.1	Schematic representation of Rabi model.	58
Figure 8.2	Schematic representation of dressed states.	61
Figure 9.1	Electronic states for Hydrogen molecule and its ion.	68
Figure 9.2	Free dynamics of the initial wavefunction in the ground state of H_2^+ after a sudden ionization from H_2	69
Figure 9.3	Populations of the $2p\sigma_u$ electronic state after to excite the H_2^+ molecule with a laser pulse.	70
Figure 9.4	Coordinate system chosen for the electronic structure of LiF using the MOLPRO package, with the molecule oriented along z -axis.	71
Figure 9.5	Potential energy curves of the two lowest adiabatic ${}^1\Sigma$ states and the lowest adiabatic ${}^1\Pi$ states of LiF molecule. The states corresponding to the ${}^1\Sigma$ symmetry display a (covalent-ionic) avoided crossing at $R = 13.1$ a.u. The zero energy is set at the bottom of the ground state ${}^1\Sigma$ and the equilibrium internuclear distance is $R = 3.0$ a.u.	72
Figure 9.6	<i>Ab initio</i> diagonal and non-diagonal dipole moments along with the non-adiabatic coupling for the three lowest states of LiF. Note the different scales in the y-axis. Some coupling values are included in Table 9.5.	73
Figure 9.7	Rotation angles of the diabatization matrix \mathbf{U} for the different two methodologies of the diabatization in the LiF molecule.	74
Figure 9.8	Potential energy curves of the two lowest diabatic ${}^1\Sigma$ states of LiF molecule by implementing two diabatization procedures.	74
Figure 9.9	Adiabatic populations of the ${}^1\Sigma_i$ electronic diabatic states and ${}^1\Sigma$ electronic adiabatic states after a sudden excitation of the LiF molecule with a laser pulse.	75
Figure 9.10	Photodissociation probabilities and Kinetic energy release (KER) in the Σ electronic states after a sudden excitation to the first ${}^1\Sigma$ excited electronic state in LiF molecule.	75
Figure 10.1	Contour plots of \tilde{X}^1A_1 and \tilde{A}^1B_1 Potential energy surface (PES) of H_2O and HOD molecules.	79
Figure 10.2	3D representation of the ground (\tilde{X}^1A_1) and first excited (\tilde{A}^1B_1) electronic states of the H_2O and HOD molecules.	79
Figure 10.3	Schematic representation of the orientation of HOD molecule in space, where the xy -plane contains the three atoms of the molecule.	80
Figure 10.4	Vibrational normal modes of H_2O molecule.	81
Figure 10.5	Three lowest vibrational states in the electronic ground state \tilde{X}^1A_1 of H_2O molecule.	82
Figure 10.6	Average position of the two bond coordinates (r_{H_1} and r_{H_2}) excited along a local mode.	84
Figure 10.7	Wavepackets dynamics for the H_2O molecule subject to IR+UV pump-probe pulses at different times.	85
Figure 10.8	Photodissociation probabilities along the two dissociating channels OH_2+H_1 and H_2+OH_1	85

Figure 10.9	Three lowest vibrational states in the electronic ground state \tilde{X}^1A_1 of HOD molecule.	86
Figure 10.10	Average position of the two bond coordinates (r_H and r_D) when the HOD molecule is heating with a IR laser pulse.	87
Figure 10.11	Wavepackets dynamics for the HOD molecule subject to IR+UV pump-probe pulses at different times.	88
Figure 10.12	Photodissociation probabilities of both Hydrogen atoms when the HOD molecule.	88
Figure 10.13	Schematic representation of CO_2 molecule and its internal coordinates.	89
Figure 10.14	Fourth lowest states in the symmetry $^1A'$ of CO_2 molecule.	91
Figure 10.15	Family of the CO_2 orbitals used in the electronic structure calculations.	92
Figure 10.16	Comparison between three different types of calculations (Equations of motion coupled-cluster singles and doubles (EOM-CCSD), Multi-Configurational Self Consistent Field (MCSCF)/Multireference Configuration Interaction (MRCI) (12,11) and MCSCF/MRCI (16,10)) for the six lowest states in the CO_2 molecule.	92
Figure 10.17	Molecular orbital diagram of CO_2 molecule.	93
Figure 10.18	(a) Adibatic (b) Diabatic states in the symmetry $^1A'$ calculated at the EOM-CCSD level of theory.	95
Figure 10.19	Adibatic and diabatic electronic states of the six lowest states in the CO_2 molecule.	97
Figure 10.20	Time dependent populations and dissociation probability for the initial $^4A'$ and the coupled $^2A'$ and $^3A'$ states. The initial wave packet located at the Frank-Condon region of the $^4A'$ state.	98
Figure 10.21	Time dependent populations of $^1A'$ and $^1A''$ excited states after XUV excitation from the $^1A'$ with a laser pulse of duration $T = 3$ fs.	100
Figure 10.22	Time dependent photodissociation probability of $^1A'$ and $^1A''$ excited states after XUV excitation from the $^1A'$ with a laser pulse of duration $T = 3$ fs.	100
Figure 10.23	Time dependent populations of $^1A'$ and $^1A''$ excited states after XUV excitation from the $^1A'$ with a laser pulse of duration $T = 10$ fs.	101
Figure 10.24	Time dependent photodissociation probability of $^1A'$ and $^1A''$ excited states after XUV excitation from the $^1A'$ with a laser pulse of duration $T = 10$ fs.	101
Figure 10.25	Time dependent populations of $^1A'$ and $^1A''$ excited states after XUV excitation from the $^1A'$ with a laser pulse of duration $T = 20$ fs.	102
Figure 10.26	Time dependent photodissociation probability of $^1A'$ and $^1A''$ excited states after XUV excitation from the $^1A'$ with a laser pulse of duration $T = 20$ fs.	102
Figure 11.1	Schematic representation of CH_3 and the internal coordinates used in the calculations.	105
Figure 11.2	1D Potential energy curve (PEC) against the CH radial distance of the lowest six adiabatic states of symmetry $1A'$ of the methyl molecule CH_3	106
Figure 11.3	1D PEC against the CH radial distance of the lowest six adiabatic states of symmetry $1A'$ of the methyl molecule CH_3 with their corresponding 'avoided crossings'.	106
Figure 11.4	1D PEC against the CH radial distance of the lowest six adiabatic states of symmetry $1A'$ of the methyl molecule CH_3 with their corresponding real avoided crossings.	107
Figure 11.5	Electrostatic couplings obtained after diabatization between different $1A'$ diabatic states of the methyl molecule along the CH bond coordinate.	108
Figure 11.6	Step by step diabatization procedure of the six lowest $^1A'$ adiabatic states of CH_3 molecule.	108
Figure 11.7	Resulting 1D six lowest diabatic states in the symmetry $^1A'$ of CH_3 molecule in terms of the C-H bond distance. Notation is the same that in the adiabatic PEC to simply the explanations between diabatic and adiabatic PEC	109
Figure 11.8	PES of diabatic states $^2A'$, $^3A'$, $^4A'$ and $^6A'$ of methyl molecule as a function of the CH bond distance and the bending angle. The inset is a reference of the equilibrium bending angle of the methylene molecule.	109
Figure 11.9	Evolution of the wavefunctions in the $^1A'$ diabatic states after a sudden excitation from the $^1A'$ state to the $^6A'$ state.	110
Figure 11.10	Populations and dissociation probabilities in the $^1A'$ electronic states after a sudden excitation to the $^6A'$ electronic state in CH_3 molecule.	111
Figure 12.1	Modified potential energy curves for the light dressed states due to two different cavity mode frequencies.	115

Figure 12.2	Time-dependent population and dissociation probability corresponding to the adiabatic ground state $1^1\Sigma$ for the molecule LiF initially fully excited in the $2^1\Sigma$ and coupled with the radiation present in a cavity in the form of the Fock vacuum state	117
Figure 12.3	Snapshots of the time-dependent evolution for the probability density of the entangled radiation-molecule wave packet moving in the potential $1^1\Sigma$ energy surface.	118
Figure 12.4	Snapshots of the time-dependent evolution for the probability density of the entangled radiation-molecule wave packet moving in the potential $2^1\Sigma$ energy surface.	118
Figure 12.5	Time-dependent population and dissociation probability corresponding to the adiabatic ground state $1^1\Sigma$ for the molecule LiF initially fully excited in the $2^1\Sigma$ and coupled with the radiation present in a cavity in the form of a coherent state.	120
Figure 12.6	Snapshots of the time-dependent evolution for the probability density of the entangled radiation-molecule wave packet moving in the potential $1^1\Sigma$ energy surface when the initial state of the radiation mode is the coherent state $\alpha = 4e^{i\pi/4}$	121
Figure 12.7	Snapshots of the time-dependent evolution for the probability density of the entangled radiation-molecule wave packet moving in the potential $2^1\Sigma$ energy surface when the initial state of the radiation mode is the coherent state $\alpha = 4e^{i\pi/4}$	121
Figure 12.8	Time-dependent population and dissociation probability corresponding to the adiabatic ground state $1^1\Sigma$ for the molecule LiF initially fully excited in the $2^1\Sigma$ and coupled with the radiation present in a cavity in the form of a squeezed coherent state.	123
Figure 12.9	Snapshots of the time-dependent evolution for the probability density of the entangled radiation-molecule wave packet moving in the potential $1^1\Sigma$ energy surface when the initial state of the radiation mode is the squeezed coherent state $\bar{n} = 4$, $r = 2$ and $\psi - \theta/2 = 2\pi/5$	124
Figure 12.10	Snapshots of the time-dependent evolution for the probability density of the entangled radiation-molecule wave packet moving in the potential $1^1\Sigma$ energy surface when the initial state of the radiation mode is the squeezed coherent state $\bar{n} = 4$, $r = 2$ and $\psi - \theta/2 = 2\pi/5$	124
Figure 12.11	Time-dependent population corresponding to the adiabatic ground state $1^1\Sigma$ and the lowest excited state $2^1\Sigma$ for the molecule LiF initially fully excited in the $2^1\Sigma$ and coupled with the radiation present in a cavity in the form of the Fock vacuum state $ 0\rangle$	126
Figure 12.12	Vibrational energy distribution of the adiabatic ground state $1^1\Sigma$ for the cavity frequencies $\omega_c = 2.91$ eV and $\omega_c = 2.09$ eV and for two different evolution times.	127
Figure 12.13	Final population of the $1^1\Pi$ excited state as a function of the pump-probe delay t_0 for different cavity mode frequencies and different laser frequencies.	128
Figure 12.14	Final population of the $1^1\Pi$ excited state as a function of the pump-probe delay t_0 for different cavity mode frequencies and different laser frequencies.	129
Figure 12.15	Populations and snapshots for three different time delays of the time-dependent evolution for the probability density of the entangled radiation-molecule wave packet moving in all PES for a cavity mode frequency $\omega_c = 2.91$ eV and a laser frequency $\omega = 2.0$ eV.	130
Figure 12.16	Dissociation yields of the adiabatic electronic states $1^1\Sigma$ and $1^1\Pi$ in terms of the KER.	131
Figure 12.17	Populations for three different time delays of the time-dependent evolution for the probability density of the entangled radiation-molecule wave packet moving in all PES for a cavity mode frequency $\omega_c = 2.91$ eV and a laser frequency $\omega = 2.5$ eV.	132
Figure 12.18	Populations and snapshots for three different time delays of the time-dependent evolution for the probability density of the entangled radiation-molecule wave packet moving in all PES for a cavity mode frequency $\omega_c = 2.09$ eV and a laser frequency $\omega = 1.5$ eV.	133
Figure 12.19	Populations and snapshots for three different time delays of the time-dependent evolution for the probability density of the entangled radiation-molecule wave packet moving in all PES for a cavity mode frequency $\omega_c = 2.09$ eV and a laser frequency $\omega = 2.0$ eV.	134

LIST OF TABLES

Table 9.1	Electronic states for Hydrogen molecule and its ion.	67
Table 9.2	Parameters of the Morse potentials for the ground electronic states of the hydrogen molecule and its ion.	68
Table 9.3	Vibrational energy spectrum for the bound states of the ground electronic states for Hydrogen molecule and its ion.	69
Table 9.4	Adiabatic potential energy points calculated for the two lowest $^1\Sigma$ states and the lowest $^1\Pi$ state of LiF. All quantities are in a.u.	71
Table 9.5	Diagonal (μ_{ii}) and non-diagonal (μ_{ij}) dipole moments and non-adiabatic couplings (NAC) (f_{12}) values calculated for the two lowest $^1\Sigma$ states and the lowest $^1\Pi$ state in LiF at a series of internuclear distances. All quantities are in a.u. .	76
Table 10.1	Parameters for the parametrized electronic ground state \tilde{X}^1A_1 of HOD molecule. .	78
Table 10.2	Energy of the three lowest vibrational states in the electronic ground state \tilde{X}^1A_1 of H_2O molecule.	83
Table 10.3	Energy of the three lowest vibrational states in the electronic ground state \tilde{X}^1A_1 of HOD molecule.	84
Table 10.4	Vertical transitions energies ΔE_v of the three lowest states of CO_2 molecule in each irreducible representation of the Cs point group.	93
Table 10.5	Comparison between the vertical transitions energies to the lowest-lying excited states of CO_2 molecule.	95
Table 10.6	Vertical transitions energies and oscillator strengths for the lowest-lying excited states of CO_2 molecule.	96
Table 11.1	Parameters for the six avoided crossing in the six lowest electronic states in the $^1A'$ symmetry for CH_3 molecule.	108
Table 12.1	Set of cavity mode wavelengths λ_c and frequencies ω_c used in this work.	116
Table 12.2	Values of the probe pulse time delay τ (in fs) of maxima and minima of final population of the $1^1\Pi$ excited state.	128
Table A.1	Character Table of C_{2v} Point Group.	139
Table A.2	Product Table for C_{2v} Point Group.	139
Table A.3	Character Table of C_s Point Group.	139
Table A.4	Product Table for C_s Point Group.	139

ACRONYMS

- BO** Born-Oppenheimer
BH Born-Huang
CAP Complex absorbing potential
CASSCF Complete active space self-consistent field
CCSD Coupled-cluster singles and doubles
CoIn Conical intersection
CSF Configuration state functions
DFT Density functional theory
DOF Degree of freedom
EOM-CCSD Equations of motion coupled-cluster singles and doubles
HF Hartree-Fock
HF-SCF Hartree-Fock Self-consistent Field
KER Kinetic energy release
LIC Light induced crossing
MCTDH Multiconfigurational time-dependent Hartree
MRCI Multireference Configuration Interaction
MCSCF Multi-Configurational Self Consistent Field
NAC non-adiabatic couplings
OCT Optimal control theory
PEC Potential energy curve
PES Potential energy surface
RWA Rotating wave approximation
SPF Single particle function
TDH Time-dependent Hartree
TDSE Time-dependent Schrödinger equation
TISE Time-independent Schrödinger equation
WF Wavefunction

INTRODUCTION

Theoretical fundamentals of molecular dynamics allows to deal with many problems associated to physics and chemistry. There is a long history in the literature on developments in molecular dynamics from the early beginning of quantum mechanics. Nevertheless, even today, there is still a huge number of non-solved problems in chemical physics related to the *ab initio* study of chemical reactions. One known catalyst of chemical reactions is the radiation, in the form of continuous or pulsed fields, that in general produce intricate excursions of the reactants through a complex landscape of excited states, to finally arrive at some products. Procedures to optimize a previously selected reaction yield is at the heart of present efforts in the control of chemistry by radiation fields. This work applies *ab initio* methods for the calculation of the electronic structure of molecules and for the quantum molecular dynamics of some chosen simple molecules, when submitted to electromagnetic fields. The basic goal relies in the selection and control of different reaction pathways, like in multistate photodissociation, where several open channels are available.

In addition to laser pulse active control, nowadays in chemical physics, a new *hot topic* of research has been called *femtochemistry*, where pulsed electromagnetic fields in the range of femtoseconds (fs) or a few picoseconds (ps), called ultrashort pulses, are used to perform control over molecular systems. The field of the femtochemistry was opened in 1999 by the Nobel Prize in Chemistry of Ahmed H. Zewail for his studies using ultrashort pulses to observe how atoms move in a molecule during a chemical reaction using flashes of laser light on the timescales of the order of femtoseconds (10^{-15} seconds). One of the important points to apply ultrashort pulses is that there lies the possibility of controlling chemical reactions in the molecular natural time window. However, the light-matter interaction produced to submit the molecular system to electromagnetic fields, can be treated from the semiclassical or quantum point of view. In the semiclassical approximation, the molecular system is treated by quantum mechanics and the external electromagnetic field or laser pulse by classical electrodynamics, i. e., by the Maxwell's equations. In the quantum case, both the electromagnetic field and the molecular system must be described by quantum mechanics. In this latter case, it is necessary to incorporate the quantum theory of light, which requires the quantization of electromagnetic field from Maxwell equations. This quantum theory of light is capable to explain well known quantum effects, such as spontaneous emission [1, 2], the Lamb shift [2–4], the Casimir effect [5, 6], and the photon statistics of the laser [2, 7].

The concept of molecular system is very broad, which ranges from the simplest hydrogen molecule to complex aminoacids and DNA chains. However, this work focusses on the study of small molecules with a limited number of electrons, so that one can apply the most sophisticated *ab initio* methods developed in electronic structure theory to compute potential energy surfaces, not only for the ground states but also for a large manifold of excited states. A proper calculation of the potential energy surfaces is crucial to obtain the correct landscape in which nuclei move. One of the molecules that satisfy the conditions of being small and simple is the carbon dioxide (CO₂), which is currently one the most studied molecules due to its relation with the industry and the greenhouse effect, which makes that CO₂ emissions be the main reason of the global warming. To study and perform some control in the dissociation CO₂ molecule can be useful in the potential reduction of the greenhouse effect.

Despite many efforts in quantum optics area, where the quantum nature of light is employed using model Hamiltonians for open quantum systems with a minimal number of states (qubits), the studies of many-state molecular dynamics with a full quantum description of light are still scarce. An important part to this PhD work is related to deal with the interaction of real molecules with quantized radiation, in the context of molecules immersed in quantum optical cavities.

This thesis is divided in four parts. First, a brief introduction of the electronic structure is developed in order to explain how one reaches the adiabatic approximation and how this adiabatic approximation is necessary for the *ab initio* calculations of the potential energy surfaces. In addition, the different methods of electronic structure used along this work, from the Hartree-Fock method to the coupled cluster singles and doubles, are explained briefly to understand the differences and consequences of using one or another. The next part is dedicated to explain the molecular quantum dynamics, which includes methods to solve the time-dependent Schrödinger equation, specifically one of the most sophisticated multistate and multidimensional methods to propagate the nuclear motion of reactions, namely, the multiconfigurational time-dependent Hartree method (MCTDH) ([MCTDH](#)). Also, different types of dynamics, diabatic and adiabatic, are discussed and applied in our chosen molecular systems. This follows with a brief description of radiation, both in semiclassical and quantum treatments. Finally, the last part contains all the results obtained in this work. Since this work deals with simple molecules, examples among diatomic, triatomic and tetratomic molecules are selected. The chapters in this last part are dedicated to a specific type of molecule: diatomic, triatomic or tetratomic ones. In this way, one has a different flavor of the computational methods and approximations when enlarging the molecular system, both in the calculation of energies and the corresponding quantum dynamics. Specifically, this part of the work starts with the most simple molecules which are the ionized hydrogen molecule (H_2^+) and the hydrogen molecule (H_2), following by the lithium fluorine molecule (LiF), then it moves to triatomic molecules like water (H_2O) and CO_2 , with tetratomic molecules like the methyl radical (CH_3), and it ends up with a very important contribution, the study of the quantum photodynamics of the simple heteronuclear diatomic molecule LiF, with an intrinsic dipole moment, confined in a quantum optical cavity.

PART I

ELECTRONIC STRUCTURE

To those who do not know mathematics it is difficult to get across a real feeling as to the beauty, the deepest beauty, of nature... If you want to learn about nature, to appreciate nature, it is necessary to understand the language that she speaks in.

— Richard P. Feynman

1

ADIABATIC APPROXIMATIONS

The cornerstone of *ab initio* molecular quantum dynamics lies in the solution of the Time-dependent Schrödinger equation (TDSE), which requires a previous solution of its Time-independent Schrödinger equation (TISE) counterpart to get the stationary basis for the electronic and nuclear structure of the molecular system. This part of the work is then concerned about the time-independent description of the molecular structure and the solution of the molecular TISE. Because of mathematical and computational issues, the solution of molecular TISE, even in simple molecules, requires a set of approximations. The main body of approximations in molecules are known as the *BO*, the *adiabatic* and the *Born-Huang (BH)* approximations, which are different. To clarify this issue, first, the complete Hamiltonian used for a molecular system is described in order to introduce the previous mentioned approximations to solve the TISE.

The Hamiltonian operator for a molecule is given by

$$\hat{H}(\mathbf{Q}, \mathbf{q}) = \hat{T}_N(\mathbf{Q}) + \hat{T}_e(\mathbf{q}) + \hat{V}_{NN}(\mathbf{Q}) + \hat{V}_{Ne}(\mathbf{Q}, \mathbf{q}) + \hat{V}_{ee}(\mathbf{Q}, \mathbf{q}), \quad (1.1)$$

where \hat{T}_N and \hat{T}_e are the kinetic energy operators for the nuclei and electrons, respectively, \hat{V}_{NN} is the potential energy operator for the repulsion between nuclei, \hat{V}_{Ne} is the potential energy operator for the electrons-nuclei attraction and \hat{V}_{ee} is the repulsive potential between electrons. \mathbf{Q} and \mathbf{q} correspond to vectors for the nuclei and electrons coordinates, respectively. Eq. (1.1) can be shortened to

$$\hat{H}(\mathbf{Q}, \mathbf{q}) = \hat{T}_N(\mathbf{Q}) + \hat{H}_{el}(\mathbf{Q}, \mathbf{q}) = - \sum_{i=1}^N \frac{1}{2\mu_i} \nabla_{\mathbf{Q}_i}^2 + \hat{H}_{el}(\mathbf{Q}, \mathbf{q}), \quad (1.2)$$

where μ_i is the reduced mass for each nuclear coordinate \mathbf{Q}_i in a molecule with N atoms and $\hat{H}_{el}(\mathbf{Q}, \mathbf{q}) = \hat{T}_e(\mathbf{q}) + \hat{V}_{NN}(\mathbf{Q}) + \hat{V}_{Ne}(\mathbf{Q}, \mathbf{q}) + \hat{V}_{ee}(\mathbf{Q}, \mathbf{q})$ is the electronic Hamiltonian for n electrons, which in atomic units is given by

$$\begin{aligned} \hat{H}_{el}(\mathbf{Q}, \mathbf{q}) &= \hat{h}(\mathbf{Q}, \mathbf{q}) + \hat{g}(\mathbf{q}) + V_N(\mathbf{Q}) \\ &= \underbrace{-\frac{1}{2} \sum_{i=1}^n \nabla_{\mathbf{q}_i}^2}_{\text{kinetic operator}} - \underbrace{\sum_{j=1}^n \sum_{i=1}^n \left[\frac{Z_j}{|\mathbf{q}_i - \mathbf{Q}_j|} \right]}_{\text{nuclei-electron}} + \underbrace{\sum_{i < j=1}^n \frac{1}{|\mathbf{q}_i - \mathbf{q}_j|}}_{\text{electron-electron}} + \underbrace{\sum_{i < j=1}^n \frac{Z_i Z_j}{|\mathbf{Q}_i - \mathbf{Q}_j|}}_{\text{nuclei-nuclei}} \end{aligned} \quad (1.3)$$

where $\hat{h}(\mathbf{Q}, \mathbf{q})$ corresponds to the independent electron Hamiltonian, $\hat{g}(\mathbf{q})$ to the electron-electron interaction term and $V_N(\mathbf{Q})$ to the repulsion among nuclei. This Hamiltonian enters in the Schrödinger equation

$$\hat{H}(\mathbf{Q}, \mathbf{q})\Psi_k(\mathbf{Q}, \mathbf{q}) = E_k \Psi_k(\mathbf{Q}, \mathbf{q}) \quad (1.4)$$

where E_k are the exact total energy eigenvalues and $\Psi_k(\mathbf{Q}, \mathbf{q})$ the exact total eigenfunctions of the molecule. However, it is worth noting that Eq. (1.4) does not have exact solutions because the total Hamiltonian in Eq. (1.1) does not allow a separation of variables. Then, since no exact solution is available, the introduction of approximations is mandatory and the first approximation involved in the molecular electronic structure theory is the so called

adiabatic approximation. M. Born and J. Oppenheimer (BO) in 1927 [8] introduced a very good approximation in which the nuclear motion within the molecule can be considered stationary with respect to that of the electrons. In mathematical terms, the BO approximation establishes that the molecular Schrödinger equation quoted in Eq. (1.4) can be treated as separated equations for the electronic and nuclear motions, i.e., with a separation of variables. One of the consequences of separating the nuclear part from the electronic one is that in order to calculate the total energy of a molecular state one has to solve first the electronic Schrödinger equation for a set of nuclear geometries, which provides a PES for the nuclear motion. The subsequent solution of the nuclear equation with this electronic potential provides the total molecular energies.

Because electrons move rapidly compared to the nuclei, the fixed or stationary geometric parameters of the molecule are the nuclear coordinates. Although the nuclei are considered as stationary against electrons within the BO approximation, actually the nuclei are not stationary but they execute vibrations of small amplitude about equilibrium positions of the nuclear coordinates (in the case of dissociation they separate from each other with a given kinetic energy). As mentioned above, the calculated electronic energy for different nuclear geometries give rise to the concept of PES, and they come from the solution of the electronic Schrödinger equation given by

$$\hat{H}_{el}(\mathbf{Q}, \mathbf{q})\psi_n(\mathbf{Q}, \mathbf{q}) = \epsilon_n(\mathbf{Q})\psi_n(\mathbf{Q}, \mathbf{q}), \quad (1.5)$$

where $\epsilon_n(\mathbf{Q})$ and $\psi_n(\mathbf{Q}, \mathbf{q})$ are the n -th electronic energy eigenvalue and the n -th electronic eigenfunction, respectively. Both quantities depend upon the fixed nuclear geometry \mathbf{Q} in a parametric form. Even for diatomic molecules, the solution of the electronic Schrödinger equation is known to be exact only for H_2^+ and for the rest of many-electron molecules accurate variational solutions must be implemented computationally.

Although the simplest one-electron molecule H_2^+ allows for an exact solution for the electronic Hamiltonian, it is no longer possible to solve the Schrödinger equation for the total molecular Hamiltonian, including nuclear motion. Here one must perform non-BO variational calculations using composed nuclear-electronic basis sets, which can be very expensive computationally. Non-BO solutions provide total vibronic states and energies without making use of potential energy surfaces, a concept attached to the BO approximation.

A way to make explicit use of BO solutions is to expand the total solution for the k -th state in terms of the BO complete electronic basis set $\Psi_k(\mathbf{Q}, \mathbf{q})$, according to the BH expansion, i.e.,

$$\Psi_k(\mathbf{Q}, \mathbf{q}) = \sum_{n=1}^{\infty} \psi_n(\mathbf{Q}, \mathbf{q})\phi_n(\mathbf{Q}). \quad (1.6)$$

In practical situations this ansatz is truncated to a subspace in the Hilbert space of M electronic eigenstates. Introducing the expansion in Eq. (1.6) into Eq. (1.4), multiplying the result by $\psi_n^*(\mathbf{Q}, \mathbf{q})$ and integrating over all the electronic coordinates \mathbf{q} (to solve the electronic Schrödinger equation), one arrives to a set of coupled differential equations for the nuclear wave functions $\phi_n(\mathbf{Q})$ in the form

$$\begin{aligned} & \left[-\sum_{i=1}^{\infty} \frac{1}{2\mu_i} \nabla_{Q_i}^2 + \epsilon_n(\mathbf{Q}) - \sum_{i=1}^{\infty} \left\langle \psi_n(\mathbf{Q}, \mathbf{q}) \left| \frac{1}{2\mu_i} \nabla_{Q_i}^2 \right| \psi_n(\mathbf{Q}, \mathbf{q}) \right\rangle - E_n \right] \phi_n(\mathbf{Q}) \\ & - \sum_{n \neq m}^{\infty} \left[\sum_{i=1}^N \frac{1}{\mu_i} \langle \psi_m(\mathbf{Q}, \mathbf{q}) | \nabla_{Q_i} | \psi_n(\mathbf{Q}, \mathbf{q}) \rangle \cdot \nabla_{Q_i} \right. \\ & \left. + \sum_{i=1}^{\infty} \left\langle \psi_m(\mathbf{Q}, \mathbf{q}) \left| \frac{1}{2\mu_i} \nabla_{Q_i}^2 \right| \psi_n(\mathbf{Q}, \mathbf{q}) \right\rangle \right] \phi_n(\mathbf{Q}) = 0, \end{aligned} \quad (1.7)$$

or in a compact form

$$\begin{aligned} & [\hat{T}_N(\mathbf{Q}) + \epsilon_n(\mathbf{Q}) + \langle \psi_n(\mathbf{Q}, \mathbf{q}) | \hat{T}_N(\mathbf{Q}) | \psi_n(\mathbf{Q}, \mathbf{q}) \rangle - E_n] \phi_n(\mathbf{Q}) \\ & - \sum_{n \neq m}^{\infty} \left[\sum_{i=1}^N \left(\frac{1}{\mu_i} \mathbf{F}_{mn}^i(\mathbf{Q}) \cdot \nabla_{Q_i} - \frac{1}{2\mu_i} \mathbf{G}_{mn}^i(\mathbf{Q}) \right) \right] \phi_n(\mathbf{Q}) = 0, \end{aligned} \quad (1.8)$$

where $F_{mn}^i(Q)$ and $G_{mn}^i(Q)$ are the non-diagonal coupling terms that read

$$F_{mn}^i(Q) = \int \psi_m^*(Q, q) \nabla_{Q_i} \psi_n(Q, q) dq \equiv \langle \psi_m(Q, q) | \nabla_{Q_i} | \psi_n(Q, q) \rangle \quad (1.9)$$

$$G_{mn}^i(Q) = \int \psi_m^*(Q, q) \nabla_{Q_i}^2 \psi_n(Q, q) dq \equiv \langle \psi_m(Q, q) | \nabla_{Q_i}^2 | \psi_n(Q, q) \rangle. \quad (1.10)$$

These two latter terms are called non-adiabatic couplings (NAC) and they introduce the coupling between different electronic states caused by the variation in the nuclear motion (gradient and laplacian with respect to the nuclear coordinates). If the electronic WFs ψ_n change rapidly against small changes in the nuclear geometry, this couplings must be accounted for. If not, these NAC can be neglected and the term in the second line of Eq. (1.8) vanishes together with the diagonal correction term, and the BO solution reduces to an equation for the nuclear motion with a single PES (BO separation) and it refers to the adiabatic solution.

Nevertheless, different adiabatic approximations are in use [9]

1. Crude diabatic approximation.
2. Born-Oppenheimer approximation.
3. Born-Huang adiabatic approximation,

where the differences between them is in the terms neglected for the solution in each particular case. All these adiabatic approximations have the same startpoint which is the time-independent electronic Schrödinger equation given in Eq. (1.5).

1.1 CRUDE DIABATIC APPROXIMATION

The key point of the crude diabatic approximation is to take the nuclear coordinates $Q = Q_0$, where Q_0 is a fixed geometrical configuration of the system at point Q_0 , in other words, one can assumed that the nuclei are fixed in the space. Hence, the electronic Hamiltonian in Eq. (1.3) can be written as

$$\begin{aligned} \hat{H}_{el}(Q, q) &= \hat{T}_{el}(q) + \hat{V}(Q, q) = \hat{T}_{el}(q) + \hat{V}(Q_0, q) + \Delta\hat{V}(Q, Q_0, q) \\ &= \hat{H}_{el}(Q_0, q) + \Delta\hat{V}(Q, Q_0, q), \end{aligned} \quad (1.11)$$

where $\Delta\hat{V}(Q, Q_0, q) = \hat{V}(Q, q) - \hat{V}(Q_0, q)$ and $\hat{H}_{el}(Q_0, q)$ corresponds to the electronic Hamiltonian at the geometry Q_0 , for which the TISE is

$$\hat{H}_{el}(Q_0, q)\psi_n^0(Q_0, q) = \epsilon_n^0(Q_0)\psi_n^0(Q_0, q), \quad (1.12)$$

and the total wavefunction in the crude adiabatic approximation $\psi_k^{CA}(Q_0, q)$ is

$$\psi_k^{CA}(Q, q) = \sum_{n=1}^{\infty} \psi_n^0(Q_0, q)\phi_n^{CA}(Q), \quad (1.13)$$

where the completeness of the electronic basis set at point Q_0 is used to expand the the k -th wave function $\psi_k^{CA}(Q, q)$. Now this expansion can be inserted in the total molecular Schrödinger equation. Since the electronic wave function is defined at a fixed point, the matrix elements for the NAC vanish and, consequently, the remaining uncoupled equation has the form

$$\left[\hat{T}_N(Q) + \epsilon_n^0(Q_0) + \hat{V}(Q) + \langle \psi_n^0(Q_0, q) | \Delta\hat{V}(Q, Q_0, q) | \psi_n^0(Q_0, q) \rangle - E_n^{CA} \right] \phi_n^{CA}(Q) = 0. \quad (1.14)$$

Eqs. (1.11) to (1.14) define the crude adiabatic approximation and it is called in this form following the work performed by Ballhausen and Hansen [10].

1.2 BORN-OPPENHEIMER ADIABATIC APPROXIMATION

The **BO** is the keystone to perform molecular calculations to elucidate their chemical structure and dynamics. In contrast to the crude adiabatic approximation, a complete electronic basis set is used for each nuclear geometry \mathbf{Q} , i.e., the eigensolutions of the electronic Schrödinger equation

$$\hat{H}_{\text{el}}(\mathbf{Q}, \mathbf{q})\psi_n(\mathbf{Q}, \mathbf{q}) = \epsilon_n(\mathbf{Q})\psi_n(\mathbf{Q}, \mathbf{q}), \quad (1.15)$$

that allows for the Born-Huang expansion [11]

$$\Psi_k^{\text{BO}}(\mathbf{Q}, \mathbf{q}) = \sum_{n=1}^{\infty} \psi_n(\mathbf{Q}, \mathbf{q})\phi_n^{\text{BO}}(\mathbf{Q}), \quad (1.16)$$

In contrast to the *crude diabatic approximation*, explained in the previous section, in the **BO** approximation there is no a reference nuclear configuration \mathbf{Q}_0 , i.e., for each nuclear configuration one can obtain a different value for the electronic energy, which allows to represent molecules as a set of moving nuclei over a **PES** provided by the electronic interactions. These **PES** (given in this case by $\epsilon_n(\mathbf{Q})$) are obtained by solving the time-independent electronic Schrödinger equation (see Eq. (1.15)). To get the nuclear wave functions $\phi_n^{\text{BO}}(\mathbf{Q})$, from Eq. (1.8) one neglects all terms coming from the action of \hat{T}_N operator over the electronic Wavefunction (**WF**), which means

$$\begin{aligned} \langle \psi_n(\mathbf{Q}, \mathbf{q}) | \hat{T}_N(\mathbf{Q}) | \psi_n(\mathbf{Q}, \mathbf{q}) \rangle &= 0 \\ \sum_{n \neq m}^{\infty} \left[\sum_{i=1}^N \left(\frac{1}{\mu_i} \mathbf{F}_{mn}^i(\mathbf{Q}) \cdot \nabla_{Q_i} - \frac{1}{2\mu_i} \mathbf{G}_{mn}^i(\mathbf{Q}) \right) \right] &= 0. \end{aligned} \quad (1.17)$$

Consequently, the nuclear **TISE**, after Eq. (1.8) in the **BO** approximation is given by

$$[\hat{T}_N(\mathbf{Q}) + \hat{V}(\mathbf{Q}) + \epsilon_n(\mathbf{Q}) - E_n^{\text{BO}}] \phi_n^{\text{BO}}(\mathbf{Q}) = 0, \quad (1.18)$$

which depends only on the diagonal **PES** $\epsilon_n(\mathbf{Q})$ explicitly.

One of the properties of the **BO** approximation is that the **PES** are independent of the nuclear masses, therefore they are the same for isotopic molecules. However, whereas the validity of this approximation for the vast majority of chemistry is not in doubt, the **BO** approximation breaks down in many important cases. This breakdown is particularly present in molecular photochemistry, when two or more **PES** show near degeneracies for one or more nuclear degrees of freedom [12]. An example already comes from diatomic molecules like lithium fluoride (LiF). Beyond the equilibrium bond distance the electronic cloud in LiF is strongly polarized, i.e., the electronic structure is described by an ionic state ($1^1\Sigma$) with a typical $-Q_1Q_2/R$ Coulomb behavior for the **PES**. However, if the molecule dissociates into neutral atoms, Li + F, the corresponding **PES** behaves with a covalent character, whose long-range trend follows that of a van der Walls interaction, usually represented through exponential Morse or Lennard-Jones potentials. Since the asymptotic energy of the ionic fragments $\text{Li}^+ + \text{F}^-$ is higher than the fragmentation into neutrals Li+F, the ground state and the lowest excited state must cross at a given internuclear distance. Because these two states have the same $^1\Sigma$ symmetry, they do not cross due to the Wigner-von Neumann non-crossing rule [13] and they form an adiabatic avoided crossing. From the equilibrium distance, when the LiF molecule reaches the region of the avoided crossing, the ground state electronic **WF** abruptly changes from being ionic to covalent (here the two electronic states are strongly coupled) and the **BO** approximation breaks down here. This avoided crossing is illustrated in Fig. 1.1. The energy of the ionic state is given by the red line, while the energy of the covalent state is shown by the line in blue. For bond distances near 6.5 Å, the **WF** with the lowest (adiabatic) energy suddenly switches from being almost ionic to being covalent (region enclosed by the black circle), and the two **PEC** get closer but with a narrow separation of 0.21 a.u.

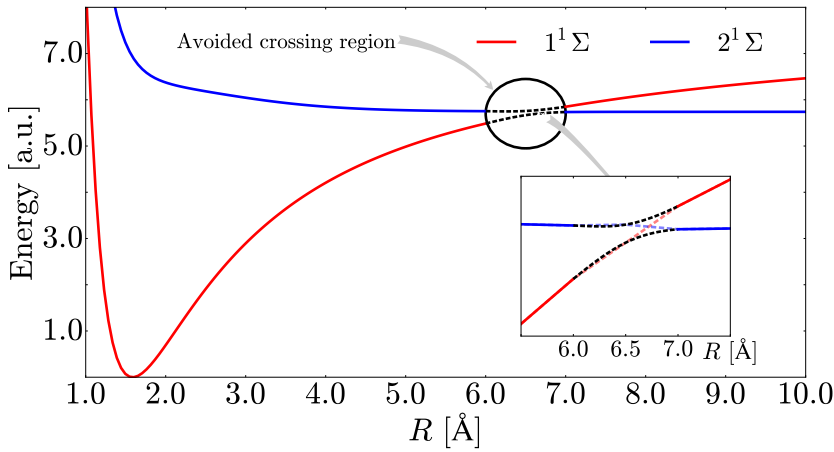


Figure 1.1: The **BO** approximation breaks down at the location of the avoided crossing between the two lowest $^1\Sigma$ states in LiF. The plot shows a diabatic representation of the two lowest states (following a smooth topological connection), whose energies actually cross to each other (see inset).

1.3 BORN-HUANG ADIABATIC APPROXIMATION

The Born-Huang adiabatic approximation starts like the adiabatic approximations explained above, with the Born-Huang expansion. Following the electronic Schrödinger equation in Eq. (1.15) and the corresponding total wavefunction $\Psi_k^{\text{BH}}(\mathbf{Q}, \mathbf{q})$ given by

$$\Psi_k^{\text{BH}}(\mathbf{Q}, \mathbf{q}) = \sum_{n=1}^{\infty} \psi_n(\mathbf{Q}, \mathbf{q}) \phi_n^{\text{BH}}(\mathbf{Q}), \quad (1.19)$$

where the nuclear WF $\phi_n^{\text{BH}}(\mathbf{Q})$ arise to introduce Eq. (1.6) into Eq. (1.4) and to solve the time-independent resultant Schrödinger equation. Compared with the crude diabatic approximation the **BH** approximation takes the same picture of the **BO** approximation, where the nuclei moving over PES provided by the electrons. However, compared with the “Born-Oppenheimer approximation”, to obtain the nuclear WF ϕ_n^{BH} , all non-diagonal terms are neglected in Eq. (1.8), as result

$$\begin{aligned} \langle \psi_m(\mathbf{Q}, \mathbf{q}) | \hat{T}_N(\mathbf{Q}) | \psi_n(\mathbf{Q}, \mathbf{q}) \rangle &= 0 \quad \text{for } m \neq n \\ \sum_{n \neq m}^{\infty} \left[\sum_{i=1}^N \left(\frac{1}{\mu_i} \mathbf{F}_{mn}^i(\mathbf{Q}) \cdot \nabla_{Q_i} - \frac{1}{2\mu_i} \mathbf{G}_{mn}^i(\mathbf{Q}) \right) \right] &= 0, \end{aligned} \quad (1.20)$$

but, in contrast to the **BO** approximation, the diagonal term $\langle \psi_n(\mathbf{Q}, \mathbf{q}) | \hat{T}_N(\mathbf{Q}) | \psi_n(\mathbf{Q}, \mathbf{q}) \rangle$ survives. Therefore, the nuclear TISE in the **BH** adiabatic approximation reads

$$\left[\hat{T}_N(\mathbf{Q}) + \hat{V}(\mathbf{Q}) + \epsilon_n(\mathbf{Q}) - E_n^{\text{BH}} + \langle \psi_n(\mathbf{Q}, \mathbf{q}) | \hat{T}_N(\mathbf{Q}) | \psi_n(\mathbf{Q}, \mathbf{q}) \rangle \right] \phi_n^{\text{BH}}(\mathbf{Q}) = 0. \quad (1.21)$$

This last equation, which corresponds to the Born-Huang adiabatic approximation, which sometimes is called the *first correction to the Born-Oppenheimer approximation* or the *diagonal correction for nuclear motion* [14, 15].

Nature isn't classical dammit, and if you want to make a simulation of nature, you'd better make it quantum mechanical, and by golly it's a wonderful problem because it doesn't look so easy.

— Richard P. Feynman

2

HARTREE-FOCK MOLECULAR ORBITAL THEORY

As it was seen in the previous chapter, once the **BO** approximation is considered, one is bound to the **PES** concept, which can be seen as a relation between the molecular energy and its molecular shape. Then, this chapter provides a brief summary of electronic structure calculations in quantum chemistry, that allow to build the molecular **PES**. The well-known starting point in *ab initio* many-electron theory is the Hartree-Fock (HF) method, from which other more elaborated *ab initio* methods can be built on top.

Within the **BO** approximation the knowledge of the forces driving the nuclei in molecular reactions is a preliminary step in molecular dynamics. These forces can be computed locally close to the position of nuclei or globally, thus having the full landscape for the nuclear motion. The latter approach means to systematically compute the **PES** for extensive regions of the molecular geometry. A molecule with N nuclei has $3N - 6$ ($3N - 5$ for linear molecules) internal nuclear degrees of freedom. A non-biased accurate calculation of a molecular **PES** may contain hundreds of energy points calculated for each set of $3N - 6$ nuclear coordinates, thus producing a $3N - 5$ dimensional surface. In most cases, this effort is computationally prohibitive. Fortunately, not all internal coordinates contribute on equal footing and some of them can be safely eliminated or be frozen at rest, which yields **PES** with a reduced dimensionality but still sound for realistic calculations.

For instance, in this thesis, the dissociation dynamics of a water molecule is treated using only two internal coordinates or modes, then with a 3D **PES**. In this case, the bending angle of the water molecule plays a minor role compared to bond distances. With similar arguments, the dissociation of the carbon dioxide molecule is studied. Also, the dissociation of the methyl radical $\text{CH}_3 \rightarrow \text{CH}_2 + \text{H}$ can be simplified with a single reaction coordinate (the radial distance between any of the equivalent hydrogen atoms and the center of mass of the residual CH_2 fragment). Notwithstanding, these reduced models may already show enough complex structures.

Not all *ab initio* methods provide energy points with the required accuracy or the correct behavior. Hartree-Fock methods are relatively good for ground states at equilibrium but they do not provide the correct energy at dissociation. Also a single HF configuration is far from enough to describe excited states at any molecular geometry.

Since post-HF methods are usually required to obtain reliable **PES**, the computational cost to get each single-point of energy can be large, and a tug of war between necessity and capacity begins.

2.1 HARTREE-FOCK METHOD: BASIC PRINCIPLES OF AB INITIO CALCULATIONS

The starting point to solve the electronic Schrödinger equation (Eq. (1.5)) in molecular systems is the Hartree-Fock (HF) method [16]. The fundamental assumption of the **HF** theory is that each electron feels the other electrons as an average field, thus considering the electronic motion as an effective independent particle problem. However, the neglect of electron correlation at its full action leads to acute consequences in the determination of molecular energies,

wavefunction and properties. The Pauli antisymmetry effects were incorporated in the Hartree method by Fock [17], producing the electron exchange terms. Later Slater [18] introduced the Pauli antisymmetry using antisymmetrized products of orbitals (one-electron wave functions) to build the many-electron wave function in the form of determinants. The **HF** method consist in a set of integrodifferential equations that must be solved from an initial electronic guess density up to self-consistency for the electronic energies and density. Hence the procedure is called Hartree-Fock Self-consistent Field (**HF-SCF**). Each n -th orbital for the j -th electron, $\phi_n(\mathbf{Q}, \mathbf{q}_j)$, is defined as the product of the spatial function $\varphi_n(\mathbf{q}_j)$ times the spin function $\chi(s_j)$, such that

$$\phi_n(\mathbf{Q}, \mathbf{q}_j) = \varphi_n(\mathbf{q}_j) \chi(s_j), \quad (2.1)$$

where the j -th electron coordinate $\mathbf{q}_j = \{\mathbf{q}_j, s_j\}$ contains the spatial and spin parts.

According to the variational principle [19, 20], the best approximation to the ground state for a molecular system with N electrons is described by the wave function $\Psi(\mathbf{Q}, \mathbf{q})$ that minimizes the electronic energy

$$E_{el} = \langle \Psi | \hat{H}_{el} | \Psi \rangle. \quad (2.2)$$

Taking into account the electronic Hamiltonian in Eq. (1.3) and the complete electronic wave function built as a Slater determinant

$$|\Psi\rangle = |\phi_1 \cdots \phi_i \cdots \phi_j \cdots \phi_N\rangle, \quad (2.3)$$

the **HF** electronic energy E_{el} is demonstrated to be

$$E_{el} = \langle \Psi | \hat{h} | \Psi \rangle + \sum_{ab}^N [J_{ab} - K_{ab}] + V_N, \quad (2.4)$$

where J_{ab} and K_{ab} are the Coulomb and exchange terms, respectively, given by the two-electron integrals

$$J_{ab} = \langle \phi_a \phi_b | 1/r_{ij} | \phi_a \phi_b \rangle \quad (2.5)$$

$$K_{ab} = \langle \phi_a \phi_b | 1/r_{ij} | \phi_b \phi_a \rangle. \quad (2.6)$$

The eigensystem for the optimized **HF** i -th orbital is the Hartree-Fock equation [21]

$$\hat{F}(\mathbf{q}_j) \phi_a(\mathbf{q}_j) = \left\{ \hat{h}_{\mathbf{q}_j} + \sum_b^N [J_b(\mathbf{q}_j) - K_b(\mathbf{q}_j)] \right\} \phi_a(\mathbf{q}_j) = \varepsilon_a \phi_a(\mathbf{q}_j), \quad (2.7)$$

where $\hat{F}(\mathbf{q}_j)$ is the Fock operator. The Fock operator contains the one-electron Hamiltonian $\hat{h}_{\mathbf{q}_j}$, which only describe the electron-nuclei interactions (see Eq. (1.3)), and the one-electron effective potential called **HF** potential (\hat{V}_{HF}) corresponding to the average-field potential produced over the i th-electron due to the presence of all other electrons. This potential can be written as

$$\hat{V}_{HF}(\mathbf{q}_i) = \sum_b^N [J_b(\mathbf{q}_i) - K_b(\mathbf{q}_i)]. \quad (2.8)$$

The replacement of a complex N -electron problem by N one-electron systems subject to an averaged-field potential is at the heart of the **HF-SCF** method. Hartree-Fock potential has two contributions, Coulomb interaction between electron i and the electrons density cloud $|\chi_j(\mathbf{q}_i)|^2$ defined in Eq. (2.5) and the exchange interaction which arises that the fact the wave function is antisymmetric respect to the electrons interchange.

Eq. (2.7) provides the optimized set of spin-orbitals $\{\phi_a(\mathbf{q}_i)\}_{a=1}^N$ that minimizes the electronic energy for a single Slater determinant. However, this is a coupled integrodifferential equation where the Fock operator depends upon the same orbitals that are required. It means that the **HF-SCF** method must be solved by successive iterations until convergence (self-consistency).

These kind of equations are known as *self-consistent equations* and it has to be solving by iterative methods.

The solution by self-consistent methods uses as a starting point a set of guess orbitals, which generate a mean-field potential \hat{V}_{HF} for each electron. The iterative solution of Eq. (2.7) gives a new set of improved spin-orbitals at each step. These improved orbitals are then used to obtain a new mean field, and so on until the HF energy or the HF WF converge. The HF-SCF method requires that the number of spin-orbitals M be larger than the number of electrons N , to allow for the variational method a variety of functional space to build the Slater determinant with N electrons occupied by N spin-orbitals. The latter N spin-orbitals with the lowest energies are named occupied orbitals and the Slater determinant built with them represents the HF many-electron WF. The other unoccupied spin-orbitals of the trial space are usually named virtual orbitals.

The solution of the HF-SCF equations using the iterative procedure for the set of coupled integrodifferential equations is very demanding. Instead, as proposed by Roothan in the fifties, the HF-SCF equations can be transformed to an algebraic method with the introduction of basis set to expand the spin-orbitals. Hence, the variational effort aims at the optimization of the expansion coefficients $C_{\alpha\alpha}$ of the orbitals $\phi_{\alpha}(q_i)$ in terms of the chosen basis set $\xi_{\alpha}(q_i)$, in the form

$$\phi_{\alpha}(q_i) = \sum_{\alpha=0}^{\infty} C_{\alpha\alpha} \xi_{\alpha}(q_i). \quad (2.9)$$

Now the HF-SCF solution transforms as an eigenvalue problem for the Fock operator (now a function of the expansion coefficients), whose converged eigenvalues are the orbital energies and its eigenvectors are the orbitals (both occupied and unoccupied).

There are different types of basis for atomic orbitals currently employed in the solution of Hartree-Fock equations [22, 23]. The most common basis set are the Gaussian type orbitals (GTOs) and the exponential Slater type orbitals (STOs) [24], the former usually chosen because all required integrals (including the two-electron integrals) can be written in closed form.

2.2 GAUSSIAN BASIS SETS FUNCTIONS

One of the simplest forms to describe the electron density distribution around an atom within a molecule is through Slater and Gaussian functions, which are the currently used in ab initio molecular computational packages like GAUSSIAN [25] and MOLPRO [26]. The general functional form of a normalized Gaussian-type orbital (GTO) is atom-centered Cartesian coordinate is

$$\xi(x, y, z; \alpha, i, j, k) = \left(\frac{2\alpha}{\pi}\right)^{3/4} \left[\frac{(8\alpha)^{i+j+k} i! j! k!}{(2i)!(2j)!(2k)!} \right]^{1/2} (x - X_A)^i (y - Y_A)^j (z - Z_A)^k e^{-\alpha[(x - X_A)^2 + (y - Y_A)^2 + (z - Z_A)^2]}, \quad (2.10)$$

where (X_A, Y_A, Z_A) are the coordinates of the A atom in the molecule, α accounts as the width of the Gaussian function and i, j and k are non-negative integers that represent the nature of the orbital in the space. Depending on the integer number for i, j and k , the GTO has a specific symmetry and therefore will represent s, p or d-type orbitals.

In particular, to achieve the HF limit the basis set has to be drop at some point, i. e., employing a linear combination of M ξ_{α} functions, i. e.,

$$\phi_i \xi(x, y, z; \{\beta\}, i, j, k) = \sum_{\beta=1}^M C_{\beta i} \xi_{\beta}(x, y, z; \alpha, i, j, k). \quad (2.11)$$

Nonetheless, if it is a linear combination of Gaussian functions, the basis set ϕ_i is referred to *Contracted Gaussian Functions* and each Gaussian function of the linear combination is called *primitive Gaussian*. In other words, a basis set composed by contracted GTOs is defined by the 'contraction' coefficients $C_{\beta i}$ and exponents α of each of its primitive Gaussian functions.

Additionally, M defines the degree or the number of primitive Gaussian functions used in the linear combination.

Currently, the most common family of GTOs used is the self-consistent correlated (*cc*) basis defined by Dunning [27–31]. The basic idea of these type of basis sets is that the functions that contribute approximately with the same correlation energy amount have to be put together. These basis set are usually shortened as *aug-cc-pVXZ* with $X = D, T, Q, 5, \dots$, where *aug* indicates that diffuse functions are included, i. e., small values for α in Eq. (2.10), X is the basis cardinal number that represents the highest spherical harmonic included in the basis and *p* indicates that the basis also includes effects of polarization. More details about each of the effects of these type of basis sets can be found in Cramer [19] and Dunning [27–31].

It is worth mentioning that diffuse functions are the utmost important to describe excited states. In particular, these diffuse electron distributions are found in molecules with heteroatoms and anions, and therefore it is necessary to include the spin-orbitals with small exponents α_i in the Gaussian basis set. These small values give enough weight to the coefficients of diffuse functions in the HF-SCF to generate electron densities at large distances of the nuclei. Typically a basis set with diffuse functions has one such function, which is composed only by a single Gaussian, for each valence atomic orbital of the heavier atoms of the molecule.

We have seen that computer programming is an art, because it applies accumulated knowledge to the world, because it requires skill and ingenuity, and especially because it produces objects of beauty.

— Donald E. Knuth

POST HARTREE-FOCK AB INITIO METHODS

3

Ab initio calculations are based in quantum mechanics principles to solve the electronic Schrödinger equation [Eq. \(1.5\)](#). Concerning the *ab initio* calculation of [PES](#), it is important to identify the most crucial regions where the reactivity takes place (reaction paths) in both ground and excited molecular states. These regions must be computed with the enough required accuracy, which implies to find methodologies able to achieve error thresholds to describe with the best possible accuracy the electronic structure, which are the chemistry precision and the spectroscopy precision. In general, those thresholds were established as ≈ 1 kcal/mol (≈ 0.044 eV ≈ 1.2 a.u.) and ≈ 1 cm $^{-1}$ (≈ 0.0044 eV ≈ 0.11 a.u.), respectively. In spite of the computer technology available nowadays, the computation of, for instance, an extensive [PES](#) for a triatomic molecule with three degrees of freedom is very expensive computationally. Hence, a previous selection of methods, of adequate basis sets and active spaces is crucial before performing the computations in different molecular geometries for the [PES](#).

High precision methods have been developed to compute *ab initio* energies at the post-Hartree-Fock level of theory, i.e., that go beyond the representation of the [WF](#) in terms of a single Slater determinant. The chosen method to compute energies for the [PES](#) in the light molecules study in this work is the Multi-Configurational Self Consistent Field method ([MCSCF](#)), then followed by a Multireference Configuration Interaction method ([MRCI](#)). The latter procedure improves the values of energies over the [MCSCF](#) values, but it is not designed to produce the better [WF](#). Consequently, some molecular properties calculated with the [WF](#) (dipole moments, non-adiabatic couplings, etc) are computed only at the [MCSCF](#) level, which produces both energies and [WFs](#).

Different post-HF methods usually employed to compute energies for [PES](#) are outlined here, specifically, [MCSCF](#), [MRCI](#) and Coupled-cluster singles and doubles ([CCSD](#)). All these methods deal with the description of all electron correlation effects absent at the [HF](#) level.

3.1 MULTI-CONFIGURATIONAL SELF-CONSISTENT FIELD (MCSCF) METHOD

As previously mentioned the [HF](#) method is based in the optimization of a single Slater determinant, which is also called a *reference configuration* (of occupied orbitals). Highly electron correlated molecular systems need a description beyond a single configuration, even for the ground state. Consequently, the multiconfigurational methods propose the [WF](#) as a linear combination of Slater determinants like, for example, in the [MCSCF](#) method, in the form

$$\Phi_{\text{MCSCF}} = \sum_I C_I \Phi_I, \quad (3.1)$$

where in this case the optimization method is performed simultaneously over the coefficients of molecular orbitals $C_{\beta i}$ (see [Eq. \(2.9\)](#)) and the C_I coefficients in the multi-determinant expansion. Thus, the molecular orbitals (MOs) are optimized given a combination of configurations.

[MCSCF](#) calculations require some *art* and technical expertise, specifically in the selection of the number of MOs that remain in the so called *active space*, which ultimately can be accessed to be partially occupied. Examples for the choice of the active space are illustrated in [Section 10.2](#) for the CO₂ molecule and in [Section 11.1](#) for the CH₃ molecule.

3.2 MULTIREFERENCE CONFIGURATION INTERACTION (MRCI) METHOD

MRCI belongs to the family of configuration interaction (CI) methods. In any CI method, the **WF** is represented by a superposition of of Slater determinants or a Configuration state functions (**CSF**) which reads

$$|\mathbf{C}\rangle = \sum_i C_i |i\rangle, \quad (3.2)$$

where the coefficients C_i are determined by a variational optimization of the expectation value of the electronic energy, that reduces to solve an eigenvalue problem of linear algebra given by

$$\hat{H}\mathbf{C} = E_{\text{CI}}\mathbf{C}, \quad (3.3)$$

where \hat{H} is the electronic Hamiltonian matrix with elements $H_{ij} = \langle i | \hat{H} | j \rangle$ and \mathbf{C} is the vector that contains the expansion coefficients C_i . Hence, to construct the wave function of the CI method one can diagonalize the Hamiltonian matrix and combining with iterative methods, one can find different options to extract selected eigenvalues and eigenvectors in order to simplify the calculations [20]. CI methods only optimize the configuration expansion and MOs are frozen, usually taken from previous calculations at lower level, either **HF** or **MCSCF**.

The construction of **MRCI** wave function begins with the generation of a set of orbitals and a reference space of configurations, usually from a previous **MCSCF** calculation. While it is computationally considerably more difficult from the computational point of view to build a **MCSCF WF** than a **HF WF**, the optimization of orbitals within **MCSCF** methods can make CI methods using these MOs to converge faster. Nonetheless, in **MRCI** calculations the number of matrix elements can be huge, and hence this method is usually employed in small molecules with a reasonable number of electrons. Electronic structure calculations in molecules like LiF, CO₂ and CH₃ are calculated in this work at the **MRCI** level.

To build a full **MRCI** wave function all possible excitations (from single excitations to multiple excitations) from occupied orbitals to unoccupied virtual orbitals must be included. This full CI **WF** has the expansion form

$$\phi_{\text{FCI}} = \phi_0 + \sum_i C_i^s \phi_i^s + \sum_j C_j^d \phi_j^d + \dots + \sum_m C_m^{n-\text{th}} \phi_m^{n-\text{th}}, \quad (3.4)$$

where ϕ_0 is the zeroth-order reference configuration from which one generates excited determinants, and the determinants ϕ_k^α represent different excitations, singles (s), doubles (d), up to n excitations for n electrons. When all possible excitations are included within a large set of virtual MOs, one may reach almost exact variational calculations. However, the full CI method becomes computationally intractable since it scales exponentially with respect to the size of the orbital bases and the number of chosen active electrons.

3.3 COUPLED CLUSTER SINGLES AND DOUBLES (CCSD)

Since the beginning of the coupled clusters (CC) methods for molecular electronic structure calculations in the 60's [32, 33], the CC is widely used for *ab initio* calculations because it could be more accurate in some specific parts of the **PES** and even faster than methods explained above. However, some years later Hurley included an improvement to the method developed by Cízek and Paldus where double excitations are considered. This improvement was called coupled clusters doubles (CCD) [34, 35]. Finally, Purvis and Barlett created computational packages with singles and doubles excitations, method known as **CCSD** [34, 35]. However, it was initially developed only for the ground state. Incidentally, other methods like equation of motion (EOM) have been coupled with coupled cluster method, **EOM-CCSD**, a cheaper methodology which is mostly used to search for highly excited states. This **EOM-CCSD** method has been used in this work to uncover Rydberg states in the carbon dioxide molecule (see [Section 10.2](#)), for which other sophisticated methods are computationally very expensive.

The fundamental equation in the **CCSD** is given by [36]

$$\phi_{CC} = e^{\hat{T}} \Phi_0, \quad (3.5)$$

where ϕ_{CC} is the non-relativistic ground state molecular electronic wave function and Φ_0 is the reference wave function, generally, obtained by a previous **HF** calculation. The operator $e^{\hat{T}}$ defined by a Taylor series reads

$$e^{\hat{T}} = 1 + \hat{T} + \frac{\hat{T}^2}{2!} + \frac{\hat{T}^3}{3!} + \dots = \sum_{k=0}^{\infty} \frac{\hat{T}^k}{k!}, \quad (3.6)$$

and the *cluster operator* $+\hat{T}$ is given by

$$\hat{T} = \hat{T}_1 + \hat{T}_2 + \hat{T}_3 + \dots + \hat{T}_n, \quad (3.7)$$

where n is the number of electrons and \hat{T}_i are the excitation operators of i particles with $i = 1, \dots, n$, which for one and two particles is defined as

$$\hat{T}_1 \Phi_0 = \sum_{\alpha=n+1}^{\infty} \sum_{i=1}^n t_i^{\alpha} \Phi_i^{\alpha}, \quad (3.8)$$

$$\hat{T}_2 \Phi_0 = \sum_{\beta=\alpha+1}^{\infty} \sum_{\alpha=n+1}^{\infty} \sum_{j=i+1}^n \sum_{i=1}^{n-1} t_{ij}^{\alpha\beta} \Phi_{ij}^{\alpha\beta}, \quad (3.9)$$

where Φ_i^{α} and $\Phi_{ij}^{\alpha\beta}$ are Slater determinants with in which one or two MOs (ϕ_i and ϕ_j) are replaced by virtual orbitals (ϕ_{α} and ϕ_{β}), respectively, and t_i^{α} and $t_{ij}^{\alpha\beta}$ are numerical coefficients. The effect to apply the operator $e^{\hat{T}}$ in Eq. (3.5) is to express the wave function ϕ_{CC} as a linear combination of Slater determinants which includes the reference function Φ_0 and all possible electron excitations from the occupied to the virtual molecular orbitals. The effect of electron correlation is introduced in the calculation through the inclusion of Slater determinants with MO excitations.

The **CCSD** method aims at getting the expansion coefficients $t_i^{\alpha}, t_{ij}^{\alpha\beta}, t_{ijk}^{\alpha\beta\gamma}$ and in order to obtain these amplitudes, some of the \hat{T}_i operators are taken in \hat{T} . The electronic Schrödinger equation that results employing the ansatz in Eq. (3.5) can be solved by iterative methods by applying the Condon-Shortley rules [37] to simplify the calculations. As a result one obtains the CC **WF** and the CC energy [36]. It worth mentioning that one of the most important characteristics of CC methods is the fact that they are consistent in size and they are not variational.

Following the previous approach, in the CC methods only certain excitation operators are included in typical applications. For instance, if the operator \hat{T} is reduced to \hat{T}_2 , the **CCD** method results [32]. Similarly, if \hat{T} is truncated to \hat{T}_1 and \hat{T}_2 , the **CCSD** method is obtained [38]. This method is already able to describe approximately 95% of the correlation energy in molecules in regions close to their equilibrium geometries. The **CCSDT** method comes from the additional introduction of \hat{T}_3 in the operator expansion [39, 40]. **CCSDT** calculations give very accurate results that can collect more than 99% of the correlation energy [21]. Nonetheless, it is a method with high computational requirements, i. e., they consume a lot of calculation time and consequently, they are mostly adapted for small molecules, with a limited number of electrons and basis set. Due to the computational issue, several approximate forms of **CCSDT** have been developed, where currently the most used is the **CCSD(T)** approach, which includes a non-iterative perturbative treatment to describe triple excitations and it is able to calculate total and relative electronic energies with high precision within reasonable computational times. This has made the **CCSD(T)** method very popular from the plethora of high-precision *ab initio* methods. Currently, further sophistications such as the **CCSDT(Q)** method [41] are being produced but are not yet available in commercial *ab initio* packages.

Although this method works better than the multi-configurational methods explained previously, it is important to note, again, **CCSD** is a method to perform molecular calculations

only in the ground state and in regions close to the molecular equilibrium geometry. Hence, the EOM-CCSD arises to perform calculations for excited states [20]. In this method excited states are calculated using a linear expansion in the form

$$|\mathbf{c}\rangle = \sum_{\mu} c_{\mu} \hat{\tau}_{\mu} |\phi_{CC}\rangle = e^{\hat{T}} \sum_{\mu} c_{\mu} \hat{\tau}_{\mu} |\phi_0\rangle, \quad (3.10)$$

where the summation is over the excitation operator present in the cluster operator \hat{T} . The expansion of the wave function performed in Eq. (3.10) is the starting ansatz for the EOM-CCSD method [42]. Notwithstanding, the EOM-CCSD method is useful to calculate electronic states that are orthogonal to each other. In some cases the electronic states calculated are not orthogonal which makes difficult the process to identify them.

PART II

MOLECULAR QUANTUM DYNAMICS

The laws of physics and chemistry are statistical throughout.

— Erwin Schrödinger

4

TIME-DEPENDENT METHODS

Molecular quantum dynamics focuses in the study of the motion and interactions of atoms and molecules using computational simulations based on first principles in quantum mechanics. The keystone of these simulations is the **TDSE** derived by Erwin Schrödinger in 1925 and published it in 1926 [43], which is analogous to the Newton's second law equation in classical mechanics. It is well known that if the differential equations of Newton's second law are solved, the solution predicts the motion of a given mechanical system when a set of initial conditions are provided. However, in the case of quantum mechanics, if the **TDSE** is solved, the solution describes the time-evolution of the wave function of the system. The concept of a wave function is a fundamental postulate of quantum mechanics and it is the mathematical description for the state of the system that contains all the information about it. In the Copenhagen interpretation of quantum mechanics, the wavefunction is the form to describe a given physical system, and in mathematical terms, the wavefunction is a complex function and its square absolute value represents the probability distribution of the position of the system. In addition to solve the **TDSE** there are another formulations to study quantum mechanics, such as the path integral formulation developed by Richard Feynman [44, 45].

Chapter 1 describes adiabatic approximations to solve the molecular **TISE**. However, to perform a molecular quantum dynamics it is necessary to introduce the coupling terms into the **TDSE**. The nuclear dynamics is governed by the **TDSE**, which can be read in the most general form as

$$\Psi(\mathbf{Q}, t) = \Psi(\mathbf{Q})e^{-iE t/\hbar}, \quad (4.1)$$

where $\Psi(\mathbf{Q}, t)$ corresponds to the nuclear time-dependent wavepacket. Thus, Time-dependent Schrödinger equation in the most general form is given by

$$i\hbar \frac{\partial}{\partial t} \Psi(\mathbf{Q}, t) = \hat{H}(\mathbf{Q}, t) \Psi(\mathbf{Q}, t). \quad (4.2)$$

According to the molecular system required to be simulated, the solution of the **TDSE** using spectral methods based on basis expansions, requires the previous calculation of energies (**PES**) and couplings (let them be **NAC**, spin-orbit or radiative couplings). The time-propagation allows for a detailed study of the mechanism involved during the action of the coupling interactions and the final propagated wave function is the object from which observables like cross sections can be obtained. The dynamic analysis of the system requires to perform calculations of different observables like cross-sections, photo-dissociation, photo-ionization, photo-isomerization, etc.

The number of quantum systems for which the **TISE** is solvable is scarce. There is even a lesser number of systems for which the **TDSE** is exactly solvable (usually toy models). Molecular systems are characterized by a large amount of degrees of freedom. Although the computational efficiency has increased hugely in the last decades, present calculations on *ab initio* molecular dynamics by solving the **TDSE** is limited to no more than 10 nuclear degrees of freedom. Therefore, in these specific cases, this limitation has produced a notorious development of classical and semiclassical methods in molecular dynamics [46]. The molecules subject to study in this thesis are small (from diatomic to tetraatomic species) and the methods used are fully quantum-mechanical. This chapter provides the most common methods used to solve the **TDSE** for small molecular systems, i. e., when the system does not exceed ten degrees of freedom.

4.1 SPECTRAL METHODS USING BASIS EXPANSIONS

This method employs the *Dirac's method of variation constants* to solve the TDSE. This method expands the nuclear wave function in the form of a time dependent superposition of direct products of (independent particle model) single-coordinate wave functions in the form

$$\Psi(Q_1, \dots, Q_f, t) = \sum_{j=1}^{n_s} \sum_{k_1 \dots k_f=1}^{\infty} C_{k_1 \dots k_f}^j(t) \phi_{k_1}^j(Q_1) \phi_{k_2}^j(Q_2) \dots \phi_{k_f}^j(Q_f) \exp\left(-\frac{iE_{k_1 \dots k_f}^j t}{\hbar}\right), \quad (4.3)$$

where $\phi_{k_i}^j(Q_i)$ correspond to the k -th vibrational wave function for the nuclear coordinate i in the j electronic state, $C_{k_1 \dots k_f}^j(t)$ are the time-dependent coefficients and n_s is the number of electronic states involved in the dynamics. Note that the functions $\phi_{k_i}^j(Q_i)$ form a complete set and are orthonormal providing $\Psi(Q, t)$ is normalized to unity.

Although the expansion in Eq. (4.3) is very accurate to describe the molecular behaviour, due to the expansion in terms of products of complete vibrational sets for each degree of freedom, this requires huge computational resources. Hence, this method is usually employed to solve small molecules, specially diatomic molecules as it is the case in this work. For instance, in the case of diatomic molecules, the wave packet can be represented by one nuclear degree of freedom (internuclear distance Q) and the ansatz for the nuclear wave packet reads

$$\Psi(Q, t) = \sum_{j=1}^{n_s} \sum_{k=1}^{\infty} C_k^j(t) \phi_k^j(Q) \exp\left(-\frac{iE_k^j t}{\hbar}\right). \quad (4.4)$$

In the case that the system does not have any temporal perturbation, i. e., its Hamiltonian does not depend of time, the coefficients remain constant along the time evolution and the temporal dependency only remains in the phase term in Eq. (4.4). This method of solution for the TDSE is suitable for the study of laser-matter interaction, for which the total nuclear Hamiltonian can be split in the molecular unperturbed Hamiltonian and the time-dependent interactions, in the form

$$\hat{H}_t(Q, t) = \hat{H}(Q) + \hat{V}(Q, t), \quad (4.5)$$

where $\hat{H}(Q)$ is the nuclear molecular Hamiltonian and $\hat{V}(Q, t)$ is the interaction Hamiltonian which describes how the molecule is coupled to a laser fields.

4.1.1 MOLECULAR SYSTEM COUPLED TO A LASER FIELD IN A SINGLE ELECTRONIC STATE

Following the *Dirac's method of variation of constants*, the time-dependent molecular wave function for an isolated electronic state, i. e., $n_s = 1$ can be expanded as

$$\Psi(Q, t) = \sum_{n=1}^{\infty} C_n(t) \phi_n(Q) e^{-iE_n t / \hbar}. \quad (4.6)$$

Introducing Eq. (4.5) and Eq. (4.6) in the TDSE expressed in Eq. (4.2), TDSE reads

$$i \frac{\partial}{\partial t} \left[\sum_{n=1}^{\infty} C_n(t) \phi_n(Q) e^{-iE_n t} \right] = [\hat{H}(Q) + \hat{V}(Q, t)] \left[\sum_{n=1}^{\infty} C_n(t) \phi_n(Q) e^{-iE_n t} \right], \quad (4.7)$$

where after a little of algebra one reaches, in the Dirac notation [47]

$$\sum_{n=1}^{\infty} [i\dot{C}_n(t) - \hat{V}(Q, t)C_n(t)] e^{-iE_n t} |\phi_n\rangle = 0, \quad (4.8)$$

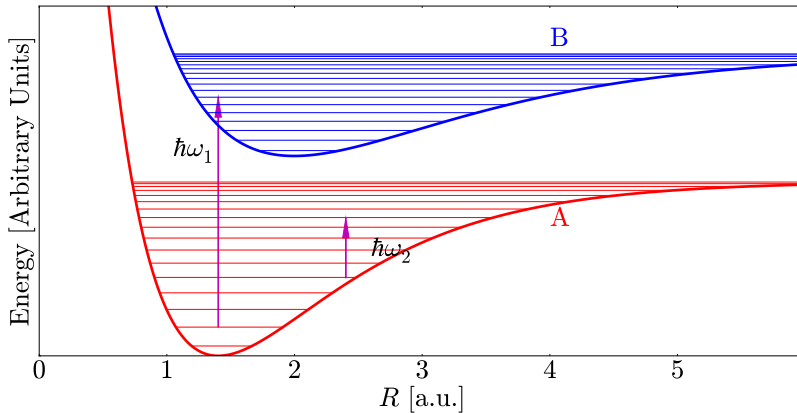


Figure 4.1: Schematic representation of two electronic states A and B in the BO approximation for a diatomic molecule, with their corresponding vibrational states. Vibrational transitions within the electronic ground state are produced with IR radiation ($\hbar\omega_2$) and vibronic transitions between A and B are due to UV absorption ($\hbar\omega_1$).

where $\dot{C}_n(t)$ denotes the first derivative in time of the coefficient $C_n(t)$. Taking the scalar product with $\langle \phi_m |$ and the orthonormality property $\langle \phi_m | \phi_n \rangle = \delta_{mn}$, one arrives to a set of coupled differential equations for the expansion coefficients in the form:

$$\dot{C}_m(t) = -i \sum_{n=1}^{\infty} C_n(t) \langle \phi_m | \hat{V} | \phi_n(Q) \rangle e^{-i(E_n - E_m)t}. \quad (4.9)$$

Most often, specially in molecular dynamics, the interaction Hamiltonian $\hat{V}(Q, t)$ is expressed by the scalar product between the dipole moment $\vec{\mu}(Q)$ and the laser field $\vec{E}(t)$. It is worth mentioning that in the case of homonuclear diatomic molecules, $\vec{\mu}(Q) = 0$, and as a consequence there is not excitation by a laser field in the dynamics of one single electronic state, which gives rise to spontaneous vibrational excitations.

4.1.2 MOLECULAR SYSTEM COUPLED TO A LASER FIELD IN N ELECTRONIC STATES

The procedure described in this section will be used in this work for diatomic molecules only. A typical diatomic heteronuclear molecule under the action of laser fields is considered. A schematic representation is shown in Fig. 4.1, where the electronic state A is coupled to electronic state B through the laser field with a central UV frequency ω_1 . Additionally, the vibrational states inside each electronic state can be coupled among them using laser fields with a smaller IR frequency ω_2 . As in the case of one single electronic state, first step is to take the complete wavefunction, in this case, in a general form for n_s electronic states. In fact the expansion made for the nuclear time dependent WF $\Psi(Q, t)$ in terms of the BO nuclear eigenfunctions ϕ_n^k within each electronic state)

$$\Psi(Q, t) = \sum_{k=1}^{n_s} \sum_{n=1}^{\infty} C_n^k(t) \phi_n^k(Q) e^{-iE_n^k t/\hbar}, \quad (4.10)$$

where the index k represents the electronic state number. In the case of two electronic states, the complete WF is given by

$$\Psi(Q, t) = \sum_{n=1}^{\infty} C_n^1(t) \phi_n^1(Q) e^{-iE_n^1 t/\hbar} + \sum_{m=1}^{\infty} C_m^2(t) \phi_m^2(Q) e^{-iE_m^2 t/\hbar}, \quad (4.11)$$

where, for simplicity, indexes n and m run over the vibrational states of the first and second electronic state, respectively.

Once the ansatz for the **WF** is set, Eq. (4.5) and Eq. (4.11) are inserted in the **TDSE** in Eq. (4.2), which gives as a result

$$\begin{aligned} & i \frac{\partial}{\partial t} \left[\sum_{n=1}^{\infty} C_n^1(t) \psi^1(\mathbf{Q}, \mathbf{q}) \phi_n^1(\mathbf{Q}) e^{-iE_n^1 t/\hbar} + \sum_{m=1}^{\infty} C_m^2(t) \psi^2(\mathbf{Q}, \mathbf{q}) \phi_m^2(\mathbf{Q}) e^{-iE_m^2 t/\hbar} \right] \\ &= [\hat{H}(\mathbf{Q}, \mathbf{q}) + \hat{V}(\mathbf{Q}, t)] \times \\ & \quad \left[\sum_{n=1}^{\infty} C_n^1(t) \psi^1(\mathbf{Q}, \mathbf{q}) \phi_n^1(\mathbf{Q}) e^{-iE_n^1 t/\hbar} + \sum_{m=1}^{\infty} C_m^2(t) \psi^2(\mathbf{Q}, \mathbf{q}) \phi_m^2(\mathbf{Q}) e^{-iE_m^2 t/\hbar} \right], \quad (4.12) \end{aligned}$$

$$\begin{aligned} & i \frac{\partial}{\partial t} \left[\sum_{n=1}^{\infty} C_n^1(t) \psi^1(\mathbf{Q}, \mathbf{q}) \phi_n^1(\mathbf{Q}) e^{-iE_n^1 t/\hbar} + \sum_{m=1}^{\infty} C_m^2(t) \psi^2(\mathbf{Q}, \mathbf{q}) \phi_m^2(\mathbf{Q}) e^{-iE_m^2 t/\hbar} \right] \\ &= [\hat{T}(\mathbf{Q}) + \hat{H}_{\text{el}}(\mathbf{Q}, \mathbf{q}) + \hat{V}(\mathbf{Q}, t)] \times \\ & \quad \left[\sum_{n=1}^{\infty} C_n^1(t) \psi^1(\mathbf{Q}, \mathbf{q}) \phi_n^1(\mathbf{Q}) e^{-iE_n^1 t/\hbar} + \sum_{m=1}^{\infty} C_m^2(t) \psi^2(\mathbf{Q}, \mathbf{q}) \phi_m^2(\mathbf{Q}) e^{-iE_m^2 t/\hbar} \right], \quad (4.13) \end{aligned}$$

taking into account the expressions

$$\hat{H}_{\text{el}}(\mathbf{Q}, \mathbf{q}) \psi^k(\mathbf{Q}, \mathbf{q}) = V^k(\mathbf{Q}) \psi^k(\mathbf{Q}, \mathbf{q}) \quad \wedge \quad [\hat{T}(\mathbf{Q}) + V^k(\mathbf{Q})] \phi_n^k(\mathbf{Q}) = E_n^k \phi_n^k(\mathbf{Q}), \quad (4.14)$$

and projecting over $\langle \psi^1 \phi_{n'}^1 | e^{iE_n^1 t/\hbar} \rangle$, and taking the orthonormality property $\langle \psi^1 | \psi^2 \rangle = 0$, the differential equations for the coefficients of the first and second electronic states read

$$\begin{aligned} i \dot{C}_{n'}^1(t) &= \sum_{n=1}^{\infty} C_n^1(t) \int_0^{\infty} d\mathbf{Q} \phi_{n'}^1(\mathbf{Q}) \langle \psi^1 | \hat{V}(\mathbf{Q}, t) | \psi^1 \rangle (\mathbf{Q}) \phi_n^1(\mathbf{Q}) e^{-i(E_n^1 - E_{n'}^1)t} \\ &+ \sum_{n=1}^{\infty} C_n^2(t) \int_0^{\infty} d\mathbf{Q} \phi_{n'}^1(\mathbf{Q}) \langle \psi^1 | \hat{V}(\mathbf{Q}, t) | \psi^2 \rangle (\mathbf{Q}) \phi_n^2(\mathbf{Q}) e^{-i(E_n^2 - E_{n'}^1)t} \end{aligned} \quad (4.15)$$

$$\begin{aligned} i \dot{C}_{n'}^2(t) &= \sum_{n=1}^{\infty} C_n^1(t) \int_0^{\infty} d\mathbf{Q} \phi_{n'}^2(\mathbf{Q}) \langle \psi^2 | \hat{V}(\mathbf{Q}, t) | \psi^1 \rangle (\mathbf{Q}) \phi_n^1(\mathbf{Q}) e^{-i(E_n^1 - E_{n'}^2)t} \\ &+ \sum_{n=1}^{\infty} C_n^2(t) \int_0^{\infty} d\mathbf{Q} \phi_{n'}^2(\mathbf{Q}) \langle \psi^2 | \hat{V}(\mathbf{Q}, t) | \psi^2 \rangle (\mathbf{Q}) \phi_n^2(\mathbf{Q}) e^{-i(E_n^2 - E_{n'}^2)t} \end{aligned} \quad (4.16)$$

At this point, the problem reduces to calculate the transition dipole moments between the electronic states, properties of the system that can be calculated using the methods explained in Chapter 3. Although the solution of Eqs. (4.15) and (4.16) is given for the dynamics with a laser field in two electronic states, this can be generalized for a finite number of electronic states as

$$i \dot{C}_{n'}^k(t) = \sum_{i=1}^{n_s} \sum_{n=1}^{\infty} C_n^i(t) \int_0^{\infty} d\mathbf{Q} \phi_{n'}^k(\mathbf{Q}) \langle \psi^k | \hat{V}(\mathbf{Q}, t) | \psi^i \rangle (\mathbf{Q}) \phi_n^i(\mathbf{Q}) e^{-i(E_n^i - E_{n'}^i)t} \quad (4.17)$$

where n_s is the number of electronic states.

4.2 TIME-DEPENDENT HARTREE (TDH)

One of the approximated methods for many Degree of freedom (**DOF**) systems is the Time-dependent Hartree (**TDH**) where the nuclear **WF** is written as a product of (one-dimensional) independent particle or **DOF** functions as follows

$$\Psi(Q_1, \dots, Q_f, t) = a(t) \prod_{j=1}^f \phi_j(Q_j, t) = a(t) \cdot \Phi(\mathbf{Q}, t), \quad (4.18)$$

where f is the total number of nuclear **DOF** considered and where $\Phi(Q, t) = \phi_1(Q_1, t) \cdots \phi_j(Q_j, t) \cdots \phi_f(Q_f, t)$ is a simple product. The functions $\phi_j(Q_j, t)$ are known as single particle function (**SPF**) and $a(t)$ is a time-dependent coefficient. These functions change during the propagation time because they are time-dependent. This is a great computational advantage since less Single particle function (**SPF**) are necessary to describe the system under study with a good accuracy. Now, each **SPF** is expanded in terms of time-independent functions known as primitive bases sets $\chi_{i_k}^{(\kappa)}$, in the form

$$\phi_{j_k}^{(\kappa)}(Q_k, t) = \sum_{i_k=1}^{N_k} c_{i_k}^{(\kappa, j_k)}(t) \chi_{i_k}^{(\kappa)}(Q_k). \quad (4.19)$$

The primitive basis functions only depend upon the κ -th **DOF** and they are usually represented in terms of a collocation type basis set like discrete variable representation (DVR) functions [48–50].

One of the problems in the use of **TDH** is that the wavefunction solution is not unique. One can multiply any **SPF** by a complex factor and divide another by the same factor and to obtain the same total wavefunction. Hence, the way to ensure uniqueness in the total wavefunction is necessary to include constraints that fix the time evolution of these free factors [51, 52]. These kind of constraints are given by

$$i\langle \phi_k(Q_k, t) | \dot{\phi}_k(Q_k, t) \rangle = g_k(t) \quad (4.20)$$

where $\kappa = 1, \dots, f$, and g_k are arbitrary constraints. Once constraints have been chosen, through the Dirac-Frenkel variational principle [53, 54], $\langle \delta \Psi | \hat{H} - i\partial/\partial t | \Psi \rangle$, equations of motion are derived both for $a(t)$ and for the **SPF** $\phi_k(Q_k, t)$ as [55]

$$i\dot{a}(t) = \left(E - \sum_k^f g_k \right) a(t) \quad (4.21)$$

$$i\dot{\phi}_k(Q_k, t) = \left(\mathcal{H}^{(\kappa)} - E + g_k \right) \phi_k(Q_k, t). \quad (4.22)$$

where

$$\mathcal{H}^{(\kappa)} = \left\langle \prod_{\substack{v=1 \\ v \neq \kappa}}^f \phi_v(Q_v, t) \middle| H \middle| \prod_{\substack{v=1 \\ v \neq \kappa}}^f \phi_v(Q_v, t) \right\rangle, \quad (4.23)$$

known as a mean field and E is the expectation value of the Hamiltonian H . On the other hand, although the constraint g_k is arbitrary, generally there are two constraints that are used with more frequency than others, which are $g_k = E$ and $g_k = 0$ and depend on the choice, the solution of [Eqs. \(4.21\)](#) and [\(4.22\)](#) has to be treated in a different way in each case. In the case of the simplest choice, i. e., $g_k = 0$, solution of [Eqs. \(4.21\)](#) and [\(4.22\)](#) reads

$$a(t) = a(0) \cdot \exp \left(-i \int_0^t dt' E(t') \right), \quad (4.24)$$

$$i\dot{\phi}_k(Q_k, t) = \left(\mathcal{H}^{(\kappa)} - E \right) \phi_k(Q_k, t). \quad (4.25)$$

Nonetheless, the dynamics to be solved does not always have an associated Hermitian Hamiltonian, thus the Dirac-Frenkel variational principle cannot ensure that the norm and the mean energy of the **WF** are conserved during the propagation, in such a way that $E(t)$ is a real function and time-independent. In the case of Hermitian time-dependent Hamiltonians, the total energy $E(t)$ becomes time-dependent but stays real. However, in non-Hermitian Hamiltonians $E(t)$ becomes both complex and time-dependent so that the constraint $g_k = 0$ is not a good choice and other alternatives like $g_k = E$ should be used. Thus, [Eqs. \(4.21\)](#) and [\(4.22\)](#) will be different from [Eqs. \(4.24\)](#) and [\(4.25\)](#).

Notwithstanding **TDH** gives good results in general if there is not sudden changes in the potential [52]. Additionally, since the **SPF** are time-dependent one-dimensional

wavefunctions, the wavepacket is usually more localized and could give accurate results with less computational requirements compared with standard methods explained in the previous section. The decrease in the computational cost is due to the reduction from $f \times n$ equations in the spectral method of eigenstates to $f + 1$ equations in the **TDH** method, assuming n as the number of nuclear eigenfunctions in each electronic state.

Although **TDH** is very accurate when potentials are smooth, this is not the case of chemical reactions with molecular fragmentation along several **PES**, in which sudden changes in the **PES** appear with ensuing **NAC**. Therefore, alternative methods with approximations have been developed during the last decades to solve the **TDSE** based on spectral methods.

4.3 MULTICONFIGURATIONAL TIME-DEPENDENT HARTREE METHOD (MCTDH)

The multiconfigurational time-dependent Hartree method (**MCTDH**) is widely used in quantum dynamics due to its flexibility in the requirements to obtain accurate results in dynamical studies of molecular systems. This method developed in 1990 [56] combines the previously defined as standard method with the **TDH** to get a most general ansatz. In other words, it takes the idea of the time-dependent coefficients from the eigenstates spectral method and the use of single particle **WF** for each **DOF**. Along these ideas, the ansatz of the **TDH** is improved to solve the **TDSE** considering that the total wavefunction for f **DOF** is a linear combination of Hartree products instead of one Hartree product (hence it takes the name multiconfigurational). Hence, the nuclear wave function has the form

$$\Psi(Q_1, \dots, Q_f, t) = \sum_{j_1=1}^{n_1} \dots \sum_{j_f=1}^{n_f} A_{j_1 \dots j_f}(t) \prod_{k=1}^f \phi_{j_k}^{(k)}(Q_k, t) = \sum_J A_J \Phi_J \quad (4.26)$$

where the coordinates Q_k are the nuclear degrees of freedom, $A_{j_1 \dots j_p}$ are the time-dependent expansion coefficients and $\phi_{j_k}^{(k)}$ are the **SPF** for each degree of freedom k of the molecular system defined as in the **TDH** by [Eq. \(4.19\)](#). The sum with j_k takes into account a number of n_k excitations for the nuclear **DOF** Q_k . Note that the upper limit of the sums in [Eq. \(4.26\)](#) is n_k contrary to the standard method where this limit is N_k and usually $N_k \geq n_k$. The difference refers to that whereas N_k represents the number of one-dimensional vibrational states of the degree of freedom k , n_k represents the number of **SPF** used to described the degree of freedom k , and the number of configurations or Hartree products is given by the product $n_1 \dots n_f$. This is very useful because the two time-dependent terms (coefficients and **SPF**) reduce the number of configurations necessary to describe the molecular system in the total **WF** compared with the spectral method using eigenstates or the **TDH**. It implies a lesser number of equations of motion to be solved and thus the possibility of treating larger molecular systems. In other words, a contraction of the basis set is performed since a smaller active space from the original space is chosen and built with the primitive functions. Multiconfigurational time-dependent Hartree (**MCTDH**) could be compared to the **MCSCF** methods (see [Section 3.1](#)) used in quantum chemistry to solve the **TISE** without the constraint of indistinguishability for fermions. **MCTDH** is an **MCSCF** method but instead of being used for the electronic coordinates it is for the nuclear coordinates. In solving the **TISE** but using the **MCTDH** theory, one obtains the vibrational states similar to the molecular orbitals for the electrons, and the contracted basis functions in the solution of the nuclear coordinates are called, as it is expressed above, **SPF** rather than molecular orbitals (MO). Besides, contrary to the case of electrons, there is no exchange operator since which means that **WF** is symmetric. Finally, other advantage of **MCTDH** is that one can decrease the number of degree of freedom creating combined modes $Q_k = (Q_1, Q_2, \dots)$ which are d -dimensional basis functions that depend upon one or more degrees of freedom of the molecular systems. These combined modes can be treated as *one particle or one degree of freedom*.

Since the interest of all this work is to perform dynamical calculations in different molecular systems, the ansatz of **MCTDH** expressed in [Eq. \(4.26\)](#) has to be propagated and a set of dynamical equations of motion are to be solved. Hence, the next step is to find or give a brief explanation about the equations of motion to propagate the **MCTDH-WF** type.

4.3.1 MCTDH EQUATIONS OF MOTION

The starting point to derive the equations of motion in the **MCTDH** is the ansatz in Eq. (4.26). The Dirac-Frenkel variational principle provides a solution of the **TDSE** in the form of a set of equations for the time-dependent terms in the **MCTDH** ansatz. These terms are the expansion coefficients (\mathbf{A} -vector) and each set of **SPF**. Therefore, this set of equations in matrix notation for the \mathbf{A} coefficients reads

$$i\dot{\mathbf{A}} = \left(\mathcal{K} - \sum_k \mathbf{g}^k \right) \mathbf{A}, \quad (4.27)$$

$$(4.28)$$

where \mathcal{K} is the matrix of the Hamiltonian operator given by

$$\mathcal{K}_{JL} = \langle \Phi_J | \hat{H} | \Phi_L \rangle, \quad (4.29)$$

and \mathbf{g}^k is a constraint operator included in the derivation of the **MCTDH** equations of motion, because, both in **MCTDH** as in the **TDH**, the coefficients ($\mathbf{A}(t)$ and $\mathbf{a}(t)$, respectively) and the **SPF** are time-dependent, which generates an ambiguity that give arises to the **WF** solution to be not unique. Moreover, the equations for each set of **SPF** in matrix notation is given by

$$i\dot{\Phi}^{(k)} = \left[(\mathbf{g}^k)^T + (1 - P^{(k)}) (\rho^{(k)})^{-1} \mathcal{H}^{(k)} \right] \Phi^{(k)}, \quad (4.30)$$

where $\Phi^{(k)} = (\phi_1^k, \dots, \phi_f^k)^T$ is the vector of the **SPF**. P^k is the projector onto the space spanned by the **SPF** and the operator $(1 - P^k)$ ensures that the time derivative of the **SPF** is orthogonal to the space spanned by the functions [51]. \mathcal{H}^k is the mean-field operator matrix which reads

$$\mathcal{H}_{ab}^{(k)} = \langle \Psi_a^{(k)} | \hat{H} | \Psi_b^{(k)} \rangle, \quad (4.31)$$

and ρ^k is the density matrix given by

$$\rho_{ab}^{(k)} = \langle \Psi_a^{(k)} | \Psi_b^{(k)} \rangle = \sum_{J^k} A_{J_a^k}^* A_{J_b^k}. \quad (4.32)$$

In these last equations, the function $\Psi_i^{(k)}$ is called the *single-hole function* and it represents the **WF** related with the j -th **SPF** of the k -th particle and is given by

$$\Psi_a^{(k)} = \sum_{J^k} A_{J_a^k} \Phi_{J^k}, \quad (4.33)$$

where J^k is an index with the position k -th removed. Similarly with the single-hole coefficient $A_{J_a^k}$ and the single-hole Hartree product Φ_{J^k} , which describes a configuration with the k -th **SPF** removed from the sum.

Finally, since Eqs. (4.27) and (4.30) depend on the choice of the constraint, if $\mathbf{g}^{(k)} = 0$, the variational solution of the **TDSE** for the coefficients \mathbf{A} and the **SPF** in Eqs. (4.27) and (4.30) results in the matrix form as

$$i\dot{\mathbf{A}} = \mathcal{K}\mathbf{A} \quad (4.34)$$

$$i\dot{\Phi}^{(k)} = (1 - P^{(k)}) (\rho^{(k)})^{-1} \mathcal{H}^{(k)} \Phi^{(k)}, \quad (4.35)$$

or

$$i\dot{\mathbf{A}}_J = \sum_L \langle \Phi_J | \hat{H} | \Phi_L \rangle \mathbf{A}_L, \quad (4.36)$$

$$i\dot{\phi}_j^{(k)}(Q_k, t) = (1 - P^{(k)}) \sum_{k,l=1}^{n_k} (\rho^{(k)-1})_{jk} \mathcal{H}_{kl}^{(k)} \phi_l^{(k)}(Q_k, t). \quad (4.37)$$

Although the Dirac-Frenkel variational principle needs some specific variants to derive the **MCTDH** equations of motion, it preserves the norm and, for time-independent Hamiltonians, the total energy. As it is described above, **MCTDH** is an intermediate point between the eigenstates spectral method and the **TDH**, if all $n_k = 1$, the **MCTDH** ansatz in Eq. (4.26) reduces to the **TDH** and on the other hand, if the number of primitive functions n_k increases until it reaches the value N_k , the spectral method is recovered.

This work mainly uses the the **MCTDH** for the dynamical calculations. The complete details of the method, calculations and derivations are not shown here. For more details of the method and its corresponding history and applications see Gatti et al., 2009 [51] and for more details of the calculations and derivations of the equations of motion see Gatti et al., 2017 [52].

The **MCTDH** equations of motion described above assumes dynamics on a single **PES**. However, in realistic applications using laser pulses one solves a dynamics evolving in more than one **PES**. The strength of **MCTDH** is that it is also adapted to perform multi-dimensional multistate molecular dynamics.

4.3.2 MCTDH MULTISTATE CALCULATIONS

In solving the **MCTDH** equations of motion there are two different forms to treat the **WF** when more than one electronic state is involved in the dynamics of a particular molecular system. One of these is to write the ansatz in Eq. (4.26) for more than one electronic including an extra **DOF** to represent the electronic states involved in the dynamics. Thus, the first **MCTDH** ansatz for more than one electronic state reads

$$\Psi(Q_1, \dots, Q_f, \alpha, t) = \sum_{j_1=1}^{n_1} \dots \sum_{j_p=1}^{n_p} A_{j_1 \dots j_p}(t) \phi_{j_1}^{(1)}(Q_1, t) \dots \phi_{j_{p-1}}^{(p-1)}(Q_{p-1}, t) \phi_{j_p}^{(p)}(\alpha, t), \quad (4.38)$$

where α is the label for the **DOF** of the electronic state, and there are **SPF** representing each electronic **DOF**.

Although the inclusion of another **DOF** can be useful in the propagation of the nuclear molecular **WF**, through this methodology is not possible to distinguish between the wavefunctions associated with each electronic state. Something important in the study of different photo-effects like bond making, chemical reactions, dissociation, isomerization or light-matter interactions when molecules are inside of quantum optical cavities. Hence, the other form to treat many electronic states in the **MCTDH** methodology is to introduce the electronic state functions $|\alpha\rangle$, so that

$$\Psi(Q_1, \dots, Q_f, \alpha, t) = \sum_{j_1=1}^{n_1} \dots \sum_{j_{p-1}=1}^{n_{p-1}} \sum_{\alpha=1}^{\sigma} A_{j_1 \dots j_{p-1}}(t) \phi_{j_1}^{(1)}(Q_1, t) \dots \phi_{j_{p-1}}^{(p-1)}(Q_{p-1}, t) |\alpha\rangle, \quad (4.39)$$

where $n_p = \sigma$ is the number of electronic states involved in the dynamics. The expression in Eq. (4.41) is called in the **MCTDH** terminology as *single-set* formulation because only one set of **SPF** defines the dynamics in all the electronic states. This formulation may be useful in chemical reaction dynamics or in the study of chemical bond making [57]. Hence, a different form to add the electronic state functions $|\alpha\rangle$ in multistate calculations is the *multi-set* formulation which makes use of one set of **SPF** for each one of the electronic states. Thus, the **MCTDH** ansatz in the multi-set formalism reads

$$\Psi(Q_1, \dots, Q_f, t) = \sum_{\alpha=1}^{\sigma} \Psi^{(\alpha)}(Q_1, \dots, Q_f, t) |\alpha\rangle, \quad (4.40)$$

where $\Psi^{(\alpha)}(Q_1, \dots, Q_f, t)$ is the **WF** associated with the α -th electronic state given by

$$\Psi^{(\alpha)}(Q_1, \dots, Q_f, t) = \sum_{j_1=1}^{n_1^{\alpha}} \dots \sum_{j_p=1}^{n_p^{\alpha}} A_{j_1 \dots j_p}^{(\alpha)}(t) \phi_{j_1}^{(1,\alpha)}(Q_1, t) \dots \phi_{j_p}^{(p,\alpha)}(Q_p, t). \quad (4.41)$$

One of the advantages of using this last formulation is that one can distinguish between the WF of each electronic state, an useful characteristic in photodissociation and photoionization dynamics.

In the same way, the equations of motion given in Eqs. (4.27) and (4.30) need the inclusion of the labels for the electronic states taking the electronic state function formulation. For the simplest constraint choice $g^{(k)} = 0$, the equation of motion in matrix form reads

$$i\dot{\mathbf{A}}^{(\alpha)} = \sum_{\beta=1}^{\sigma} \mathcal{K}^{(\alpha\beta)} \mathbf{A}^{(\beta)} \quad (4.42)$$

$$i\dot{\Phi}^{(k,\alpha)} = (1 - P^{(k,\alpha)})(\rho^{(k,\alpha)})^{-1} \sum_{\beta=1}^{\sigma} \mathcal{H}^{(k,\alpha\beta)} \Phi^{(k,\beta)}, \quad (4.43)$$

with

$$\mathcal{K}_{JL}^{(\alpha\beta)} = \langle \Phi_J^{(\alpha)} | \hat{H}^{(\alpha\beta)} | \Phi_L^{(\beta)} \rangle \quad (4.44)$$

and

$$\mathcal{H}_{ab}^{(\alpha\beta)} = \langle \Psi_a^{(k,\alpha)} | \hat{H}^{(\alpha\beta)} | \Psi_b^{(k,\beta)} \rangle \quad (4.45)$$

where $\hat{H}^{(\alpha\beta)} = \langle \alpha | \hat{H} | \beta \rangle$ is the (α, β) component of the Hamiltonian. Additionally, the single-set formalism can be an advantage in the requirements of the propagation if the electronic states involved in the are similar, e. g., when the surfaces are almost parallel. In contrast to the multi-set formalism which is more efficient when the dynamics on the various diabatic states is rather different.

Before the discovery of quantum mechanics, the framework of physics was this: If you tell me how things are now, I can then use the laws of physics to calculate, and hence predict, how things will be later.

— Brian Greene

5

MOLECULAR DYNAMICS

In previous chapters it was explained the emerging concept of the **PES** within the **BO** paradigm and the different existing methods to compute them. In addition, when the **BO** approximation breaks down and **NAC** must be incorporated, one must be aware that some **NAC** may behave with a strong singularity around the avoided crossing or Conical intersection (**CoIn**). In some cases, this behavior is not so acute and the dynamical equations can be integrated straightforwardly including the **NAC** in the adiabatic picture. When this is not possible a diabatic picture is preferred, in which by definition the adiabatic couplings vanish (at the cost of the emergence of other kind of couplings). A molecular dynamics study can be performed using different approaches according to the system and reaction in consideration. The molecular system can undergoes an adiabatic dynamics (if only one adiabatic **PES** is involved) or a non adiabatic dynamics (several **PES** involved). Moreover, the latter non-adiabatic dynamics can be studied with an adiabatic picture or a diabatic picture. Additionally, it worth mentioning that this work only focusses on the internal degrees of freedom of the molecular system and as a consequence the translation and rotation degrees of freedom are removed or neglected. Take also in consideration that for the vibrational motions here considered the time is short enough so that effects due to full translation or rotation of the molecule can be neglected since they occur at a much longer time scale.

5.1 ADIABATIC VS. NON-ADIABATIC DYNAMICS

The **BO** approximation is often valid and it considerably facilitates the calculation of **PES** and the ensuing dynamics occurring on them. However, when the dynamics involves a manifold of coupled electronic states that display avoided crossings, the **BO** approximation usually breaks down. For example, consider the reaction of a halogen molecule X_2 with an alkali metal atom M . As the halogen molecule approaches to the metal atom it draws away an electron to leave the ions M^+ and X_2^- . The system therefore transfers from a purely-covalent picture to an ionic one if one refers to the type of interaction between the fragments. In the neighborhood of an anticrossing a small modification of the nuclear geometry results into a sudden change in the electronic wave function. Here the electronic and nuclear motions are strongly coupled and the **BO** approximation is no longer valid, as mentioned in [Chapter 1](#). Instead, the system can be viewed as a pair of intersecting potential energy curves, one corresponding to the covalent curve and the other to the ionic curve.

Quasidegeneracies between the eigenvalues $\epsilon_n(Q)$ at a given geometry Q gives a potential indication for the presence of non adiabatic avoided crossings in the case of **PEC** or **CoIn** in the case of **PES**. The **NAC** are dominant in this region of avoided crossings, and they can be computed and included as essential ingredients in the subsequent dynamics, which then takes the name *non-adiabatic dynamics*. These terms have to be calculated and included in a subsequent dynamics, which is known as *non-adiabatic dynamics*. One of the problems that arises with **NAC** is that usually they are difficult to compute, since they depend on the derivatives of a numerical wave function. Nonetheless, this calculation depends on the type of molecule and the number of possible avoided crossings or **CoIn** in the desired region.

Thus, the non-adiabatic dynamics implies to solve TDSE given by

$$i\hbar \frac{\partial}{\partial t} \Psi(\mathbf{Q}, t) = \hat{H}_{ij}(\mathbf{Q}, t) \Psi(\mathbf{Q}, t) \quad (5.1)$$

$$= (\hat{T}_n(\mathbf{Q}) + \hat{V}_i(\mathbf{Q})) \Psi_i(\mathbf{Q}, t) + \sum_j \hat{\Lambda}_{ij}(\mathbf{Q}) \Psi_j(\mathbf{Q}, t) \quad (5.2)$$

where the $\hat{V}_j(\mathbf{Q})$ are the adiabatic electronic states (i.e., derived from electronic Schrödinger equation) and $\hat{\Lambda}_{ij}(\mathbf{Q})$ is the non-adiabatic coupling operator which connects the terms in Eqs. (1.9) and (1.10), i.e., the NAC operator given by

$$\hat{\Lambda}_{ij}(\mathbf{Q}) = \frac{1}{2\mu_i} [2\mathbf{F}_{ij}(\mathbf{Q}) \cdot \nabla + \mathbf{G}_{ij}(\mathbf{Q})]. \quad (5.3)$$

Although both terms should be calculated to perform a complete and accurate dynamics, in this work only the NAC that correspond to the first derivative is calculated, i.e., $\mathbf{F}_{ij}(\mathbf{Q})$ in Eq. (5.3). The second term in Eq. (5.3) is not calculated but it can be approximated for two electronic states by the following procedure. From the non-adiabatic operator one has that

$$\hat{\Lambda}_{ij}(\mathbf{Q}) = -\frac{1}{2\mu_i} \left[2 \langle \Psi_i(\mathbf{Q}, \mathbf{q}) | \nabla_{Q_i} | \Psi_j(\mathbf{Q}, \mathbf{q}) \rangle(\mathbf{Q}) \frac{\partial}{\partial \mathbf{Q}} + \langle \Psi_i(\mathbf{Q}, \mathbf{q}) | \nabla_{Q_i}^2 | \Psi_j(\mathbf{Q}, \mathbf{q}) \rangle(\mathbf{Q}) \right] \quad (5.4)$$

In compact matrix form this Hermitian term reads

$$\hat{\Lambda} = -\frac{1}{2\mu_i} [2\mathbf{F} \cdot \nabla_{Q_i} + \mathbf{G}]. \quad (5.5)$$

The term \mathbf{G} with second derivatives with respect to some Q_i nuclear coordinate is more difficult to compute in general. If one inserts the completeness $\hat{1} = \sum_{i=1,2} |\Psi_i(\mathbf{Q}, \mathbf{q})\rangle \langle \Psi_i(\mathbf{Q}, \mathbf{q})|$ in $\mathbf{G}_{ij}(\mathbf{Q})$, taking into account two electronic states, one arrives to the identity $\mathbf{G} = \mathbf{F}^2 + \nabla_{Q_i} \cdot \mathbf{F}$. In this particular case

$$\mathbf{F} = \begin{pmatrix} 0 & f_{12} \\ -f_{21} & 0 \end{pmatrix} \quad (5.6)$$

is an anti-Hermitian matrix, so that

$$\mathbf{G} = \begin{pmatrix} -|f_{12}|^2 & \frac{df_{12}}{dQ_i} \\ -\frac{df_{12}}{dQ_i} & -|f_{12}|^2 \end{pmatrix}. \quad (5.7)$$

Here \mathbf{G} is also an anti-hermitian matrix but, compensated with the term $2\mathbf{F} \cdot \nabla_{Q_i}$, the full matrix $\hat{\Lambda}$ is Hermitian and the propagation preserves unitarity and in short, only one NAC, $f_{12}(Q_i)$ must be computed. In this way, the non-adiabatic TDSE, i.e., Eq. (5.2) for a diatomic molecule evolving in a two-state manifold of electronic states has the matrix form

$$i\frac{\partial}{\partial t} \begin{bmatrix} \Psi_1(Q, t) \\ \Psi_2(Q, t) \end{bmatrix} = \left\{ \begin{pmatrix} -\frac{1}{2\mu} \frac{\partial^2}{\partial Q^2} + V_1(Q) & 0 \\ 0 & -\frac{1}{2\mu} \frac{\partial^2}{\partial Q^2} + V_2(Q) \end{pmatrix} + \Lambda(Q) \right\} \begin{bmatrix} \Psi_1(Q, t) \\ \Psi_2(Q, t) \end{bmatrix}, \quad (5.8)$$

where μ is the reduced nuclear mass that corresponds to the nuclear coordinate Q . Here it is represented the case corresponding a single nuclear degree of freedom Q , but it could be generalized to more internal coordinates, where avoided crossings are replaced by conical intersections.

5.1.1 CONICAL INTERSECTIONS

CoIn are a particular type of non-adiabatic interaction between two or more electronic states [58, 59]. CoIn occur when the states are degenerate in an $(N - 2)$ -dimensional subspace known

as the *seam space*, where N is the number of internal degrees of freedom of the molecule ($N = 3n - 5$ for linear molecules containing n atoms, $N = 3n - 6$ for non-linear). The name of a *seam* comes from the region where the two electronic states approach to each other, this intersection looks like a seam. Some examples about seams can be seen in CO_2 PES in [Chapter 10](#). The degeneracy of the electronic states is lifted in the remaining two degrees of freedom, which are termed the *branching space*. The name *conical* refers to the geometrical structure in the adiabatic states in the region of the intersection when it is viewed in the branching space, [Fig. 5.1](#) illustrates the shape of a **CoIn**. Where **CoIn** are present radiationless transitions between surfaces can occur very rapidly. Originally thought to be rare, **CoIn** have been found to be a fairly ubiquitous feature in polyatomic molecules.

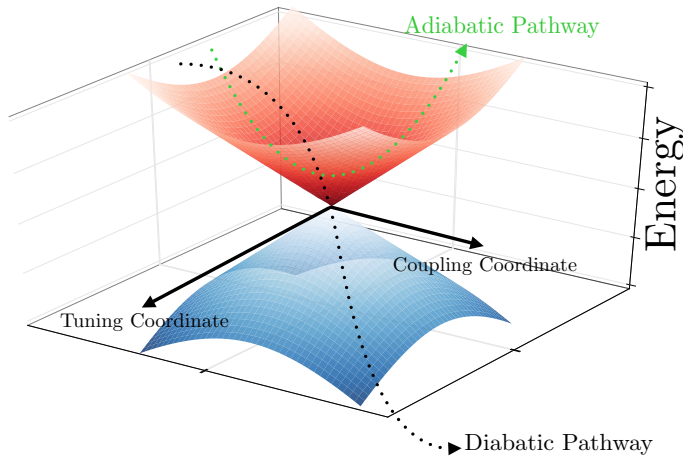


Figure 5.1: Schematic representation of a Conical intersection in its branching space. Green and black lines indicate adiabatic and diabatic pathways, respectively.

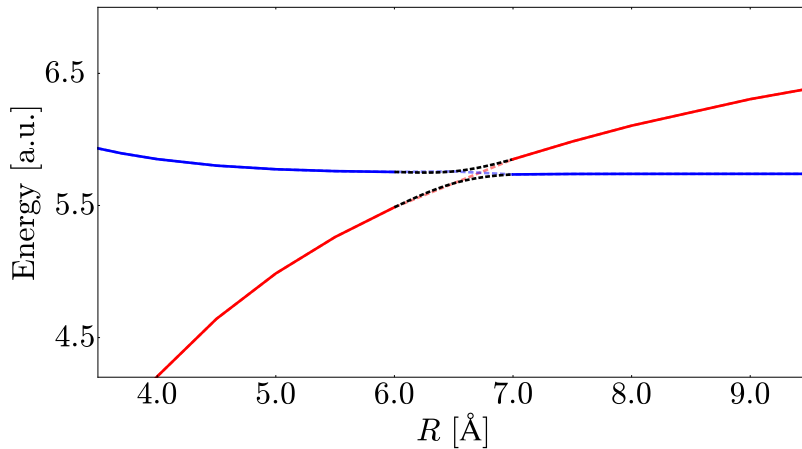
The presence of **CoIn** and avoided crossings may pose difficulties for the integration of the dynamics across these features due to the presence of sharp **NAC**. Instead, one may choose a diabatic representation which avoids the introduction of highly non-integrable **NAC**.

5.2 DIABATIC DYNAMICS

As stated in the previous section, an alternative to the adiabatic picture is to perform a change to a diabatic picture using a unitary transformation for the basis. In the new diabatic basis, the **NAC** corresponding to the first and second derivatives respect to the nuclear coordinate are zero or as small as possible.

The concept of diabatic states is most easily understood when one considers the case of two molecular states whose energies display an avoided crossing as a function of the nuclear geometry. It is well known that the character of the molecular **WF** changes abruptly across a narrow pseudocrossing, if one follows the adiabatic curves. In fact, the smoothest topological correlation of the **WF** indicates that the two states actually cross to each other instead of avoiding the crossing. One usually says that the adiabatic states interchange some character in the avoided crossing region. In order to avoid this, it may be helpful to look inside a diabatic picture or diabatic surfaces. These are the surfaces in which the electronic characters of the states are maintained, as opposed to simply ordering them by energy. If one follows red and blue lines in [Fig. 5.2](#), this gives a sketch of how the same states would appear in the diabatic representation. Thus, the adiabatic representation is given following the continuity of the red and blue lines with the dashed black lines, respectively.

Since the diabatic representation can be useful to describe a dynamics, this can be straightforward when one considers a diatomic molecule or a one-dimensional system. In this kind of systems, some methodologies can be applied to obtain the diabatic curves and their

Figure 5.2: Avoided crossing between states $^1\Sigma_1$ and $z^1\Sigma_1$ in LiF molecule.

corresponding diabatic or electrostatic couplings. The methodologies that can be employed to diabatize are a simple orthogonal transformation, the diagonalization of an operator which corresponds to a physical property or the use of a model function that simulates the behaviour of the orthogonal transformation. These methodologies are explained in detail below. However, in the case of polyatomic molecules, i.e., more than two atoms, there is generally a single or discrete set of isolated points where the surfaces are degenerated, these points, as it is mentioned above generate the *seam* which makes that the orthogonal transformation from adiabatic to diabatic picture begins to be a challenge.

5.2.1 ORTHOGONAL TRANSFORMATION: FROM ADIABATIC TO DIABATIC BASES

The strong values of the coupling at the avoided crossing region arise from the interchange of character between two adiabatic wavefunctions Ψ_1^a and Ψ_2^a with the variation along the internuclear distance R (close to the avoided crossing) and hence each one of them has a component of the other in the form

$$\Psi_1^a(R + dR) \simeq \Psi_1^a(R) + \Psi_2^a(R)d\theta \quad (5.9)$$

$$\Psi_2^a(R + dR) \simeq \Psi_2^a(R) - \Psi_1^a(R)d\theta \quad (5.10)$$

from which one obtains the value of the radial **NAC** as

$$\left\langle \Psi_1^a(R) \left| \frac{\partial}{\partial R} \right| \Psi_2^a(R) \right\rangle = -\frac{d\theta(R)}{dR} = P_{12}^a(R), \quad (5.11)$$

where the variation $d\theta/dR$ is the interchange of character or the **NAC**. However, as it was mentioned above, the **NAC** will be large at some point and in some cases this integration could be complicated since $P_{12}^a(R)$ must be calculated in the complete grid of the internuclear distance R . Although **NAC** can be calculated using *ab initio* techniques, they are usually expensive. Then, one solution to study some chemical process as the electron transfer $\text{Li} + \text{F} \rightarrow \text{Li}^+ + \text{F}^-$ is to propose linear combinations $\Psi_1^d(R)$ and $\Psi_2^d(R)$ from $\Psi_1^a(R)$ and $\Psi_2^a(R)$ in such a form that the **NAC** terms are not present in the transformation. These new combinations are defined diabatic states whose energies, contrary to the adiabatic states, are energy degenerate at the crossing. Also, the new diabatic states show minimal or zero **NAC**. The two basis, the diabatic $\Psi_i^d(R)$ and the adiabatic $\Psi_i^a(R)$ states can be related through an unitary transformation as

$$\Psi_i^a(R) = \sum_k U_{ik}(R) \Psi_k^d(R). \quad (5.12)$$

According to the first general definition of diabatic states, proposed by Smith [60] where the diabatic states have zero non-diagonal couplings, it is obtained that diabatic non-diagonal matrix elements are $P_{ij}^d(R) = 0$, then since

$$P_{ij}^a(R) = \left\langle \Psi_i^a(R) \left| \frac{\partial}{\partial R} \right| \Psi_j^a(R) \right\rangle \quad \text{and} \quad P_{ij}^d(R) = \left\langle \Psi_i^d(R) \left| \frac{\partial}{\partial R} \right| \Psi_j^d(R) \right\rangle, \quad (5.13)$$

one obtains in compact matrix form [61]

$$P^d = \mathbf{U}^T P^a \mathbf{U} + \mathbf{U}^T \frac{\partial}{\partial R} \mathbf{U}. \quad (5.14)$$

According to the Smith's definition ($P_{ij}^d(R) = 0$) the matrix \mathbf{U} is defined by the equation

$$\frac{\partial \mathbf{U}}{\partial R} = -P^a \mathbf{U}, \quad (5.15)$$

where P^a is the matrix of the non-adiabatic coupling elements. In the most simple two-state case, the inverse transform of Eq. (5.12) assuming that diabatic and adiabatic representations are identical at infinite internuclear separation yields

$$\Psi_1^d(R) = U_{11} \Psi_1^{\text{ad}}(R) + U_{21} \Psi_2^{\text{ad}}(R) = \cos \theta \Psi_1^{\text{ad}}(R) - \sin \theta \Psi_2^{\text{ad}}(R), \quad (5.16)$$

$$\Psi_2^d(R) = U_{12} \Psi_1^{\text{ad}}(R) + U_{22} \Psi_2^{\text{ad}}(R) = \sin \theta \Psi_1^{\text{ad}}(R) + \cos \theta \Psi_2^{\text{ad}}(R), \quad (5.17)$$

so that the matrix \mathbf{U} has the form of a rotation matrix

$$\mathbf{U} = \begin{pmatrix} \cos \theta & -\sin \theta \\ \sin \theta & \cos \theta \end{pmatrix}, \quad (5.18)$$

and the angle of the transformation according to Eq. (5.11) is given by

$$\theta(R) = - \int_{\infty}^R dR' \left\langle \Psi_1^{\text{ad}}(R') \left| \frac{\partial}{\partial R'} \right| \Psi_2^{\text{ad}}(R') \right\rangle. \quad (5.19)$$

As a consequence of this unitary transformation, the diabatic states are not eigenvalues of the electronic Hamiltonian. Hence, the new diabatic energies (potential energy curves) must be calculated according to the unitary transformation

$$V_{ij}^d(R) = \sum_k U_{ki}(R) V_k^a(R) U_{kj}(R), \quad (5.20)$$

where V_k^a are the eigenvalues of the adiabatic Hamiltonian. After that, the subsequent dynamics will be diabatic with new couplings due to the electronic Hamiltonian (named electrostatic coupling), that replace the **NAC** in the dynamics (in fact, they are much smoother than **NAC**).

5.2.2 DIAGONALIZATION OF AN OPERATOR THAT CORRESPONDS TO A PHYSICAL PROPERTY

One of the techniques to find an appropriate rotation angle of the matrix \mathbf{U} is to diagonalize the matrix of any operator \hat{A} that correspond to a physical property like the dipole moment $\hat{\mu}_z$ in the adiabatic representation ($\hat{\mu}_{ij}(R) = \left\langle \Psi_i^a(R) \left| \hat{\mu}_z \right| \Psi_j^a(R) \right\rangle$). The selected physical property in the diabatic representation will be diagonal and the rotation angle $\theta(R)$ that brings the matrix A (with adiabatic matrix elements $\hat{A}_{ij}(R)$) to its diagonal form is given by

$$\theta(R) = \begin{cases} \frac{1}{2} \tan^{-1} \left(\frac{2A_{12}(R)}{A_{11}(R) - A_{22}(R)} \right) & R \leq R_{\text{CI}} \\ \frac{1}{2} \tan^{-1} \left(\frac{2A_{12}(R)}{A_{11}(R) - A_{22}(R)} \right) + \frac{\pi}{2} & R > R_{\text{CI}} \end{cases} \quad (5.21)$$

where R_{CI} corresponds to the point where the potential energy curves display the avoided crossing. The splitting of the angular function in Eq. (5.21) is performed because the expectation values of the operator \hat{A} also cross to each other at the avoided crossing point R_{CI} . This methodology should give the same results, i. e., the rotation angle of the matrix of transformation \mathbf{U} given in Eq. (5.19), as long as the *ab initio* calculations of **NAC** and expectation values of the operator $\hat{A}(R)$ are calculated with the same good accuracy.

5.2.3 DIABATIZATION MODEL USING A SPECIFIC FUNCTION

Since an orthogonal transformation is not unique, one can take infinite types of transformations in order to diabatize the electronic molecular states or surfaces of the system. Due to this, another solution that one can propose is to employ a model function for the rotation angle $\theta(R)$ with a similar behaviour found in the two methodologies described above for diatomic molecules, i. e., to perform a fitting of the function for the rotation angle with the an appropriate expansion and parameters. In this work a two-parameter fitting function is proposed with the form

$$\theta(R) = \frac{1}{2} \tan^{-1} [\alpha(R - R_{CI})] + \frac{\pi}{4}, \quad (5.22)$$

where α is a smoothing factor for this switching function and R_{CI} is the location of the avoided crossing. The physical meaning of α is related with the energy difference between the two states in the avoided crossing region in the adiabatic representation, which can be used to reproduce its corresponding peak in the [NAC](#). It is worth mentioning that this model can be extrapolated to more dimensions in order to model the [NAC](#) in the case of [CoIn](#). A specific example for this diabatization procedure for the two ${}^1\Sigma$ adiabatic states in LiF is carried out in [Section 9.2](#).

PART III

THE NATURE OF RADIATION

The energy produced by the breaking down of the atom is a very poor kind of thing. Anyone who expects a source of power from transformation of these atoms is talking moonshine.

— Sir Ernest Rutherford

6

CLASSICAL APPROACH

In physics, the definition of an ultrashort pulse of light corresponds to an electromagnetic wavepacket with a duration within the atomic and molecular natural timescales. In chemical physics, a new *hot topic* of research has been called *femtochemistry*, where the term ultrashort refers to the range of femtoseconds (fs) and a few picoseconds (ps), although such pulses no longer hold the record for the shortest pulses generated in the laboratory nowadays, down to the attosecond scale [62, 63]. The field of the femtochemistry was opened in 1999 by the Nobel Prize in Chemistry of Ahmed H. Zewail for his studies using ultrashort pulses to observe how atoms move in a molecule during a chemical reaction using flashes of laser light on the timescales of the order of femtoseconds (10^{-15} seconds) [64]. One of the important points to apply ultrashort pulses is that there lies the possibility of controlling chemical reactions using fs laser pulses, its natural time window.

This chapter briefly describes the laser-matter interaction based on the semiclassical approximation, where the atomic or molecular system is treated by quantum mechanics and the external electromagnetic field by classical electrodynamics. Within classical electrodynamics, the ultrashort pulses are described by the Maxwell's equations. Thus, this chapter starts presenting the mathematical definition for an isolated pulse and characterizing its most relevant parameters. In addition, the frequency representation of the pulse is obtained by the well-known Fourier transform, and its connection to the spectral population distribution for any molecular target.

6.1 MATHEMATICAL DEFINITION OF ULTRASHORT PULSES

A mathematical definition of ultrashort laser pulses is based on electromagnetic waves freely propagated in space. In addition, the long-wave or dipole approximation is used, i.e., it is assumed that the fields only depend upon time and the wavelength λ_0 of the ultrashort laser pulse is long compared with the dimensions of the molecule, i.e., $|\mathbf{k} \cdot \mathbf{r}| \ll 1$ [65]. Within this approximation, the behavior of electromagnetic waves are described essentially by the electric $\mathbf{E}(t)$ and magnetic $\mathbf{B}(t)$ field vectors whose expressions arise from the solution of the Maxwell's equations. Further, electromagnetic waves can be also described by other two physical magnitudes, the vector potential $\mathbf{A}(t)$ and the scalar potential $\phi(t)$ which are related with the electric field and the magnetic field, respectively. Hence, assuming that the pulse spreads freely in space, i.e., an isolated pulse, mathematically the linearly polarized pulse with a finite duration T can be defined by its vector potential as [66]

$$\mathbf{A}(t) = \begin{cases} A_0 f(t) \sin[\Phi(t)] \epsilon_p & t \in [0, T] \\ 0 & \text{elsewhere,} \end{cases} \quad (6.1)$$

where A_0 is the vector potential amplitude, $f(t)$ is the shape or carrier-envelope function that defines the time duration T , ϵ_p is the polarization vector and $\Phi(t)$ is the sine whole phase given by

$$\Phi(t) = \varphi + \omega_0 t + bt^2, \quad (6.2)$$

where φ is the carrier-envelope phase, ω_0 is the carrier-envelope frequency or the pulse central frequency and b is the chirp parameter that introduces a time-dependence of the pulse

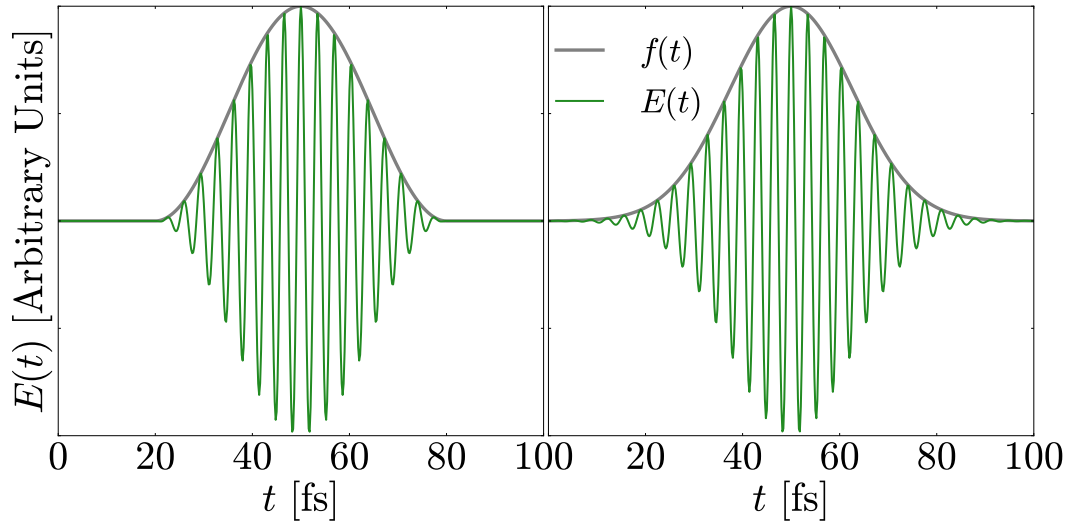


Figure 6.1: Electric field vector in the polarization direction (green line) and its carrier-envelope function (gray line) in arbitrary units. Pulse parameters for the sine squared carrier-envelope (left panel) are $T = 60$ fs, $\omega_0 = 1.2$ eV, chirping parameter $b = 0$, initial time of set-up $\tau = 50$ fs and the carrier-envelope phase ϕ is chosen to obtain the maximum of the electric field at the center of the carrier-envelope function. For the Gaussian carrier-envelope (right panel) $\sigma = 30$ fs and the other parameters are the same that in the left panel.

frequency [67]. In order to get an idea on how the vector potential defines an electromagnetic wave, the relation between the vector potential $\mathbf{A}(t)$ with the electric field vector $\mathbf{E}(t)$, in atomic units, yields

$$\mathbf{E}(t) = -\frac{\partial \mathbf{A}(t)}{\partial t}. \quad (6.3)$$

For simplicity in the calculations, the length gauge is used, and therefore of the electric field vector $\mathbf{E}(t)$ instead of the vector potential $\mathbf{A}(t)$.

6.1.1 CARRIER-ENVELOPE FUNCTION

Several mathematical functions have been used to describe the carrier-envelope function $f(t)$. The choice of the function depends on the system under study and the experimental conditions to be simulated. The most widely used carrier-envelope functions are Gaussian and sine/cosine squared. Each one has its advantages and disadvantages, e. g., the disadvantage to employ a Gaussian carrier-envelope is that the amplitude only vanishes at $t \pm \infty$ and its duration is defined in terms of the full width at half maximum (FWHM). Then the initial amplitude for the field is not strictly zero in simulations. At variance, the sin-squared envelope is zero at the time endpoints. However, Gaussian is used because it better reproduces the experimental pulse and the FWHM is widely used among experimentalist.

6.1.1.1 SINE/COSINE SQUARED CARRIER-ENVELOPE

In this work, pulses are chosen with a sin/cos squared envelope. The expression, after Eqs. (6.1) and (6.3), the electric field vector $\mathbf{E}(t)$ with a sine squared carrier-envelope reads

$$\mathbf{E}(t) = \Theta(t - \tau + T/2) \mathbf{E}_0 \sin^2 \left[\frac{\pi}{T} (t - \tau + T/2) \right] \sin [\Phi(t - \tau + T/2)] \Theta(T/2 + \tau - t) \epsilon_p, \quad (6.4)$$

where $\Theta(t)$ is the Heaviside function and τ is the time delay of the pulse against the initial time set at $t = 0$. The sine squared function has a factor of π/T , which ensures that this type

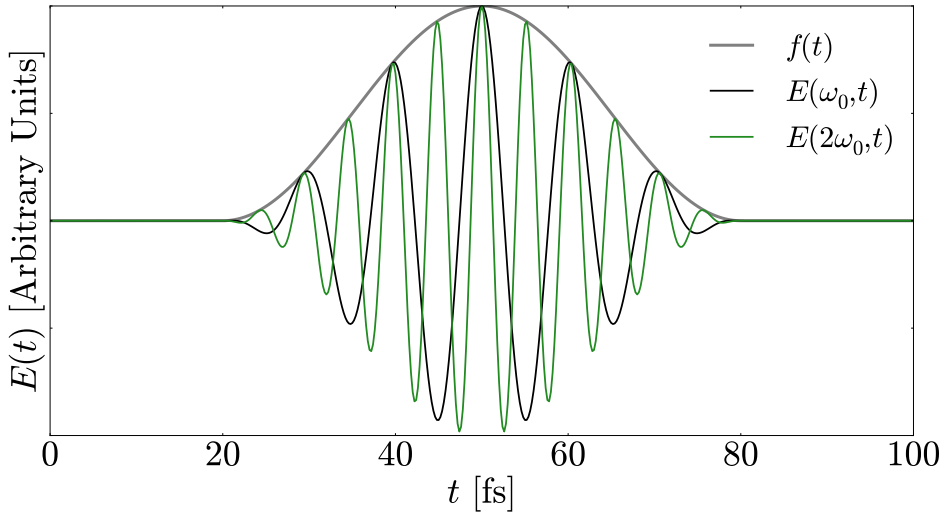


Figure 6.2: Electric field vector in the polarization direction with the central frequency ω_0 (black line) and $2\omega_0$ (green line) and its sine carrier-envelope function (gray line) in arbitrary units. Pulse parameters are $T = 60$ fs, $\omega_0 = 0.4$ eV, $b = 0$, $\tau = 50$ fs and the carrier-envelope phase φ is chosen to obtain the maximum of the electric field in the center of the carrier-envelope function.

of envelope is just the positive half cycle of a complete oscillation between the initial $\tau - T/2$ and the final time $\tau + T/2$ of the pulse duration and with its maximum value located at time τ . Left panel in Fig. 6.1 illustrates an example for a pulse, with an amplitude E_0 (related to the intensity), a central frequency $\omega_0 = 1.2$ eV, a duration $T = 60$ fs and a time delay $\tau = 50$ fs from the initial time $t = 0$.

6.1.1.2 GAUSSIAN CARRIER-ENVELOPE

Another carrier-envelope function used frequently in the literature is the Gaussian carrier-envelope, which, according to Eq. (6.1) and Eq. (6.3), generates the electric field vector $E(t)$ given by

$$E(t) = E_0 e^{\left[\frac{(t-\tau)^2}{2\sigma^2} \right]} \sin [\Phi(t-\tau)] \epsilon_p, \quad (6.5)$$

where σ is the standard deviation of the Gaussian pulse, which is defined in terms of full width at half maximum (FWHM) of the peak, from a Gaussian function according to

$$\text{FWHM} = 2\sqrt{2\ln 2}\sigma. \quad (6.6)$$

As it is well known, the Gaussian function is only zero at infinite time $t \rightarrow \pm\infty$. Right panel in Fig. 6.1 shows a laser pulse with a Gaussian envelope function, which shows that the field still oscillates far outside the FWHM region. It means that in the computations the field does not start smoothly from a zero value, but it switches on with a given non-zero value.

6.1.2 CARRIER-ENVELOPE FREQUENCY OR CENTRAL FREQUENCY

Among all pulse parameters defined above, the central frequency is the most relevant. From the concept of wave mechanics, the frequency is defined as the number of oscillations per unit of time. Hence, for an ultrashort pulse, the central frequency ω_0 is defined as the number of full

oscillations of the vector potential or electric field vector per unit of time. The relation between the laser intensity I and the electric field amplitude E_0 reads

$$E_0 = \sqrt{\frac{2I}{c\epsilon_0}}, \quad (6.7)$$

where c and ϵ_0 are the speed of light and the permittivity of free space, respectively.

Taking into account the definition of the carrier-envelope function, which confines the pulse in a time window where the pulse is non-zero, one can determine the number of cycles n_c within the laser pulse. This number of cycles is related with the central frequency ω_0 and the pulse time duration T . The total duration of the laser pulse T can be expressed in terms of the period of a cycle $T_c = 2\pi/\omega_0$ and an integer number of cycles n_c , with $T = T_c n_c$. [Fig. 6.2](#) shows two pulses with different frequencies, ω_0 and $2\omega_0$. In this, it is possible to see that because the carrier-envelope function confines the time range in which the pulse is non-zero, when the central frequency is higher, the maximum number of full oscillations or cycles is larger.

For simplicity, the chirp parameter and the carrier-envelope phase have been taking as zero, i.e., $b = 0$ and $\phi = 0$ in the explanation of previous parameters. However, all calculations in the present work take the maximum value of electric field vector at the center of the pulse. The pulse parameter used to obtain this value is the carrier-envelope phase ϕ defined in [Eq. \(6.2\)](#). The value of the carrier-envelope phase (CEP) can be obtained from [Eq. \(6.4\)](#) if the sine function, responsible of the oscillations of the pulse, at the time t when the maximum of the carrier-envelope function is equal to one. According to [Eq. \(6.4\)](#) evaluated at the time corresponding with the center of the carrier-envelope function $t = \tau$

$$E(t = \tau) = \sin [\Phi(\tau - \tau + T/2)] = \sin [\Phi(T/2)] = \sin [\phi + \omega_0 T/2 + b(T/2)^2] = 1, \quad (6.8)$$

the carrier-envelope phase reads

$$\phi = \frac{\pi}{2} - \frac{\omega_0 T}{2} - \frac{b T^2}{4}, \quad (6.9)$$

which explicitly depends on the central frequency ω_0 and the chirp parameter b .

6.1.3 FREQUENCY DOMAIN

As it is mentioned above, the central frequency is the most relevant pulse parameter and the cornerstone of the analysis of how a pulse interacts with a molecular system, due to the its energetic relation. For analysis purposes, specially in spectral methods, the next section is dedicated to explain the frequency domain of different pulses.

As it is shown in [Chapters 3 and 4](#), when one performs a molecular quantum dynamics, it is necessary to know the excited states that lead to photo-chemical reactions as photodissociation or photoionization, i.e., to know the energy region where any pulse can excite the system under study leading to this photo-chemical processes. Following these last ideas and according to the value of the central frequency it is possible to get an idea, with the frequency domain of the pulse, of the states that play an important role in the process under study in the multi-state molecular quantum dynamics, which involves two or more states of the system.

The fundamental mathematical definition to study the pulses in the frequency domain is through the Fourier transform, which is used for analysis purposes in many fields of science, such as optics, random processes, probability theory and quantum physics. The well known Fourier transform of the pulse, which leads the time dependent electric field vector $E(t)$ to its respective frequency dependent function, $\mathcal{F}[E(t)](\omega) = \mathcal{E}(\omega)$ reads

$$\mathcal{E}(\omega) = \frac{1}{\sqrt{2\pi}} \int_{-\infty}^{\infty} dt E(t) e^{-i\omega t}. \quad (6.10)$$

It is worth to mention that the reciprocal variable of time is the frequency ν which arises from the definition of the angular frequency $\omega = 2\pi\nu$. One important aspect in the use of the Fourier

transform of the pulse in the analysis is that depending on its shape or bandwidth, one can define if the pulse is composed by one or more than one central frequency. Since in this work the sine-square envelope is mostly used, its Fourier transform (with a chirp parameter $b = 0$) reads

$$\mathcal{E}(\omega) = \frac{E_0}{\sqrt{2\pi}} \int_{-\infty}^{\infty} dt \Theta(t - t_0 + T/2) \sin^2 \left[\frac{\pi}{T} (t - t_0 + T/2) \right] \times \sin [\omega_0 (t - t_0 + T/2) + \varphi] \Theta(T/2 + t_0 - t) e^{-i\omega t}. \quad (6.11)$$

With the substitution $t = t + t_0 - T/2$ the last expression reduces to

$$\mathcal{E}(\omega) = \frac{E_0}{\sqrt{2\pi}} e^{-i\omega(t_0 - T/2)} \int_0^T dt \sin^2 \left(\frac{\pi}{T} t \right) \sin(\omega_0 t + \varphi) e^{-i\omega t},$$

a simpler expression to integrate. The result of the Fourier transform of a laser pulse with a sine square carrier-envelope function is given by

$$\mathcal{E}(\omega) = E_0 e^{-i\omega t_0} \sqrt{\frac{\pi^3}{2}} \times \left\{ \frac{e^{i\varphi} e^{-i\omega_0 T/2} (e^{[i(\omega_0 - \omega)T]} - 1)}{(\omega_0 - \omega)[T^2(\omega_0 - \omega)^2 - 4\pi^2]} + \frac{e^{-i\varphi} e^{i\omega_0 T/2} (e^{[-i(\omega_0 + \omega)T]} - 1)}{(\omega_0 + \omega)[T^2(\omega_0 + \omega)^2 - 4\pi^2]} \right\}. \quad (6.12)$$

In order to get a simplified expression for the module of the Fourier transform, the well-known Rotating wave approximation (RWA) is used, which implies that only the absorption (or emission) term is considered [7]. Thus, the Fourier transform module of the laser pulse with a sine square carrier-envelope function $|\mathcal{E}(\omega)|$ reads

$$|\mathcal{E}(\omega)| = E_0 \sqrt{2\pi^3} \frac{\sin \left[\frac{(\omega_0 - \omega)T}{2} \right]}{(\omega_0 - \omega)[T^2(\omega_0 - \omega)^2 - 4\pi^2]}. \quad (6.13)$$

Note that the module of the Fourier transform in Eq. (6.13) does not depend on the initial time t_0 and the carrier-envelope phase φ . This makes that the distributions obtained for photoexcitation processes will be independent of the carrier-envelope phase φ for one-photon transitions.

In Fig. 6.3 one observes that the highest value of the amplitude in the Fourier transform $\mathcal{E}_0(\omega_0)$ is centered at the value of the central frequency ω_0 . Additionally, the amplitude of the Fourier transform $\mathcal{E}_0(\omega_0)$ also depends on the pulse time duration T . This can be extracted from the fact that the peak of the amplitude is in the value of the central frequency and taking the limit $\omega \rightarrow \omega_0$ in Eq. (6.13), the maximum value of the Fourier transform amplitude is given by

$$\mathcal{E}_0(\omega_0) \approx \frac{E_0}{4\sqrt{2\pi}} T. \quad (6.14)$$

Thus, it can be inferred that when the distributions are higher and narrower, the pulse time duration has been increased from another reference pulse.

Another important parameter used continuously in spectral analysis is the bandwidth $\Delta\omega$, which is defined as the full width at half maximum (FWHM) of the Fourier transform module and is given by

$$\Delta\omega = \frac{4\pi}{T}. \quad (6.15)$$

This expression indicates that longer pulses produce higher and narrower frequencies distributions, i. e., it selects the central frequency in a sharper way.

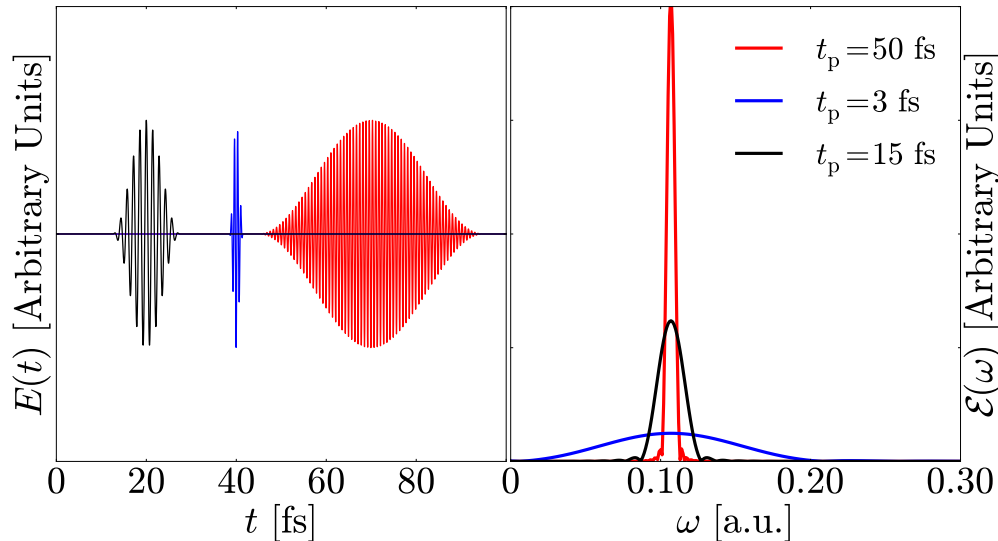


Figure 6.3: (Left panel) Laser pulses for pulse time durations of $T = 3$ fs (blue line), $T = 15$ fs (black line) and $T = 50$ fs (red line). (Right panel) Module of the Fourier transform of the electric field for the laser pulses in the left panel. All pulses have a central frequency $\omega_0 = 3.0$ eV or $\omega_0 \approx 0.11$ a.u.

6.2 COHERENT CONTROL THEORY

Currently one of the challenges in chemical-physics is to control the synthesis of new types of molecules or to control the final products in a chemical reaction. For instance, one of the techniques employed in chemistry is catalysis, which works in some type of chemical reactions. Light is here used as an universal catalyst to direct the course of reactions by manipulating the quantum wavepacket along the chosen reaction coordinate through a landscape of excited and ground PES.

The control of chemical reactions using light has been implemented for a long time and also continues to be investigated. Mode-Selective chemistry, by which the energy is selectively distributed in a mode of a molecule thus promoting the reaction in that area, initially thought to be a viable method of control. In fact, there was some success with small molecules, in particular controlling the dissociation of the HOD by exciting the levels of vibrational energy in any of the HO or DO bonds [68].

However, when one performs the analysis on larger molecules, the problem of intramolecular vibrational energy redistribution (IVR) arises. In this, the energy simply does not remain in a single mode. In fact, mode-selective chemistry is only viable for molecules in which the selected mode is weakly coupled to all other modes, which means that the energy will remain localized for enough time so that reaction occurs. This is only true for a handful of species, and therefore this approach has very limited applicability. Then, coherent control seeks to overcome these problems using light as a catalyst in all cases. The basic idea is the interference of a wavepackets, where a wavepacket is a coherent superposition of states. If a system is driven coherently from an initial state to a final state through more than one path, an interference pattern can be created between the different components of the wavepacket, it allows to go towards the desired products. For instance, consider the following experiment in a molecular system. Suppose that there is an initial state E_i and a final state E_f , the state one wants to reach. There is more than one path between these two states and they are indistinguishable from each other, if the energy gap between them is ω_0 , the state can be reached with a photon with an energy of $\hbar\omega_0$, but it is also possible to reach the final state with two, three or more photons, each one with an energy of $\hbar\omega/n$, where n is the number of photons. This idea is the control theory developed by Brumer and Shapiro [69, 70].

Along the time some methodologies have been introduced for coherent control, such as bichromatic control, traditional excitation [71], pump-dump [71, 72], pulse train and specially one that merges almost all the previous methods, which is called Optimal control theory (OCT) [73–75]. OCT has the goal to maximize or minimize certain transition probabilities, i. e., to find a specific wave function Ψ at a specific time t_f which maximize or minimize the desired goal or product. For example, to maximize or minimize the photo-dissociation, photo-isomerization probability for one or more specific modes of the system. Notwithstanding OCT can be the best form to perform coherent control in molecular systems, but the final results or the optimal control function (the form of the laser pulse) usually cannot be reproduced in the experiments. Therefore, this work focuses in the development of two methodologies which are the traditional excitation and pump-dump or pump-probe control, reproducible experimentally. Hence, the next step in this section is to describe the main characteristics of these two theories.

6.2.1 PUMP-DUMP CONTROL

Brumer and Shapiro introduced a new form to perform control over molecular systems in 1986 [70, 76]. This theory can be explained briefly as follows. Fig. 6.4 shows two possible pathways between the initial and final states of the system. The absorption of two photons of frequency ω_0 and the absorption of one photon of frequency $\omega_1 = 2\omega_0$. In experimental terms, these photons can be provided by two cw lasers with a enough large duration which allows a narrow bandwidth necessary to reach the desired final state. Suppose that in the energy level E_2 more than one product channel is available, e. g., a molecule that can ionize or dissociate depending of the different pulse parameters used, and one wants to manipulate the branching ratio of ionization or dissociation.

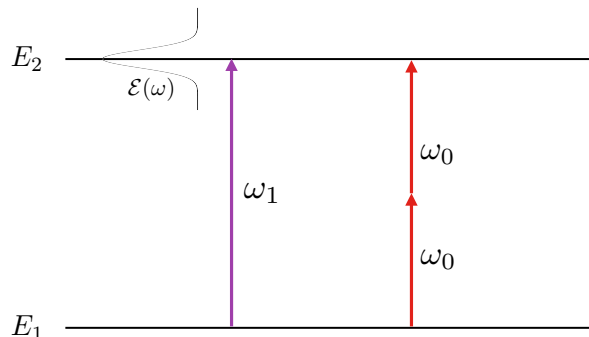


Figure 6.4: Schematic representation of the Brumer-Shapiro control theory. To reach the excited state E_2 from the initial state E_1 there are two possible pathways, the absorption of two photons (red arrows) or the absorption of one photon (magenta arrow).

Nonetheless, although Brumer and Shapiro idea seems relatively simple, it was materialized in 1995 in experiments with diatomic molecules HI [77] and DI [78]. The HI or DI was held in a chamber containing a variable pressure of H_2 gas and was excited using the fundamental and third harmonic of an excimer-pumped dye laser. The refractive index of the H_2 gas was very different for the two wavelengths used, and hence by varying the pressure their relative phases could be changed. The results from this experiment clearly showed a phase-lag between the two product channels, with the yield of I^+ increasing as that of DI^+ decreased, and vice-versa.

However, control of the molecular systems via a pump-dump scenario was initially introduced by Tannor and Rice in the perspective of the time domain [73], contrary to the Brumer and Shapiro method. This theory can be explained as follows. Left panel of Fig. 6.5 shows a wavepacket which is excited from an initial PES to a higher PES using an ultrashort laser pulse. After the excitation, the wavepacket evolves along the upper PES until a second ultrashort laser pulse, i. e., the dump pulse, transfers the wavepacket down to the initial PES.

In this case, the delay between the *pump* and *dump* pulses is the control parameter to get the desired final products. This is achieved because different regions of the [PES](#) give rise to different probability of the final products in the chemical reaction. It is worth mentioning that the *dump* pulse does not normally bring the wavepacket to the initial [PES](#), it is also possible to excite the system to a higher [PES](#) depending on the central frequency used in the dump pulse.

Once theory describes how is the phenomenon, it is time to go through the experiment. The first experimental achievement of pump-dump control was performed by Baumert et al. using the dissociation and ionization of Na_2 [79, 80]. They found that if the probe laser comes when the wavepacket excited by the pump pulse is located at the inner turning point of the [PES](#), Na_2^+ is produced, but if the wavepacket moves closer to the outer turning point, then Na^+ is produced.

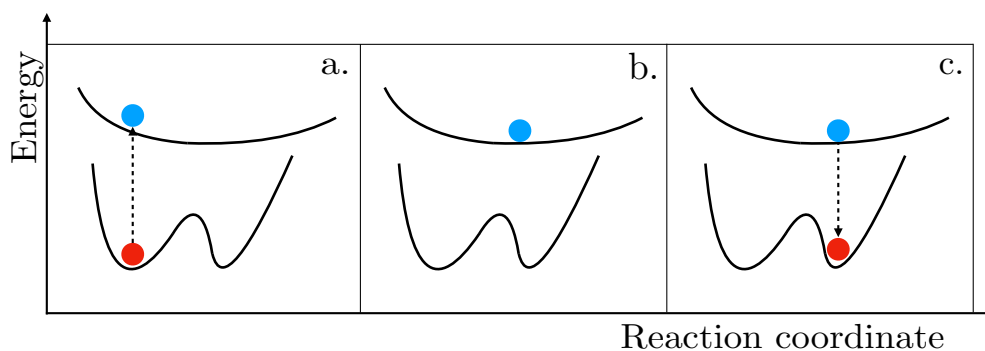


Figure 6.5: Schematic representation of the Tannor-Rice control theory.

6.2.2 PUMP-PROBE CONTROL

One ultrashort single isolated pulse excites the ground state of a molecular system into excited and/or ionic states of the system, which generates vibronic (vibrational and electronic) wavepackets that evolve in time and space. Although most of the actual techniques are capable of measuring the final probabilities and cross sections in the long time limit, they are not capable to completely access to the dynamic information of the wavepacket itself. To follow the dynamics in detail, it would be necessary to *take pictures* at different times (stroboscopic techniques) to reconstruct the wavepacket dynamics, similar to a video camera that takes snapshots. In this way, it becomes necessary to use a combination of different pulses, to first create the excitation of the molecule, i. e., to launch the dynamics, and after that to trace this dynamics during its evolution.

The pump-probe techniques in femtochemistry are the logical evolution of previous pump-dump experiments. In order to control chemical reactions with pump-dump experiments [73, 81–83], the initial population in the electronic ground state (depend on the kind of study, *ground* refers to initial) is excited by the pump laser pulse, which generates a vibronic wavepacket that evolves in time and space in the electronic excited state. Once the wavepacket has evolved and it arrives to the region of interest, e. g., dissociation or isomerization regions, the dump laser pulse produces a second light-induced transition, which aims at depopulating the excited state in favour of the desired products. However, with pump-dump experiments it is not possible to obtain the dynamical information of the intermediate wavepacket, i. e., the part of the wavepacket that contains the information about the transition state between the reactants and products. Hence, to get the *snapshots* the protocol is changed using a combination of infrared (IR) pulses [84], where the pump pulse creates the excitation into the electronic excited state of the system and the probe pulse gives the position of the intermediate wavepacket as a function of the time delay between both pulses, which gives the dynamical information of the wavepacket.

Since the description of the pulses used in this work are limited to linearly polarized light pulses, the total electric field, $E(t)$ in the dipole approximation in a pump-probe description is given by

$$E(t) = E_1(t) + E_2(t), \quad (6.16)$$

where $E_1(t)$ is the vector of the electric field corresponding to the pump pulse and $E_2(t)$ is the vector of the electric field of the probe. In this case, both the pump pulse and probe pulse are defined by [Eq. \(6.4\)](#) or [Eq. \(6.5\)](#) with its own pulse parameters such as the pulse time duration, central frequency, carrier-envelope, amplitude and time delay.

The time delay between the pulses τ depends on the convention used for the delay of each pulse. As it is defined in [Eq. \(6.4\)](#), the time delay of a single pulse is given by $\tau_i - T/2$ and therefore

$$\tau = \left(\tau_2 - \frac{T_2}{2} \right) - \left(\tau_1 - \frac{T_1}{2} \right), \quad (6.17)$$

where τ_i and T_i correspond to the time delay and time duration of each pulse, respectively. Taking into account that index 1 represent the pump pulse and the index 2 the probe pulse.

In all calculations performed in this work, the carrier-envelope-phase has been fixed to have the maximum of the amplitude of the electric field in the center of the pulse. One of the interest of this choice is that in light-matter interaction processes the CEP is associated with the number of oscillations of the pulse. A pulse with a central frequency that ensures a considerable number of oscillations inside the envelope does not have physical consequences if the maximum is not locked, according to the CEP. Nonetheless, in the case of IR pulses, the pulse has a smaller number of oscillations and therefore the structure of the pulse may be affected by a change in the CEP. Thus, in a XUV pump - IR probe scheme becomes necessary to fix the maximum of the electric field amplitude in the center of the pulse, i. e., to set the phase ϕ of the pulse according to [Eq. \(6.9\)](#).

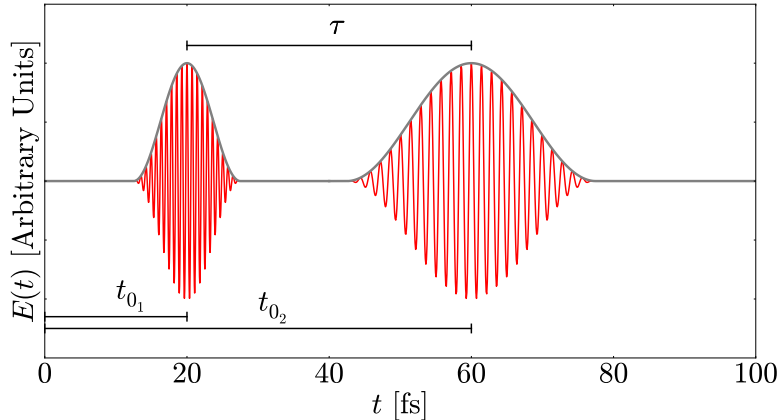


Figure 6.6: Schematic representation of the pump-probe pulse. The pump and probe pulses have frequencies of 5.71 eV and 2.72 eV, pulse time duration of 15 fs and 35 fs and pulse time delays of 20 fs and 60 fs, respectively.

[Fig. 6.6](#) shows a XUV pump - IR probe pulse scheme. It is possible to see the pump probe with a higher frequency and shorter cycle period than the probe pulse. In this case, the pump pulse is used to launch the dynamics to electronic excited states ($\omega_0_1 \sim 5.71$ eV) and the probe pulse ($\omega_0_2 \sim 2.72$ eV) to get or control the final products in the chemical reaction under study.

A scientist in his laboratory is not a mere technician: he is also a child confronting natural phenomena that impress him as though they were fairy tales.

— Marie Curie

7

QUANTUM APPROACH FOR LIGHT

Light has a special position in the formulation of quantum mechanics and it has a long story related to its nature (wave-particle duality) and its representation (classical vs quantum). The classical description of light comes from the Maxwell's electromagnetic equations. However, because the era of quantum initiated by the Planck's law, where the energy is discretized following the Einstein's ideas and the introduction of photon concept, it makes necessary to study the quantum features of light. The quantum theory of light requires the quantization of electromagnetic field from Maxwell equations. The quantization of the radiation field is necessary to explain well known quantum effects, such as spontaneous emission [1, 2], the Lamb shift [2–4], the Casimir effect [5, 6], and the photon statistics of the laser [2, 7]. Keeping in mind that this work studies the dynamics of molecules confined in optical cavities, the interaction of the cavity radiation with confined molecules can only be understood by using the quantum formalism of radiation. This chapter describes how the electromagnetic field is quantized and gives a brief outline of the different quantum states of light and their properties.

7.1 QUANTIZATION OF ELECTROMAGNETIC FIELD

The quantization of the electromagnetic field allows to visualize the quantum-mechanical properties and effects of the radiation field that are not present in its classical counterpart. Hence, to quantize the electromagnetic field, it is convenient to begin from the Maxwell's equations in free space. These equations provide relations between the electric and magnetic fields, represented by the vectors \mathbf{E} and \mathbf{B} , respectively. The Maxwell's equations in free space are given by

$$\nabla \times \mathbf{E} = -\frac{\partial \mathbf{B}}{\partial t}, \quad (7.1)$$

$$\nabla \times \mathbf{B} = \mu_0 \epsilon_0 \frac{\partial \mathbf{E}}{\partial t}, \quad (7.2)$$

$$\nabla \cdot \mathbf{E} = 0, \quad (7.3)$$

$$\nabla \cdot \mathbf{B} = 0, \quad (7.4)$$

where μ_0 and ϵ_0 are the magnetic permeability and electric permittivity of free space, respectively, which are related with the speed of light in vacuum c as $\mu_0 \epsilon_0 = 1/c^2$. From Eqs. (7.1) to (7.4) one arrives to the wave equation for \mathbf{E} which is given by

$$\nabla^2 \mathbf{E} - \frac{1}{c^2} \frac{\partial^2 \mathbf{E}}{\partial t^2} = 0. \quad (7.5)$$

Assuming that the radiation field is confined to a one-dimensional cavity along the z -axis with perfectly conducting walls, i. e., the electric field vanishes at the boundaries and takes the form of a standing wave. Additionally, if the electric field $\mathbf{E}(\mathbf{r}, t)$ is assumed to be polarized along the x -axis direction, i. e., $\mathbf{E}(\mathbf{r}, t) = E_x(z, t) \hat{\mathbf{e}}_x$ the solution for a single-mode field is given by

$$E_x(z, t) = \left(\frac{2\omega^2}{V\epsilon_0} \right)^{1/2} q(t) \sin(kz), \quad (7.6)$$

where ω is the frequency mode, $k = \omega/c$ is the wave number, V is the effective volume of the cavity and $q(t)$ is a time-dependent factor that depends on the cavity length and it plays the

role as the canonical position. The boundary conditions of the cavity lead to recognize that only some frequencies are allowed, i.e., $\omega_m = c(m\pi/L)$ with $m = 1, 2, \dots$ with L the length of the cavity. Since the electromagnetic field can be viewed as the combination of an electric field and a magnetic field, the magnetic field has the same wave equation as Eq. (7.5) with the solution

$$B_y(z, t) = \left(\frac{\mu_0 \epsilon_0}{k} \right) \left(\frac{2\omega^2}{V\epsilon_0} \right)^{1/2} \dot{q}(t) \cos(kz). \quad (7.7)$$

Contrary to the case of the electric field, $\dot{q}(t)$ plays the role of a canonical momentum p for a particle of mass unity. The next step is to quantize the canonical position q and momentum p , as usual in quantum mechanics, which transforms the expressions for the E and B fields into operators. The classical Hamiltonian can also be transformed to its quantum version.

From classical mechanics, it is well known that the Hamiltonian represents the total energy of the system, hence, the total energy of the classical field of a single mode is given by

$$H = \frac{1}{2} \int dV \left[\epsilon_0 E^2(\mathbf{r}, t) + \frac{1}{\mu_0} B^2(\mathbf{r}, t) \right] = \frac{1}{2} \int dV \left[\epsilon_0 E_x^2(z, t) + \frac{1}{\mu_0} B_y^2(z, t) \right], \quad (7.8)$$

where the integration is carried out over the volume of the cavity. Replacing Eqs. (7.6) and (7.7) into Eq. (7.8) and integrating over the volume, one obtains a remarkable result for the Hamiltonian

$$H = \frac{1}{2}(p^2 + \omega^2 q^2). \quad (7.9)$$

The latter equation indicates that a single-mode field can be described in terms of a harmonic oscillator for a particle with unit mass. Taking into account that position q and momentum p are canonical variables, in the quantum approach these variables are chosen by its corresponding position \hat{q} and momentum \hat{p} operators. Thus, the canonical transformation from the quantum canonical variables to the ladder operators is defined by

$$\hat{a} = \frac{1}{\sqrt{2\hbar\omega}}(\omega\hat{q} + i\hat{p}), \quad (7.10)$$

$$\hat{a}^\dagger = \frac{1}{\sqrt{2\hbar\omega}}(\omega\hat{q} - i\hat{p}), \quad (7.11)$$

and as a consequence the electric and magnetic field operators are

$$\hat{E}_x(z, t) = \mathcal{E}_0(\hat{a} + \hat{a}^\dagger) \sin(kz), \quad (7.12)$$

$$\hat{B}_y(z, t) = -i\mathcal{B}_0(\hat{a} - \hat{a}^\dagger) \cos(kz), \quad (7.13)$$

where $\mathcal{E}_0 = (\hbar\omega/\epsilon_0 V)^{1/2}$ and $\mathcal{B}_0 = (\mu_0/k)(\hbar\omega/\epsilon_0 V)^{1/2}$ are called the electric and magnetic field *per photon*, respectively [7]. The ladder operators obey the commutation relation

$$[\hat{a}, \hat{a}^\dagger] = 1, \quad (7.14)$$

the Hamiltonian in terms of these operators is given by

$$\hat{H} = \hbar\omega \left(\hat{a}^\dagger \hat{a} + \frac{1}{2} \right), \quad (7.15)$$

which, as expected, is the Hamiltonian of a quantum harmonic oscillator.

7.2 QUANTUM STATES OF LIGHT

7.2.1 FOCK OR NUMBER STATES

The operator $\hat{a}^\dagger \hat{a}$ in Eq. (7.15) is defined as the number operator \hat{n} . Each vector in the Hilbert space in the Dirac form can be taken as an eigenstate, hence, let $|n\rangle$ be the energy eigenstate corresponding to the energy eigenvalue E_n , i.e.,

$$\hat{H}|n\rangle = \hbar\omega \left(\hat{a}^\dagger \hat{a} + \frac{1}{2} \right) |n\rangle = E_n |n\rangle, \quad (7.16)$$

where

$$E_n = \hbar\omega \left(n + \frac{1}{2} \right) \text{ with } n = 0, 1, 2, \dots \quad (7.17)$$

According to Eq. (7.17), the number operator $\hat{n} = \hat{a}^\dagger \hat{a}$ applied over the Fock state $|n\rangle$ gives as a result

$$\hat{n} |n\rangle = n |n\rangle, \quad (7.18)$$

and \hat{a} and \hat{a}^\dagger applied over a Fock state is

$$\hat{a} |n\rangle = \sqrt{n} |n-1\rangle \quad (7.19)$$

$$\hat{a}^\dagger |n\rangle = \sqrt{n+1} |n+1\rangle, \quad (7.20)$$

which means that from the vacuum state one can generate any Fock state applying n times the creation operator, using

$$|n\rangle = \frac{(\hat{a}^\dagger)^n}{\sqrt{n!}} |0\rangle. \quad (7.21)$$

Because \hat{H} and \hat{n} are Hermitian operators, Fock states with different label n are orthogonal, i.e., $\langle n' | n \rangle = \delta_{nn'}$ and furthermore, they form a complete basis set of states for a Hilbert space so that the completeness expression for this discrete basis reads

$$\sum_{n=0}^{\infty} |n\rangle \langle n| = 1. \quad (7.22)$$

7.2.1.1 FOCK STATES OF LIGHT IN THE POSITION SPACE REPRESENTATION

The Fock state position space representation can be obtained projecting Eq. (7.21) with a position vector basis $\langle x|$, which gives as a result

$$\Psi_n(x) = \langle x | n \rangle = \frac{1}{\sqrt{2^n n!}} \left(\frac{\omega}{\pi \hbar} \right)^{1/4} e^{-\frac{\omega}{2\hbar} x^2} H_n \left(\sqrt{\frac{\omega}{\hbar}} x \right), \quad (7.23)$$

where $H_n(q)$ are the Hermite polynomials and ω is the frequency of the light mode.

7.2.2 COHERENT STATES

Fock states describe the light in terms of the photon number, but this is not the only form to represent quantum optical fields. The coherent states are quantum states whose properties are closer to those from a classical description of radiation. These coherent states can be represented as a superposition of Fock states, thus with an average number of photons and they are also minimum uncertainty states [7].

Coherent states are defined by a label which is a complex number α , with its modulus related with the average number of photons in the field, i.e., $\bar{n} = |\alpha|^2$. It can be generated by three forms, *i*) as the right eigenstates of the annihilation operator $\hat{a} |\alpha\rangle = \alpha |\alpha\rangle$, *ii*) by a displacement of the vacuum state and *iii*) as states that minimize the uncertainty relation for the two orthogonal field quadratures with equal uncertainties in each quadrature and as the displacement of the vacuum state [7]. In the complex plane, the displacement operator is defined by [85]

$$\hat{D}(\alpha) = e^{\alpha \hat{a}^\dagger - \alpha^* \hat{a}}, \quad (7.24)$$

with which the coherent state $|\alpha\rangle$ is generated from the vacuum state with zero photons $|0\rangle$, as follows

$$|\alpha\rangle = \hat{D}(\alpha) |0\rangle, \quad (7.25)$$

where a displacement α is applied over the vacuum state $|0\rangle$. Taking into account the Zassenhaus formula, the displacement operator $\hat{D}(\alpha)$ can be separated as

$$\hat{D}(\alpha) = e^{\alpha\hat{a}^\dagger - \alpha^*\hat{a}} = e^{-|\alpha|^2/2} e^{\alpha\hat{a}^\dagger} e^{-\alpha^*\hat{a}}, \quad (7.26)$$

where the commutator $[\alpha\hat{a}^\dagger, -\alpha^*\hat{a}] = |\alpha|^2$. Thus, applying each part of the displacement operator in Eq. (7.26) into the vacuum state (see Eq. (7.25)), one obtains the expressions

$$e^{-\alpha^*\hat{a}} |0\rangle = \sum_{m=0}^{\infty} \frac{(-\alpha^*\hat{a})^m}{m!} |0\rangle = |0\rangle \quad (7.27)$$

$$e^{\alpha\hat{a}^\dagger} |0\rangle = \sum_{n=0}^{\infty} \frac{(\alpha\hat{a}^\dagger)^n}{n!} |0\rangle = \sum_{n=0}^{\infty} \frac{\alpha^n}{\sqrt{n!}} |n\rangle, \quad (7.28)$$

thus providing a final form for the coherent state in terms of the Fock basis

$$|\alpha\rangle = e^{-|\alpha|^2/2} \sum_{n=0}^{\infty} \frac{\alpha^n}{\sqrt{n!}} |n\rangle. \quad (7.29)$$

Additionally, the average photon number \bar{n} in the coherent state is evaluated with the number operator $\hat{n} = \hat{a}^\dagger\hat{a}$, which is given by $\bar{n} = |\alpha|^2$.

7.2.2.1 COHERENT STATES OF LIGHT IN THE POSITION SPACE REPRESENTATION

Fock number states $|n\rangle$ can be represented in position space (this does not imply that there is a spatial wave function for the photon). Similarly the coherent states can also be represented in position space using the projection of the position basis $\langle x|$.

Thus, projecting in Eq. (7.29) one obtains that

$$\Psi_\alpha(x) = \langle x|\alpha\rangle = e^{-|\alpha|^2/2} \sum_{n=0}^{\infty} \frac{\alpha^n}{\sqrt{n!}} \langle x|n\rangle = \langle x|\alpha\rangle = e^{-|\alpha|^2/2} \sum_{n=0}^{\infty} \frac{\alpha^n}{\sqrt{n!}} \Psi_n(x), \quad (7.30)$$

where $\langle x|\alpha\rangle = \Psi_\alpha(x)$ is the wave function for the coherent state in terms of the eigenfunctions of the harmonic oscillator of unit mass given in Eq. (7.23). Therefore,

$$\Psi_\alpha(x) = \left(\frac{\omega}{\pi\hbar}\right)^{1/4} e^{-|\alpha|^2/2} e^{-\frac{\omega}{2\hbar}x^2} \sum_{n=0}^{\infty} \frac{(\alpha/\sqrt{2})^n}{n!} H_n\left(\sqrt{\frac{\omega}{\hbar}}x\right), \quad (7.31)$$

and according with the generating function of Hermite polynomials

$$e^{-t^2+2tq} = \sum_{n=0}^{\infty} \frac{t^n}{n!} H_n(q), \quad (7.32)$$

with $t = \alpha/\sqrt{2}$ and $q = \sqrt{\frac{\omega}{\hbar}}x$, the coherent wavefunction can be expressed in closed form

$$\Psi_\alpha(x) = \left(\frac{\omega}{\pi\hbar}\right)^{1/4} e^{-|\alpha|^2/2} e^{-\frac{\omega}{2\hbar}x^2} e^{-(\alpha/\sqrt{2})^2 + 2(\alpha/\sqrt{2})(\sqrt{\frac{\omega}{\hbar}}x)}. \quad (7.33)$$

As mentioned above, the label α that characterizes the coherent state is a complex number. Given that it is easy to show that

$$\Delta x_\alpha = \sqrt{\frac{\hbar}{2\omega}} \quad (7.34)$$

$$\langle x \rangle_\alpha = \sqrt{\frac{\hbar}{2\omega}}(\alpha + \alpha^*) \quad (7.35)$$

$$\langle p \rangle_\alpha = -i\sqrt{\frac{\hbar\omega}{2}}(\alpha - \alpha^*), \quad (7.36)$$

the wave function for the coherent state can be written in terms of average values as follows

$$\Psi_\alpha(x, t) = \left(\frac{1}{2\pi\Delta x_\alpha^2} \right)^{1/4} e^{-\frac{1}{4} \left(\frac{x - \langle x \rangle_\alpha}{\Delta x_\alpha} \right)^2} e^{i\langle p \rangle_\alpha x / \hbar} e^{i\theta} \quad (7.37)$$

where $\theta = -\Re[\alpha]\Im[\alpha]$ and Δx_α , $\langle x \rangle_\alpha$ and $\langle p \rangle_\alpha$ are the width, position and momentum, respectively, of the Gaussian function in Eq. (7.37).

This is the expression suitable to be introduced as an input in the **MCTDH** method in [Chapter 12](#), considering that the radiation field lives in a virtual space (similar to the spin space) here represented by the Hamiltonian of a harmonic oscillator in position space. Again, it is important to stress that this representation of light in position space is not the same Hilbert space as that corresponding to position space representation in which atomic and molecular wave functions are represented.

7.2.3 SQUEEZED STATES

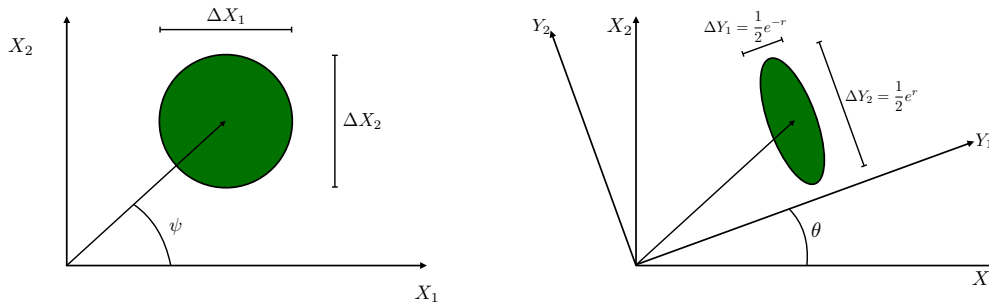
Squeezed states are quantum states of radiation characterized because they show less uncertainty than a coherent state in one of the quadratures (position or momentum) at the price of enlarging the other. Thus, the first step to understand better what is the effect of the *squeezing* is to define the variances for the position and momentum operators for the harmonic oscillator, where in the case of a coherent state are given by

$$(\Delta q_\alpha)^2 = \frac{\hbar}{2\omega}, \quad (\Delta p_\alpha)^2 = \frac{\hbar\omega}{2}, \quad (7.38)$$

which minimizes the well-known uncertainty principle (a property of coherent states) as follows

$$(\Delta q_\alpha \Delta p_\alpha) = \frac{\hbar}{2}. \quad (7.39)$$

In the case of quadrature operators (see Gerry et al. [7] for a deeper explanation), similar to Eq. (7.39), the coherent state has a particular minimum uncertainty state given by $\Delta \hat{X}_1 = \Delta \hat{X}_2 = 1$, which gives as a result that $\Delta \hat{X}_1 \Delta \hat{X}_2 \geq 1$, where \hat{X}_1 and \hat{X}_2 are the dimensionless quadrature operators in terms of ladder operators. Thus, a coherent state can be represented by a circle in phase space whose axis are X_1 for position and X_2 for momentum (see [Fig. 7.1a](#)).



(a) Phase space representation for a coherent state. (b) Phase space representation for a squeezed coherent state.

Figure 7.1: Phase space representation for a coherent state $|\alpha\rangle$ with $\alpha = |\alpha|e^{i\psi}$ and squeezed coherent state $|\alpha, \xi\rangle$ with $\xi = r e^{i\theta}$ where its corresponding average photon numbers $|\alpha|^2$ and $|\alpha|^2 + \sinh^2 r$, respectively.

Once the uncertainty relation has been analyzed in coherent states, a special case of another type of states is the *squeezed state*, states where the uncertainty of one quadrature is reduced and the other increase, e. g., $\Delta \hat{X}_1 < 1 < \Delta \hat{X}_2$. Squeezed states can be generated by the unitary squeezing operator given by [86]

$$\hat{S}(\xi) = \exp \left[\frac{1}{2} (\xi^* \hat{a}^2 - \xi \hat{a}^{\dagger 2}) \right], \quad (7.40)$$

with the complex variable $\xi = r e^{i\theta}$, where r is the squeezed parameter and $0 \leq r \leq \infty$ and $e^{i\theta}$ the squeezing phase with $0 \leq \theta \leq 2\pi$. For instance, the squeezing operator $\hat{S}(\xi)$ can be applied to the vacuum state $|0\rangle$ to produce a *vacuum squeezed state*

$$|\xi\rangle = \hat{S}(\xi)|0\rangle. \quad (7.41)$$

Nonetheless, a more general squeezed state may be obtained by applying the displacement operator to Eq. (7.41) in order to obtain

$$|\alpha, \xi\rangle = \hat{D}(\alpha)\hat{S}(\xi)|0\rangle. \quad (7.42)$$

In this case the average photon number is

$$\langle n \rangle = \langle \alpha | \hat{a}^\dagger \hat{a} | \alpha \rangle = |\alpha|^2 + \sinh^2 r, \quad (7.43)$$

where in contrast to the coherent state the average photon number also depends on squeezing parameter r .

7.2.3.1 SQUEEZED COHERENT STATES OF LIGHT IN THE POSITION SPACE REPRESENTATION

Since squeezed coherent states will be employed in the MCTDH dynamics, it is necessary to find their expression in the position representation. This derivation is not straightforward and details can be found in [87]. Thus, the squeezed coherent state in the position representation is given by

$$\Psi_{r,\alpha}(x) = \left(\frac{\omega}{\pi\hbar}\right)^{1/4} \left(\frac{1}{\cosh r + e^{i\theta} \sinh r}\right)^{1/2} e^{-\frac{1}{4}\left(\frac{x-\langle x \rangle_\alpha}{\Delta x_\alpha}\right)^2} e^{\frac{i}{\hbar}\langle p \rangle_\alpha(x-\langle x \rangle_\alpha/2)} \quad (7.44)$$

with the width given by $\Delta x_\alpha = \sqrt{\frac{\hbar}{2\omega}} \left(\frac{\cosh r + e^{i\theta} \sinh r}{\cosh r - e^{i\theta} \sinh r}\right)^{1/2}$ and the initial position $\langle x \rangle_\alpha = \sqrt{\frac{\hbar}{2\omega}}(\alpha + \alpha^*)$ and momentum $\langle p \rangle_\alpha = -i\sqrt{\frac{\hbar\omega}{2}}(\alpha - \alpha^*)$, with $\alpha = |\alpha|e^{i\psi}$, the coherent parameter.

7.2.3.2 TIME EVOLUTION OF COHERENT AND SQUEEZED COHERENT STATES

Along the previous sections in this chapter the main properties about the coherent and squeezed coherent states have been discussed. However, because they can be seen as a linear combination of the Fock states, i.e., the eigenvectors of the quantum harmonic oscillator, they evolve along the harmonic oscillator potential in different specific forms. In the case of coherent state, the Gaussian in Eq. (7.37) evolves without changing its shape and whose centroid follows the motion of a classical point particle in a harmonic oscillator potential, as represented by the upper row of Fig. 7.2.

Nonetheless, in the case of the squeezed state, the square absolute value of the wavefunction in Eq. (7.44) evolves as shown in the lower row in Fig. 7.2. In this case, one observes that the width of the Gaussian changes (breathing) periodically in time and, thus, the localization in space of the wave packet is periodically modified. In contrast to the other columns, where the wavefunction extends over more than 50 a.u., which makes that the ‘particle’ is not localized in space.

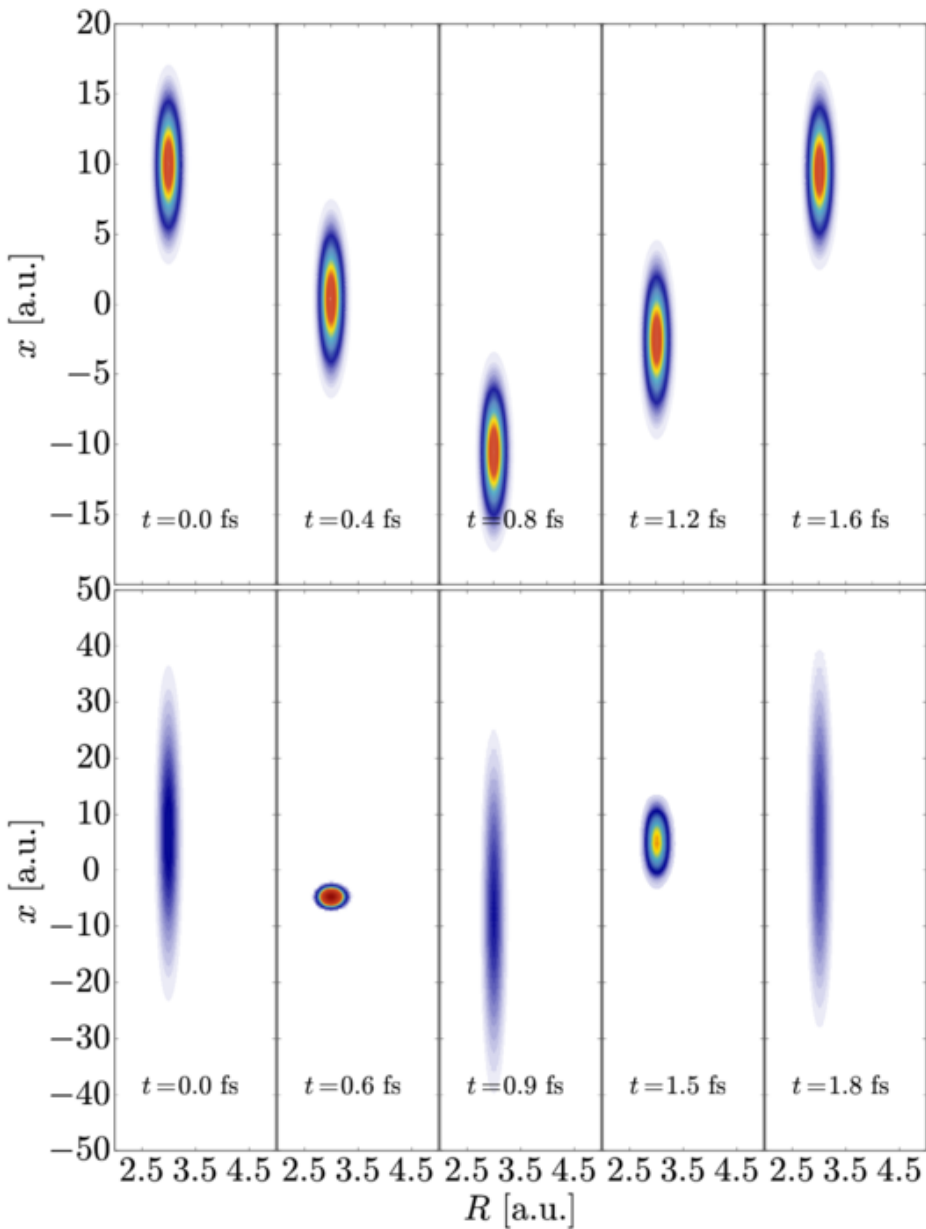


Figure 7.2: (Upper row) Evolution of a coherent state ($\alpha = 3e^{i\pi/4}$) wavefunction moving inside the harmonic oscillator potential (frequency $\omega = 2.47$ eV) along the x -coordinate, back and forth between the two classical turning points and without spreading. (Lower row) Evolution of a squeezed coherent state ($\alpha = 3e^{i\pi/4}$ and $\xi = 2e^{i\pi/50}$) wavefunction moving in the harmonic potential (frequency $\omega = 2.47$ eV) along x -coordinate. The periodical dispersion of the wave packet obeys the variation of one of its quadratures.

A scientist in his laboratory is not a mere technician: he is also a child confronting natural phenomena that impress him as though they were fairy tales.

— Marie Curie

8

LIGHT-MATTER INTERACTION

The main purpose in this chapter is to give an introduction about light-matter interactions both in the semiclassical approach and the quantum approach. In the latter case, the prototypical Jaynes-Cummings quantum model is briefly described, from which the picture of light-dressed states can be understood.

8.1 LIGHT-MATTER INTERACTION WITH A CLASSICAL FIELD

Firstly, it is convenient to define the Hamiltonian including the interaction term which, in the length gauge and in the dipole approximation, takes the form

$$\hat{H}(\hat{Q}, t) = \frac{\hat{P}^2}{2m} + \hat{V}(\hat{Q}) + q\hat{Q} \cdot \mathbf{E}(t) = \hat{H}_0(\hat{Q}) + \hat{H}_I(\hat{Q}, t), \quad (8.1)$$

where $\hat{V}(\hat{Q})$ is the binding potential of the particle, \hat{P} the momentum operator, q is the particle charge and \mathbf{E} the electric field. The term $-q\hat{Q}$ is known as the dipole moment operator $\hat{d} = -q\hat{Q}$. The last term in Eq. (8.1) is the light-matter interaction term in the form $\hat{H}_I(\hat{Q}, t) = \hat{d} \cdot \mathbf{E}(t)$.

First of all, the electric field may be considered as a monochromatic wave with frequency ω with the expression $\mathbf{E}(t) = \mathbf{E}_0 \cos(\omega t)$. This field is suddenly turned on at $t = 0$ and it has a duration T . At $t < 0$ the quantum system is only described by the unperturbed Hamiltonian \hat{H}_0 and it is prepared in a given state $|i\rangle$. When the field switches on, the state of the system evolves according to the TDSE

$$i\frac{\partial |\psi(t)\rangle}{\partial t} = (\hat{H}_0 + \hat{H}_I) |\psi(t)\rangle. \quad (8.2)$$

The time dependent wavepacket can be expanded in the complete set of eigenstates of the unperturbed Hamiltonian, i.e.,

$$|\psi(t)\rangle = \sum_k C_k(t) e^{-iE_k t} |k\rangle, \quad (8.3)$$

where the time-dependent amplitudes $C_k(t)$ satisfy the normalization requirements and unitary condition $\sum_i |C_i(t)|^2 = 1$. If one replaces Eq. (8.3) in Eq. (8.2) and projects with $\langle l | e^{iE_l t}$, it leads to a set of coupled differential equations for the expansion coefficients, which play the role of transition amplitudes from the chosen initial state $|i\rangle$ to any final $|k\rangle$ state

$$\dot{C}_l(t) = -i \sum_k C_k(t) \langle l | \hat{V}_I | k \rangle e^{i\omega_{lk} t}, \quad (8.4)$$

where $\omega_{lk} = E_l - E_k$ are the transition frequencies between the corresponding energy levels l and k . It is worth mentioning that this set of coupled differential equations provide an exact solution for complete expansions, subject to an initial condition for the coefficients at $t = 0$. At final time $t = T$, the integration of equations provide the transition amplitudes from the initial state to the final state $|f\rangle$, given by $C_f(T)$ and the corresponding transition probabilities by $P_{i \rightarrow f}(T) = |C_f(T)|^2$.

When the quantum system can be reduced to two interacting states, one arrives to the well-known Rabi model. In this case, for convenience, the two states are customary labelled $|g\rangle$ and $|e\rangle$ (after ground and excited, respectively). [88]. These states are characterized by the transition frequency $\omega_0 = E_e - E_g$, which corresponds to the energy difference between them. Now, the expansion in Eq. (8.3) takes the form

$$|\Psi(t)\rangle = C_g e^{-iE_g t} |g\rangle + C_e e^{-iE_e t} |e\rangle, \quad (8.5)$$

and the associated set of two coupled differential equations are

$$\dot{C}_g(t) = -i\mathcal{V} \cos(\omega t) e^{-i\omega_0 t} C_e \quad (8.6)$$

$$\dot{C}_e(t) = -i\mathcal{V} \cos(\omega t) e^{-i\omega_0 t} C_g, \quad (8.7)$$

where $\mathcal{V} = -\mathbf{d}_{eg} \cdot \mathbf{E}_0$ with $\mathbf{d}_{eg} = \langle e | e \mathbf{Q} | g \rangle$ being the dipole matrix element. If initial conditions are set as $C_g(0) = 1$ and $C_e(0) = 0$ and the **RWA** for $\cos(\omega t)$ is employed, the solution for the Rabi model is completely analytical and given by

$$C_e(t) = i \frac{\mathcal{V}}{\Omega_R} e^{i\Delta t/2} \sin(\Omega_R t/2) \quad (8.8)$$

$$C_g(t) = e^{i\Delta t/2} \left\{ \cos(\Omega_R t/2) - i \frac{\Delta}{\Omega_R} \sin(\Omega_R t/2) \right\}, \quad (8.9)$$

where $\Omega_R = \sqrt{\Delta^2 + \mathcal{V}^2}$ is the Rabi frequency and $\Delta = \omega_0 - \omega$ is the detuning, the difference between the laser frequency and the natural frequency, as Fig. 8.1 shows. Thus, the probability to populate the excited state $|e\rangle$ at any time t is

$$P_e(t) = \frac{\mathcal{V}^2}{\Omega_R^2} \sin^2(\Omega_R t/2). \quad (8.10)$$

This basic result shows that the time evolution of the excitation probabilities is oscillatory with a Rabi frequency Ω_R which in turn depends on the interaction strength \mathcal{V} and the detuning Δ .

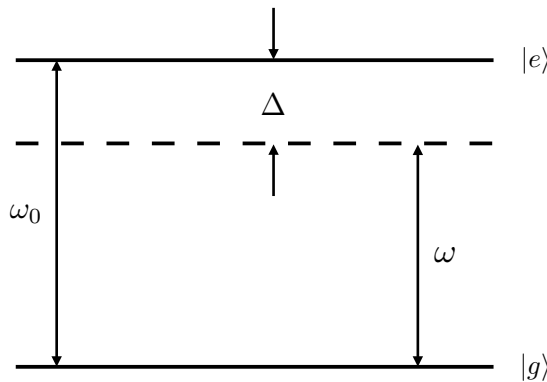


Figure 8.1: Schematic representation of Rabi model. The laser frequency ω with which the system is excited is close to the natural transition frequency ω_0 . The difference Δ is called detuning.

8.2 LIGHT-MATTER INTERACTION WITH A QUANTIZED FIELD

In the previous section, the electric field was assumed classical while the atomic system is quantized (hence the name semiclassical method). However, there are some situations where the classical approach of the radiation fails to explain the experimental results and as a consequence a quantized version of radiation is necessary. For instance, to describe the spontaneous emission. Here the quantum counterpart of the classical Rabi model is also described, and the same approximations, dipole and **RWA** are maintained.

Considering a single field mode, the interaction term in Eq. (8.1), similar to the classical case, becomes

$$\begin{aligned}\hat{H}_I &= \hat{\mathbf{d}} \cdot \mathcal{E}_0 (\hat{a} + \hat{a}^\dagger) \sin(kz) \\ &= \hat{a}g(\hat{a} + \hat{a}^\dagger),\end{aligned}\quad (8.11)$$

where the $g = \mathcal{E}_0 \sin(kz)$ and $\hat{a} = \hat{\mathbf{d}} \cdot \hat{\mathbf{e}}$, where $\hat{\mathbf{e}}$ is the polarization unit vector of the quantized field. Now it is convenient to introduce the ‘matter’ transition operators

$$\hat{\sigma}_+ = |e\rangle\langle g|, \quad \hat{\sigma}_- = |g\rangle\langle e| = \hat{\sigma}_+^\dagger, \quad (8.12)$$

which in the case of matter, in analogy to photonic operators \hat{a} and \hat{a}^\dagger , annihilates or creates a state of matter. For convenience, an inversion operator is defined as $\hat{\sigma}_3 = |e\rangle\langle e| - |g\rangle\langle g|$. These transition and projection operators obey the Pauli spin algebra and by parity considerations only the non-diagonal elements of the dipole operator $\hat{\mathbf{d}}$ are nonzero, i.e.,

$$\langle e | \hat{a} | e \rangle = \langle g | \hat{a} | g \rangle = 0. \quad (8.13)$$

This allows for the representation of the dipole operator in the form

$$\hat{a} = d |g\rangle\langle e| + d^* |e\rangle\langle g| = d\hat{\sigma}_- + d^*\hat{\sigma}_+ = d(\hat{\sigma}_- + \hat{\sigma}_+), \quad (8.14)$$

assuming that, generally, $d = \langle e | d | g \rangle$ is real. Thus, from Eq. (8.11) the interaction term in the Hamiltonian takes the form (as a function of photonic plus matter transition operators)

$$\hat{H}_I = \hbar\lambda(\hat{\sigma}_- + \hat{\sigma}_+)(\hat{a} + \hat{a}^\dagger), \quad (8.15)$$

where $\lambda = dg/\hbar$ represents the coupling strength between light and matter. Finally, one arrives to the quantum version of two-state $\{|g\rangle, |e\rangle\}$ Rabi model with dipolar coupling \hat{a} , which is called Jaynes-Cummings model [7], whose Hamiltonian before the RWA reads

$$\begin{aligned}\hat{H} &= \hat{H}_M + \hat{H}_F + \hat{H}_I \\ &= \frac{1}{2}\hbar\omega_0\hat{\sigma}_3 + \hbar\omega\left(\hat{a}^\dagger\hat{a} + \frac{1}{2}\right) + \hbar\lambda(\hat{a} + \hat{a}^\dagger)(\hat{\sigma}_+ + \hat{\sigma}_-)\end{aligned}\quad (8.16)$$

where \hat{H}_M and \hat{H}_F are the matter and field Hamiltonians, respectively, and $\omega_0 = (E_e - E_g)/\hbar$ is the natural frequency or transition frequency. Since the Jaynes-Cummings model admits a general time dependent solution in the interaction picture and within the RWA, the Jaynes-Cummings model Hamiltonian inside the RWA results

$$\hat{H} = \frac{1}{2}\hbar\omega_0\hat{\sigma}_3 + \hbar\omega\left(\hat{a}^\dagger\hat{a} + \frac{1}{2}\right) + \hbar\lambda(\hat{a}\hat{\sigma}_+ + \hat{a}^\dagger\hat{\sigma}_-),$$

where the counter-rotating terms are neglected. The time dependent solution in the interaction picture in the entangled form [7] is given by

$$|\Psi(t)\rangle = \sum_{n=0}^M [a_n(t)|g, n\rangle + b_n(t)|e, n\rangle], \quad (8.17)$$

which for any initial matter state assumed as a superposition in the form

$$|\Psi(0)\rangle_M = C_g|g\rangle + C_e|e\rangle, \quad (8.18)$$

and any radiation field represented in the Fock basis of photons, i.e.,

$$|\Psi(0)\rangle_F = \sum_{n=0}^M C_n|n\rangle, \quad (8.19)$$

which can be a Fock state, a coherent state, a vacuum squeezed state, a squeezed coherent state, etc. For subsequent molecular problems which will be explained in Chapter 12, the number of states M in the superposition in the Fock space can be very large, which makes this route of

solution very demanding. To circumvent the difficulties related to the representation of light in a Fock basis one can rely in the direct representation of the cavity light mode as a quantum harmonic oscillator of mass unity in coordinate space [89]. With this fundamental idea for the representation, one requires the position coordinate representation of a given quantum light state, be a Fock state, a coherent state or any other.

It is worth mentioning that the Hamiltonian in Eq. (8.16) is widely studied in quantum optics, because it admits an analytical solution which helps to explain diverse quantum optical effects, including those in optical cavities [90–92].

8.3 DRESSED STATES BASIS

Molecules in cavities may reach a strong coupling regime in the light-matter interaction. In this regime the structure and dynamics can be better understood using light-modified (or dressed) potential energy surfaces. The strong coupling regime is favored by the small volume of the cavity, hence the potential use of confinements in micro or nano-cavities. The typical treatment in quantum optics for these coupled systems is based in the two-state Jaynes-Cummings model introduced in the previous section. The eigenstates of the Jaynes-Cummings model are called dressed states, where the name comes from the fact that these states are *dressed* by the light. From the eigenvalues of the dressed states one can extract the new dressed potential energy surfaces of the molecule, that in the molecular case display new avoided crossings or conical intersections induced by the light. These phenomena of light induced crossings (LIC) and light induced conical intersections (LICI) is already described in the literature [93]. Additionally, most of the interesting molecular photo-reactivity is produced through electronic excited states. The molecular wave packets promoted to these excited states find different light-modified landscapes for its subsequent dynamics, thus opening new channels for photophysical or photochemical reactions. One of the goals in this work is to control or select a specific reaction path by manipulating the evolution of the wave packet in the manifold of excited states. Note that in this strong coupling regime the molecular modes of motion and the light cavity modes become entangled in a combined non-separable light-matter wave function.

According to Eq. (8.17), the only possible transitions in the complete system (light + matter) are

$$|e\rangle|n\rangle \leftrightarrow |g\rangle|n+1\rangle \text{ or } |e\rangle|n-1\rangle \leftrightarrow |g\rangle|n\rangle, \quad (8.20)$$

where the product states between the light and matter states is known as *bare* states of the Jaynes-Cummings model. For instance, in the case of emission $|e\rangle \rightarrow |g\rangle$ releasing one photon, $|n\rangle \rightarrow |n+1\rangle$, these bare states are

$$\begin{aligned} |\Psi_1\rangle &= |e\rangle|n\rangle \\ |\Psi_2\rangle &= |g\rangle|n+1\rangle. \end{aligned} \quad (8.21)$$

In this basis the representation of the Jaynes-Cummings Hamiltonian reads

$$H = \begin{pmatrix} \hbar[n\omega + \frac{1}{2}\omega_0] & \hbar\lambda\sqrt{n+1} \\ \hbar\lambda\sqrt{n+1} & \hbar[(n+1)\omega - \frac{1}{2}\omega_0] \end{pmatrix}, \quad (8.22)$$

with its corresponding eigenvalues given by

$$\epsilon_{\pm}(n) = \hbar\omega \left(n + \frac{1}{2} \right) \pm \hbar\Omega_n(\Delta), \quad (8.23)$$

where $\Delta = \omega_0 - \omega$ is the detuning and $\Omega_n(\Delta) = \sqrt{\Delta^2 + 4\lambda^2(n+1)}$ the Rabi frequency. The corresponding eigenstates have the form

$$\begin{aligned} |n,+\rangle &= \cos(\Phi_n/2)|\Psi_1\rangle + \sin(\Phi_n/2)|\Psi_2\rangle \\ |n,-\rangle &= -\sin(\Phi_n/2)|\Psi_1\rangle + \cos(\Phi_n/2)|\Psi_2\rangle, \end{aligned} \quad (8.24)$$

with a rotation angle given by $\Phi_n = \arctan(2\lambda\sqrt{n+1}/\Delta)$. These eigenstates in Eq. (8.24) are known as *dressed states* and they are linear combinations of the bare states in Eq. (8.21). The dressing of matter induced by the light produces a new splitting of energy similar to a Stark shift, as represented in Fig. 8.2. Note that whereas the energy difference between the bare states equals the detuning Δ , the energy difference between dressed states corresponds to the Rabi energy $\Omega_n(\Delta)$. Also note that even with detuning zero, there is a splitting between dressed states.

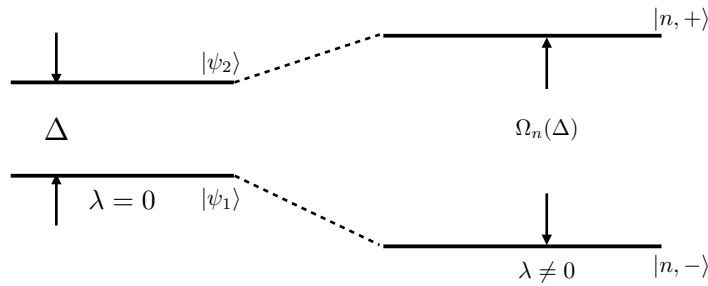


Figure 8.2: Schematic representation for the splitting of dressed states $|n, \pm\rangle$ respect to bare states $|\psi_i\rangle$ due to the light-matter interaction with a quantized field.

PART IV

POTENTIAL ENERGY SURFACES AND PHOTODYNAMICS

“No, this trick won’t work... How on earth are you ever going to explain in terms of chemistry and physics so important a biological phenomenon as first love? ”.

— Albert Einstein

9

DIATOMIC MOLECULES

There have been lots of efforts to study control of chemical reactions in different kind of molecular systems. The term molecular system is very broad, which ranges from the simplest hydrogen molecule to complex aminoacids and DNA chains. Therefore, different formalisms and methods have been developed according to the size of the molecules, to study their electronic structure within a reasonable computer time. This makes that different methodologies are employed depending on the number of atoms (and electrons) within the molecular system. To reveal the electronic molecular structure is the first step for any dynamic study, where the TDSE is to be solved for the nuclear motion in a landscape given the PES. The accuracy in the calculation of PES strongly depends not only on the size of the system (number of nuclei) but also on the number of active electrons considered. The approach in this work is to use small molecules with a limited number of electrons, so that one can apply the most sophisticated *ab initio* methods in electronic structure theory to compute PES, not only for the ground states but also for a large manifold of excited states. A proper calculation of PES is crucial to obtain the correct landscape in which nuclei move, and a clear example of this is our study of CO₂ excited states.

Then this work focuses in the study of simple molecules, molecules with no more than four atoms. The next chapters are dedicated to a specific type of molecule: diatomic, triatomic or tetratomic ones. In this way, one has a different flavor of the computational methods and approximations when enlarging the molecular system, both in the calculation of energies and the corresponding quantum dynamics. Specifically, this part of the work starts with the most simple molecules which are the ionized hydrogen molecule (H₂⁺) and the hydrogen molecule (H₂), following by the lithium fluorine molecule (LiF), then it moves to triatomic molecules like water (H₂O) and CO₂ and it ends up with tetratomic molecules like the methyl radical (CH₃).

9.1 H₂ AND H₂⁺ (HYDROGEN MOLECULE)

The hydrogen molecular ion (H₂⁺) is the simplest three-body molecule where one electron binds two protons. The hydrogen molecule is the simplest four-body molecule with electron correlation. These molecules can be fully studied using *ab initio* methods that yield exact (H₂⁺) or extremely accurate (H₂) potential energy curves. This makes of them true benchmarks to test methods of solution for photodynamic processes.

The interest as well as the complexity of molecular systems lies in the accurate representation of the electronic correlation between both electrons and the coupled motion of the electrons and nuclei. The large difference in masses between electrons and nuclei allows for the application of the adiabatic approximation introduced in [Chapter 1](#), which simplifies the procedure to solve the TISE because the total wave function (nuclei + electrons) can be expressed as a product of an electronic wave function and a nuclear one.

Although different methods, including configuration interaction methods [\[19, 37\]](#), have been developed to calculate the electronic states of H₂ and H₂⁺ [\[94, 95\]](#), this work only uses the electronic ground state of the H₂ and two electronic states for H₂⁺. These electronic states are taken from existing data in the literature.

9.1.1 POTENTIAL ENERGY CURVES

H_2 and H_2^+ are the simplest molecules that have been widely studied since the 50's [94–96] both theoretically and experimentally. The adiabatic PEC for the ground state and many excited states have been calculated by Kolos et al. for H_2 [97], and Sharp for H_2^+ [96]. In addition, some of these PEC have been fitted to model potentials, like the Morse potential [98].

The Morse potential is an approximated model to the *ab initio* PEC, that accounts for the binding and dissociation into fragments and it is widely used due to its simplicity. The Morse potential is given by

$$V(R) = D_e \left(1 - e^{-\alpha(R - R_e)}\right)^2 - D_e \quad (9.1)$$

where R is the internuclear distance between the two hydrogen atoms, R_e is the molecular equilibrium bond distance, D_e is the well depth and α is a parameter to control the width of the potential. The dissociation energy, i. e., the energy necessary to break the bond between the atoms, can be calculated by subtracting from D_e the zero point energy E_0 , corresponding to the energy of the vibrational ground state. The Morse potential in Eq. (9.1) has been expressed in that form to ensure that the energy corresponding to the dissociation into fragments is set to zero.

At this point, it is worth mentioning that this part of the work is focused to briefly describe some methodologies that will be employed in the next sections. Hence, although many electronic states for the hydrogen molecule and its ion have been calculated and are available in the literature [96, 97], as mentioned above, this work only makes use of the electronic ground state of the H_2 and the two lowest electronic states of H_2^+ . The points used for these states are taken from Kolos et al. [97] and Sharp [96] and they are included in Table 9.1. Additionally, the points of these electronic states and its interpolations performed with cubic splines are shown in Fig. 9.1. However, to simplify the numerical calculations and to get a comparison between the two methodologies in the photodynamics of a diatomic molecule, the potential energy curves of these selected states are fitted with different functional forms. The ground state of the hydrogen molecule and its ion are fitted with a Morse potential given by Eq. (9.1) with the parameters given by Table 9.2. The first excited state of the H_2^+ molecule, i. e., the $2p\sigma_u$ electronic state, is instead fitted with

$$V(R) = -0.514105 + 1.95863e^{-R} + \frac{0.112197}{R} + \frac{0.0671384}{R^2} + \frac{0.0641367}{R^3} - \frac{0.0122782}{R^4}, \quad (9.2)$$

that yields an error with respect to the exact one no larger than 10^{-3} a.u.

Once the PEC are chosen for the system, it is exposed to an excitation by a laser pulse. From Fig. 9.1, the photon energy required to ionize H_2 (from the ground vibronic state) must be above 0.6 a.u.. In addition to the ionizing pulse, one may use a second laser pulse to excite the residual H_2^+ ion, from the $1s\sigma_g$ state to the $2p\sigma_u$ state. The latter state is fully dissociative and one reaches the complete break up of the system.

9.1.2 PHOTODYNAMICS IN H_2 AND H_2^+ MOLECULES

Examples of photodynamics in H_2 and H_2^+ are chosen to test the solution given by the MCTDH method by comparing with other *ab initio* spectral methods, as explained in Chapter 4. The basis set selected for the *ab initio* spectral method will be composed by a large set of vibrational states of the ground state of H_2 and the two lowest states of H_2^+ . These wave functions $\chi_k^j(R)$ (as quoted in Chapter 4) and their corresponding energies have been calculated using the Fourier Grid Hamiltonian Method (FGHM) [99], which makes use of the representation of the wave function in a grid of points in coordinate space for the internuclear distance R . To compare with, the MCTDH is also employed to find the eigenfunctions (vibrational wave functions) and eigenvalues (energies).

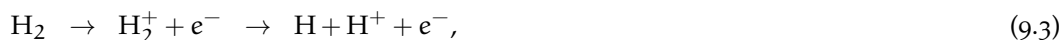
The parameters of the Morse potentials used to find the vibrational states are quoted in Table 9.2 and the number of the grid points for the internuclear distance R are 1001, inside a

Table 9.1: Ground electronic state X¹Σ_g⁺ for Hydrogen molecule H₂ and the two lowest electronic states 1sσ_g and 2pσ_u for its ion H₂⁺. R corresponds to the internuclear distance at which the electronic energy is given. All quantities are given in atomic units (a.u.).

H ₂		H ₂ ⁺			
X ¹ Σ _g ⁺		1sσ _g		2pσ _u	
R	Energy	R	Energy	R	Energy
0.40	-0.120203	0.25	2.10145	0.25	3.49581
0.45	-0.350928	0.50	0.26501	0.50	1.48312
0.50	-0.526627	0.75	-0.249052	0.75	0.795598
0.55	-0.662771	1.00	-0.451785	1.00	0.435185
0.65	-0.854361	1.25	-0.541795	1.25	0.205425
0.70	-0.922026	1.50	-0.582323	1.50	0.043497
0.75	-0.976336	1.75	-0.598716	1.75	-0.076451
0.80	-1.02006	2.00	-0.602635	2.00	-0.167535
0.90	-1.08364	2.25	-0.599951	2.25	-0.237636
1.00	-1.12454	2.50	-0.593825	2.50	-0.29207
1.10	-1.15006	2.75	-0.586019	2.75	-0.334629
1.40	-1.17447	3.00	-0.577562	3.00	-0.368087
1.60	-1.16858	3.50	-0.560856	3.50	-0.415496
1.80	-1.15507	4.00	-0.546085	4.00	-0.44555
2.00	-1.13813	4.50	-0.533938	4.50	-0.464828
2.40	-1.10241	5.00	-0.524442	5.00	-0.47729
2.80	-1.07067	5.50	-0.517232	5.50	-0.485382
3.20	-1.04578	6.00	-0.511968	6.00	-0.490643
3.80	-1.02153	6.50	-0.508214	6.50	-0.494059
4.50	-1.00797	7.00	-0.505593	7.00	-0.496273
5.00	-1.00376	8.00	-0.50257	8.00	-0.498605
7.00	-1.00019	10.0	-0.50058	10.0	-0.4999
10.0	-1.00009	12.0	-0.500167	12.0	-0.500057

radial box of size 20 with $R \in [0.3, 20.3]$ a.u. In Table 9.3 the energies for the bound vibrational states computed with FGHM and MCTDH are included. Both methods yield the same energies up to the figures included in the table, with a precision of ten significant figures. However, it is worth noting that the MCTDH does not make use of the vibrational eigenstates as the basis expansion, but a shorter expansion in terms of SPF, as explained above in Chapter 4.

In order to simulate the process of photodissociative ionization, i. e.,



it is assumed that the hydrogen molecule is previously ionized from its ground state and it implies a sudden excitation transfer of the initial vibrational wave function of H₂ into the H₂⁺ potential following the Franck-Condon principle. After that, the wavepacket generated in the ground state of H₂⁺ has a dynamics within the H₂⁺ 1sσ_g PEC since this excited wavepacket is not an eigenfunction of the nuclear potential of H₂⁺. The dynamics obtained solving the TDSE with the spectral method using vibrational eigenstates (solving Eq. (4.17)) can be seen in Fig. 9.2. In this figure, the initial vibrational state generated suddenly in the ground state of the H₂⁺ (red line at $t = 0$ fs) moves to the right within its PEC (dot-dashed light grey line) and it

Table 9.2: Parameters of the Morse potentials for the ground electronic states of the hydrogen molecule (H_2) and its ion (H_2^+). All quantities are in atomic units (a.u.).

H_2	H_2^+
$D_e = 0.1744$	$D_e = 0.1026$
$\alpha = 1.02764$	$\alpha = 0.732$
$R_e = 1.40201$	$R_e = 1.9972$

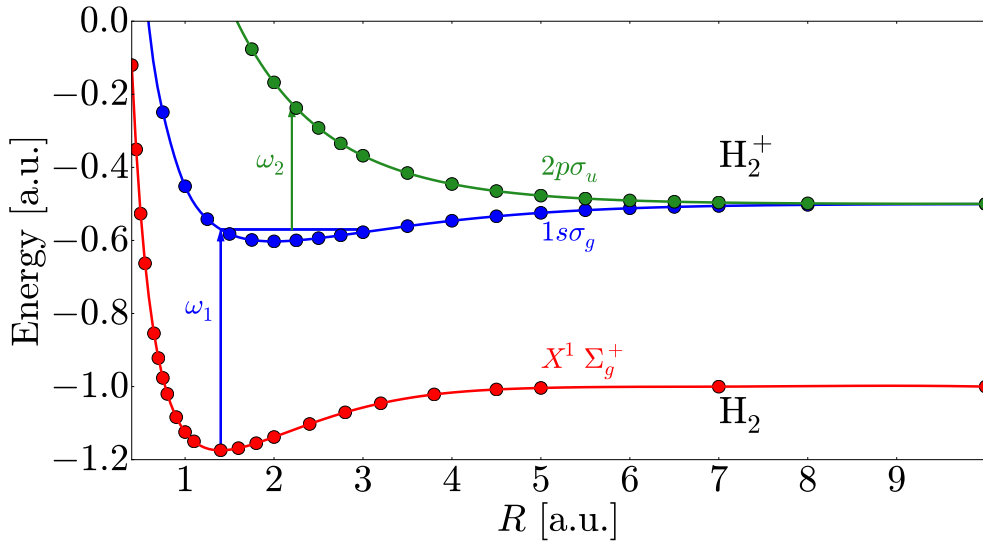


Figure 9.1: Ground electronic state $X^1\Sigma_g^+$ (red line) for the hydrogen molecule H_2 , and ground state $1s\sigma_g$ (blue line) and first excited state $2p\sigma_u$ (green line) of H_2^+ . Blue and green arrows represent the excitations with pulses of central frequencies ω_1 and ω_2 , respectively.

will continue moving until it finds the classical turning point located at ~ 4.5 a.u. of the nuclear coordinate. This dynamics or motion of the wavepacket along the R coordinate can be used to control the dissociation and ionization of the H_2^+ molecule.

Although the dipole moment $\mu(R)$ between the two lowest states of H_2^+ is known, a model for the dipole moment is chosen using also a Morse function, using the parameters $D_e = 0.2$, $\alpha = 0.8$ and $R_e = 1.5$, all in atomic units. Populations of the $2p\sigma_u$ electronic state after excitation with a laser pulse for different central frequencies ω_0 and different pulse time delays τ are shown in Fig. 9.3. The first noticeable difference to be stressed in Fig. 9.3 is that when the pulse time delay is longer (right panel) the populations decrease compared with shorter delays (left panel). This is because the dipole moment used in the calculations has a lower value when the wavepacket moves to the right away from the equilibrium point of H_2^+ molecule and therefore the populations transferred to the excited electronic state decrease. Although it will be possible to use less energetic pulses with longer delays to dissociate the system at larger internuclear distances (the energy difference between the $1s\sigma_g$ and $2p\sigma_u$ decreases), in this example the vanishing dipole moment at large R does not allow to transfer efficiently population to the $2p\sigma_u$ state.

One of the differences between the two time delays used in Fig. 9.3 is the time at which the excited $2p\sigma_u$ state becomes populated. For a time delay of $\tau = 5$ fs, the population of the $2p\sigma_u$ state and its eventual dissociation begins earlier for the pulse with the largest central frequency $\omega_0 = 12$ eV but nevertheless it gives the lowest dissociation yield. On the contrary, for the longer delay 10 fs, the laser pulse with the smaller central frequency (6 eV) produces the highest yield for photodissociation. This is because the energy difference between the $1s\sigma_g$ and $2p\sigma_u$ PEC decrease with increasing R , i.e., while the wavepacket moves to large R (see Fig. 9.2) and at a given time the energy difference matches the pulse central frequency ω_0 . When the electronic transition dipole moment is almost constant at some distances, the transition probability mostly

Table 9.3: Vibrational energy spectrum for the vibrational bound states of the electronic ground state for H₂ and H₂⁺, calculated with FGHM and MCTDH. All quantities are in atomic units (a.u.) and ν represents the label for the vibrational state.

ν	H ₂	H ₂ ⁺
	FGHM/MCTDH	FGHM/MCTDH
0	0.0098714202	0.0053999137
1	0.0287515513	0.0157620129
2	0.0464814033	0.0255404742
3	0.0630609763	0.0347352979
4	0.0784902703	0.0433464838
5	0.0927692852	0.0513740320
6	0.1058980211	0.0588179424
7	0.1178764779	0.0656782151
8	0.1287046557	0.0719548500
9	0.1383825545	0.0776478472
10	0.1469101742	0.0827572066
11	0.1542875148	0.0872829283
12	0.1605145765	0.0912250123
13	0.1655913590	0.0945834585
14	0.1695178626	0.0973582670
15	0.1722940871	0.0995494378
16	0.1739200325	0.1011569708
17	—	0.1021808660

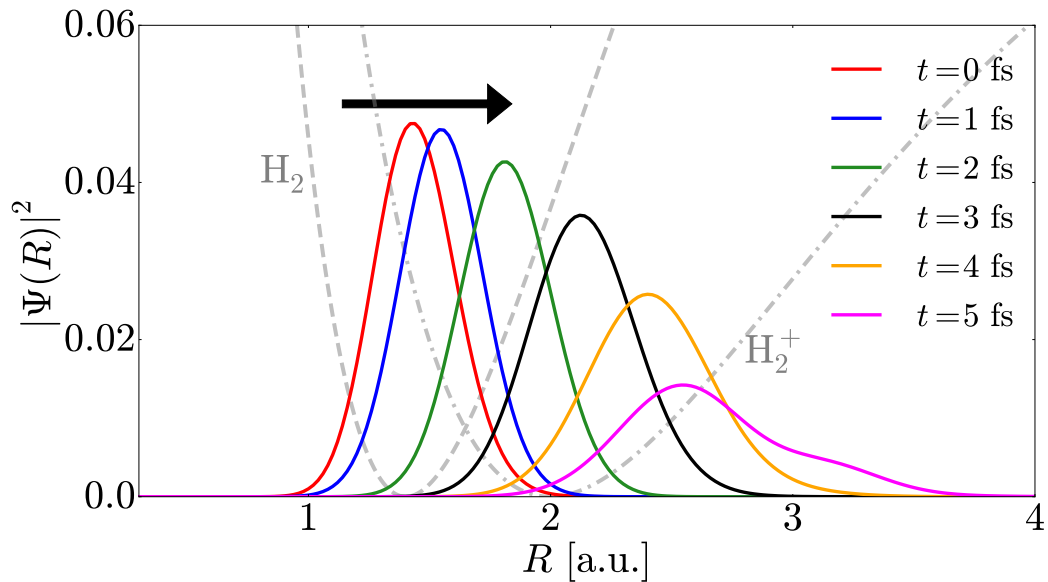


Figure 9.2: Free dynamics of the initial wavefunction in the ground state of H₂⁺ after a sudden ionization from H₂. The continuous lines show the position of the density for the vibronic wavepacket at different propagation times. The black arrow indicates the direction of motion of the wavepacket and the dashed and dot-dashed grey lines correspond to the PEC of H₂ and H₂⁺, respectively.

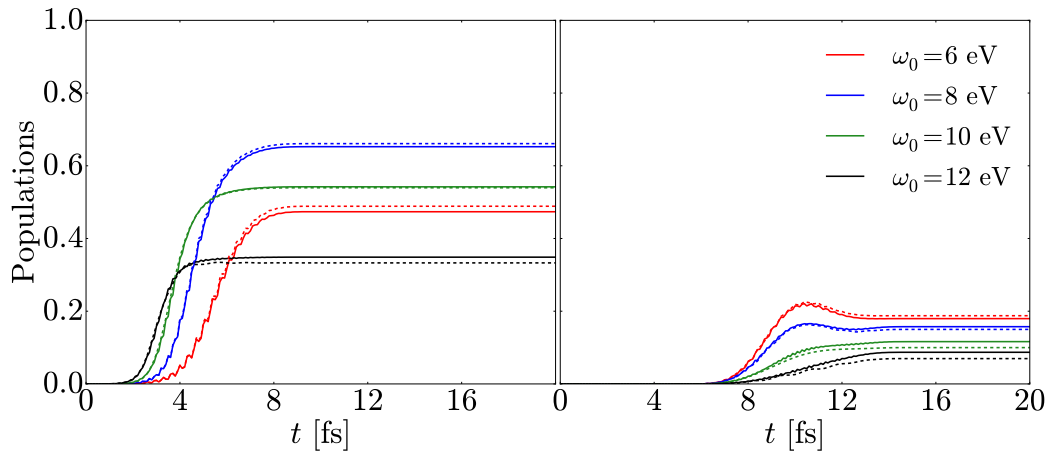


Figure 9.3: Populations of the $2p\sigma_u$ electronic state after to excite the H_2^+ molecule with a laser pulse for different central frequencies ω_0 and for a pulse time delay $\tau = 5$ fs (left panel) and $\tau = 10$ fs (right panel). The others pulse parameters are $E_0 = 0.25$ a.u. and $T = 10$ fs. Continuous lines are the populations performed with the standard method and dashed lines are the populations performed with [MCTDH](#).

depends upon the overlap of the vibrational states of the two [PEC](#) involved. This is known as the *Franck-Condon approximation* and validates the principle of vertical transitions between the localized wavepacket moving within the $1s\sigma_g$ and the stationary vibrational states of the $2p\sigma_u$ state.

[Fig. 9.3](#) shows that results for the excitation to $2p\sigma_u$ (that leads to a Coulomb explosion dissociation) obtained with the spectral method and [MCTDH](#) method basically coincide. Difference can be attributed to the fact that the time-dependent integrator in the spectral method is a fourth-order Runge-Kutta method and the [MCTDH](#) method uses a fifth-order approximation. This brief study lead to endorse the [MCTDH](#) method to simulate diatomic molecules exposed to laser pulses. It is worth noting that the implementation of laser pulses within the [MCTDH](#) suite of codes is not trivial and this study on H_2^+ photodynamics was used as a benchmark before moving to other more complex molecules.

9.2 LIF (LITHIUM FLUORIDE)

Lithium fluoride (LiF) is one of the simplest molecules to observe an avoided crossing between two [PEC](#) (ionic and covalent). One of the first studies on this molecule ([PEC](#) and dipole moments) was carried out by Werner and Meyer [100] who used the [MCSCF](#) method. Another study on LiF, including the dynamics was performed by S. Scheit et al. [101] showing a controlled dynamics in the avoided crossing region by implementing a pump-dump laser scheme within the two lowest $^1\Sigma$ states.

In this work, electronic structure calculations for LiF have been performed at the [MRCI](#) level, for the energies, dipole moments and non adiabatic couplings. Also, both adiabatic and diabatic dynamical calculations have been carried out using [MCTDH](#).

9.2.1 POTENTIAL ENERGY CURVES AND DIPOLE MOMENTS

Previous studies in LiF have been performed using the ab initio calculations of the [PEC](#) and couplings (dipolar plus non-adiabatic) at the level of [MCSCF](#) [100] and at the level of [MRCI](#) [101, 102]. However, these previous studies have only focused in the two lowest $^1\Sigma$ states. In addition to these two $^1\Sigma$ states, this work also considers a third state of symmetry $^1\Pi$ in the work for reasons discussed later.

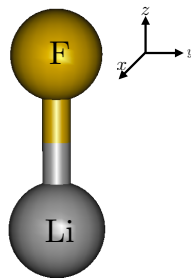


Figure 9.4: Coordinate system chosen for the electronic structure of LiF using the MOLPRO package, with the molecule oriented along z -axis.

Table 9.4: Adiabatic potential energy points calculated for the two lowest $^1\Sigma$ states and the lowest $^1\Pi$ state of LiF. All quantities are in a.u.

R	$^1\Sigma$	$^2\Sigma$	$^1\Pi$	R	$^1\Sigma$	$^2\Sigma$	$^1\Pi$
1.60	-106.54194413	-106.34662029	-106.14423470	8.50	-107.12399702	-107.07830326	-107.08024467
1.70	-106.74265662	-106.51852229	-106.36799621	9.00	-107.11684291	-107.07888064	-107.08028143
1.80	-106.88407924	-106.63883218	-106.52937378	9.50	-107.11054491	-107.07929043	-107.08028990
1.90	-106.99307312	-106.73267591	-106.65456406	10.00	-107.10492669	-107.07957384	-107.08028237
2.00	-107.07617556	-106.80605172	-106.75187079	11.00	-107.09538756	-107.07988539	-107.08024481
2.20	-107.18687957	-106.90690986	-106.88471574	11.50	-107.09127494	-107.07995402	-107.08022311
2.40	-107.24774485	-106.96729638	-106.96371617	12.00	-107.08750724	-107.07997374	-107.08020196
2.60	-107.27897350	-107.00358833	-107.01063096	12.50	-107.08424125	-107.07992902	-107.08018105
2.80	-107.29258104	-107.02552125	-107.03836082	12.60	-107.08361926	-107.07990128	-107.08017725
3.00	-107.29575729	-107.03890144	-107.05462076	12.80	-107.08245055	-107.07980005	-107.08016933
3.20	-107.29281817	-107.04718800	-107.06404268	12.90	-107.08192355	-107.07970763	-107.08016576
3.40	-107.28636849	-107.05244549	-107.06941883	13.00	-107.08145773	-107.07956122	-107.08016113
3.60	-107.27799100	-107.05590915	-107.07243665	13.10	-107.08108157	-107.07933650	-107.08015755
3.80	-107.26865137	-107.05831816	-107.07411323	13.20	-107.08081047	-107.07901614	-107.08015404
4.00	-107.25893892	-107.06011490	-107.07505634	13.30	-107.08063184	-107.07861076	-107.08014993
4.20	-107.24921198	-107.06156339	-107.07562336	13.60	-107.08039357	-107.07715247	-107.08013963
4.40	-107.23968619	-107.06281966	-107.07601813	14.00	-107.08029114	-107.07510376	-107.08012518
4.60	-107.23048821	-107.06397312	-107.07635026	14.20	-107.08026554	-107.07409988	-107.08011839
4.80	-107.22168879	-107.06507286	-107.07667265	14.50	-107.08023881	-107.07263555	-107.08010832
5.00	-107.21332274	-107.06614301	-107.07700487	14.80	-107.08022040	-107.07122536	-107.08009937
5.50	-107.19434632	-107.06872797	-107.07786803	15.00	-107.08020958	-107.07031419	-107.08009284
6.00	-107.17798733	-107.07113218	-107.07866363	16.00	-107.08016910	-107.06608834	-107.08006302
6.50	-107.16391728	-107.07325235	-107.07928775	18.00	-107.08010892	-107.05893846	-107.08001075
7.00	-107.15174696	-107.07501685	-107.07972137	20.00	-107.08005729	-107.05331131	-107.07996420
7.50	-107.14122266	-107.07642435	-107.07999838	22.00	-107.08000509	-107.04863770	-107.07991667
8.00	-107.13204585	-107.07750264	-107.08016001	24.00	-107.07996349	-107.04479853	-107.07987852

In this *ab initio* study on LiF for energies and couplings (dipole and non-adiabatic), the electronic structure package MOLPRO is used to perform the calculations [26]. A complete active space (CAS) calculation of the two lowest $^1\Sigma$ states and the lowest $^1\Pi$ of LiF has been performed using a **MCSCF** method, then followed by **MRCI** method, using the *aug-cc-pVQZ* basis set, with the LiF molecule oriented along the z axis, as seen in Fig. 9.4. In addition, the

NAC $f_{12}(R)$, and dipole moments $\mu_{ij}(R)$ (diagonal and non-diagonal) were computed with the wave functions at the **MRCI** level. In the case of the non-adiabatic couplings, these were calculated with MOLPRO using a finite differences method for the derivatives involving the **MRCI** wave function [100]. Table 9.4 includes some illustrative energy points of the calculated **PEC** for the two lowest $^1\Sigma$ states and the lowest state of $^1\Pi$ states in LiF. Additionally, Fig. 9.5 shows the **PEC** for these selected states. Similarly, points are calculated for the diagonal dipole moments for the $^1\Sigma$ state $\mu_{11}(R)$ and $\mu_{22}(R)$, for the $^1\Pi$ state $\mu_{\Pi\Pi}$ due to the permanent dipole of LiF, the non-diagonal transition dipole moment between the $^1\Sigma$ states $\mu_{12}(R)$ and between the $^1\Sigma$ and $^1\Pi$ states $\mu_{1\Pi}(R)$ and $\mu_{2\Pi}(R)$ and **NAC** $f_{12}(R)$. Illustrative values for these quantities are included in Table 9.5 and they are also plotted in Fig. 9.6.

The existence of the **NAC** $f_{12}(R)$ indicates a strong coupling between the two $^1\Sigma$ states at the avoided crossing located at $R = 13.1$ a.u. Due to this anticrossing the electronic wave functions exchange their character and, consequently, their adiabatic molecular properties (like μ_{11} and μ_{22}) follow the behavior seen in Fig. 9.6a. It is important to note that whereas μ_{22} is close to zero from the Franck-Condon region to the avoided crossing region, μ_{11} is clearly dominant against μ_{12} , so that diagonal couplings cannot be disregarded in the dynamics, as done in some previous studies of its dynamics [89, 103]. However, the implementation of non-adiabatic dynamics is not straightforward since the **NAC** at the avoided crossing position usually are sharp functions against R (narrow and high) and this poses numerical difficulties at the integration of the **TDSE**. For instance, a way to compute **NAC** (assuming one has exact wave functions) is through the use of the off-diagonal version of the Hellman-Feynman theorem [104, 105], that reads

$$\left\langle \Psi_n(\mathbf{Q}, \mathbf{q}) \left| \frac{\partial}{\partial \mathbf{Q}} \right| \Psi_m(\mathbf{Q}, \mathbf{q}) \right\rangle = \frac{1}{\epsilon_m(\mathbf{Q}) - \epsilon_n(\mathbf{Q})} \left\langle \Psi_n(\mathbf{Q}, \mathbf{q}) \left| \frac{\partial \hat{H}_{\text{el}}(\mathbf{Q}, \mathbf{q})}{\partial \mathbf{Q}} \right| \Psi_m(\mathbf{Q}, \mathbf{q}) \right\rangle. \quad (9.4)$$

Eq. (9.4) is valid under the adiabatic approximation and it shows that when the energies are very close (avoided crossing region), the value of the **NAC** at this position diverges and consequently the **TDSE** is difficult to integrate at this point. Thus, to avoid this numerical problem in the solution of the non-adiabatic dynamics, a diabatic dynamics can be performed instead of a non-adiabatic one using adiabatic **PEC** to solve the **TDSE** (see Section 5.2).

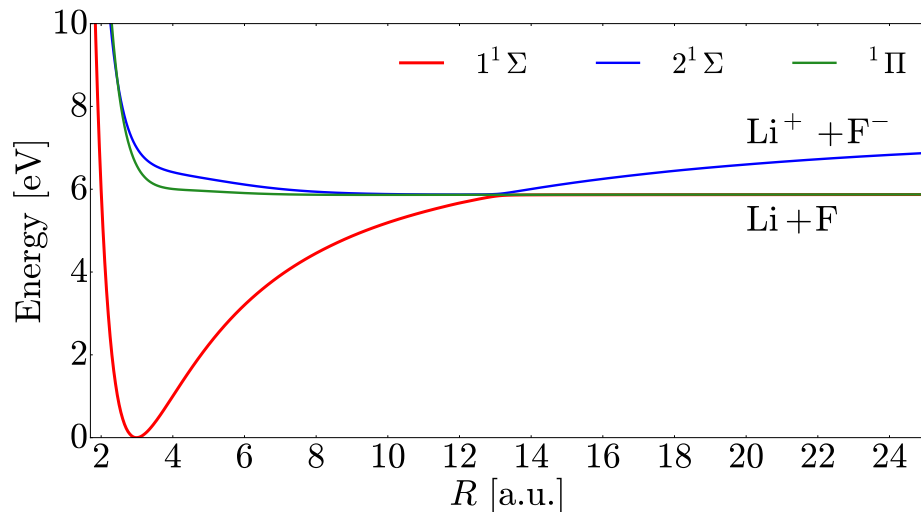
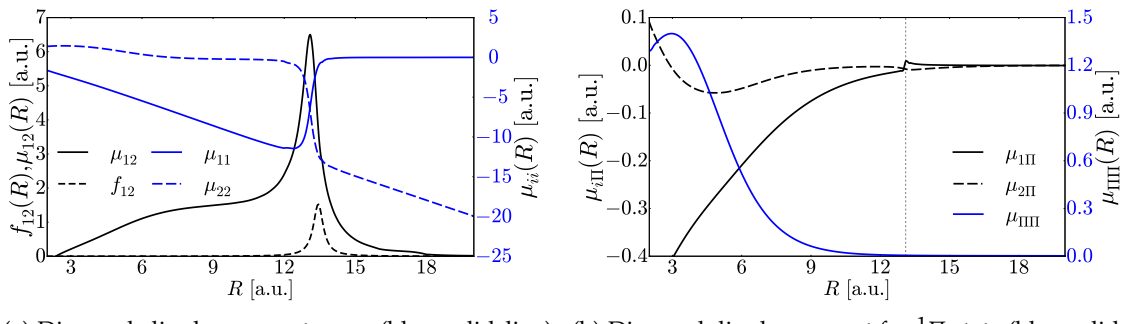


Figure 9.5: Potential energy curves of the two lowest adiabatic $^1\Sigma$ states and the lowest adiabatic $^1\Pi$ states of LiF molecule. The states corresponding to the $^1\Sigma$ symmetry display a (covalent-ionic) avoided crossing at $R = 13.1$ a.u. The zero energy is set at the bottom of the ground state $^1\Sigma$ and the equilibrium internuclear distance is $R = 3.0$ a.u.



(a) Diagonal dipole moments μ_{11} (blue solid line) and μ_{22} (blue dashed line), and non-diagonal dipole moment (black solid line) for the two $^1\Sigma$ states in LiF. The **NAC** between the two states, f_{12} , is also included (black dashed line). (b) Diagonal dipole moment for $^1\Pi$ state (blue solid line) and non-diagonal dipole moment $\mu_{1\Pi}$ between the $^1\Sigma$ and the $^1\Pi$ states (black solid line), and $\mu_{2\Pi}$ between the $^1\Sigma$ and the $^1\Pi$ states (black dashed line).

Figure 9.6: *Ab initio* diagonal and non-diagonal dipole moments along with the non-adiabatic coupling for the three lowest states of LiF. Note the different scales in the y-axis. Some coupling values are included in Table 9.5.

9.2.2 TWO-STATE PHOTO-DISSOCIATION OF LITHIUM FLUORIDE MOLECULE

Since the **NAC** and dipole moments in LiF are not specially sharp, non-adiabatic calculations can be performed using the adiabatic **PEC** and the **NAC** introduced directly in the dynamic equations of **MCTDH**. At variance, a diabatic calculation is also performed by transforming the **NAC** into smooth electrostatic couplings and the adiabatic **PEC** into diabatic ones that effectively show a crossing.

A nuclear box for the nuclear coordinate $R \in [1.7, 60]$ a.u. is used for all calculations included in this section. In this part of the work only the two lowest $^1\Sigma$ states and all (dipole plus **NAC**) couplings involved are used to study the wavepacket dynamics using **MCTDH**.

Although a diabatization procedure can be efficient to perform a subsequent dynamic calculation, the procedure of diabatization is not unique, but the different forms usually yield similar results. In order to diabatize the set of two states involved in the dynamics, two of the methods already described in Section 5.2 are employed. The two selected methods are the diagonalization of an operator that correspond to a physical property of the molecule (method I) and the diabatization model using an arctangent function (method II). The physical property chosen in the first method is the transition dipole moment between the states and its corresponding diagonal dipole moments. The rotation angle of the matrix \mathbf{U} for both methodologies is plotted in Fig. 9.7. Some light differences can be seen in the value of the rotation angle $\theta_i(R)$ obtained from the two methodologies. However, Fig. 9.8 shows that the differences in the electronic diabatic states obtained by using both methods are quite similar. The difference is produced in the electrostatic couplings or non-diagonal couplings found after the diabatization procedure. As the inset of Fig. 9.8 shows, the electrostatic couplings $V_{12}(R)$ calculated by the method I are larger than the calculated by method II. Nevertheless, both methods essentially provide the same results for the dynamics, as shown in Fig. 9.9. Also, if one performs the diabatization using Eq. (5.19), i.e., the transformation of electronic states with the rotation angle calculated through the *ab initio* calculations of the **NAC**, the results are also quite similar.

Non-adiabatic dynamics using adiabatic **PEC** and **NAC** are also performed in the **MCTDH** method. The populations of the two $^1\Sigma$ adiabatic states are shown with dashed lines in Fig. 9.9 and they are similar to those found in the diabatic case.

Finally, Fig. 9.9 shows the time-dependent populations of the two $^1\Sigma$ states calculated using diabatic **PEC** and electrostatic couplings calculated with two different rotation angles (solid lines) and using adiabatic **PEC** with non-adiabatic couplings (dashed lines).

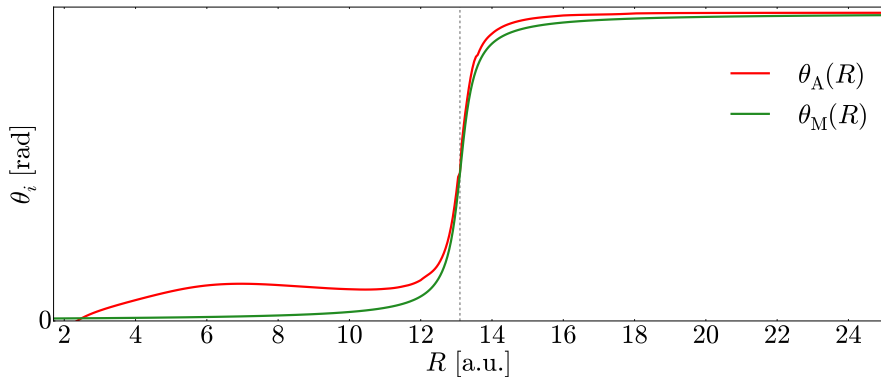


Figure 9.7: Rotation angles of the diabatization matrix \mathbf{U} for the two different diabatizations used with rotation angles $\theta_A(R)$ and $\theta_M(R)$, which correspond to the angle found by the method I and II, respectively (see text).

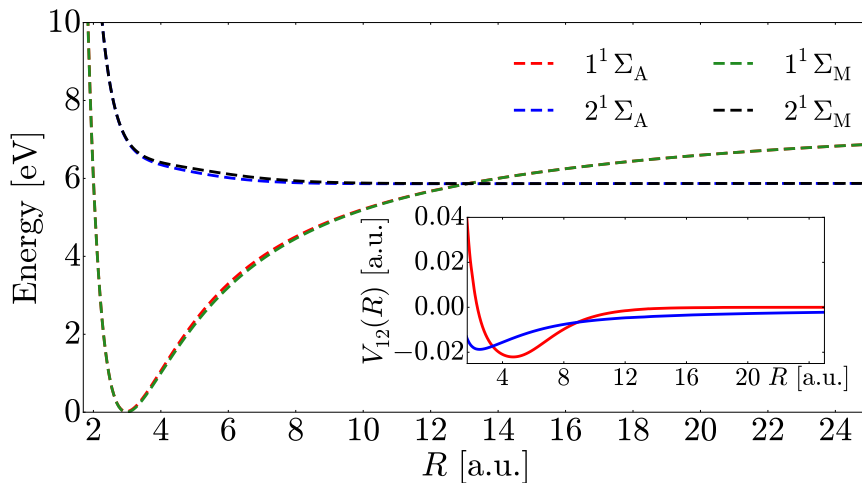


Figure 9.8: Potential energy curves of the two lowest diabatic $^1\Sigma$ states of LiF molecule by implementing the two diabatization procedures. The states $^1\Sigma_A$ and $^1\Sigma_M$ correspond to the states generated with the method I and II, respectively (see text). (Inset) Electrostatic couplings $V_{12}(R)$ resulting from the diagonalization using rotation angle of method I (red solid line) and method II (blue solid line) [see text].

Fig. 9.9 also shows that at $t \approx 400$ fs population decreases its value due to a complex absorbing potential (CAP) located at $R = 58$ a.u., close to the edge of the radial box [106]. This Complex absorbing potential (CAP) is necessary to calculate the photo-dissociation probabilities and the kinetic energy release (KER) of the nuclei. In order to control the dissociation probabilities once the nuclei of the molecule have been separated, it is convenient to know the dissociation probabilities in the absence of any external laser field, in other words, to increase or decrease the dissociation probability in a specific dissociation channel. The only dissociative channel available in the two $^1\Sigma$ states dynamics is given by the covalent chemical reaction



as it is shown in Fig. 9.5, it is the dissociation path that comes from the $2^1\Sigma$ diabatic state (see Fig. 9.8) or $1^1\Sigma$ adiabatic electronic state. Dissociation probabilities into $\text{Li} + \text{F}$ and the corresponding KER are shown in Fig. 9.10. Fig. 9.10a shows the dissociation probabilities of both the diabatic and adiabatic (plus NAC) dynamics, that yield similar results. Additionally, Fig. 9.10b shows the KER calculated for both types of dynamics. The three dynamics are quite similar and the only visible difference is a small shift of the peak for the diabatic dynamics performed with the method I in contrast to the other two dynamics (method II and adiabatic

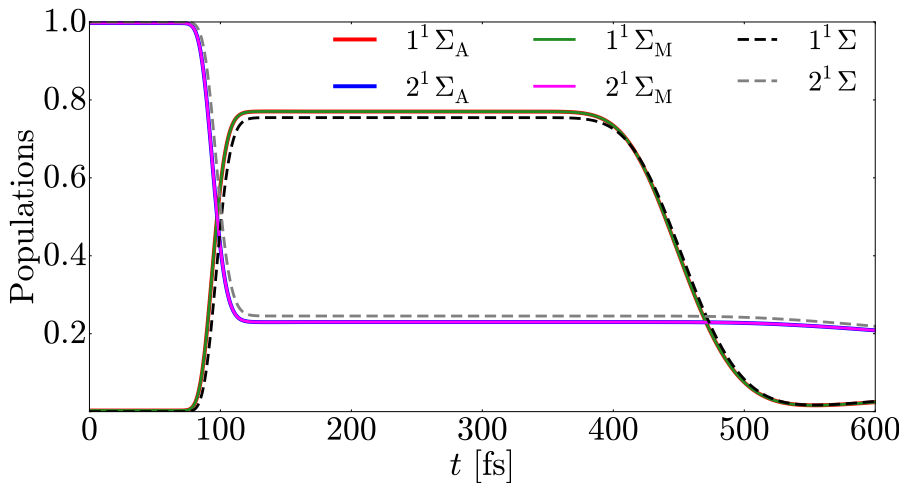
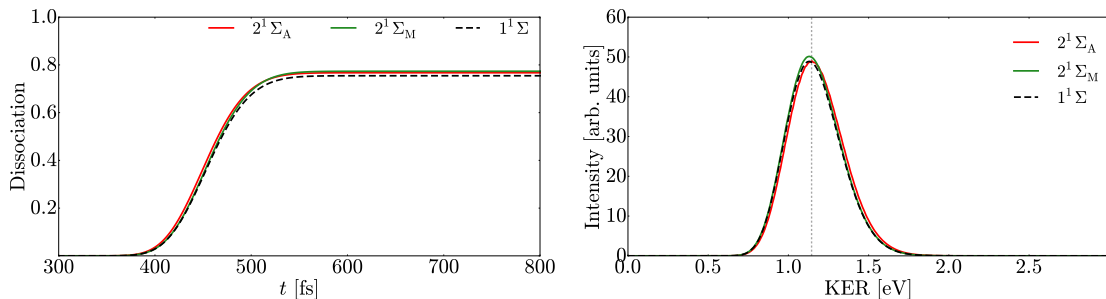


Figure 9.9: Time-dependent populations of the two ${}^1\Sigma$ states in LiF, with the initial wavepacket located in the excited state after a sudden excitation of LiF by a pump laser pulse. The plot compares different results: MCTDH calculations with diabatic PEC including electrostatic couplings (method I with subscript A and method II with subscript M) and with adiabatic PEC including NAC.

plus NAC). This small shift in the KER can be attributed to the fact that the diabatic potential energy value of the ${}^2\Sigma_A$ at equilibrium is different compared with the adiabatic potential energy value of the ${}^1\Sigma$ state.



(a) Photodissociation probabilities of diabatic electronic ${}^2\Sigma$ state including electrostatic couplings (continuous lines, method I with subscript A and method II with subscript M) with the photodissociation of the adiabatic ${}^1\Sigma$ state including NAC (dashed line) in LiF molecule.

(b) Total kinetic energy distributions obtained from the CAP in the of diabatic electronic ${}^2\Sigma$ state including electrostatic couplings (continuous lines) and the adiabatic ${}^1\Sigma$ state including NAC (dashed line) in LiF molecule. The vertical dashed grey line corresponds to the difference between the dissociation limit and the value of the ${}^2\Sigma_i$ state at the equilibrium point.

Figure 9.10: Photodissociation probabilities and KER in the Σ electronic states after a sudden excitation to the first ${}^1\Sigma$ excited electronic state in LiF molecule.

Although the dissociation probability for LiF is considerably high (around 77%), once the molecule is excited by the laser pulse, one could control this yield if one previously excites the LiF molecule with an IR field to start a preliminary dynamics in the ground state ${}^1\Sigma$. In this case, a second XUV laser pulse applied with a given delay against the IR field, launches a wavepacket in the ${}^2\Sigma$ excited state but in a region quite different from the equilibrium disantce ($R = 3.0$ a.u.). Moreover, the excitation produced by a delayed XUV pulse can also control the KER spectra, since the KER strongly depends on the dynamical Franck-Condon excitation between a wavepacket moving in the ground state and the dissociative states in the ${}^2\Sigma$ state. Examples of the effects and control with a pump-dump pulse (the set of an IR and XUV pulses) is shown in the next chapter in the water molecule.

Table 9.5: Diagonal (μ_{ii}) and non-diagonal (μ_{ij}) dipole moments and **NAC** (f_{12}) values calculated for the two lowest $^1\Sigma$ states and the lowest $^1\Pi$ state in LiF at a series of internuclear distances. All quantities are in a.u.

R	$\mu_{11}\hat{z}$	$\mu_{22}\hat{z}$	$\mu_{\Pi\Pi}\hat{z}$	$\mu_{12}\hat{z}$	$\mu_{1\Pi}\hat{x}$	$\mu_{2\Pi}\hat{x}$	f_{12}
1.80	-1.42952279	1.35172556	1.29502083	-0.48262777	0.12573465	-0.33261965	-
2.00	-1.63921474	1.38495804	1.28959959	-0.48411938	0.09001356	-0.17490275	0.22181170
2.20	-1.83153225	1.42335909	1.32491481	-0.47216251	0.06576562	-0.06731546	0.15555688
2.40	-2.01515778	1.44402079	1.35638730	-0.45666430	0.04429012	0.01643088	0.11902085
2.60	-2.19555142	1.45222803	1.38085123	-0.43953761	0.02476496	0.08745339	0.09682487
2.80	-2.37517651	1.44987931	1.39524407	-0.42199171	0.00754667	0.15159505	0.07556994
3.00	-2.55535108	1.43759899	1.39895870	-0.40454247	-0.00729618	0.21210850	0.07024636
3.20	-2.73686206	1.41544745	1.39056828	-0.38768177	-0.01976740	0.27091319	0.06133326
3.40	-2.92022677	1.38354761	1.36983374	-0.37155456	-0.02994174	0.32929847	0.05378916
3.60	-3.10569677	1.34187509	1.33714078	-0.35627565	-0.03812119	0.38802600	0.04704137
3.80	-3.29337439	1.29062977	1.29335420	-0.34183057	-0.04457762	0.44757616	0.04152599
4.00	-3.48325480	1.23018912	1.23971872	-0.32814136	-0.04954997	0.50820643	0.03642270
4.20	-3.67526361	1.16116728	1.17773537	-0.31509759	-0.05324005	0.56997340	0.03178603
4.40	-3.86926885	1.08448489	1.10910142	-0.30257049	-0.05581489	0.63272461	0.02752869
4.60	-4.06509025	1.00127972	1.03555758	-0.29043688	-0.05740387	0.69613001	0.02356139
4.80	-4.26249732	0.91327055	0.95890991	-0.27850607	-0.05773174	0.75962662	0.01984717
5.00	-4.46129662	0.82152291	0.88088501	-0.26682074	-0.05767194	0.82266195	0.01628500
5.50	-4.96302831	0.58926046	0.69002271	-0.23800799	-0.05462729	0.97339095	0.00844537
6.00	-5.47005870	0.37387665	0.51976947	-0.20959706	-0.04857170	1.10668807	0.00157874
6.50	-5.98176591	0.19329660	0.37993143	-0.18204412	-0.04097119	1.21702450	0.00421113
7.00	-6.49795674	0.05293553	0.27161202	-0.15596587	-0.03304640	1.30498328	0.00875458
7.50	-7.01801147	-0.04887545	0.19109239	-0.13193758	-0.02579892	1.37131432	0.01183443
8.00	-7.54063468	-0.11914512	0.13296000	-0.11035818	-0.01960234	1.42101690	0.01359273
8.50	-8.06412188	-0.16536559	0.09187484	-0.09142075	-0.01458765	1.45893707	0.01413596
9.00	-8.58597911	-0.19619037	0.06328815	-0.07503499	-0.01074628	1.49345659	0.01338450
10.00	-9.61791516	-0.23322743	0.03037462	-0.04935877	-0.00581994	1.57223293	0.00773004
11.00	-10.60667600	-0.28326703	0.01518376	-0.03161612	-0.00344804	1.75413685	0.00446872
12.00	-11.40565880	-0.50701982	0.00852003	-0.01972635	-0.00293207	2.40566529	0.04578326
12.50	-11.40271739	-1.01752932	0.00674048	-0.01527331	-0.00356928	3.40452983	0.12329190
12.60	-11.24728606	-1.27434241	0.00646179	-0.01442490	-0.00390169	3.78401995	0.15510233
12.80	-10.45116234	-2.27311885	0.00596426	-0.01259524	-0.00497672	4.87221336	0.26057904
12.90	-9.56653921	-3.25898534	0.00574331	-0.01152073	-0.00582981	5.58183320	0.35131098
13.00	-8.11938159	-4.80733036	0.00553658	-0.01017180	-0.00690751	6.24586014	0.48971149
13.10	-6.10761515	-6.92029606	0.00534645	0.00847285	-0.00801961	6.49952069	0.70608268
13.20	-4.02537976	-9.10352362	0.00516998	0.00669308	-0.00890805	6.05157438	1.04394351
13.30	-2.45732131	-10.77258782	0.00500502	0.00509679	-0.00929209	5.14274934	1.50969160
13.60	-0.61325756	-12.91961242	0.00457859	0.00240812	-0.00880708	2.81020470	1.37685572
14.00	-0.15861669	-13.77774032	0.00413135	0.00112557	-0.00737691	1.46938708	0.32564367
14.50	-0.04627987	-14.39391279	0.00371665	0.00050584	-0.00576572	0.80002251	0.09898342
14.80	-0.02536055	-14.71687704	0.00352445	0.00030294	-0.00495327	0.58972985	0.06004652
15.00	-0.01768821	-14.92583019	0.00341309	0.00020126	-0.00447198	0.48902510	0.04445202
16.00	-0.00422753	-15.94482859	0.00306197	-0.00013446	-0.00266043	0.21565327	0.01362038
18.00	-0.00088298	-17.95611009	0.00260524	-0.00042944	-0.00090903	0.05481679	0.00246707
20.00	-0.00035309	-19.96218538	0.00234381	-0.00057550	-0.00030289	0.01596356	0.00060793

“No, this trick won’t work... How on earth are you ever going to explain in terms of chemistry and physics so important a biological phenomenon as first love? ”.

— Albert Einstein

10

TRIATOMIC MOLECULES

The use of ultrashort laser pulses to gain active control in the yields of fotoinduced chemical reactions is nowdays a well-established topic of research. In spite of the great advances in *ab initio* theoretical and computational procedures, the prediction of the branching ratios of photofragmentation channels is still a challenging task, even in the case of simple molecules. In this part of the work, the **MCTDH** is implemented to carry out multistate non-adiabatic photodynamics in the H_2O molecule and its isotopomers subject to different laser pulse protocols. For instance, the composition of intense pump IR few-cycle pulses along with time-delayed ultrashort UV pulses may drive the molecular system to selective bond breaking [107–109]. Using **MCTDH** as the solution method for the nuclear dynamics, the photofragmentation dynamics of neutral H_2O is studied, as well as of its isotopomers HOD and D_2O , in a two state photoexcitation (ground state $\tilde{\chi}^1\text{A}_1$ and first excited $\tilde{\text{A}}^1\text{B}_1$ electronic state). In this case, where forces in both states are not bond-selective due to symmetry, the use of pump-IR pulses prior to a UV pulse with a controlled delay becomes crucial to produce a selective bond breaking.

This part of the work goes from the two-state photodynamics in H_2O to the multistate non-adiabatic photodynamics of CO_2 . For the latter a careful preliminary study of the electronic structure of excited states (valence and Rydberg states) is mandatory when excitation is due to high-energy photons. In this line, recent experiments with ~ 12 eV UV radiation on the photofragmentation of CO_2 have produced evidence for the formation of $\text{CO}+\text{O}(^1\text{S}, ^1\text{D})$ fragments as well as $\text{C}+\text{O}_2$ fragments [110], the former by non-adiabatic transitions between the $4^1\text{A}'$ and $3^1\text{A}'$ valence states via the seam of conical intersections and the latter with the possibility of a roaming mechanism. The first step to any dynamical calculation of these processes is to generate the multidimensional **PES**, dipolar couplings and **NAC** with a high degree of accuracy (at the level of **MRCI/MCSCF**). This chapter describes the proceedings on the structure and photodynamics of these two triatomic molecules.

10.1 H_2O (WATER) AND HOD (SEMIHEAVY WATER)

Photofragmentation dynamics of the simple triatomic molecule H_2O and its isotopomers HOD and D_2O is revisited using the **MCTDH** [111] as the method of solution for the **TDSE**. Whereas OH and OD vibrations in HOD behave as good uncoupled local modes that can be excited by the primer IR pulse almost independently to predispose the molecule to fragment into one of the arrangement channels ($\text{H}+\text{OD}$ or $\text{D}+\text{OH}$) after UV-excitation into the first electronic excited state $\tilde{\text{A}}^1\text{B}_1$. The chemical branching scheme for water and semiheavy water may be based instead on the IR-preexcitation of the symmetric and asymmetric normal modes. *Ab initio* **PES** of the water molecule have been adapted from the literature [109, 112, 113] and a Mecke-type bond dipole model for the electric dipole moments is also used, along with ultrashort IR-pump-UV-probe laser protocols introduced in the **MCTDH**. In this example, in which the forces of the excited **PES** are non-bond selective, the IR-preparation in the ground electronic state $\tilde{\chi}^1\text{A}_1$ becomes crucial. A deeper understanding of this simple case will pave the way to embark ourselves on the analysis of the multistate non-adiabatic photodynamics of more complex three- and four-atoms molecules, using the powerful **MCTDH** approach, for which some applications in laser pulse-molecule interactions are already implemented but still scarce.

10.1.1 POTENTIAL ENERGY SURFACES

Two electronic states employed in this part of the work are the ground state \tilde{X}^1A_1 and the first excited electronic state \tilde{A}^1B_1 . The model is restricted by fixing the bond angle to its equilibrium value $\theta = 104^\circ$, which reduces the nuclear Hamiltonian to only two radial degrees of freedom, in terms of coordinates r_H and r_D for the OH and OD bond lengths. Here, it is assumed that one of the hydrogens is changed by a deuterium. In terms of these mentioned coordinates, the \tilde{X}^1A_1 PES is parametrized, in atomic units, by Morse potentials with a coupling term between the bond length coordinates given by [113]

$$V_g(r_H, r_D) = D(1 - e^{-\beta(r_H - r_0)})^2 + D(1 - e^{-\beta(r_D - r_0)})^2 - \frac{A(r_H - r_0)(r_D - r_0)}{1 + e^{[(r_H - r_0) + (r_D - r_0)]}}, \quad (10.1)$$

where the parameters D , β , r_0 and A are given in Table 10.1. The \tilde{A}^1B_1 PES was parametrized by Engel et al. [112] in terms of the distance between the atoms in the H_2O molecule, i.e., the two bond lengths r_H and the distance between the hydrogen atoms r_{HH} . The calculated energies for 250 points $[r_H, r_{HH}]$ with ranges $1.6 \leq r_H \leq 2.6$ a.u. and $1.6 \leq r_{HH} \leq 4.0$ a.u., are fitted to an analytic expression given by

$$V_e(r_H, r_{HH}, r_H) = V_{OH}(r_H)\chi(r_{HH}, r_H) + V_{OH}(r_H)\chi(r_H, r_{HH}) + V_I(r_H, r_{HH}, r_H), \quad (10.2)$$

where V_{OH} is a Morse potential and the $\chi(r_i, r_j)$ are cutoff functions given by

$$\chi(r_i, r_j) = (1 - e^{-\delta r_i^2})(1 - e^{-\delta r_j^2}), \quad (10.3)$$

and where the V_I is the interaction function given by

$$V_I(r_H, r_{HH}, r_H) = \sum_{i=1}^{50} c_i P_i(S_H, S_{HH}, S_H) \prod_{j=1}^3 (1 - \tanh \alpha_j S_j), \quad (10.4)$$

where P_i is a polynomial up to sixth order in all variables with $S_j = r_j - 1$ Å. The necessary parameters to produce the first excited state of H_2O are found in Table I of [112]. Since the fit for the \tilde{A}^1B_1 electronic state given in Eq. (10.2) is in terms of the distance between the Hydrogen atoms, a coordinate transformation to the bond angle is performed. For instance, in the case of the isotopomer of the water molecule, HOD, the transformation between the r_{HH} coordinate and r_i bond lengths is straightforward and it is given by a cosine law of the form

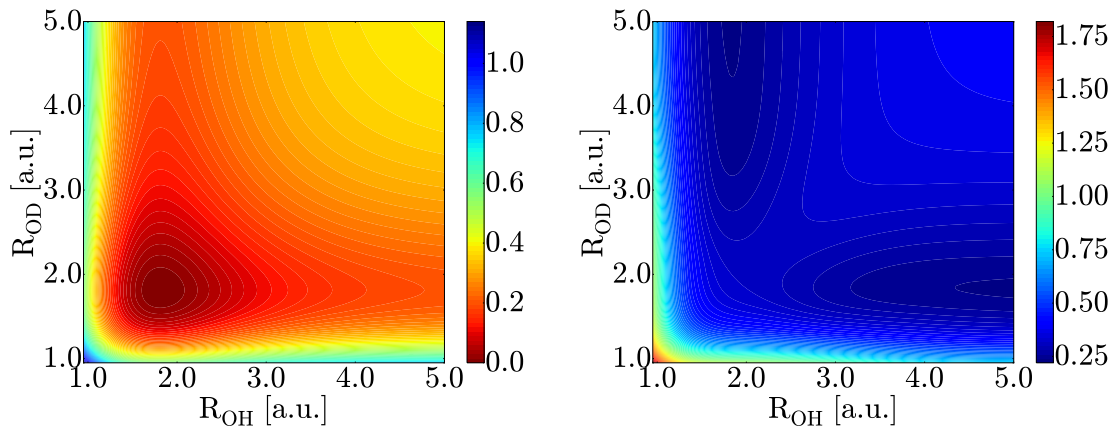
$$r_{HH}^2 = r_H^2 + r_D^2 - 2r_H r_D \cos(\theta), \quad (10.5)$$

where θ takes the equilibrium value 104° .

Table 10.1: Parameters used in the fitting formula Eq. (10.1) for the ground state \tilde{X}^1A_1 of the H_2O and HOD molecules. All values in atomic units.

Parameter	Value
D	0.2092
β	1.1327
r_0	1.81
A	0.0676

Fig. 10.1 includes the contour plots of the two lowest PES. Fig. 10.1a shows the electronic state \tilde{X}^1A_1 in which it is possible to visualize that at the equilibrium point ($r_H = 1.81, r_D = 1.81$) there is a minimum and it has the expected form of a 2D Morse potential according to Eq. (10.1). Additionally, Fig. 10.1b shows the excited state \tilde{A}^1B_1 in which at the point ($r_H, r_D = (2.3, 2.3)$ a.u. a saddle point is located. The localization of a saddle point along the bisection $r_H = r_D$ and the symmetry of the potential makes of this a non-bond selective potential. If in a sudden



(a) Ground electronic state \tilde{X}^1A_1 of HOD molecule. (b) First excited electronic state \tilde{A}^1B_1 of HOD molecule.

Figure 10.1: Contour plots of \tilde{X}^1A_1 and \tilde{A}^1B_1 PES of H₂O and HOD molecules.

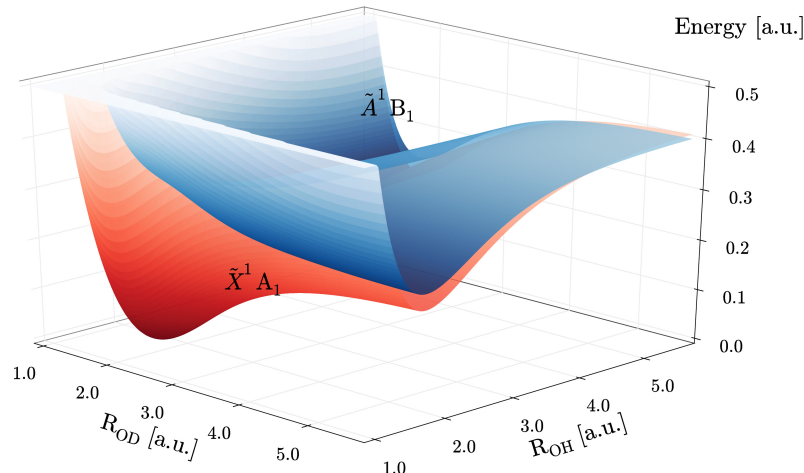


Figure 10.2: 3D representation of the ground (\tilde{X}^1A_1) and first excited (\tilde{A}^1B_1) electronic states of the H₂O and HOD molecules.

photoexcitation, the ground vibrational state of \tilde{X}^1A_1 is excited to the \tilde{A}^1B_1 state, the newly created wavepacket sits on the bisection line and half of the wavepacket dissociates along the r_H coordinate and the other half along the r_D one. Also, Fig. 10.2 shows a 3D representation of the PES of the two electronic states \tilde{X}^1A_1 and \tilde{A}^1B_1 when the bond angle is fixed at $\theta = 104^\circ$

To model the dynamics induced by laser pulses, it is necessary to include the corresponding transition dipole moments between the electronic states. In this case, the molecular dipole operator for the electronic ground state is constructed as a superposition of two Mecke-type dipole functions for the OH and OD bonds given by

$$\mu_{gg}(r_H, r_D) = \cos \left[\frac{90^\circ - \theta}{2} \right] \mu_g(r_H) + \sin \left[\frac{90^\circ - \theta}{2} \right] \mu_g(r_D), \quad (10.6)$$

where each Mecke-type dipole function $\mu_g(r_i)$ is of the form

$$\mu_g(r_i) = \mu_0 r_i e^{-r_i/r_0}, \quad (10.7)$$

with the parameters $\mu_0 = 7.85 \text{ D}^\circ \text{A}^{-1}$ and $r_0 = 0.6 \text{ \AA}$ for the bond angle $\theta = 104^\circ$ and the molecule oriented as in Fig. 10.3. Since the transition dipole moment μ_{ge} given in [113] is almost constant in the domain of the FC region and since the values off the FC region are

almost irrelevant for the calculations performed in this work, the transition dipole moment is set to a constant value $\mu_{ge} = 1.25 \text{ e}\text{a}_0$. Moreover, all the effects due to the intra-state dipole moment of the excited state are neglected ($\mu_{ee} = 0$).

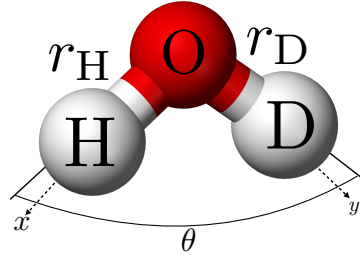


Figure 10.3: Schematic representation of the orientation of HOD molecule in space, where the xy -plane contains the three atoms of the molecule.

10.1.2 IR PUMP - UV DUMP PHOTODYNAMICS

Selective bond breaking by means of impulsive IR + UV laser pulses will be demonstrated for the H_2O and HOD molecules in order to find the differences in the photodissociation of the two molecules. The scheme for the photodynamics can be described in the following way. The initial state is set as the vibrational ground state ($v'' = 0$) of the electronic ground state $\tilde{X}^1\text{A}_1$, then this state is excited by an IR laser pulse in order to generate excitations in the normal or local modes within the ground state $\tilde{X}^1\text{A}_1$, then followed by a subsequent excitation to the electronic excited state $\tilde{A}^1\text{B}_1$ by a second UV laser pulse. Note that in this model the molecular rotation is neglected and the bending mode is frozen. In order to test the effect to excite first with a IR laser pulse, different experiments in the water molecule and its isotopomers were performed by Crim et al. [114-116]. In these experiments it is shown that variation of the IR laser wavelength results in a very large variation of the branching ratios of the fragments distributions after the excitation by a second UV laser pulse.

Ab initio photodynamics requires the solution of the TDSE for the two nuclear wavepackets $\Psi_g(t)$ and $\Psi_e(t)$ that move in the ground $\tilde{X}^1\text{A}_1$ and excited $\tilde{A}^1\text{B}_1$ states, respectively. The dynamic equation $i\frac{\partial}{\partial t}\Psi(Q, t) = \hat{H}(Q, t)\Psi(Q, t)$ in matrix compact form is given by

$$i\frac{\partial}{\partial t} \begin{pmatrix} \Psi_g(Q, t) \\ \Psi_e(Q, t) \end{pmatrix} = \begin{pmatrix} \hat{H}_{gg}(Q) & \hat{H}_{ge}(Q, t) \\ \hat{H}_{eg}(Q, t) & \hat{H}_{ee}(Q) \end{pmatrix} \begin{pmatrix} \Psi_g(Q, t) \\ \Psi_e(Q, t) \end{pmatrix} \quad (10.8)$$

where $\hat{H}_{ii}(Q)$ are the Hamiltonian operators for the electronic states and $\hat{H}_{ij}(Q, t)$ the Hamiltonian interaction between both electronic states. Thus, the complete Hamiltonian $\hat{H}_{ij}(Q, t)$ is given by

$$\hat{H}_{ij}(Q, t) = [\hat{T}(Q) + \hat{V}_{ij}(Q)]\delta_{ij} - \vec{\mu}_{ij}(Q) \cdot \vec{E}(t), \quad (10.9)$$

where $\hat{T}(Q) + \hat{V}_{ij}(Q)$ are the kinetic and potential energy operators for the i -th electronic state and δ_{ij} the Kronecker delta. In addition, the form of the nuclear Hamiltonian depends upon the choice of the set of nuclear coordinates. Hence, valence or bond coordinates r_D and r_H are chosen for the HOD molecule, for which the Hamiltonian reads

$$\begin{aligned} \hat{H}_{ij}(Q, t) = & \left[-\frac{1}{2\mu_D} \frac{\partial^2}{\partial r_D^2} - \frac{1}{2\mu_H} \frac{\partial^2}{\partial r_H^2} - \cos \theta \frac{1}{M_O} \frac{\partial^2}{\partial r_D \partial r_H} + \hat{V}_{ij}(r_D, r_H) \right] \delta_{ij} \\ & - \vec{\mu}_{ij}(r_D, r_H) \cdot \vec{E}(t), \end{aligned} \quad (10.10)$$

where μ_i are the reduced masses for the internal coordinates r_i , with $i=\text{H,D}$, and M_O is the mass of the Oxygen atom. Additionally, the PES operators $\hat{V}_{ii}(r_D, r_H)$ and the diagonal and non-diagonal matrix elements contain the interaction with the field through the vector dipole moments $\vec{\mu}_{ij}(r_D, r_H)$ given in Eqs. (10.1), (10.2) and (10.6).

The radiation that interacts with the water molecule is a superposition of IR and UV laser pulses, following the schemes of control of Tannor-Rice and Brumer-Shapiro outlined in [Section 6.2](#), in the form

$$\vec{E}(t) = \vec{E}_{\text{IR}}(t) + \vec{E}_{\text{UV}}(t - \tau), \quad (10.11)$$

where τ is the delay of the UV laser pulse with respect to the IR laser pulse. The expressions for the IR and UV pulses are given in [Eq. \(6.4\)](#).

10.1.2.1 VIBRATIONAL NORMAL MODES AND SELECTION RULES

All type of vibrations in polyatomic molecules can be expressed as a superposition of fundamental motions which are called normal modes of vibration, which is assumed to be a complete basis for the vibrational nuclear motion. In general, each molecule has a defined number of normal modes which are of different types and symmetries, where these symmetries in particular depend on the molecular shape. Each normal mode form a basis for an irreducible representation of the point group to which the molecule belongs. In the case of the water molecule, it belongs to the point group C_{2v}, whose corresponding character table is given in [Table A.1](#).

The three vibrational normal modes of the water molecule ν_1 , ν_2 and ν_3 are shown in [Fig. 10.4](#). Both ν_1 and ν_2 , the symmetric and the bending mode, respectively, belong to the A₁ irreducible representation of the C_{2v} point group of symmetry since it remains invariant against any symmetry operation of the C_{2v} point group. However, in the case of the asymmetric normal mode ν_3 , the operation C₂ changes the direction of vibration, i.e., each atom moves in the opposite direction after this operation. Additionally, the plane $\sigma(xz)$ also changes the vibration in the opposite direction and as a result the ν_3 normal mode belongs to B₂ irreducible representation.

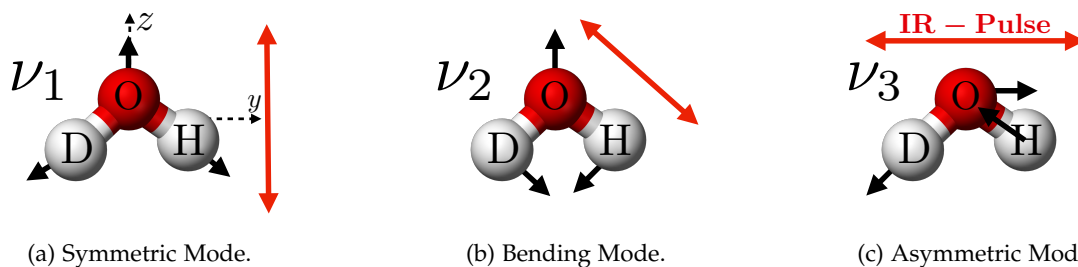


Figure 10.4: Vibrational normal modes of H₂O molecule. The thick black arrows represent the motion of each atom in a normal mode. Red lines in (a) and (c) represent the polarization direction of the IR laser pulse to excite the molecule in the corresponding normal mode and the red line in (b) represents the polarization direction of the IR laser pulse to excite the local mode OH.

To follow particular atomic motions within the collective normal mode vibration in water it may be useful to gain control on the molecular fragmentation. The vibrational selection rules are well known for the water molecule. The allowed or forbidden excitations depend upon the transition integral

$$M = \int_{-\infty}^{\infty} d\mathbf{Q} \Psi_g(\mathbf{Q}) \vec{\mu}(\mathbf{Q}) \phi_{\nu}(\mathbf{Q}), \quad (10.12)$$

where $\phi_{\nu}(\mathbf{Q})$ represents the wavefunction of the ν vibrational normal mode. Each component of the integral in [Eq. \(10.12\)](#) is defined under an irreducible representation of the C_{2v} point group. The ground state $\Psi_g(\mathbf{Q})$ is always totally symmetric, i.e., it has the A₁ symmetry. The dipole moment operator $\vec{\mu}(\mathbf{Q})$ has the symmetry of three cartesian directions, x, y and z which in the C_{2v} correspond to irreducible representations B₁, B₂ and A₁, respectively. $\phi_{\nu}(\mathbf{Q})$ corresponds to the wavefunction of ν_1 and ν_3 vibrational normal modes of the molecule which

correspond to irreducible representations A_1 and B_2 in the C_{2v} point group of symmetry. This can be written in a matrix form as

$$M = A_1 \begin{pmatrix} x \\ y \\ z \end{pmatrix} \begin{pmatrix} \nu_1 \\ \nu_3 \end{pmatrix} = A_1 \begin{pmatrix} B_1 \\ B_2 \\ A_1 \end{pmatrix} \begin{pmatrix} A_1 \\ B_2 \end{pmatrix}, \quad (10.13)$$

where only the combinations (see [Table A.2](#)) that yield the totally symmetric irreducible representation A_1 contribute for the dipole integral M . It means that vibrational normal modes ν_1 (symmetric stretching) and ν_3 (asymmetric stretching) can only be excited by lasers with polarization along the z -axis and y -axis, respectively, as indicated in [Figs. 10.4a](#) and [10.4c](#).

10.1.2.2 H₂O PHOTODYNAMICS

In order to control the photodissociation with a IR-pump-UV-dump laser pulse in water molecule, the vibrational states of the electronic ground state \tilde{X}^1A_1 are required. These vibrational states are calculated using the [MCTDH](#) package [111] by performing a propagation in imaginary time to produce the lowest 2D-vibrational states of H₂O molecule. As a rule, a radial box for each bond coordinate have been used with $r_i \in [0.95, 5.70]$ a.u., with $i = H$ and D , large enough indeed to accommodate the different vibrational states under study. In the [MCTDH](#) calculation, $n_i = 15$ SPF were used to represent both coordinates in the nuclear boxes. The number of primitive basis sets is $N_i = 96$ for both valence coordinates.

The three lowest vibrational states are shown in [Fig. 10.5](#) with its corresponding energy values quoted in [Table 10.2](#). The first state corresponds to the vibrational ground state (left panel in [Fig. 10.5](#)) and the other two vibrational states correspond to the first and second excited vibrational states. The first excited vibrational state (middle panel in [Fig. 10.5](#)) corresponds to the excitation $(\nu_1, \nu_3) = (1, 0)$, which in terms of the vibrational normal modes is the symmetric normal mode. Similarly, the second excited vibrational state (right panel in [Fig. 10.5](#)) corresponds to the excitation $(\nu_1, \nu_3) = (0, 1)$, which in terms of the vibrational normal modes is the asymmetric normal mode. To excite the water molecule in one of these normal modes it is necessary to pump the molecule with a IR laser pulse.

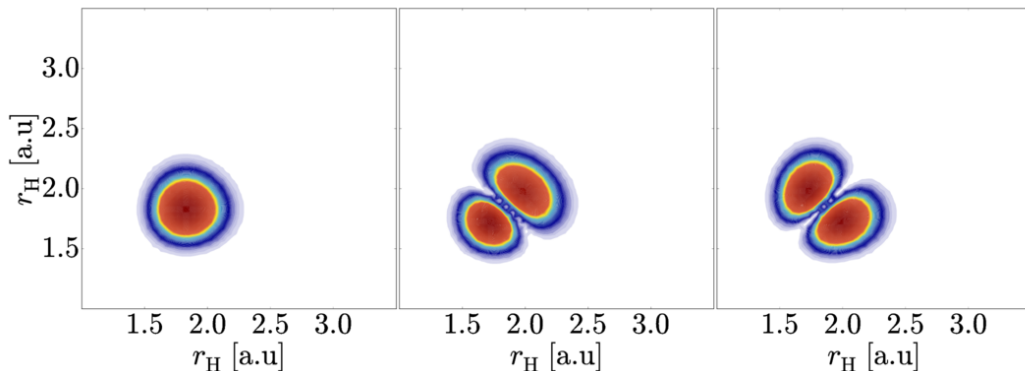


Figure 10.5: The three lowest vibrational states in the electronic ground state \tilde{X}^1A_1 of H₂O molecule. (Left panel) Vibrational ground state. (Middle panel) First excited vibrational state of A_1 symmetry or symmetric mode. (Right panel) First excited vibrational state of B_1 symmetry or asymmetric mode.

In order to control the dissociation along a chosen bond in the water molecule, it is necessary to study the behaviour of the bond coordinates in the molecule. Hence, [Fig. 10.6](#) shows the average position of the bond coordinates for different types of excitation. The pulse to generate a local excitation OH1 in water molecule H₂O, that involves a local stretching with coordinate r_H (in this case represented along the x-axis in [Fig. 10.5](#)). The crucial fact is that the frequency 0.463 eV or 3735 cm⁻¹ applied along the local mode produces its excitation. The other pulse parameters for the IR-pump pulse are $I_{IR} = 3.3 \times 10^{14}$ W/cm² and $T_{IR} = 50$ fs while the pulse

Table 10.2: Energy of the three lowest vibrational states in the electronic ground state $\tilde{\chi}^1A_1$ of H₂O molecule.

(ν_1, ν_3)	Energy (eV)	Energy (cm ⁻¹)
(0,0)	0.0	0.0
(1,0)	0.455	3666.4
(0,1)	0.464	3742.8

parameters for the UV-dump pulse are $I_{UV} = 1.6 \times 10^{14}$ W/cm², $\omega_{UV} = 6.8$ eV or $\omega_{UV} = 54845$ cm⁻¹, $T_{UV} = 3$ fs with pulse time delays of 19 and 31 fs as it is shown in Fig. 10.6. The time delays correspond to values where the average bond length has almost its maximum value and it increases with the momentum in the direction of dissociation (see Fig. 10.6). Results of the wavepacket dynamics when the local model OH1 is excited are shown in the top row of Fig. 10.7 for different propagation times, from the onset of the IR pulse at $t = 0$. In this, it is possible to observe that the wavepacket represented with contours in black, that corresponds to the wavepacket moving in the upper $\tilde{\chi}^1B_1$ state, after UV excitation with a IR-UV delay of $\tau_{UV} = 19$ fs (recall $T_{IR}/2 + \tau_{UV} \sim 44$ fs). In this case, since the r_{H1} is expanding, one expects dissociation H₂O+H₁. However, with a longer delay $\tau_{UV} = 31$ fs the r_{H2} increases while the r_{H1} simultaneously decreases (see Fig. 10.6) and the expected dissociation is H₁+OH₂. On the contrary, if the goal is to achieve the maximum possible yield for the dissociation H₂ + OH₁ by driving the wavepacket along the r_{H_2} direction, a different time delay has to be selected for the arrival of the UV pulse. With this second chosen delay of $\tau_{UV} = 31$ fs the excited wavepacket is represented in green in Fig. 10.7. In this case the time delay to excite the IR driven wavepacket into the $\tilde{\chi}^1B_1$ electronic state with the UV pulse is $\tau = 31$ fs. One can appreciate that whereas the former chosen delay produces a much better specificity for the dissociation in the H₁ + OH₂ channel (almost the full wavepacket goes into that direction), the second delay is less specific, because the wavepacket may dissociate in both channels, although the H₁O + H₂ channel dominates.

Then, it is showed that the control over dissociation can be achieved by exciting a local mode, by some IR-heating of the wavepacket prior to the UV electronic excitation, that occurs at a well selected time delay. It is interesting to translate this conclusion from local modes to the excitation of normal modes. The case of the excitation of the symmetric mode (first vibrational excited state) could be trivial to explain in the case of H₂O molecule, due to the symmetry of the molecule but not in the case of its isotopomer HOD. In the symmetric stretching mode, the bond distances r_{H_1} and r_{H_2} are the same at any time (see middle panel in Fig. 10.6). Here the water molecule is excited with an IR pulse with the parameters $I_{IR} = 3.3 \times 10^{14}$ W/cm², $\omega_{IR} = 0.455$ eV or $\omega_{IR} = 3666.4$ cm⁻¹ and $T_{IR} = 50$ fs. The parameters for the delayed UV pulse are the same as described above. With this symmetric excitation (both coordinates r_{H_1} and r_{H_2} share the same average position value in Fig. 10.6), the evolution of the dissociating wavepacket in the excited PES is plotted in middle row of Fig. 10.7. The probability density spreads equally over the two halfspaces separated by the bisection plane that contains the saddle point in the excited PES. Then, this symmetric excitation is not bond-selective. Also the dissociation per channel is smaller than in the local excitation case (see Fig. 10.8).

At variance, the IR excitation of an asymmetric mode can be more useful to separate specific hydrogen atoms from the molecule. To excite the asymmetric mode the IR laser is tuned this time to $\omega_{IR} = 0.464$ eV or $\omega_{IR} = 3742.8$ cm⁻¹ fs while the pulse parameters for the UV-dump pulse are the same. It is worth mentioning that although the frequencies ω_{IR} are similar to excite the different modes, each mode is independent since the laser polarization in each case is different. The right panel in Fig. 10.6 shows the average position of the two bond distances r_{H_1} and r_{H_2} when the asymmetric normal mode is excited by the IR pulse. Of course, the asymmetric stretching must show an alternating complementary behavior in these two distances. In this asymmetric case, the IR-heating works to prepare the wavepacket in the ground state $\tilde{\chi}^1A_1$ until a given time in which the selected bond coordinate (r_{H_1} or r_{H_2}) has a long expansion with a given momentum (see Fig. 10.6). Assuming a sudden UV

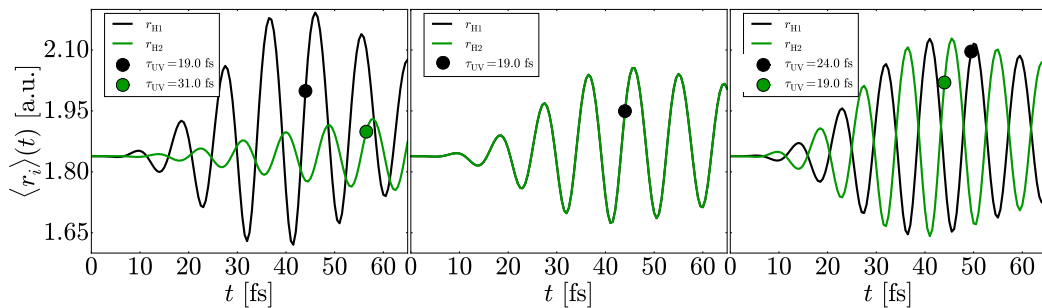


Figure 10.6: Average position of the two bond coordinates (r_{H_1} and r_{H_2}) excited along a local mode (left panel), symmetric mode (middle panel) and asymmetric mode (right panel) only with the IR pulse. Black and green dots indicate the position and time delay of the UV-dump pulse. From $t = 0$ the duration of the IR field is $T_{IR} = 50$ fs ($\omega_{IR} = 0.455$ eV) and the UV short pulse with duration $T_{UV} = 3$ fs ($\omega_{UV} = 6.8$ eV) is applied after a peak-peak delay between the two pulses of $\tau_{UV} = 19$ fs and $\tau_{UV} = 31$ fs (for the local mode); delay of $\tau_{UV} = 19$ fs for the symmetric model and delays of 24 and 19 fs for the asymmetric mode.

excitation at $t = 44.5$ fs and 41.5 fs for the r_{H_1} and r_{H_2} , respectively, the wavepackets initiate their dynamics in the upper excited state (see second panel at the bottom row in Fig. 10.7). It is clearly appreciated that the IR-preheated wavepackets launched at different time delays with UV lasers (here a difference of 3 fs) follow very different dissociation paths, with a very high selectivity against the case of heating the symmetric mode (see right panel in Fig. 10.8).

10.1.2.3 HOD PHOTODYNAMICS

From the experimental point of view it is impossible to distinguish between the two hydrogen atoms in any fragmentation of the water molecule. Hence, calculations in its isotopomer HOD are performed since the two isotopes hydrogen and deuterium are distinguishable, because the latter has almost double mass than hydrogen. Again, the first step is to obtain and analyze the vibrational states in the ground \tilde{X}^1A_1 PES. Thus, in order to control the photodissociation with a IR-pump-UV-dump laser pulse in the isotopomer HOD of water molecule, one has to know the vibrational states of the electronic ground state. The same procedure with MCTDH as explained for water in the previous section is used.

The three lowest vibrational states are shown in Fig. 10.9 with its corresponding energy values (the ground state is set to zero energy) in Table 10.3. The first state corresponds to the vibrational ground state (left panel in Fig. 10.9) while the another two correspond to the first and second excited vibrational states. Note the differences with those vibrational states in the water molecule. HOD has no longer a C_{2v} symmetry for the vibrations and the vibrations cannot be classified as symmetric and asymmetric stretchings. Moreover, due to the difference of masses, the OH and the OD bonds can be treated as quasi-independent local modes. In fact, this is reflected in the form of the excited states in Fig. 10.9 in which the first state is excited along the r_D coordinate and the second along the r_H coordinate.

Table 10.3: Energy of the three lowest vibrational states in the electronic ground state \tilde{X}^1A_1 of HOD molecule.

(v_1^D, v_3^D)	Energy (eV)	Energy (cm^{-1})
(0,0)	0.0	0.0
(1,0)	0.338	2727.5
(0,1)	0.460	3706.4

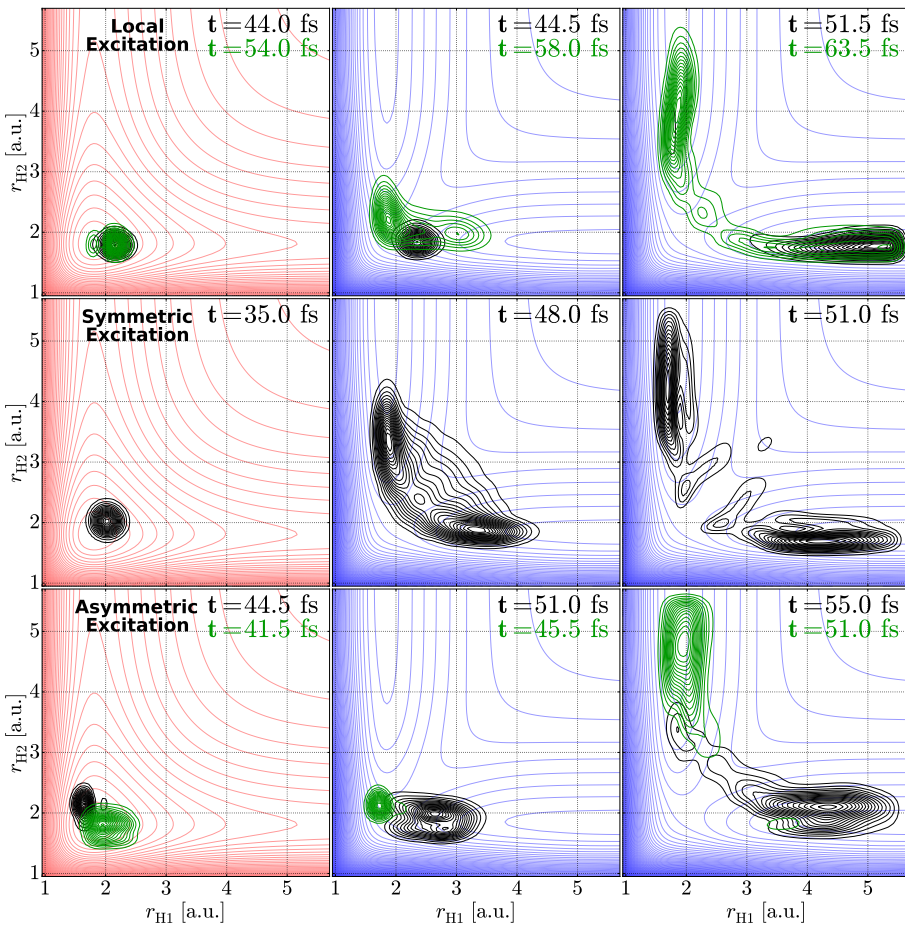


Figure 10.7: Wavepacket dynamics for the H₂O molecule subject to IR+UV pump-probe pulses at different times. The wavepackets shown in the left column are those heated by the IR laser within the electronic ground state, just prior to the UV excitation. After arrival of the UV pulse, the wavepacket is excited to the upper electronic state and they evolve differently according to the chosen UV delay. Red and blue diffuse contours represent the electronic ground and excited state of the molecule, respectively, where the wavepacket moves. Contour colors of the wavepackets follow the same color scheme represented in Fig. 10.6 for the pulse time delays.

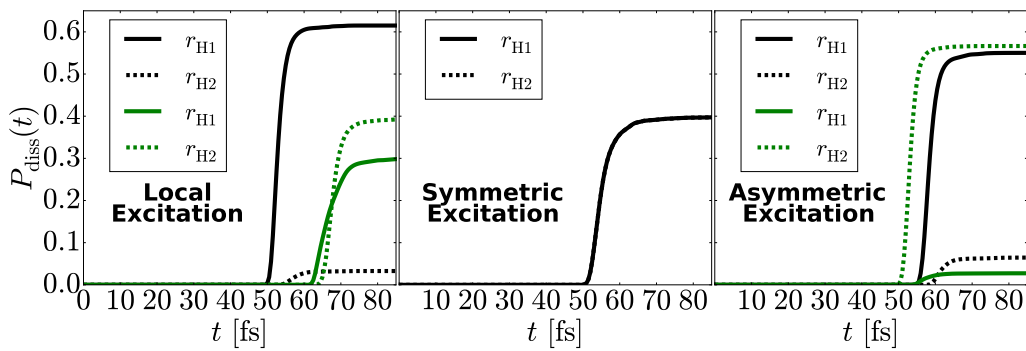


Figure 10.8: Photodissociation probabilities along the two dissociating channels OH₂+H₁ and H₂+OH₁, when the H₂O molecule is excited into a local mode (left panel), symmetric mode (middle panel) and asymmetric mode (right panel). Colors black and green are dissociations for the wavepackets indicated in Fig. 10.7 with the same color scheme.

Similar as in the procedure in water, Fig. 10.10 shows the average position of the bond coordinates r_H and r_D for different types of excitation of the HOD molecule. The pulse to

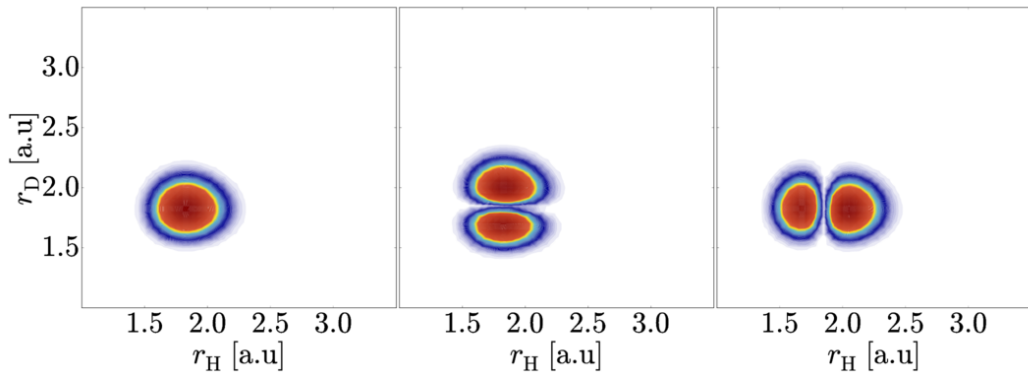


Figure 10.9: Three lowest vibrational states in the electronic ground state $\tilde{\chi}^1 A_1$ of HOD molecule. (Left panel) Vibrational ground state. (Middle panel) First vibrational excited state. (Right panel) Second vibrational excited. The latter two look like the first excited states of two independent orthogonal harmonic oscillators, along the r_D direction and the r_H direction, respectively.

generate the local excitation of the r_H coordinate has the parameters for the IR-pump pulse are $I_{IR} = 3.3 \times 10^{14} \text{ W/cm}^2$, $\omega_{IR} = 0.463 \text{ eV}$ or $\omega_{IR} = 3735 \text{ cm}^{-1}$, same frequency used in [109], $T_{IR} = 50 \text{ fs}$ while the pulse parameters for the UV-dump pulse are $I_{UV} = 1.6 \times 10^{14} \text{ W/cm}^2$, $\omega_{UV} = 6.8 \text{ eV}$ or $\omega_{UV} = 54845 \text{ cm}^{-1}$, $T_{UV} = 3 \text{ fs}$ with the pulse time delays show in Fig. 10.10. In this case, similarly to the case of H_2O molecule, the time delay for the UV sudden excitation is chosen when the average position of the local coordinate reaches a large value and a momentum in the direction of dissociation. Results of the wavepacket dynamics when the local mode r_H atom is excited are shown in the top row of Fig. 10.11 for different times of propagation and for two different time delays τ_{UV} , 19.5 fs (in black) and 24 fs (in green). The average position of the wavepacket in black plotted in the top row-left panel in Fig. 10.11 is displaced from its equilibrium position ($r_H \approx 1.8 \text{ a.u.}$) when $t = 44 \text{ fs}$, i.e., it is found in the position represented by the black dot in the left-panel of Fig. 10.10. At this propagation time, which corresponds to a delay of $\tau = 19.5 \text{ fs}$ between both pulses, the wavepacket is UV-excited to the $\tilde{\chi}^1 B_1$ electronic state (see top-row-middle-panel in Fig. 10.11) conserving the momentum that carries from the ground state and it starts to move in the direction where the bond distance OH increases. This wavepacket will eventually dissociate in the channel $\text{DO}+\text{H}$ (top-row-right-panel in Fig. 10.11). The wavepacket in green indicates the dynamics for another delay $\tau_{UV} = 24 \text{ fs}$, in which the detachment of deuterium D from OH prevails. The corresponding dissociation probabilities for each dynamics are shown in Fig. 10.12. The left-panel shows that the highest photodissociation probability corresponds to the detachment of H, which precisely corresponds to the excited local mode, while the fragmentation to obtain D is very small.

Now, the collective vibrations due to excitation to the first and second vibrational states of HOD are explained. When the IR field excites the first vibrational state of HOD, the photodissociation probabilities obtain are shown in the middle-panel of Fig. 10.12. In this case, the molecule is excited with an IR pulse with central frequency $\omega_{IR} = 0.338 \text{ eV}$ or $\omega_{IR} = 2727.5 \text{ cm}^{-1}$ and the same for the UV pulse that in previous case. Now, the IR pulse excites the first vibrational state and a superposition of the ground and first excited vibrational states results. According to the form of the first excited state in Fig. 10.9, the motion of this superposition (specifically the portion of wavepacket moving in the upper electronic state) does mainly in the r_H direction. Nonetheless, due to intramolecular coupling the r_D coordinate also moves but with a smaller amplitude (see Fig. 10.9). In spite of selecting an appropriate time delay for the r_D coordinate (at its best position and momentum), the result is very disappointing, since most of the fragmentation goes to hydrogen instead of deuterium. Here excitation of the heavier mode leads to dissociation of the lighter mode, due to the intramolecular vibrational coupling.

Now, the HOD is excited with the IR tuned resonant with the second vibrational state. The pulse responsible of the excitation of the second vibrational excited state has the same parameters for the IR-pump pulse except its frequency which is $\omega_{IR} = 0.460 \text{ eV}$ or $\omega_{IR} = 3706.4$

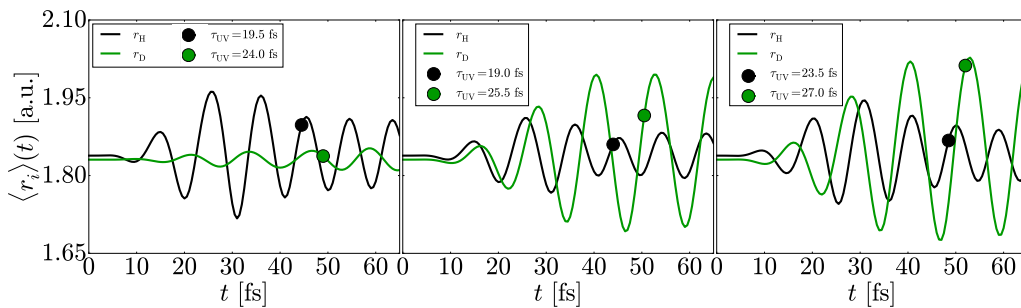


Figure 10.10: Average position of the two bond coordinates (r_H in black and r_D in green) when the HOD molecule is excited into a local mode (left panel), first vibrational excited state (middle panel) and second vibrational excited state (right panel) using the IR pulse with central frequencies close to the defined in Table 10.3. Black and green dots indicate the position and time delay of the UV-dump pulse. From $t = 0$ the duration of the IR field is $T_{IR} = 50$ fs and the UV short pulse with duration $T_{UV} = 3$ fs ($\omega_{UV} = 6.8$ eV) is applied after a peak-peak delay between the two pulses of $\tau_{UV} = 19.5$ fs and $\tau_{UV} = 24$ fs (for the local mode); delays of $\tau_{UV} = 19$ fs and $\tau_{UV} = 25.5$ fs for the first vibrational excited state and delays of $\tau_{UV} = 23.5$ and $\tau_{UV} = 27$ fs for the second vibrational excited state.

cm^{-1} fs while the pulse parameters for the UV-dump remain the same. The right-panel in Fig. 10.10 shows the average position of the two bond distances when the second vibrational excited state is excited with the IR pulse. Here the lighter local mode r_H is mainly excited (see Fig. 10.9 with the form of the excited state, and the larger amplitude of the average position in Fig. 10.10) which affects less to the heavier mode, resulting in a less coupled system to allow for a better selection of fragments.

In conclusion, from the calculations of H₂O and HOD molecules, it is shown that a previous knowledge of the structure of the system (normal modes, vibrational states, PES, etc) helps to control the final products in specific chemical reactions by using pump-dump control methodology.

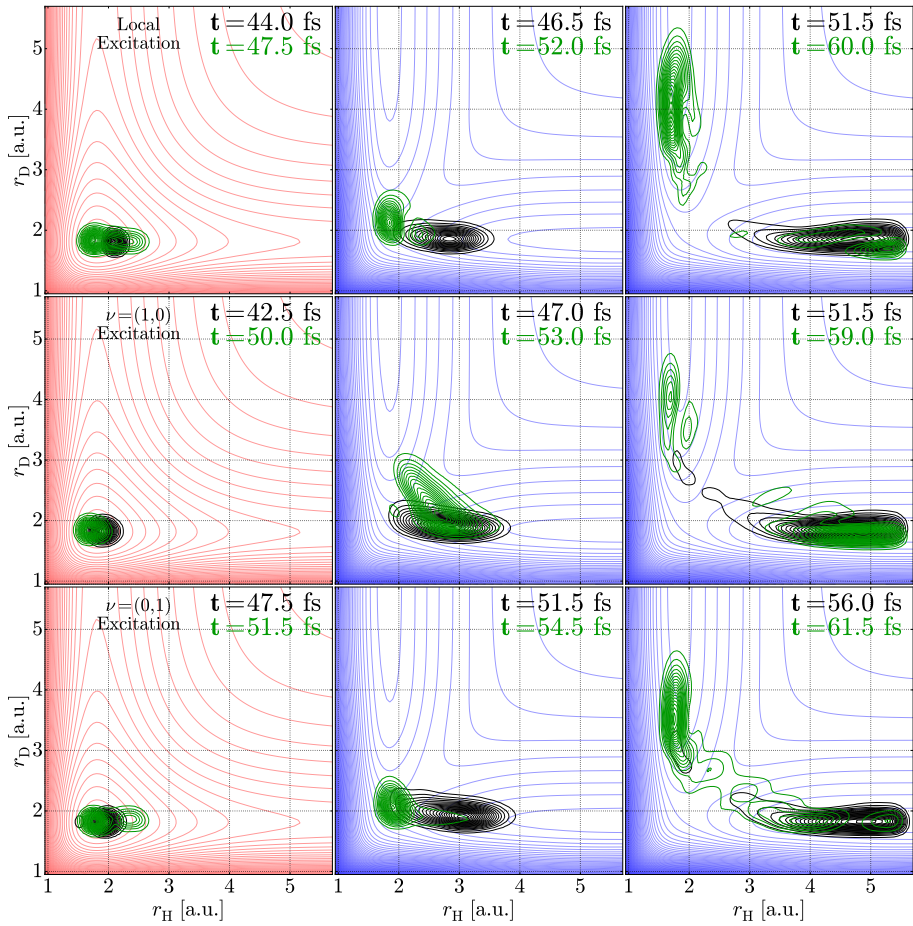


Figure 10.11: Wavepacket dynamics for the HOD molecule subject to IR+UV pump-probe pulses at different times. The wavepackets shown in the left column are those heated by the IR laser within the electronic ground state, just prior to the UV excitation. After arrival of the UV pulse, the wavepacket is excited to the upper electronic state and they evolve differently according to the chosen UV delay. Red and blue diffuse contours represent the electronic ground and excited state of the molecule, respectively, where the wavepacket moves. Contour colors of the wavepackets follow the same color scheme represented in Fig. 10.10 for the pulse time delays.

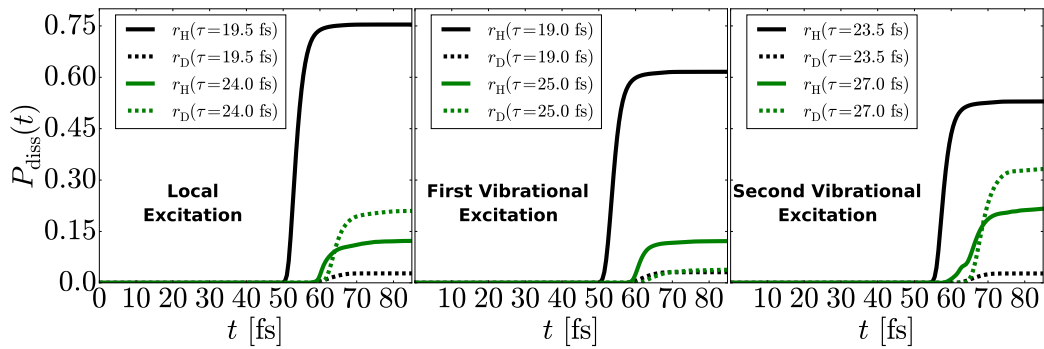


Figure 10.12: Photodissociation probabilities along the two dissociating channels H+OD and D+OH when the HOD molecule is excited into a local mode (left panel), first vibrational excited state (middle panel) and second vibrational excited state (right panel). Colors black and green are dissociation yields associated to the wavepacket dynamics included in Fig. 10.7 with the same color scheme for two different time delays τ_{UV} .

10.2 CO₂ (CARBON DIOXIDE)

Carbon dioxide is a colorless gas which is a linear and centrosymmetric molecule composed by a carbon atom covalently double bonded to two oxygen atoms, as it is shown in Fig. 10.13. The equilibrium carbon-oxygen bond length is 2.2 a.u., noticeably shorter than the bond length of a CO single bond. In addition, it is not only produced by all aerobic organisms when they metabolize carbohydrates and lipids to produce energy by respiration, but it is also a versatile industrial material, used in diverse fields of the industry, as in fire extinguishers or a supercritical fluid solvent in decaffeination of coffee. Similarly, it is included in carbonated beverages to add effervescence. However, in industry, the carbon dioxide is released into the atmosphere as a result of the use of fossil fuels that makes CO₂ to be the most significant long-lived greenhouse gas in Earth's atmosphere. From the beginning of the industrial revolution, the emission of CO₂ has rapidly increased its concentration of this gas in the atmosphere, leading to global warming. Hence, there exists a large interest to study and perform some control over CO₂ molecule in order to reduce the greenhouse effect.

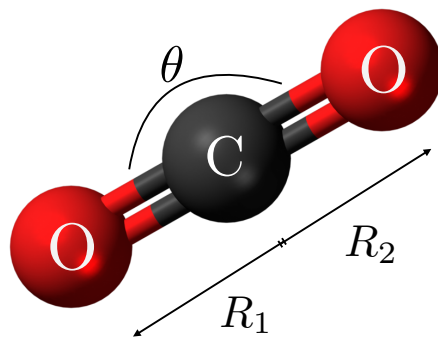


Figure 10.13: Schematic representation of CO₂ molecule and its internal coordinates.

For the time being, the atmospheric levels of CO₂ are increasing steadily. Possibilities to reduce the contents of CO₂ include its decomposition with radiation in chemical reactions, such as



or



From previous studies in carbon dioxide it is known that it absorbs and emits infrared radiation. This causes carbon dioxide to warm the surface and lower atmosphere while cooling the upper atmosphere. In this section, the structure and dynamics of CO₂ is studied. Before entering into the electronic structure and dynamics, it is important to describe the coordinates and the Hamiltonian that will be used in the calculations. Coordinates chosen are the internal coordinates of the molecule which represent the carbon-oxygens bond lengths R₁ and R₂, and the O-C-O bending angle θ (see Fig. 10.13). Because CO₂ is a linear and centrosymmetric molecule, the point group of symmetry that represents the molecule is D_{∞h}. However, continuous groups are not implemented in large scale electronic structure codes for molecules, and these packages (Gaussian, MOLPRO, etc) make use discrete point groups instead. For CO₂, the point groups of symmetry used to perform different calculations are the C_{2v} and C_s. In this direction, the CO₂ can be calculated as a non-linear molecule, with analogous symmetries as water H₂O (C_{2v} point group) or without any symmetry (C_s point

group). Using the analogy with the water molecule, the full nuclear Hamiltonian for CO_2 , including the interaction term with radiation, is given by

$$\hat{H} = -\frac{1}{2\mu_1} \frac{\partial^2}{\partial R_1^2} - \frac{1}{2\mu_2} \frac{\partial^2}{\partial R_2^2} - \frac{\cos \theta}{M_C} \frac{\partial^2}{\partial R_1 \partial R_2} - \left(\frac{1}{2\mu_1 R_1^2} + \frac{1}{2\mu_2 R_2^2} \right) \left(\frac{1}{\sin \theta} \frac{\partial}{\partial \theta} \sin \theta \frac{\partial}{\partial \theta} + \frac{k^2}{\sin^2 \theta} \right) \\ + \frac{1}{2M_C R_1 R_2} \left[\cos \theta \left(\frac{1}{\sin \theta} \frac{\partial}{\partial \theta} \sin \theta \frac{\partial}{\partial \theta} + \frac{k^2}{\sin^2 \theta} \right) + \left(\frac{1}{\sin \theta} \frac{\partial}{\partial \theta} \sin \theta \frac{\partial}{\partial \theta} + \frac{k^2}{\sin^2 \theta} \right) \cos \theta \right] \\ + \frac{1}{M_C} \left(\frac{1}{R_1} \frac{\partial}{\partial R_2} + \frac{1}{R_2} \frac{\partial}{\partial R_1} \right) \frac{\partial}{\partial \theta} \sin \theta + V(R_1, R_2, \theta) - \vec{\mu}(R_1, R_2, \theta) \cdot \vec{E}(t), \quad (10.16)$$

where M_C is the mass of the carbon atom, μ_i are the reduced masses of the C-O bond lengths R_i , θ is the OCO bending angle and k is the angular momentum label.

10.2.1 ELECTRONIC STRUCTURE

Carbon dioxide is one of the most studied molecules in the literature, both experimental and theoretically, with emphasis in its absorption spectra and electronic structure [110, 117–123]. However, the Rydberg character of some low electronic states makes that calculations of these states it is not straightforward. Here it is discussed some details on the electronic structure of CO_2 before embarking in multistate dynamics calculations. Because of recent experimental results obtained from the absorption spectrum by optical and electron impact spectroscopy of CO_2 molecule [120, 121, 124], it is necessary to find all relevant excited electronic states, valence and Rydberg, present in this molecule in a given energy window. England and Ermler [118] and Nakatsuji [119] performed *ab initio* calculations of these states at MCSCF/MRCI level including a description for the Rydberg orbitals because the character of the excitation to the $^1\Pi_g$ state is Rydberg and they also made a description of the bent states. They point out that due to the $^1\Pi_g$ Rydberg state lies below the valence states, which ultimately means that they strongly mix with the valence excited states. Hence, their *ab initio* calculation is not straightforward. Nevertheless, almost ten years ago, Spielfiedel *et al.*, [121] calculated the singlets and triplets bent valence excited states but they included diffuse functions to describe the Rydberg orbitals, similarly at the level of MCSCF/MRCI level of theory in order to reproduce experimental results found thirty years ago [125]. Likewise, Buenker *et al.* [122] made a theoretical study of the sixteen lowest singlets states to describe the different excitation energies of the states and their characters. At this point, all these theoretical studies were performed taking into account the Rydberg character of the first excited state and the Rydberg states above 11.0 eV. More recently, two works were published in which the lowest states in the C_s point group symmetry were calculated in order to perform a dynamics [126, 127] or, better said, to describe possible dynamics [110] on these states. Although these works have good results and explain some part of the CO_2 spectrum and the photodissociation process, they are only based in the valence states and as a consequence, a description of the spectrum below 11.0 eV could be valid. Now, in the present work, an exhaustive search and analysis of these Rydberg states is performed to describe with high accuracy the absorption spectrum and the photodissociation process in the energy range between 11 and 13.77 eV, where this last energy value correspond to the ionization energy of the CO_2 molecule.

Additionally, in the present study the electronic structure of PEC of CO_2 in the energy region of 11–14 eV is also described. Several types of calculations in the symmetries $^1A'$ and $^1A''$ of the point group C_s and in the irreducible representations of the C_{2v} point group are performed to stress the differences when Rydberg states are included or not.

10.2.1.1 DUNNING VS. ROOS BASIS SET IN THE SEVEN LOWEST STATES OF CO_2

Global PES of the four lowest states in the symmetry $^1A'$ and the three lowest states in the symmetry $^1A''$ are calculated using the augmented correlation consistent polarized valence quintuple zeta (aug-cc-pV5Z) basis set [28]. These PES are calculated at the MRCI level, based on state-averaged full-valence MCSCF calculations (FVAS) with 16 electrons in 12 active orbitals

and 6 electrons in three fully optimized closed-shell inner orbitals. These calculations are performed taking as reference the theoretical part of Lu et al. [110]. These calculations are compared with a partial active valence space (PAVS) based on **MSCF** calculations with 12 electrons in 10 active orbitals and 10 electrons in five fully optimized closed-shell inner orbitals followed by **MRCI** calculations with 6 electrons in three fully optimized closed-shell inner orbitals. In this case, the generally contracted basis sets of atomic natural orbital (ANO) type are employed, which are obtained from C,O(14s9p4d) primitive sets [128]. These type of basis functions are so-called ANO-L basis sets. Despite the 2s₀ orbitals are closed, the results are comparable if the calculations are performed inside an active space 16/12 using the ANO-L basis set. The difference between these and the full valence active space calculations arise in the 4¹A' state before the equilibrium geometry (< 2.2 a.u.).

Fig. 10.14 shows the cuts of the four lowest A' states in the point group symmetry C_s. In this figure, it is possible to see that the 2A' and 3A' 'diabatic' states in the region between 2.0 and 3.0 a.u. are better represented in the calculations made with the ANO-L basis set because this basis set is optimized to represent diffuse orbitals [128]. In the case of the 4A' state, the region before the equilibrium distance (< 2.2 a.u.) is completely different in the two cases. This is because the 4A' state in this region has a Rydberg character. Nevertheless, the region from 2.4 a.u. is described similarly in both cases. The difference in the region before the equilibrium point is because the AV5Z basis set used in the FVAS calculations only describes valence states and it is not optimized to reproduce Rydberg states. However, the ANO-L basis set is optimized to represent the diffuse orbitals better than the Dunning bases, although it is not enough to reproduce with a good accuracy the 4¹A' state (green solid line in Fig. 10.14). This means that in the calculations the active space is not preserved and it is necessary to go beyond the valence active space.

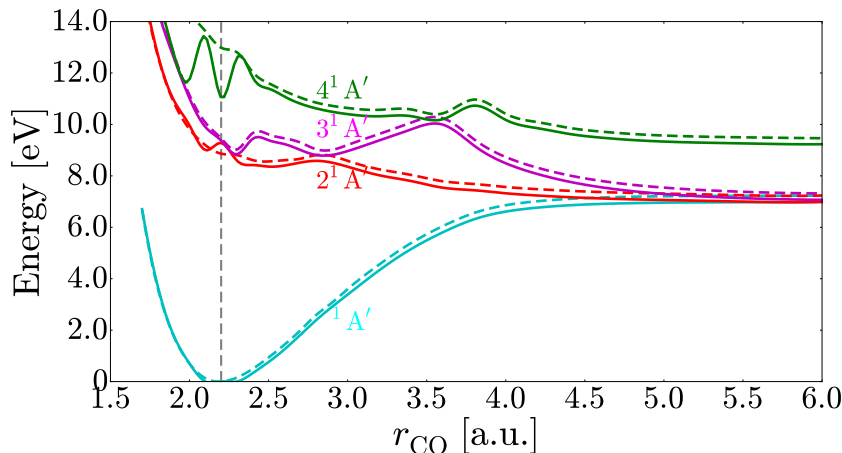


Figure 10.14: Fourth lowest states in the symmetry ¹A' of CO₂ molecule. FVAS and PVAS states are shown with dashed and solid lines, respectively. The highest represented energy is 14 eV, close to the ionization energy at 13.77 eV.

10.2.2 SIX LOWEST STATES IN THE C_s POINT GROUP OF SYMMETRY

Based on the results obtained in Section 10.2.1.1 related with the basis set chosen, two different calculations are performed to test the accuracy of the **EOM-CCSD** level of theory. Although the active space is not the same in all geometry configurations, the calculations are performed with a basis set composed by the ANO-L basis set and additional diffuse functions of s, p and d type are included for the C atom with exponents 0.023, 0.021 and 0.015 [27], respectively, in order to describe the low-lying (n = 3) Rydberg orbitals in the CO₂ spectrum. The three lowest states in each symmetry in the C_s point group of symmetry are computed using **MSCF/MRCI** level of theory. C_s point group is chosen since it is the lower symmetry that allows to represent the molecule with different bond angles and different bond distances at the same time. For this purpose, in one type of calculation eight a' and three a'' orbitals were included in the

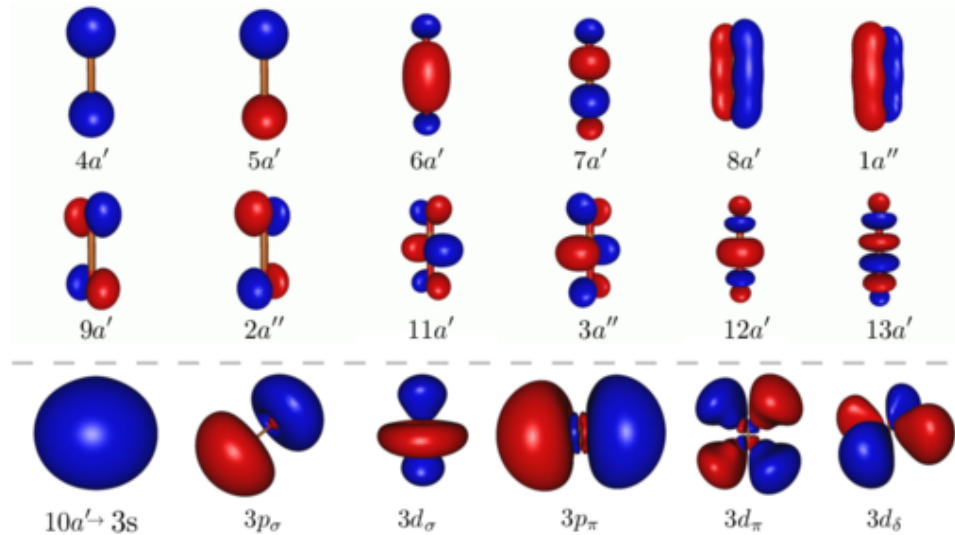


Figure 10.15: Family of the CO_2 orbitals used in the electronic structure calculations. Orbitals above and below the dashed grey line correspond to the valence and Rydberg orbitals, respectively. Core orbitals are not shown.

active space, while five internal a' orbitals were kept doubly occupied in all configurations. At the MRCI level, the core ($3a'$ orbitals) were closed. This active space has been increased by one additional a' orbital to preserve the same active space in all geometry configurations, i.e., all valence orbitals and one Rydberg orbital, the $3s$, which is the orbital responsible of the excitation that corresponds to the states $2^1A'$ and $11A''$ [122]. Fig. 10.15 shows all orbitals used in this case and subsequent calculations in the CO_2 molecule. Additionally, Table 10.4 shows the vertical transitions and excitations in the Franck-Condon region for the six lowest states of the CO_2 molecule. Another calculation was performed employing the generally contracted aug-cc-pV5Z (AV5Z) basis set reported by Dunning *et. al.* [28–31] to describe the orbitals of all atoms, i.e., following the calculations of Lu *et. al.* [110]. It results in 381 contracted Gaussian type functions.

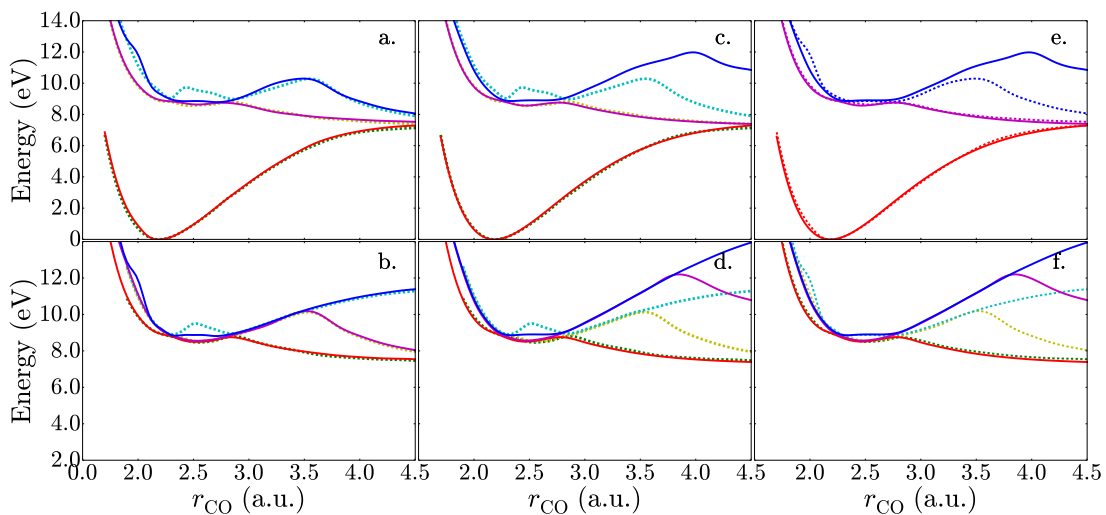


Figure 10.16: Comparison between three different types of calculations for the three lowest states in both symmetries A' (a, c, e) and A'' (b, d, f). The active space and the level of accuracy in each calculation is (a) and (b) MCSCF/MRCI (12,11) (continuous lines) vs MCSCF/MRCI (16,10) (dashed lines), (c) and (d) EOM-CCSD (continuous lines) vs MCSCF/MRCI (16,10) (dashed lines), (e) and (f) EOM-CCSD (continuous lines) vs MCSCF/MRCI (12,11) (dashed lines).

Fig. 10.16 shows the comparison between the two different types of calculations and the states calculated at EOM-CCSD level of theory (solid lines). It is important to point out that the inclusion of one 3s (a') orbital, obtained with a basis set increased by diffuse functions replace the wiggle located at $r_{CO} \sim 2.4$ a.u. for the $3^1A'$ and $3^1A''$ states (dashed lines) by a smoother behavior (solid lines), similarly to the states found in [123]. However, the behaviour or accuracy of these states is limited to the T_1 diagnostic [129] which is a criterion of the multiconfigurational nature of the wavefunction. In this case, CO₂ molecule, the potential energy surface calculated using this level of theory is valid in the region of $r_{CO} = [1.7, 2.8]$ a.u. and $\theta = [140^\circ, 180^\circ]$, which is enough to describe, initially, the three lowest Rydberg and valence states of the molecule.

Table 10.4: Vertical transitions energies ΔE_v of the three lowest states of CO₂ molecule in each irreducible representation of the Cs point group at the equilibrium geometry.

State	Excitation	ΔE_v (eV) ^a	ΔE_v (eV)
$1A'$		0.00	0.00
$2A', 1A''$	$9a' \rightarrow 10a', 2a'' \rightarrow 10a'$	9.16	8.89
$2A''$	$9a'(2a') \rightarrow 3a''(11a'')$	9.42	9.27
$3A', 3A''$	$9a'(2a'') \rightarrow 11a'(3a''), 9a'(2a'') \rightarrow 3a''(11a')$	9.54	9.39

^a Energies reported by Buenker [122].

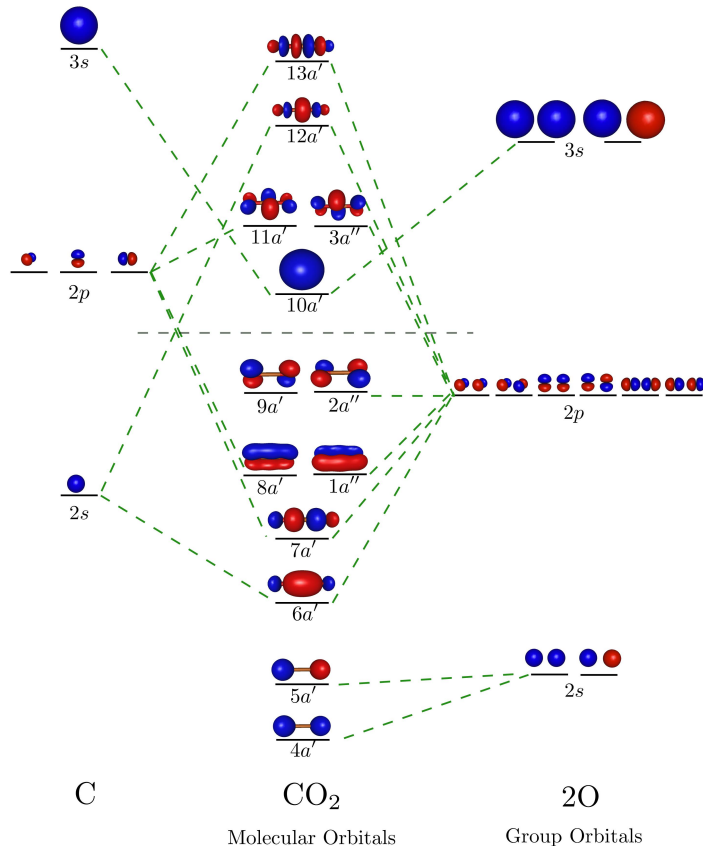


Figure 10.17: Molecular orbital diagram of CO₂ molecule. Orbitals plot below the grey line are doubly occupied by the 16 valence electrons in the ground state configuration.

Although the inclusion of the 3s (10a') Rydberg molecular orbital in the calculations does not mean that the first state in each irreducible representation is a Rydberg state, the orbital excitation to 10a' that leads to the electronic excited states $2^1A'$ and $1^1A''$ indicates the Rydberg nature of them. Hence, it is unusual or peculiar that the lowest excited states have these nature. The reason why this kind of orbital excitation to 10a' comes first can be explained following the construction of molecular orbitals in the CO₂ by the diagram in Fig. 10.17. The orbitals 11a' and 2a'' are formed by interaction of 2p_x orbitals of carbon and molecular oxygen, however, the interaction between the 3s orbitals of carbon and molecular oxygen form the 3s (10a') molecular orbital with a lower energy than the orbitals 11a' and 2a''. In addition, this implies that the Rydberg character of these states cannot be calculated using only an active space composed by valence orbitals, i. e., a full valence active space.

10.2.3 CO₂ RYDBERG STATES

After the analysis done for this six lowest states and the comparison with those performed by Lu et al. [110], it could be possible that Rydberg states be the rule instead of the exception, and more states with Rydberg character could exist between the $3^1A'$ and $4^1A'$ state in Fig. 10.14. Additionally, Buenker et al. [122] performed the calculations in the Franck-Condon region for the lowest 25 electronic states in the C_{2v} point group of symmetry, where a lot of Rydberg states are present between the $3^1A'$ and $4^1A''$ state, performing the transformation from C_{2v} to C_s. Hence, this work revisited the Franck-Condon region to compare calculations performed in previous works at the level of MRCI/MCSCF and calculations performed in this work with EOM-CCSD. Taking into account that EOM-CCSD theory does not have a limit of orbitals in contrast with MCSCF theory, calculations in the Franck-Condon region are performed with a good accuracy because at the equilibrium geometry the T₁ diagnostic is very low, ~ 0.0177 . The EOM-CCSD and MRCI/MCSCF calculations for the 14 lowest states in the C_s point group in each irreducible representation A' and A'' are performed with a basis set composed by the ANO-L basis set with additional diffuse functions of s, p and d type included at the C atom position with exponents 0.023, 0.021 and 0.015 [27], respectively. The state-averaged complete active space self-consistent field (MCSCF) calculations are performed with 12 electrons in 18 active orbitals and 10 electrons in five fully optimized closed-shell inner orbitals followed by MRCI calculations with 6 electrons in three fully optimized closed-shell inner orbitals with the same active space. Table 10.5 shows that EOM-CCSD calculations are comparable with the calculations performed by Buenker et al. [122] and the calculations performed at the MRCI/MCSCF level of theory. Given the computational difficulties associated to compute many excited states simultaneously with the MRCI/MCSCF and the large active space necessary to describe all these electronic excited states, the EOM-CCSD method is chose to perform the calculations in the FC region and below the ionization limit at 13.77 eV.

According to the main interest in this part of the work, the absorption spectrum of the CO₂ molecule, the EOM-CCSD calculations are performed in the C_{2v} point group of symmetry for the six lowest states of the 1^1A_1 and 1^1B_1 irreducible representations and for the ten lowest states in the 1^1A_2 and 1^1B_2 irreducible representations. Table 10.6 lists the values of the CO₂ absorption spectrum and the oscillator strengths for all calculated states, with the corresponding character of the excitation. As explained in the previous section, the lowest excited states are found to be the $9a'(2a'') \rightarrow 3s$ Rydberg state, with a vertical energy of 8.9495 eV. The latter is a valence state ($2^1A''$) resulting from a $2a''(9a') \rightarrow 11a'(3a'')$ excitation, i. e., the excited states go from Rydberg to valence states. The next lowest excited state ($4^1A'$) arises again from a Rydberg excitation, $9a' \rightarrow 3p_{\pi}$ with a transition energy of 11.12 eV. In contrast to the same state calculated by Lu et al. [110], this state has a transition energy of 13.28 eV at the equilibrium geometry (see intersection between light-grey vertical line and magenta dashed line in Fig. 10.14), which is an indication that there is a family of Rydberg states below the next valence state, which was not taken into account in this previous work [110]. Comparing Table 10.6 with Table II in [122], the 7th, 8th and 9th states of the 1^1A_2 and 1^1B_2 irreducible representations have lower energies than the 5th state of 1^1A_1 and 1^1B_1 irreducible representations. This is an indication that the work performed by Buenker et al. omits some states and it is not possible to find the valence state above the Rydberg family. This valence state

Table 10.5: Comparison between the vertical transitions energies to the lowest-lying excited states of CO₂ molecule. The reference energies -187.99496 a.u., -188.31694 a.u. and -188.33961 a.u. are taken from [122], MRCI/MCSCF and EOM-CCSD calculations. According to Fig. 10.15 the orbitals $\pi_g = 9a'$ or $2a''$ and $2\pi_u = 11a'$ or $3a''$.

Symmetry of states			Reference [122]	MRCI/MCSCF	EOM-CCSD
D _{∞h}	C _s	Character	ΔE (eV)	ΔE (eV)	ΔE (eV)
X ¹ Σ _g ⁺	1 ¹ A'	GS	0.00	0.00	0.00
1Π _g	2 ¹ A', 1 ¹ A''	(π_g , 3s)	9.16	8.98	8.95
1Σ _u ⁻	2 ¹ A''	(π_g , 2 π_u)	9.42	9.17	9.05
1Δ _u	3 ¹ A', 3 ¹ A''	(π_g , 2 π_u)	9.54	9.44	9.13
2 ¹ Δ _u	4 ¹ A', 4 ¹ A''	(π_g , 3p _π)	11.34	11.04	11.12
1Σ _u ⁺	5 ¹ A'	(π_g , 3p _π)	11.38	11.11	11.21
2 ¹ Σ _u ⁻	5 ¹ A''	(π_g , 3p _π)	11.40	11.13	11.26
1Π _u	6 ¹ A', 6 ¹ A''	(π_g , 3p _σ)	11.64	11.24	11.48
2 ¹ Π _g	7 ¹ A', 7 ¹ A''	(π_g , 3d _σ)	11.79	11.95	11.97

corresponds to 13¹A' or 9¹B₂ in the C_s and C_{2v} point group, respectively, and it corresponds to the 4¹A' state calculated by Lu et al. [110] and the 4¹A' state in Section 10.2.1.1, where the basis set used only describes valence states but it is not enough to model Rydberg states.

In order to perform a subsequent dynamics, the preliminary inspection of the non-vanishing values for the dipole or oscillator strengths indicates that only three Rydberg states (4¹A', 6¹A' and 6¹A'' in Table 10.6) may play a significant role in the photodynamics. To compute straightforwardly the lowest 13 states for each irreducible representation using MRCI/MCSCF for a large number of grid points of the PES is prohibitive now days. Then, the EOM-CCSD theory is chosen instead to perform the calculations of the potential energy surfaces of the thirteen lowest states in each irreducible representation with the ANO-L basis set and diffuse functions s, p and d explained above. The accuracy of this energy points is limited by the T₁ diagnostics and, consequently, there is a limited region in which EOM-CCSD results are validated (radial ranges R_i = [1.7, 2.8] a.u. and θ = [140°, 180°]). This region for the molecular geometry includes the FC region and it is enough for the time being to get an idea of the Rydberg and valence states to be incorporated in accurate multi-state quantum dynamics calculations of CO₂. Fig. 10.18 shows the thirteen lowest adiabatic and diabatic states in the 1A' symmetry. Thus, the minimum number of electronic states that have to be calculated, in each irreducible representation of the C_s point group, is thirteen because in the FC region is the next valence state with excitation character 9a'(2a'') → 11a'(3a'').

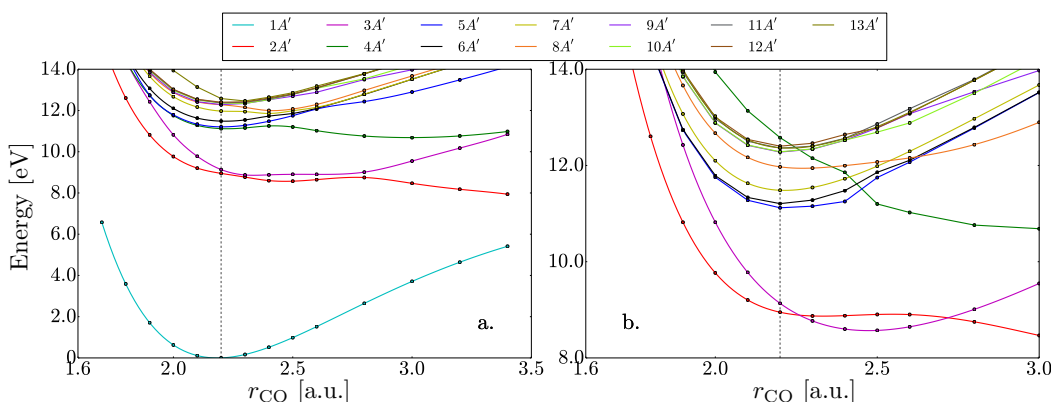


Figure 10.18: (a) Adiabatic (b) Diabatic states in the symmetry 1A' calculated at the EOM-CCSD level of theory.

Table 10.6: Vertical transitions energies and oscillator strengths (with reference to the ground state) for the lowest electronic states of CO_2 , considering both the point group C_s and C_{2v} . Dipole and oscillator strength are in atomic units.

C_s	C_{2v}	Excitation	ΔE (eV)	Dipole Strength	Oscillator Strength
$1^1\text{A}'$	1^1A_1	GS.	0.0	0.000000	0.000000
$2^1\text{A}',1^1\text{A}''$	$1^1\text{B}_{2u},1^1\text{A}_2$	$9\text{a}'(2\text{a}''),3\text{s}$	8.9495	0.000000	0.000000
$2^1\text{A}''$	2^1A_2	$2\text{a}''(9\text{a}'),11\text{a}'(3\text{a}'')$	9.0580	0.000000	0.000000
$3^1\text{A}',3^1\text{A}''$	$2^1\text{B}_{2u},3^1\text{A}_2$	$9\text{a}'(2\text{a}''),11\text{a}'(3\text{a}'')$	9.1338	0.000000	0.000000
$4^1\text{A}'$	3^1B_2	$9\text{a}',3\text{p}_\pi$	11.1203	0.641943	0.174893
$5^1\text{A}',4^1\text{A}''$	$4^1\text{B}_{2u},4^1\text{A}_2$	$9\text{a}'(2\text{a}''),3\text{p}_\pi$	11.2071	0.000000	0.000000
$5^1\text{A}''$	5^1A_2	$2\text{a}'',3\text{p}_\pi$	11.2593	0.000000	0.000000
$6^1\text{A}',6^1\text{A}''$	$2^1\text{A}_{1u},1^1\text{B}_1$	$9\text{a}'(2\text{a}''),3\text{p}_\sigma$	11.4844	0.125667	0.035358
$7^1\text{A}',7^1\text{A}''$	$5^1\text{B}_{2u},6^1\text{A}_2$	$9\text{a}'(2\text{a}''),3\text{d}_\sigma$	11.9712	0.000001	0.000000
$8^1\text{A}',8^1\text{A}''$	$6^1\text{B}_{2u},7^1\text{A}_2$	$9\text{a}'(2\text{a}''),3\text{d}_\delta$	12.2784	0.000000	0.000000
$9^1\text{A}',9^1\text{A}''$	$7^1\text{B}_{2u},8^1\text{A}_2$	$9\text{a}'(2\text{a}''),3\text{d}_\delta$	12.2846	0.000000	0.000000
$10^1\text{A}',10^1\text{A}''$	$3^1\text{A}_{1u},2^1\text{B}_1$	$9\text{a}'(2\text{a}''),3\text{d}_\pi$	12.3604	0.000000	0.000000
$11^1\text{A}',11^1\text{A}''$	$8^1\text{B}_{2u},9^1\text{A}_2$	$9\text{a}'(2\text{a}''),3\text{d}_\sigma$	12.3675	0.000000	0.000000
$12^1\text{A}''$	3^1B_1	$2\text{a}''',3\text{d}_\pi$	12.3777	0.000000	0.000000
$12^1\text{A}'$	4^1A_1	$9\text{a}',3\text{d}_\pi$	12.4013	0.000000	0.000000
$13^1\text{A}'$	9^1B_2	$9\text{a}'(2\text{a}''),11\text{a}'(3\text{a}'')$	12.5780	1.977312	0.609319
$13^1\text{A}''$	4^1B_1	$8\text{a}'(1\text{a}''),3\text{a}''(11\text{a}')$	13.0898	0.000037	0.000012
$14^1\text{A}',14^1\text{A}''$	$5^1\text{A}_{1u},5^1\text{B}_1$	$8\text{a}'(1\text{a}''),11\text{a}'(3\text{a}'')$	13.3318	0.000631	0.000206

Based on the results of electronic structure calculations, an accurate multidimensional multi-state dynamics calculation is not possible because of the high complexity and huge computational requirements necessary to compute all multidimensional PES involved in the dynamics. As an alternative, the present work focuses in a 1D dynamic study to be compared with the possible dynamics described in [110], and, in particular, what are the effect to excite only one degree of freedom and the differences avoiding the Rydberg states above 10 eV.

10.2.4 1D PHOTODYNAMICS IN THE LOWEST STATES OF THE SYMMETRY $1^1\text{A}'$ AND $1^1\text{A}''$.

A full 3D dynamics considering the internal degrees of freedom R_1 , R_2 and θ is quite complicate since a diabatization procedure of the conical intersections is formally and numerically necessary. Then, as a first step, 1D dynamics of the CO_2 molecule along the CO bond distance r_{CO} is performed. It implies a 1D diabatization procedure for the states involved. Fig. 10.19 shows the diabatic states for the symmetries $1^1\text{A}'$ and $1^1\text{A}''$, respectively. There are three sites where these states should be diabatized, two of these sites are avoided crossings between the states $2^1\text{A}'$ and $3^1\text{A}'$ around $R_1 = 2.4$ a.u. and $R_1 = 2.8$ a.u., respectively, and the avoided crossing between the states $3^1\text{A}'$ and $4^1\text{A}'$ around $r_{\text{CO}} = 3.6$ a.u. In the case of the $1^1\text{A}''$ states, there are two anticrossings between the states $1^1\text{A}''$ and $3^1\text{A}''$ around $r_{\text{CO}} = 2.4$ and $r_{\text{CO}} = 2.8$ a.u., respectively. Note that the pair $2^1\text{A}'-3^1\text{A}'$ is almost energetically degenerated with the pair $1^1\text{A}''-2^1\text{A}''$. The corresponding orbital excitation for each state is examined in order to determine the distance along the r_{CO} axis where the states show a change of character, just by looking at the natural orbitals of each state. Non-adiabatic radial couplings along the r_{CO}

distance are computed using the MOLPRO package [130], with special emphasis in the region of avoided crossings.

Once the adiabatic and diabatic representations for energies and/or surfaces and non-adiabatic couplings are obtained, a transformation angle $\Theta(r_{\text{CO}})$ is used to get the off-diagonal electrostatic couplings between the new diabatic states, following the methodology described in Section 5.2, since they are now the responsible for the non-radiative transitions among states of the same symmetry. After this multistate diabatization, the photodynamics simulations are performed using MCTDH methodology. Additionally, the transition dipole moments between all dipole-active states ${}^1\text{A}'$ and ${}^1\text{A}''$ are calculated only at the MCSCF level, along with the MRCI energies using the MOLPRO package.

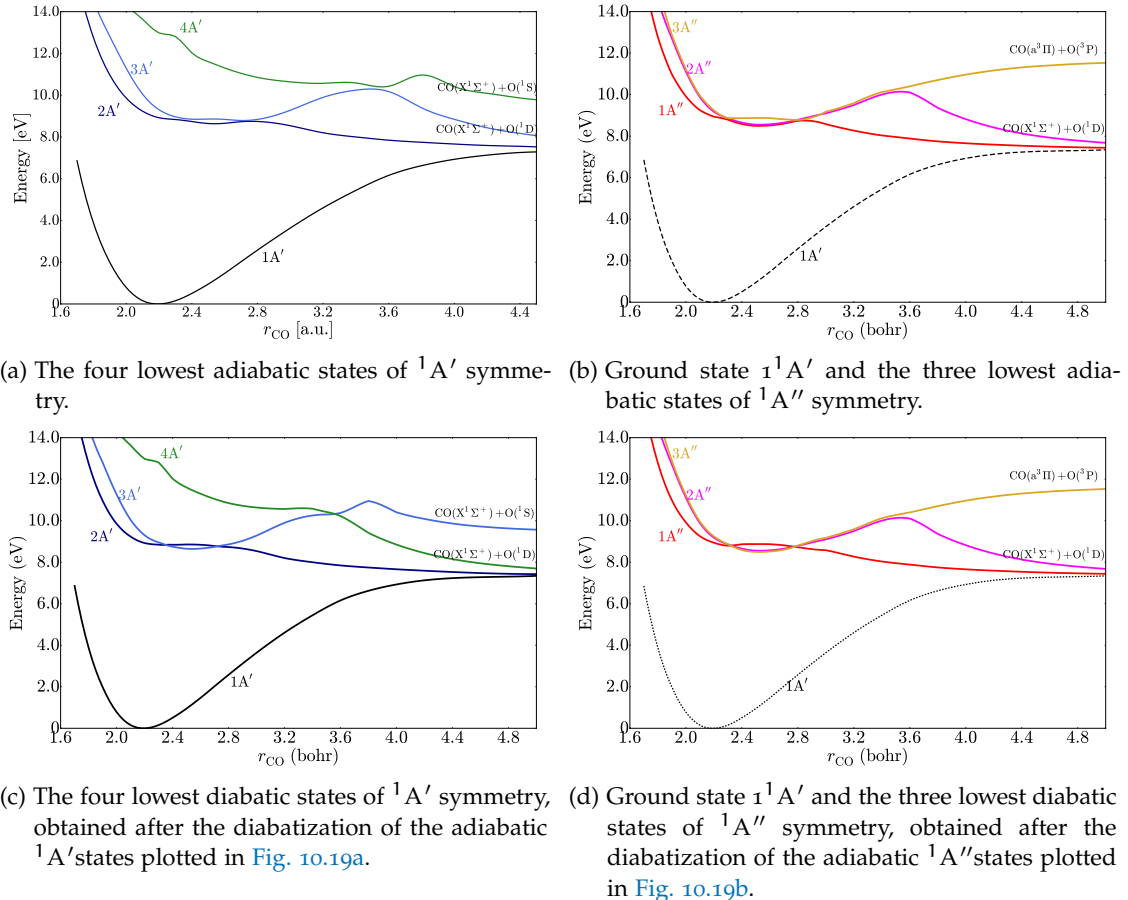


Figure 10.19: Adiabatic and diabatic electronic states of the six lowest states in the CO₂ molecule.

In order to give a broad study in the 1D-diabatic dynamics, the following series of calculations have been performed and explained below:

1. Non-adiabatic dynamics after a sudden excitation ${}^1\text{A}' \rightarrow {}^4\text{A}'$ states in the Franck-Condon region, i.e., the $v'' = 0$ vibrational state of ${}^1\text{A}'$ is the starting wave packet in the Frank-Condon region of the ${}^4\text{A}'$ state.
2. Full photodynamics using a XUV short-laser pulse to simulate all excitations from the ground state ${}^1\text{A}' \rightarrow {}^n\text{A}'$ ($n = 2, 3$, and 4) and ${}^1\text{A}' \rightarrow {}^n\text{A}''$ ($n = 2$ and 3), taking into account that (according to C_s point group symmetry) the excitations ${}^1\text{A}' \rightarrow {}^1\text{A}'$ are possible for laser polarizations along the y and z -axis and the excitations ${}^1\text{A}' \rightarrow {}^1\text{A}''$ are only possible for laser polarization along the x -axis. The CO₂ molecule is calculated with MOLPRO package with the CO₂ molecular axis (slightly bended for the C_s symmetry) located along the x coordinate axis. Dipole transition matrix elements along \hat{x} , \hat{y} and \hat{z} are obtained using MOLPRO with wave functions computed at a MCSCF level (since they are much smoother than with MRCI). Simulations are computed for each laser polarization

separately. Eventually the results can be combined to obtain the average for non-oriented OCO molecules in gas phase.

10.2.4.1 NON-ADIABATIC DYNAMICS AFTER A SUDDEN EXCITATION INTO THE $4^1A'$ STATE

The vibrational ground state $v'' = 0$ of the $1^1A'$ state is the wave packet that initiates in the $4^1A'$ state, assuming a sudden FC excitation. This approximation oversimplifies the dynamics since it means that only one state, $4^1A'$, is populated after prompt photo-absorption and the ensuing dissociation process within the $1^1A'$ symmetry is reduced to two competing paths after passing through the crossing between the $4^1A'$ and $3^1A'$ states at $r_{CO} \sim 3.6$ a.u.

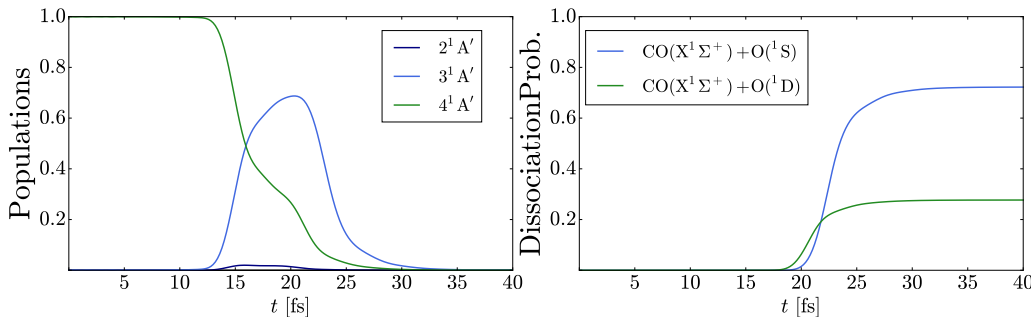


Figure 10.20: (Left panel) Time dependent populations for the initial $4^1A'$ and the coupled $3^1A'$ states. The initial wave packet located at the Frank-Condon region of the $4^1A'$ state reaches the avoided crossing at $R_1=3.6$ a.u. at $t \sim 12.4$ fs., from here onwards it splits into two wave packets that reach the absorbing layer located at $R_1 = 4.6$ a.u. at $t \sim 19.5$ fs (where the dissociation flux is computed for each dissociation channel). The total probability is unity, until the splitted wavepackets reach the CAP boundary where the dissociation flux is evaluated. (Right Panel) Dissociation probability into the channels $CO(X^1\Sigma^+) + O(^1D)$ (from the $4^1A'$ state) and $CO(X^1\Sigma^+) + O(^1S)$ (from the $3^1A'$ state as populated) after sudden excitation to the dissociative $4^1A'$ state. In this case, the total dissociation probability is also unity.

Fig. 10.20 shows the non-adiabatic dissociation probability of CO_2 into the two available channels, through the paths $4^1A' \rightarrow CO(X^1\Sigma^+) + O(^1D)$ and $4^1A' \rightarrow 3A' \rightarrow CO(X^1\Sigma^+) + O(^1S)$. The channel that clearly dominates is $CO(X^1\Sigma^+) + O(^1S)$ (ratio 0.72:0.28), produced by fast diabatic passage between $4^1A'$ and $3^1A'$ diabatic states (see Fig. 10.19). It is worth noting that a sudden excitation within the Franck-Condon region necessarily implies a laser excitation energy around 12.95 eV, which is above the radiation energy range used in [110] (11.95 - 12.22 eV). In fact, MCTDH indicates that the initial average vibronic energy of the wave packet is 13.12 eV.

10.2.4.2 FULL DIABATIC PHOTODYNAMICS AFTER EXCITATION WITH A XUV LASER PULSE.

To make the simulation more realistic, now a multistate diabatic photodynamics calculation with MCTDH is performed. In order to assess the behavior of the system under different parameters of a laser pulse: central frequency of excitation, duration, intensity and polarization, a laser pulse expression has been included in the MCTDH methodology in the form

$$E(t) = \hat{e}_p E_0 f(t) \sin(\omega t + \varphi); \quad f(t) = \sin^2\left(\frac{\pi t}{T}\right) \quad \text{with } t \in [0, T]$$

where \hat{e}_p is the polarization unit vector, E_0 is the pulse amplitude, ω is the central frequency, φ the phase and $f(t)$ is the pulse shape, chosen as a \sin^2 type with a pulse duration T , as it was explained in Chapter 6.

Three different central frequencies are used for the laser pulse in the calculations, 8, 10 and 12 eV. These values are chosen because 8 eV is below the energy levels of 2, 3 and 4¹A' states, and below the 1 and 2¹A'' states in the Frank-Condon region. 10 eV is above the intermediate levels but below the 4¹A' state and 12 eV already reaches the 4¹A' state. Similarly, three different pulse durations are implemented, namely, 3, 10 and 20 fs. In the first case, $t_p = 3$ fs, the radiation pulse is short enough to avoid much interference with the subsequent field-free non-adiabatic dynamics. In the second case, $T = 10$ fs, the excited states are still pumped by the laser while passing through the crossings located around $R_1 = 2.4$ and $R_1 = 2.8$ a.u. (in the Frank-Condon region). In the third case, for a longer pulse of $T = 20$ fs the wave packet that reaches the crossing at $R_1 = 3.6$ a.u. arrives barely dressed by the field. Also the number of vibrational or continuum states simultaneously populated by the laser pulse vary according to the spectral energy width of the pulse (FWHM is $\Delta\omega \sim 4\pi/T$). Short pulses have a large spectral width, which means that the 4¹A' state may be eventually populated even with a large detuning when using $T = 3$ fs (it is populated even when using 8 eV as a central frequency). Longer pulses act as a energy filtering for excitation and the resulting dynamics is closer to the case of a cw laser. In the case of the intensity, three laser intensities are used, $I = 8.77 \times 10^{13}$ W/cm² ($E_0 = 0.05$ a.u.), $I = 3.5095 \times 10^{14}$ W/cm² ($E_0 = 0.1$ a.u.) and $I = 1.4038 \times 10^{15}$ W/cm² ($E_0 = 0.2$ a.u.). Higher intensities not only enhance the excitation population and dissociation probabilities. It is also the responsible for surprising staircase quantum Rabi oscillations involving the vibrational excited states of the ground electronic state 1¹A' and vibrational or continuum states in the excited electronic states. This staircase excitation within the ground state due to Rabi oscillations eventually increases the final average excitation energy over that due to the central frequency taken from the $\nu = 0$ of 1¹A' only. Finally, two polarizations \hat{e}_p of the laser pulse are implemented. As mentioned before, according to selection rules dipole transitions 1¹A' \rightarrow 1¹A' are possible for laser polarizations along the y and z-axis and transitions 1¹A' \rightarrow 1¹A'' are only possible for laser polarization along the x-axis, which is the direction of the OCO internuclear axis. The dipole matrix elements for \hat{x} , \hat{y} and \hat{z} directions have been calculated with MOLPRO with special attention to the Franck-Condon region. In our **MCTDH** simulations, each polarization or orientation is computed separately.

At variance with the previous section without pumping laser (Frank-Condon approximation), the oscillator strengths for the different dipole transitions play a role in the relative populations of electronic excited states after prompt laser excitation and, in addition, the Frank-Condon approximation is not used, i.e., the electronic dipolar matrix elements are R_1 -integrated with the components of the nuclear wave packet. This will give the correct excitation branching ratios into the different excited states (both for 1¹A' and 1¹A'' manifolds) for the whole nuclear wave packet, that subsequently dissociates simultaneously (in principle with different velocities along each potential energy curve) along different paths.

Fig. 10.21 shows the time-dependent populations for all states (1-4¹A' and 1-3¹A'') involved in the photodynamics for a pulse time duration $T = 3$ fs. For $\omega = 8$ eV the excitation is dominated by the 2¹A' state in the \hat{y} polarization direction and the 1¹A'' in the \hat{x} direction. During dissociation the 1¹A'' transfers population to the 3¹A'' via electrostatic (non-adiabatic) couplings (the latter state remains with a constant population as a vibrating wave packet in the potential energy curve but not contributing to dissociation). Surprisingly the 4¹A' is populated by the 10 eV pulse at high detuning. Fig. 10.22 shows the dissociation probabilities (computed with the flux crossing a boundary layer located at 6.7 a.u.). The depletion of populations in Fig. 10.21 at $t = 30$ fs corresponds to the simultaneous onset in the dissociation probabilities of Fig. 10.22.

For $\omega = 10$ eV the dominating direct excitation is to 3¹A' but electrostatic (non-adiabatic) couplings to 2¹A' are not so efficient and most population remains bound without contribution to dissociation. It is more evident that the 1¹A'' state transfers population to the 3¹A'' via electrostatic (non-adiabatic) couplings. The only contribution to dissociation in the \hat{z} polarization direction is due to the small population of the 4¹A'.

For $\omega = 12$ eV the excitations in \hat{x} and \hat{y} directions are quenched and the contribution comes exclusively from the \hat{z} polarization. States 3-4¹A' are populated directly from the 3 fs pulse. However, the main population feeding to 3¹A' comes from the electrostatic (non-adiabatic) transfer 4¹A' \rightarrow 3¹A' around $r_{CO} \sim 3.6$ a.u., which happens to occur at a time $t \sim 15$ fs (see

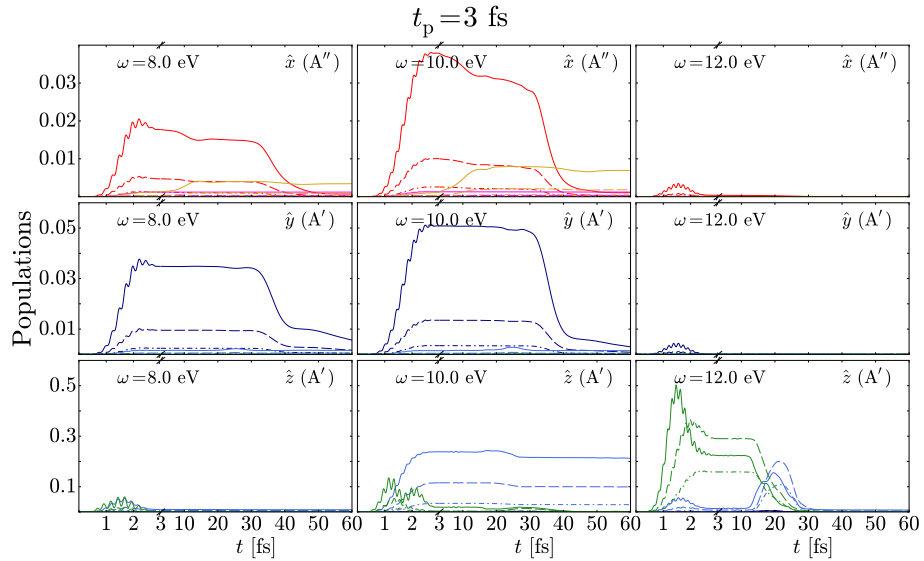


Figure 10.21: Time dependent populations of ${}^1\text{A}'$ and ${}^1\text{A}''$ excited states after XUV excitation from the ${}^1\text{A}'$ with a laser pulse of duration $T = 3$ fs, using three central photon energies of 8, 10 and 12 eV (from left to right) and three laser intensities for amplitudes $E_0 = 0.05$ (dashed-dotted lines), $E_0 = 0.1$ (dashed lines) and $E_0 = 0.2$ (solid lines). The color scheme for the lines is the same used to distinguish the states in Fig. 10.19. The direction of the laser polarization vector along with the symmetry excited in the C_s point group are indicated in each figure.

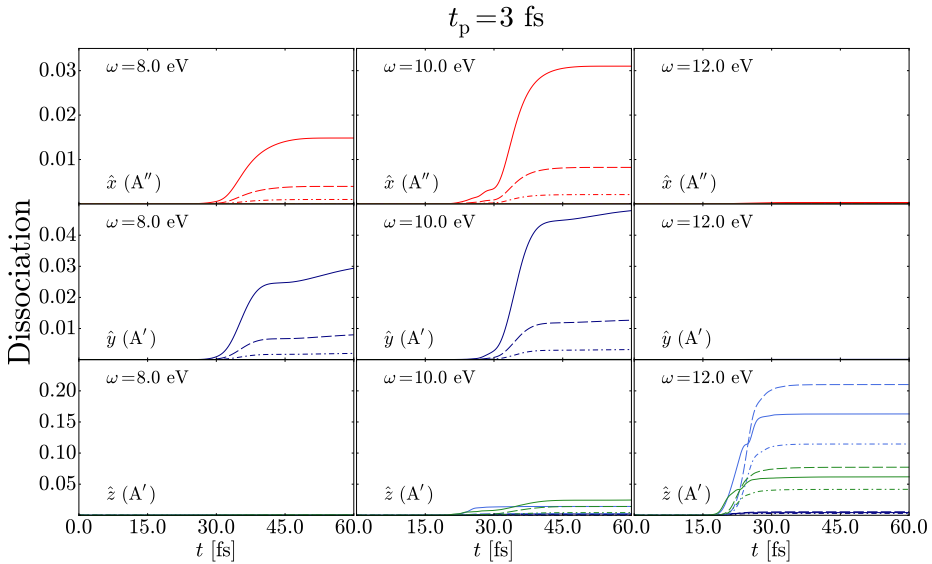


Figure 10.22: Photodissociation probability of ${}^1\text{A}'$ and ${}^1\text{A}''$ excited states after XUV excitation from the ${}^1\text{A}'$ with a laser pulse of duration $T = 3$ fs, using three central photon energies of 8, 10 and 12 eV (from left to right) and three laser intensities for amplitudes $E_0 = 0.05$ (dashed-dotted lines), $E_0 = 0.1$ (dashed lines) and $E_0 = 0.2$ (solid lines). The color scheme for the lines is the same used to distinguish the states in Fig. 10.19. The direction of the laser polarization vector along with the symmetry excited in the C_s point group are indicated in each figure. The dissociation channel for each state is indicated in Fig. 10.19.

Fig. 10.21). Although in the this case, the chosen central frequency is 12 eV, the FWHM in the energy spectrum ($\Delta\omega = 2.76$ eV) of the short XUV pulse with a duration 3 fs is wide enough to allow for the population of the ${}^1\text{A}'$ at the edge of the Franck-Condon region.

Now, a longer duration of $T = 10$ fs for the laser pulse is implemented (see Fig. 10.23 for time-dependent populations and Fig. 10.24 for the dissociation probabilities). The pulse duration

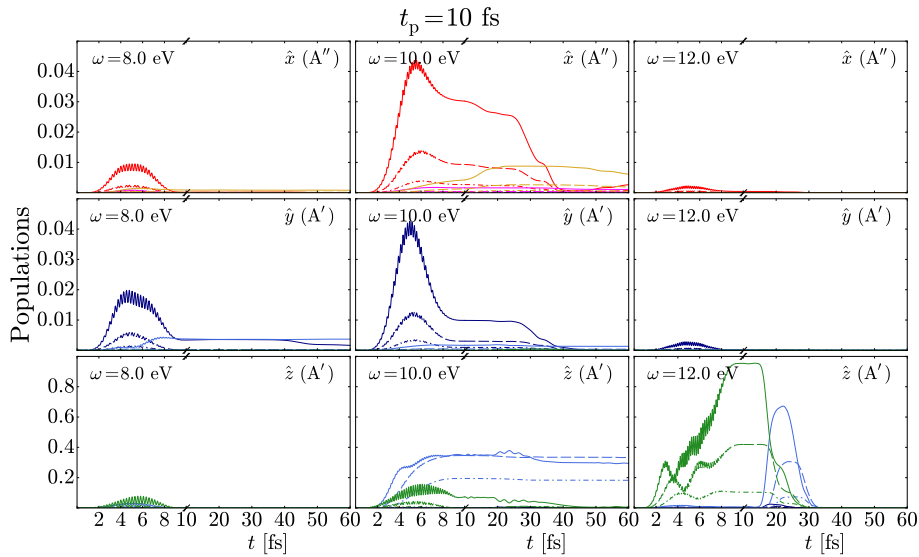


Figure 10.23: Time dependent populations of ${}^1\text{A}'$ and ${}^1\text{A}''$ excited states after XUV excitation from the ${}^1\text{A}'$ with a laser pulse of duration $T = 10$ fs, using three central photon energies of 8, 10 and 12 eV (from left to right) and three laser intensities for amplitudes $E_0 = 0.05$ (dashed-dotted lines), $E_0 = 0.1$ (dashed lines) and $E_0 = 0.2$ (solid lines). The color scheme for the lines is the same used to distinguish the states in Fig. 10.19. The direction of the laser polarization vector along with the symmetry excited in the C_s point group are indicated in each figure.

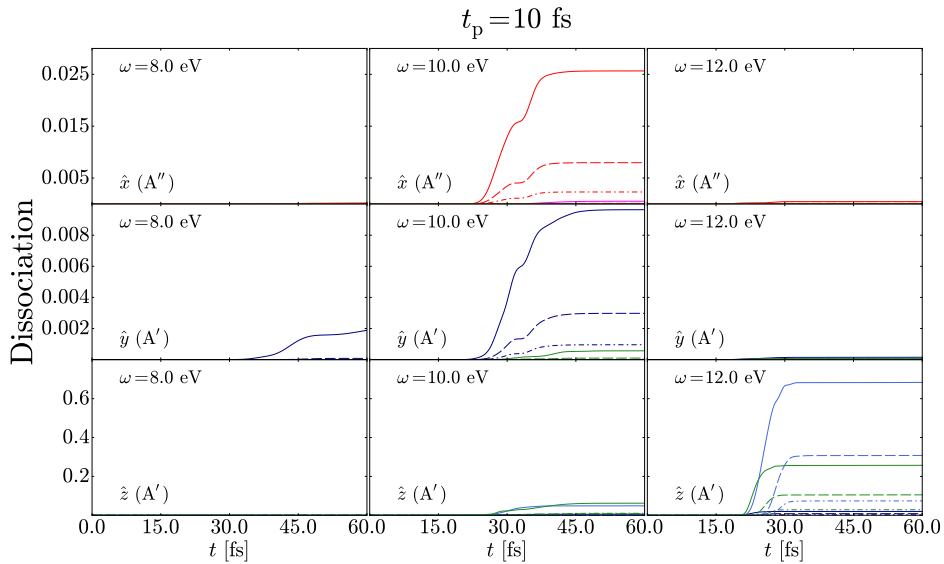


Figure 10.24: Photodissociation probability of ${}^1\text{A}'$ and ${}^1\text{A}''$ excited states after XUV excitation from the ${}^1\text{A}'$ with a laser pulse of duration $T = 10$ fs, using three central photon energies of 8, 10 and 12 eV (from left to right) and three laser intensities for amplitudes $E_0 = 0.05$ (dashed-dotted lines), $E_0 = 0.1$ (dashed lines) and $E_0 = 0.2$ (solid lines). The color scheme for the lines is the same used to distinguish the states in Fig. 10.19. The direction of the laser polarization vector along with the symmetry excited in the C_s point group are indicated in each figure. The dissociation channel for each state is indicated in Fig. 10.19.

brings the effect of the pulse area and some absorptions are fully reversed. It is the case of \hat{x} (${}^1\text{A}''$) and \hat{y} (${}^1\text{A}'$). As a result, the contribution to dissociation from the ${}^2\text{A}'$ with $\omega = 8$ eV is reduced in comparison with the 3 fs pulse. Also, the ${}^3\text{A}'$ state is more efficiently populated by the pulse but it remains vibrationally bound. The scenario for $\omega = 10$ eV and $T = 10$ fs, is similar to the shorter pulse $T = 3$ fs, although dissociation probabilities fall down because of the effect of the pulse area. And for $\omega = 12$ eV the pulse length dramatically reinforces the

population to $4^1\text{A}'$ which eventually transfers most of its population to the $3^1\text{A}'$ state, and both of them lead to a larger dissociation probability.

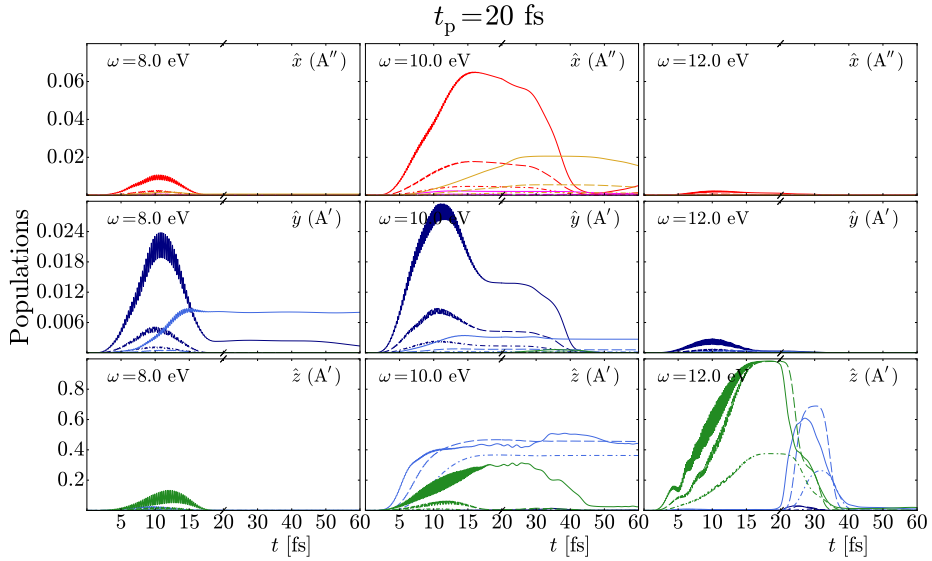


Figure 10.25: Time dependent populations of $1^1\text{A}'$ and $1^1\text{A}''$ excited states after XUV excitation from the $1^1\text{A}'$ with a laser pulse of duration $T = 20$ fs, using three central photon energies of 8, 10 and 12 eV (from left to right) and three laser intensities for amplitudes $E_0 = 0.05$ (dashed-dotted lines), $E_0 = 0.1$ (dashed lines) and $E_0 = 0.2$ (solid lines). The color scheme for the lines is the same used to distinguish the states in Fig. 10.19. The direction of the laser polarization vector along with the symmetry excited in the C_s point group are indicated in each figure.

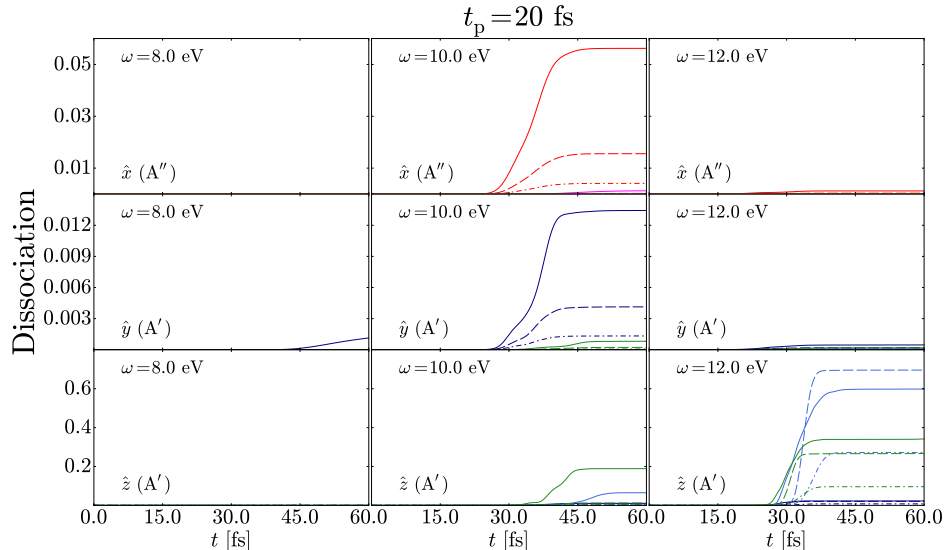


Figure 10.26: Photodissociation probability of $1^1\text{A}'$ and $1^1\text{A}''$ excited states after XUV excitation from the $1^1\text{A}'$ with a laser pulse of duration $T = 20$ fs, using three central photon energies of 8, 10 and 12 eV (from left to right) and three laser intensities for amplitudes $E_0 = 0.05$ (dashed-dotted lines), $E_0 = 0.1$ (dashed lines) and $E_0 = 0.2$ (solid lines). The color scheme for the lines is the same used to distinguish the states in Fig. 10.19. The direction of the laser polarization vector along with the symmetry excited in the C_s point group are indicated in each figure. The dissociation channel for each state is indicated in Fig. 10.19.

The next selected pulse duration is $T = 20$ fs (see Figs. 10.25 and 10.26 for time-dependent populations and for the dissociation probabilities, respectively). This simulation must show the trend for long pulses and cw radiation. At low photon energies (8 eV) both $2^1\text{A}'$ and

$3^1A'$ states are populated by the radiation. The small photodissociation contribution comes from the $2^1A'$ state in the \hat{y} polarization. The $3^1A'$ state remains vibrationally bound in the time window of the simulation up to 120 fs. By far, the main contribution to dissociation comes from the population of the $4^1A'$ state both at 10 and 12 eV for the \hat{z} polarization direction. At $\omega = 10$ eV both 3 and $4^1A'$ states are excited by the laser, most of the $3^1A'$ state remains vibrationally bound but it partially dissociates. The state $4^1A'$ later transfers part of its population to the $3^1A'$. At 12 eV, with long pulses and high intensities the excitation population to $4^1A'$ saturates to unity after the laser pulse, which produces an scenario analogous to the sudden approximation calculation in [Section 10.2.4.1](#), where, without simulated radiation, the initial population of the $4^1A'$ is set to unity. The branching ratio of dissociation between the two channels [O(¹S):O(¹D)] depends on laser intensity but approximately one obtains (0.7:0.3) for $E_0 = 0.1$, a similar ratio obtained for the sudden approximation and in the experiments performed by Lu et al. [\[110\]](#).

It is the great beauty of our science, chemistry, that advancement in it, whether in a degree great or small, instead of exhausting the subjects of research, opens the doors to further and more abundant knowledge, overflowing with beauty and utility.

— Michael Faraday

11

TETRATOMIC MOLECULES

In the case of tetratomic molecules the **MCTDH** is implemented to carry out multistate diabatic dynamics in the methyl radical CH_3 to study the dynamics along more than one conical intersection within the manifold of the six lowest states of symmetry A' (also under the point group Cs). A deeper understanding of these cases will pave the way to embark on the analysis of the multistate non-adiabatic or diabatic photodynamics in these same molecules or in more complex molecules, using the powerful **MCTDH** approach, for which some applications in laser pulse-molecule interactions are already implemented but still scarce.

Similarly to previous cases, diatomic and triatomic molecules, the first step to any dynamical calculation is to generate the multidimensional potential energy surfaces, dipolar couplings and **NAC** with a high degree of accuracy (at the level of **MRCI/MCSCF**). Progress about the multidimensional **PES** and 1D and 2D multi-state dynamics in the CH_3 molecule is presented in this chapter.

11.1 CH_3 (METHYL RADICAL)

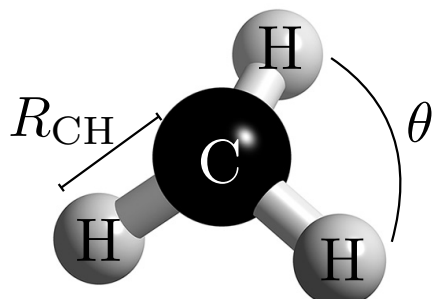


Figure 11.1: Schematic representation of CH_3 and the internal coordinates used in the calculations.

11.1.1 ELECTRONIC STRUCTURE

The absorption spectrum and electronic structure of methyl radical molecule has been previously studied both experimentally and theoretically [131, 132], in order to describe the photodissociation of one of its hydrogens by the chemical reaction $\text{CH}_3 + \hbar\omega \rightarrow \text{CH}_2 + \text{H}$ from the $3s$ and $3p_z$ Rydberg states. Following these previous calculations for the C-H bond distance, the electronic structure in terms of the two internal coordinates (CH bond distance R_{CH} and HCH bending angle θ) described in Fig. 11.1 is performed in order to give an idea of the photodissociation mechanisms from the two Rydberg states and to rationalize the experimental results, and to proceed with multidimensional multi-state dynamics calculations.

In the ground electronic state, the methyl radical is a planar molecule that belongs to the D_{3h} point group of symmetry. Since D_{3h} is not an Abelian group, all *ab initio* calculations are

performed using the C_s group representation (no assumed symmetry but the identity and a mirror plane), which is valid as long as the molecule remains in a planar configuration. In order to calculate the 2D PES of CH_3 radical along the C-H bond distance and the angle $\theta \in [108^\circ, 128^\circ]$, MCSCF calculations followed by the MRCI calculations for each geometry are performed. In all geometries, the augmented correlation-consistent polarized basis set (aug-cc-pVTZ) is employed. The orbitals included in the active space are $(2-10)a'$ and $(1-3)a''$, while the $1a'$ molecular orbital (associated with the $1s$ of the carbon atom) remains doubly occupied in all configurations. Calculations were restricted to the lowest seven states of irreducible representation $^1\text{A}'$ in C_s symmetry. The PEC against the CH bond distance (with a frozen angle $\theta = 119.99^\circ$ obtained from a previous geometry optimization) are shown in Fig. 11.2 with their respective dissociation channels. Additionally, 2D calculations in terms of the internal coordinates R_{CH} and θ are performed in order to study the energy variation of the dissociation channels, according to the difference in the bending angle θ between the initial molecule methyl (CH_3 , $\theta = 120^\circ$) and the final product methylene (CH_2 , $\theta = 135^\circ$).

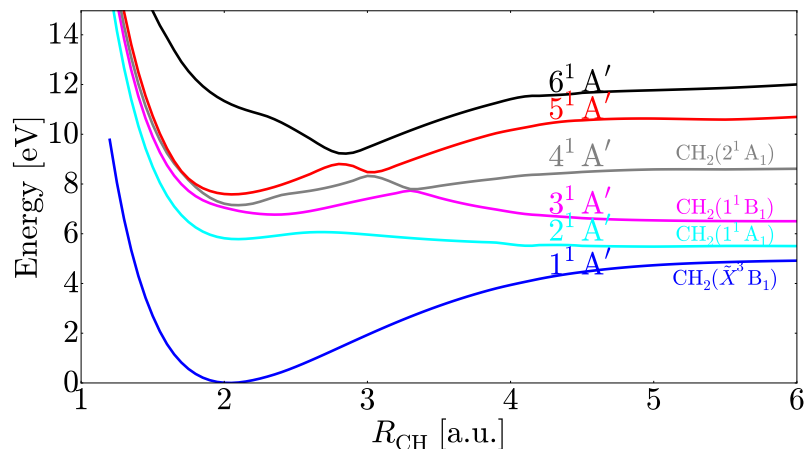


Figure 11.2: 1D PEC against the CH radial distance of the lowest six adiabatic states of symmetry $1\text{A}'$ of the methyl molecule CH_3 .

Note that up to seven avoided crossings among 1D PEC are visible in Fig. 11.2. It makes necessary to study the NAC and the behaviour of WF around the avoided crossings. These a priori visualized anticrossings are again shown and labelled in Fig. 11.3. However, by looking at the calculated NAC among states involved in the labelled crossing we realize that the apparent 3rd crossing between the $4^1\text{A}'$ and $5^1\text{A}'$ adiabatic states is not due to a NAC. Thus the avoided crossings are reduced to six and shown in Fig. 11.4.

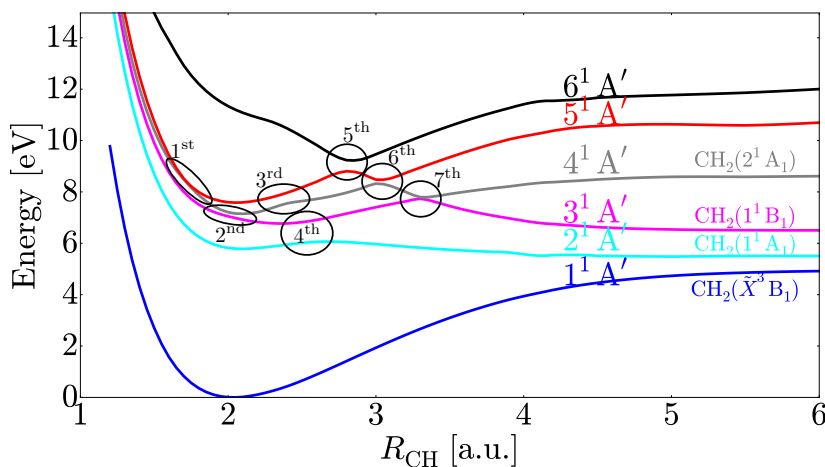


Figure 11.3: 1D PEC against the CH radial distance of the lowest six adiabatic states of symmetry $1\text{A}'$ of the methyl molecule CH_3 with their corresponding 'avoided crossings'.

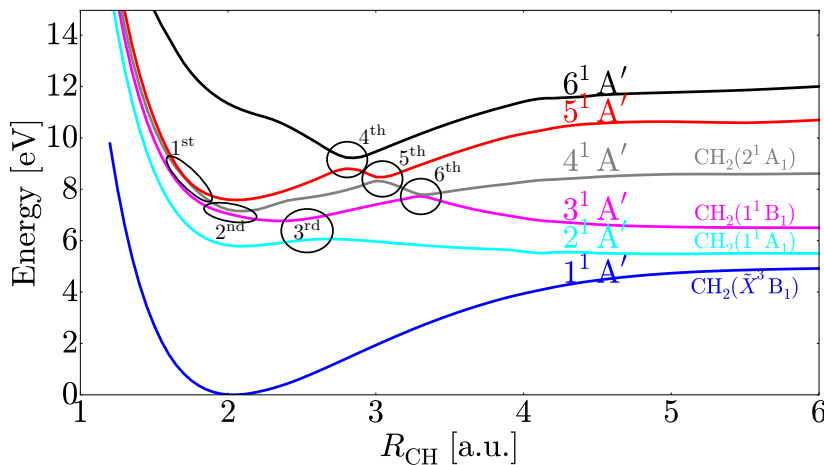


Figure 11.4: 1D PEC against the CH radial distance of the lowest six adiabatic states of symmetry $1A'$ of the methyl molecule CH_3 with their corresponding real avoided crossings.

11.1.2 DIABATIZATION METHOD

Since the number of avoided crossing among the six lowest electronic states of methyl are reduced to six, and quite close to each other, one can choose between two types of calculations *i*) a calculation of photodynamics using the adiabatic PEC and their NAC, or *ii*) to perform a simultaneous diabatization for all states. In this work, the second way is chosen and the diabatization of this multicrossing system is performed using the arctangent function explained in Section 5.2. A diabatization in the six avoided crossings will allow to transform the NAC into smooth electrostatic couplings and the adiabatic PEC into diabatic ones that effectively show a crossing.

A nuclear box with 97 grid points for the nuclear coordinate $R_{CH} \in [1.2, 6]$ a.u. is used for all calculations presented in this section. It is important to note that the diabatization procedure is not unique and different forms of the PEC and electrostatic couplings can arise from each diabatization procedure, although they usually yield similar results. In order to diabatize the set of six states involve in a subsequent dynamics, Eq. (5.22) is employed in each avoided crossing. Since the energy difference of each avoided crossing is different, the α and R_{CI} values taken for the six avoided crossings in Fig. 11.4 are given in Table 11.1. With these latter parameters, the procedure to diabatize the six adiabatic electronic states in the $1A'$ symmetry consists in the following. From the adiabatic PEC, from left to right, the six adiabatic PEC are diabatized sequentially using a 2×2 diabatization model mentioned above. This makes that each crossing is diabatized taking into account the previous diabatization done to the left. By using this procedure, the new electrostatic couplings between crossing states in the diabatic representation are calculated through Eq. (5.20) and plotted in Fig. 11.5.

Fig. 11.6 shows, step by step, the diabatization procedure for the six lowest $1A'$ adiabatic states. It is possible to observe, e.g., in the fifth and sixth step, that previous diabatizations have an influence in the results of the subsequent diabatization, specially when two or more avoided crossing are very close. This influence makes reference to the smoothness of the resulting diabatic PEC, as observed for example along the triple crossing of the $6^1 A'$ adiabatic state (see black line in Fig. 11.7).

Since the bending angle θ is different in methyl and methylene, the 2D diabatization is performed along the bond coordinate R_{CH} as the 1D case for each bending angle θ , taking into account that there is no conical intersection along the bending angle. Fig. 11.8 shows the highest electronic diabatic states from the $1A'$ manifold in a 3D plot. From this picture it is possible to conclude that the change of energy along the the variation of the bending angle is rather small, which means that the essential dynamics in photodissociation could be reduced to a 1D model along the radial coordinate.

Table 11.1: Parameters for the six avoided crossing in the six lowest electronic states in the ${}^1A'$ symmetry for CH_3 molecule. R_{CI} corresponds to the avoided crossing position where the energy difference ΔV between the electronic states is minimum along the R_{CH} bond coordinate and α is the parameter to employ Eq. (5.22). All quantities are in atomic units (a.u.).

Avoided Crossing	R_{CI}	ΔV	α
1	1.70	0.00134395	14.98833285
2	2.00	0.00588819	13.82717836
3	2.50	0.02980486	7.71593715
4	2.85	0.01536879	11.40467522
5	3.05	0.00743563	13.43177396
6	3.30	0.00361696	14.40752770

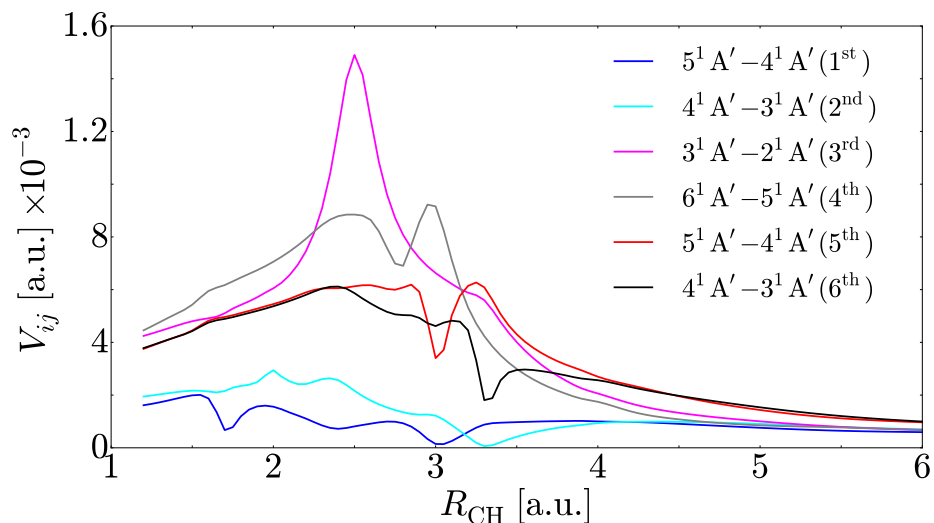


Figure 11.5: Electrostatic couplings obtained after diabatization between different ${}^1A'$ diabatic states of the methyl molecule along the CH bond coordinate.

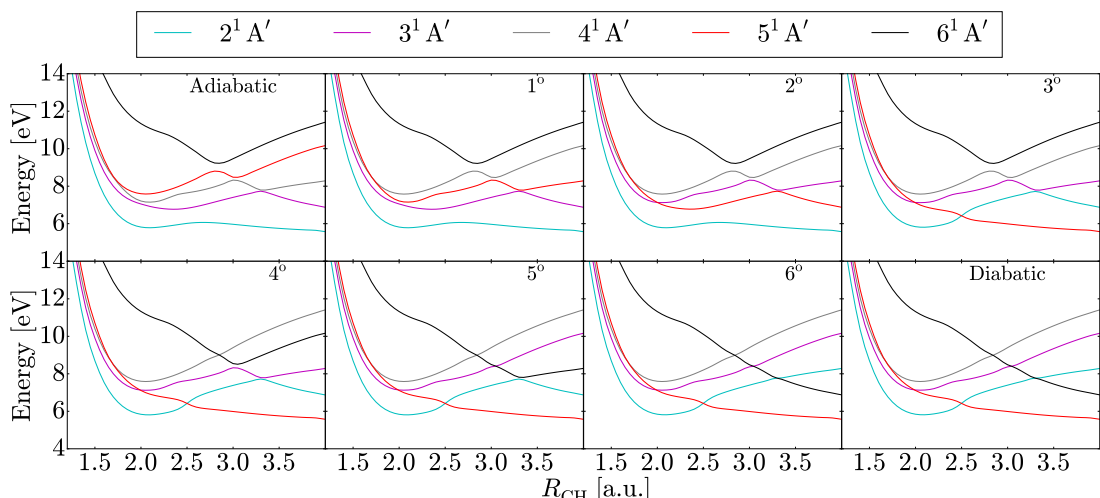


Figure 11.6: Step by step diabatization procedure of the six lowest ${}^1A'$ adiabatic states of CH_3 molecule.

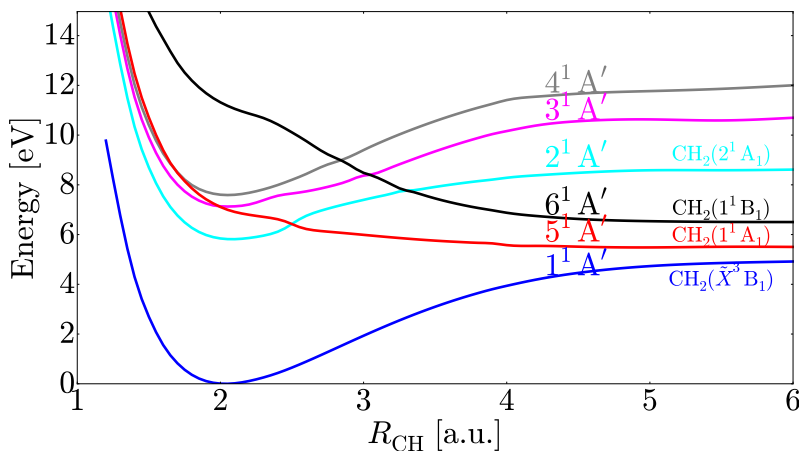


Figure 11.7: Resulting 1D six lowest diabatic states in the symmetry $^1A'$ of CH₃ molecule in terms of the C-H bond distance. Notation is the same that in the adiabatic PEC to simply the explanations between diabatic and adiabatic PEC.

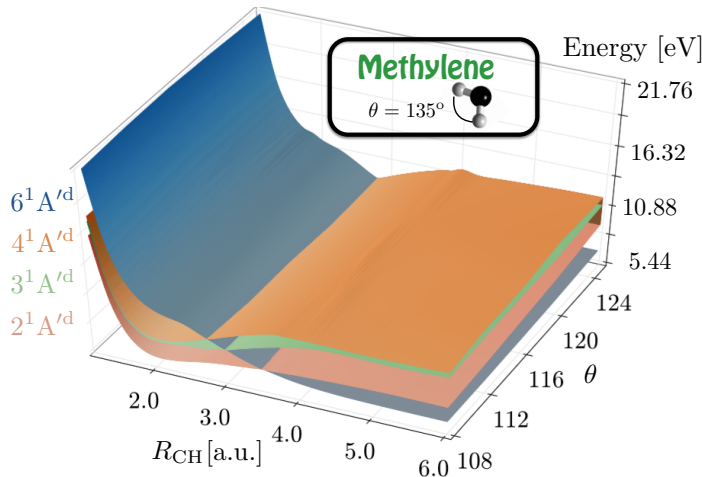
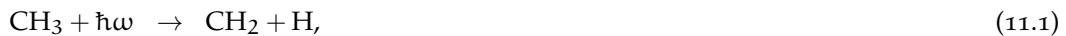


Figure 11.8: PES of diabatic states $2^1A'$, $3^1A'$, $4^1A'$ and $6^1A'$ of methyl molecule as a function of the CH bond distance and the bending angle. The inset is a reference of the equilibrium bending angle of the methylene molecule.

11.1.3 DYNAMICS

Recent works in the CH₃ molecule have been performed to study its photodissociation [131, 132]. However, in the theoretical part of these previous works, the dynamics is explained in terms of the electronic structure calculations, i. e., there is no dynamics calculation at all. Hence, this part of the work aims to explain or confirm the results of works developed by Bañares et al. [132] with the dynamics calculations using MCTDH. For this purpose, the number of the grid points for the internuclear distance R_{CH} were 97 inside a radial box with R_{CH} ∈ [1.2, 6.0] a.u., and the number of SPF used in the MCTDH is 20 for each degree of freedom in each electronic state.

In order to simulate the photodissociation process, i. e., the chemical reaction



it is assumed that the methyl radical has been previously excited from its ground state, which implies a sudden excitation transfer of the initial vibrational wave function of the ground state v_0'' into the $6^1A'$ electronic potential energy following the Franck-Condon principle. After that,

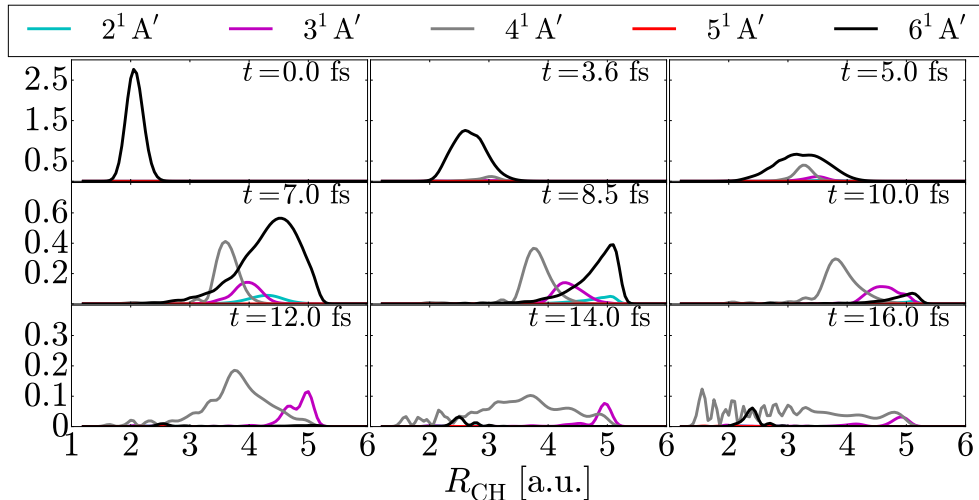
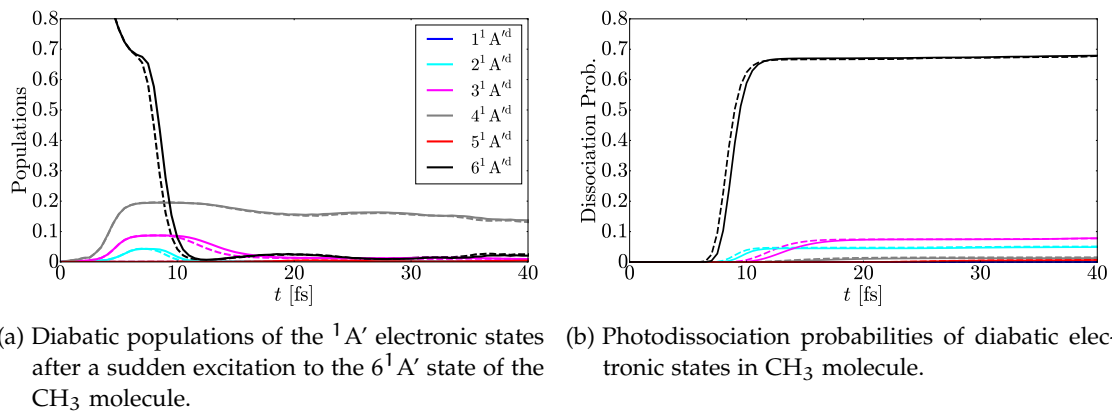


Figure 11.9: Time evolution of the wavepacket within the ${}^1\text{A}'$ manifold of states. The wavepacket starts at the 6th excited state (sudden excitation) and it spreads over the rest of states due to the action of **NAC** at the avoided crossings plot in Fig. 11.4. Color lines follow the same color scheme that in Fig. 11.7.

the wavepacket moves within the ${}^1\text{A}'$ PEC. The dynamics obtained by solving the 1D-TDSE using the **MCTDH** methodology for the six electronic diabatic states involved can be seen in Fig. 11.9. At time $t = 0$ fs, the wavepacket has only components in the ${}^1\text{A}'$ state and it is a mirror of the v_0'' ground vibrational state in ${}^1\text{A}'$. A few femtoseconds later, the wavepacket starts to move along the R_{CH} coordinate, and the wavepacket crosses three avoided crossings almost at the same time, from the 4th to the 6th. This can be seen at times $t = 5.0$ and 7.0 fs, where the wavepacket splits into others that move in the ${}^2\text{A}'$, ${}^3\text{A}'$ and ${}^4\text{A}'$ diabatic states. From $t = 8.5$ to 10.0 fs, the wavepacket in the ${}^1\text{A}'$ state reaches the **CAP** and it is absorbed, point at which the dissociation probability is calculated for the $\text{CH}_2({}^1\text{B}_1) + \text{H}({}^2\text{S})$ channel. Finally, from $t = 12.0$ to 16.0 fs, it is observed that the wavepacket emerges again in the ${}^1\text{A}'$ state. This is because the wavepackets moving in the other diabatic electronic states move back and forth between the classical turning points (note that only the ${}^5\text{A}'$ and ${}^1\text{A}'$ diabatic states are completely dissociative, see Fig. 11.7), which makes that the wavepacket moving within the ${}^2\text{A}'$, ${}^3\text{A}'$ and ${}^4\text{A}'$ diabatic states cross again the three avoided crossings with the ${}^1\text{A}'$ diabatic state.

Fig. 11.10 shows the 1D and 2D populations and the dissociation probabilities in the ${}^1\text{A}'$ electronic states for a propagation time of 40 fs. Populations in Fig. 11.10a show that the ${}^1\text{A}'$ and ${}^5\text{A}'$ electronic states practically do not contribute much to the dynamics, since its populations are close to zero during the whole propagation time. Fig. 11.10b shows the photodissociation probabilities for all open dissociation channels. The higher probability is for the $\text{CH}_2({}^1\text{B}_1) + \text{H}({}^2\text{S})$ channel with more than 60% of probability, which is in agreement with the experimental results performed by Bañares et al. [132]. As mentioned above, since the variation of energy with the bending angle is very small, both populations and photodissociation probabilities are very similar in 1D and 2D calculations. In fact, the 1D results (solid lines) are compared with the 2D results (dashed lines) in Fig. 11.10. Finally, a substantial probability for the photodissociation into the open channels $\text{CH}_2({}^2\text{A}_1) + \text{H}({}^2\text{S})$ and $\text{CH}_2({}^2\text{B}_1) + \text{H}({}^2\text{S})$ is also reported, with the residual methylene in different excited states. This opens the possibility of future control studies using probe pulses to optimize a chosen branching ratio in these dissociation channels.



(a) Diabatic populations of the $1A'$ electronic states after a sudden excitation to the $6^1A'$ state of the CH₃ molecule.

(b) Photodissociation probabilities of diabatic electronic states in CH₃ molecule.

Figure 11.10: Populations and dissociation probabilities in the $1A'$ electronic states after a sudden excitation to the $6^1A'$ electronic state in CH₃ molecule. Continuous lines indicate the 1D calculations and dashed lines correspond to the 2D calculations.

Anyone who is not shocked by quantum theory has not understood it.

— Niels Bohr

12

CAVITY FEMTOCHEMISTRY: CONTROLLING MOLECULES WITH QUANTIZED FIELDS

The interaction of molecules with light is a cornerstone in the development of molecular quantum mechanics. Along the recent decades the two different areas of i) quantum optics and ii) semiclassical molecular dynamics have evolved almost independently. The former is mostly interested in new emerging phenomena rising from the quantum nature of light, using model Hamiltonians for open quantum systems with a minimal number of states (qubits) [7, 90]. The latter focuses on the molecular structure and dynamics under conditions in which the quantum description of light is not required and the interaction with continuous wave radiaton or pulsed lasers employs semiclassical approximations, which incorporate the classical fields from Maxwell electrodynamics [74]. In this case, methods of solution involving a large number of vibronic states is the rule. A no-man's land located in between is still quite unexplored: *ab initio* polaritonic molecular photodynamics, i.e., many-state molecular dynamics (with a full vibronic description) along with a full quantum description of light. Of course, the physical situation with the conditions of application of such a full quantum theory must be met. A potential case is represented by molecules passing by or confined within optical cavities [133, 134].

Since the seminal works by Zewail [74, 135], it was clear that molecular photoreactions can be controlled with the use of ultrashort laser fields. The area of photodynamics with ultrashort laser pulses, down to the regimen of attosecond, has developed rapidly in the last years [66]. However, in these recent theoretical studies the molecule is subject to classical fields. When an atom or molecule is confined within a quantum cavity, the light must be considered as a set of quantized modes and the tools of quantum optics apply. There is a vast literature on cavity quantum electrodynamics (cavity QED) specially dedicated to atom-cavity interactions and control [133, 134]. The study of molecular photodynamics in quantum cavities is more scarce but nevertheless quite intense at present [89, 103, 136–142].

In this part of work, related with molecules coupled to quantized field, the diatomic molecule LiF inside a quantized optical cavity is studied with two applications. The first is purely theoretical and it is related with the effects created when the state of the quantized field is different from a Fock state, i.e., when the initial state of the radiation field is a coherent or a squeezed-coherent state, for example. The second corresponds to the proposal of a though experiment to reveal and characterize molecular light induced crossings induced by radiation. Although previous recent papers [89, 103, 137, 138] have studied this kind of radiation induced couplings, they are based in the heavier molecule NaI. However, from the theoretical point of view, since the LiF molecule is lighter than NaI its nuclear dynamics is faster. Then similar physics occurring in NaI also takes place in LiF but in a shorter time, which is a computational advantage.

12.1 REVEALING NON-ADIABATIC EFFECTS IN LITHIUM FLUORIDE INDUCED BY QUANTIZED FIELDS

The ideas about light-matter interaction with quantized fields, explained in [Chapter 8](#), can be applied to the solution of the two-state molecular photodynamics in the diatomic LiF molecule. In this work it is assumed for simplicity that LiF molecules within the cavity are oriented along the polarization axis of the cavity radiation field, so that only $\Sigma - \Sigma$ radiative transitions are allowed. In the absence of radiation the usual method of solution is to expand the total vibronic

wave function for a diatomic molecule in terms of the complete set of adiabatic electronic states. In this two-state model, the electronic states will have the same label explained in [Chapter 8](#) as $\{|g\rangle, |e\rangle\}$ for the ground and excited electronic states in the ${}^1\Sigma$ symmetry, respectively, whose energies $E_g(R)$ and $E_e(R)$, correspond to the [PEC](#) as functions of the internuclear distance R shown in [Fig. 9.5](#). Thus the total wave packet has the form

$$|\Psi(t)\rangle = \varphi_g(R, t)|g\rangle + \varphi_e(R, t)|e\rangle, \quad (12.1)$$

where $\varphi_i(R, t)$ ($i = e, g$) represents the time dependent nuclear wave packet moving in its respective [PEC](#). When the interaction with the quantized cavity is also included the ansatz takes instead the form

$$|\Psi(t)\rangle = \varphi_g(R, x, t)|g\rangle + \varphi_e(R, x, t)|e\rangle, \quad (12.2)$$

where now $\varphi_i(R, x, t)$ represent entangled wave packets for the joint vibrational and cavity photonic mode dynamics. In order to solve the photodynamics of the molecule in the cavity the [TDSE](#) ([Eq. \(4.2\)](#)) must be solved. In this particular problem, the total Hamiltonian [Eq. \(8.16\)](#) must include the molecular Hamiltonian for the diatom LiF, i.e.,

$$\hat{H}_M = \hat{H}_N + \hat{H}_{el}, \quad (12.3)$$

where the adiabatic basis of electronic states are eigenfunctions of the electronic Hamiltonian, i.e., $[\hat{H}_{el} - E_g(R)]|g\rangle = 0$ and $[\hat{H}_{el} - E_e(R)]|e\rangle = 0$. Hence, if the ansatz in [Eq. \(12.2\)](#) is inserted into the [TDSE](#), one obtains

$$\begin{aligned} i\hbar \frac{d}{dt} \begin{bmatrix} \varphi_g(R, x, t) \\ \varphi_e(R, x, t) \end{bmatrix} = & \left\{ \begin{pmatrix} -\frac{\hbar^2}{2\mu} \frac{\partial^2}{\partial R^2} + E_g(R) - \frac{\hbar^2}{2} \frac{\partial^2}{\partial x^2} + \frac{1}{2} \omega_c^2 x^2 & 0 \\ 0 & -\frac{\hbar^2}{2\mu} \frac{\partial^2}{\partial R^2} + E_e(R) - \frac{\hbar^2}{2} \frac{\partial^2}{\partial x^2} + \frac{1}{2} \omega_c^2 x^2 \end{pmatrix} \right. \\ & \left. + \begin{pmatrix} \chi \omega_c \sqrt{2\hbar} \mu_{gg}(R)x & \chi \omega_c \sqrt{2\hbar} \mu_{ge}(R)x \\ \chi \omega_c \sqrt{2\hbar} \mu_{eg}(R)x & \chi \omega_c \sqrt{2\hbar} \mu_{ee}(R)x \end{pmatrix} + \Lambda(R) \right\} \begin{bmatrix} \varphi_g(R, x, t) \\ \varphi_e(R, x, t) \end{bmatrix}, \end{aligned} \quad (12.4)$$

where μ is the reduced nuclear mass, ω_c is the cavity frequency, μ_{ij} are the molecular electronic dipole moments shown in [Fig. 9.6a](#) and the matrix elements

$$\Lambda_{ij}(R) = -\frac{\hbar^2}{2\mu} \left[2 \left\langle i \left| \frac{\partial}{\partial R} \right| j \right\rangle (R) \frac{\partial}{\partial R} + \left\langle i \left| \frac{\partial^2}{\partial R^2} \right| j \right\rangle (R) \right] = -\frac{\hbar^2}{2\mu} \left[2f_{ij}(R) \frac{\partial}{\partial R} + h_{ij}(R) \right], \quad (12.5)$$

correspond to the well known [NAC](#) explained in [Chapter 5](#).

In order to perform dynamics calculations, [Eq. \(12.4\)](#) is implemented in the [MCTDH](#) software package [\[111\]](#). Since [MCTDH](#) package requires the input of the [PES](#) involved, in this particular case, the two dimensional [PES](#) in R and x coordinates are given for the ground g and excited e states by

$$V_i = E_i(R) + \frac{1}{2} \omega_c^2 x^2 + \chi \omega_c \sqrt{2\hbar} \mu_{ii}(R)x, \quad (12.6)$$

with $i = (g, e)$. It means that these [PES](#) are composed by the molecular [PEC](#) of LiF (${}^1\Sigma$ for g and ${}^1\Sigma$ for e) and the harmonic oscillator potential for radiation and the diagonal terms of the interaction with the dipole moments μ_{gg} and μ_{ee} that cannot be discarded in this polar molecule. The [MCTDH](#) provides, among many other observables, the time-dependent evolution of populations for the g and e light-matter entangled states, the dissociation probabilities computed with the flux moving across a complex absorbing potential and, more interestingly, the separate entangled wave packets $\varphi_g(R, x, t)$ and $\varphi_e(R, x, t)$, evolving in the ground and excited [PES](#), which will be called from now on g -wave packet and e -wave packet. It must be noted that a temporal analysis of these wave packets helps to reveal the underlying mechanism in this complex entangled photonic-nuclear dynamics for a LiF molecule inside a cavity.

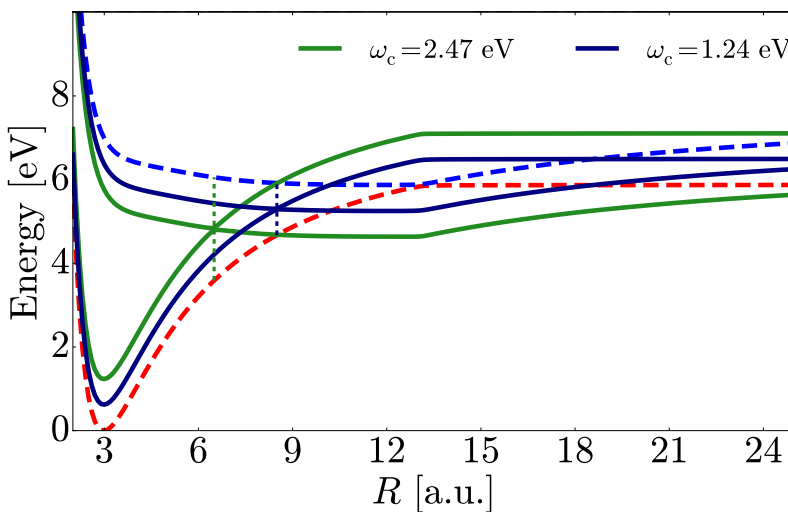


Figure 12.1: Modified potential energy curves for the light dressed states due to two different cavity mode frequencies, $\omega_c = 1.24$ eV and $\omega_c = 2.47$ eV, that show LIC located at $R = 8.5$ a.u. and $R = 6.5$ a.u., respectively (internuclear distances at which the detuning $\Delta = [E_e(R) - E_g(R)]/\hbar - \omega_c$ is zero). Adiabatic potential energy curves $E_g(R)$ and $E_e(R)$ are also introduced for comparison (dashed lines).

As it was explained in [Chapter 8](#), the presence of radiation (in the semiclassical or quantum form) induces Light induced crossing (LIC) between, in this case, electronic states coupled by the radiation. In the quantized version, within the Jaynes-Cumming model, the new two dressed states show a splitting in the form [89]

$$E_{\pm} = \frac{E_g(R) + E_e(R)}{2} \pm \frac{\hbar}{2} \Omega_{n_c}(R), \quad (12.7)$$

where $E_g(R)$ and $E_e(R)$ are the adiabatic energies and Ω_{n_c} is the Rabi frequency, i.e.,

$$\Omega_{n_c}(R) = \sqrt{4[\lambda(R)]^2(n_c + 1) + \Delta_c(R)} \quad (12.8)$$

Here λ is the interaction coupling factor, n_c stands for the Fock photon number in the cavity and $\Delta_c = [E_e(R) - E_g(R)]/\hbar - \omega_c$ is the detuning. The $^1\Sigma$ dressed states when LiF molecule interacts with the quantized field polarized in the z -axis are plotted in [Fig. 12.1](#) for two cavity mode frequencies, $\omega_c = 1.24$ eV and $\omega_c = 2.47$ eV. The LIC appears at the internuclear distance R_{LIC} where the energy difference between the adiabatic curves, $[E_e(R) - E_g(R)]/\hbar$, equals the cavity mode frequency ω_c . This means that the chosen mode frequency ω_c turns out to be an interesting control parameter in the subsequent dynamics by selecting the position of the LIC. It is worth noting that this time dependent approach expands the total wave packet in terms of the unperturbed Hamiltonian (non-interacting molecular adiabatic states plus field states), so that the effect of the LIC appears in the stationary dressed state picture must be represented by the adiabatic basis and the interaction within the dynamics. In other words, while the dipolar and non-adiabatic couplings are directly introduced in the dynamics, the LIC is not directly introduced, but nevertheless it arises as a dynamical interaction. From [Fig. 12.1](#) it is clear that the light induces effective dressed potentials in the R -direction, with shifted turning points and modified energetics.

Cavity femtochemistry in the NaI molecule has been recently studied by Ref. [103, 136–138], nonetheless the purpose of this work is to provide a more comprehensive account of the inner workings of the underlying mechanisms that give shape to the time-dependent populations and the dissociation yields in a similar molecule, Lithium Fluorine (LiF). As the cavity can be in different types of quantum states of radiation, the next sections cover the study when the cavity has Fock states, coherent states or squeezed coherent states as the initial radiation state, since they exhibit different properties.

12.1.1 PHOTODYNAMICS WITH FOCK STATES

For the case of Fock states, the initial state of the total wave packet is a direct product $\chi_{v=0}^g(R) \times \psi_{n''=0}(x)$, where $\chi_{v=0}^g(R)$ is the vibrational ground state of the $1^1\Sigma$ state and $\psi_{n''=0}(x)$ is the ground state of the HO with mass unity and frequency ω_c (i.e., the radiation Fock vacuum state $|0\rangle$ represented in coordinate space). The radial box used for the vibrational mode is $R \in [1.6, 60]$ a.u. and the box for the HO mode is $x \in [-x_{\max} : x_{\max}]$ a.u., with $x_{\max} = 30$ a.u., large enough indeed to accommodate the Fock state of radiation under study. According to MCTDH methodology, the number of SPF used in the calculations was $n_R = n_x = 15$ to represent both the molecular state in the nuclear box and the radiation state in the radiation box. Similarly, the number of primitive basis is $N_R = 1169$ for the molecular vibrational mode and $N_x = 241$ for the radiation mode.

The evolution of this initial state subject to the molecule-cavity interaction, is studied using different cavity mode frequencies. These frequencies are selected for the matching $\omega_c = [E_e(R) - E_g(R)]/\hbar$ (detuning zero) in the LiF potential energy curves in order to choose the position R_{LIC} of the LIC, where the dressed curves are nearly degenerate. Table 12.1 shows the cavity mode frequencies (and the corresponding wavelengths) used in this work, that range from the visible to the IR sectors in the electromagnetic spectrum. Additionally, Table 12.1 indicates the corresponding position of the LIC in the PEC of LiF. Note that for $\omega_c \rightarrow 0$ the LIC approaches the position of the NAC, not induced by the radiation, located at $R_{\text{NAC}} = 13.1$ a.u. in LiF.

Table 12.1: Set of cavity mode wavelengths λ_c and frequencies ω_c used in this work. The cavity frequency determines the position of the LIC at the internuclear distance R_{LIC} , where the detuning $\Delta = [E_e(R) - E_g(R)]/\hbar - \omega_c$ is zero.

λ_c [nm]	400	500	600	700	1000	2250
ω_c [eV]	3.01	2.47	2.09	1.76	1.24	0.54
R_{LIC} [a.u.]	5.8	6.5	7.0	7.5	8.5	10.5

The time-dependent populations for the g-state (linked to $1^1\Sigma$) and the dissociation yield, that comes from a portion of the e-wave packet transferred to the g-state through the different couplings are plotted in Fig. 12.2. For the largest ω_c values (3.01, 2.47 and 2.09 eV), the g-population shows short-time oscillations with a clear periodicity (the larger the frequency, the shorter the period). These oscillations tend to fade out at the long time limit. This effect is produced by the interaction with the cavity radiation, since in absence of the cavity the only effective coupling corresponds to the NAC located at $R = 13.1$ a.u. and in this case the $1^1\Sigma$ population does not show oscillations (see also Fig. 12.2). In absence of radiation, the latter NAC is an efficient coupling, since more than half of the population of the e-wave packet is transferred to the g-state from the e-state at $t \sim 100$ fs. Eventually all population transferred to the ground state $1^1\Sigma$ leads to dissociation. All dissociation yields are computed with the flux crossing a CAP located at $R = 58$ a.u., at the edge of our spatial R-grid of size 60 a.u. This absorbing layer is reached by the g-wave packet in less than 400 fs. Note that the $1^1\Sigma$ population increases steadily again from $t = 500$ fs. At this time the e-wave packet (reflected from the repulsive right side of the $2^1\Sigma$ PES) meets again the NAC and a portion is transferred once more to the ground $1^1\Sigma$ state (the increasing spreading of the e-wave packet causes the slow increase of the population during the subsequent visits to the NAC). Since the e-wave packet bounces back and forth in the $2^1\Sigma$ potential and it crosses the NAC region twice within a vibrational cycle (two transfers to the ground state), at $t \rightarrow \infty$ the whole population initially located in the upper $2^1\Sigma$ state will eventually lead to full dissociation of the LiF molecule through the $1^1\Sigma$ state. All simulations were performed with a final time of 1 ps for the propagation for computational simulations, due to this, it is not possible to observe that the e-wave packet does not complete a full vibrational cycle in the $2^1\Sigma$ state, so that the highest dissociation yield at this time is 0.6.

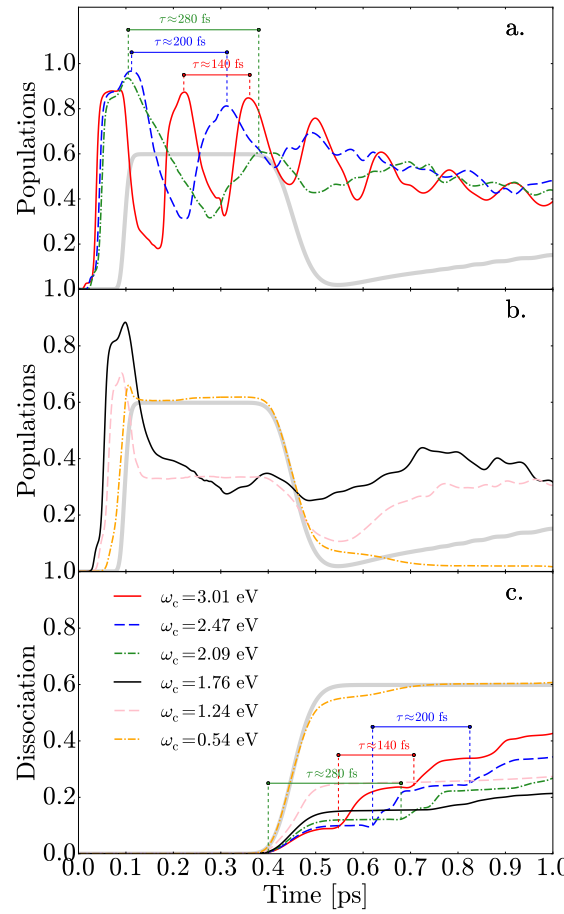


Figure 12.2: (a) Time-dependent population corresponding to the adiabatic ground state $1^1\Sigma$ for the molecule LiF initially fully excited in the $2^1\Sigma$ and coupled with the radiation present in a cavity in the form of the Fock vacuum state $|0\rangle$. Probabilities are included for three different cavity mode frequencies $\omega_c = 3.01$ eV (red solid line), $\omega_c = 2.47$ eV (blue dashed line), $\omega_c = 2.09$ eV (green dashed-dotted line), with $\chi = 0.05$. The population for isolated LiF molecule (without a cavity) is also included as a reference (thick grey line) and its rapid decay after 400 fs is due to the presence of the absorbing potential situated at $R = 58$ a.u. The periodicity between consecutive maxima is indicated in the figure. (b) Same as (a) but for smaller cavity mode frequencies: $\omega_c = 1.76$ eV (black solid line), $\omega_c = 1.24$ eV (grey dashed line) and $\omega_c = 0.54$ eV (orange dashed-dotted line). Again, the probability of cavity-undressed LiF is also included as a reference. (c) Total dissociation probability (fully represented by the flux escaping asymptotically above the dissociation threshold of the ground state $1^1\Sigma$), for the same six cavity mode frequencies ω_c present in (a) and (b).

Back to the field dressed case, the oscillations in the populations tend to disappear as ω_c decreases (see cases with $\omega_c = 1.76, 1.24$ and 0.54 eV in Fig. 12.2). As $\omega_c \rightarrow 0$, the position of the **LIC** approaches the location of the **NAC** and the effect of the cavity radiation vanishes. Also, note that the periodicity τ of the oscillations present in the time-dependent populations ($\tau = 140$ fs for $\omega_c = 3.01$ eV, $\tau = 200$ fs for $\omega_c = 2.47$ eV, and $\tau = 280$ fs for $\omega_c = 2.09$ eV in Fig. 12.2(a)) also emerges in the dissociation yields. Whereas for the undressed LiF molecule the only presence of a **NAC** produces a single burst of dissociation within the time window of the first ps, the effect of the cavity field is to produce a train of dissociating wave packets with a ω_c -dependent periodicity τ . For the three larger values of ω_c , after each period τ , the dissociation yield increases by a quantity which is almost independent of the cavity mode frequency ω_c (i.e., same amounts but at different time delays). This is because the dissociative g-wave packet always comes from the e-wave packet through the **NAC** with the same transfer rate, at variance with the variable transfer rate at the **LIC**, since this interaction strength itself depends upon ω_c . For the three smaller values of ω_c (1.76, 1.24 and 0.54 eV) the behavior

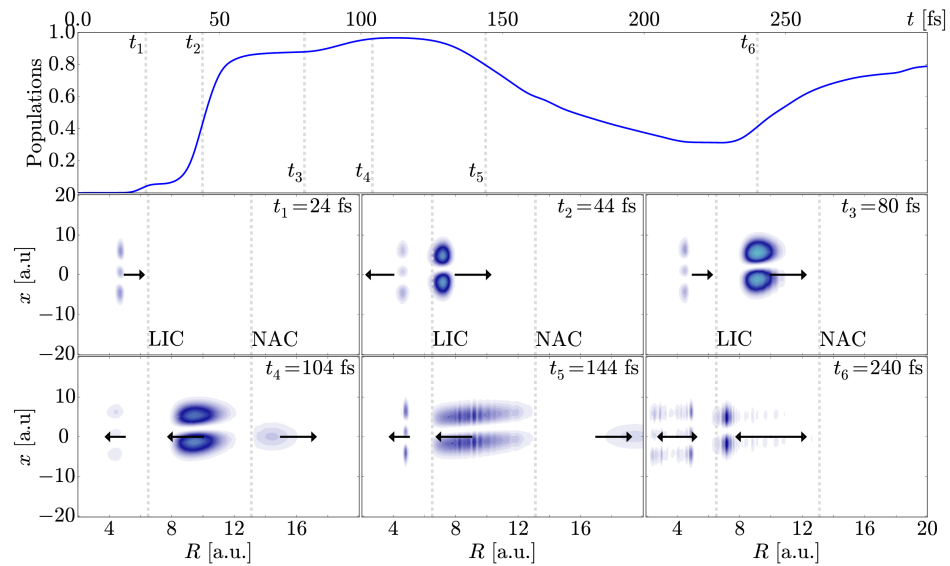


Figure 12.3: Snapshots of the time-dependent evolution for the probability density of the entangled radiation-molecule wave packet moving in the potential $1^1\Sigma$ energy surface composed by the molecular PEC of the electronic $1^1\Sigma$ state and the radiation of a HO with its corresponding interaction term (see Eq. (12.4)). The plot corresponds to a cavity mode frequency $\omega_c = 2.47$ eV, interaction factor $\chi = 0.05$ and the radiation is set up initially as the vacuum Fock state $|0\rangle$. The times t_i for the snapshots are connected with different features present in the population of the $g-$ state (upper panel). Arrows indicate the direction of motion of the wave packet and its size is related to the magnitude of its momentum. Vertical lines within the snapshots indicate the internuclear distance $R = 6.5$ a.u. for the location of light induced crossing (LIC) and the internuclear distance $R = 13.1$ a.u. for NAC.

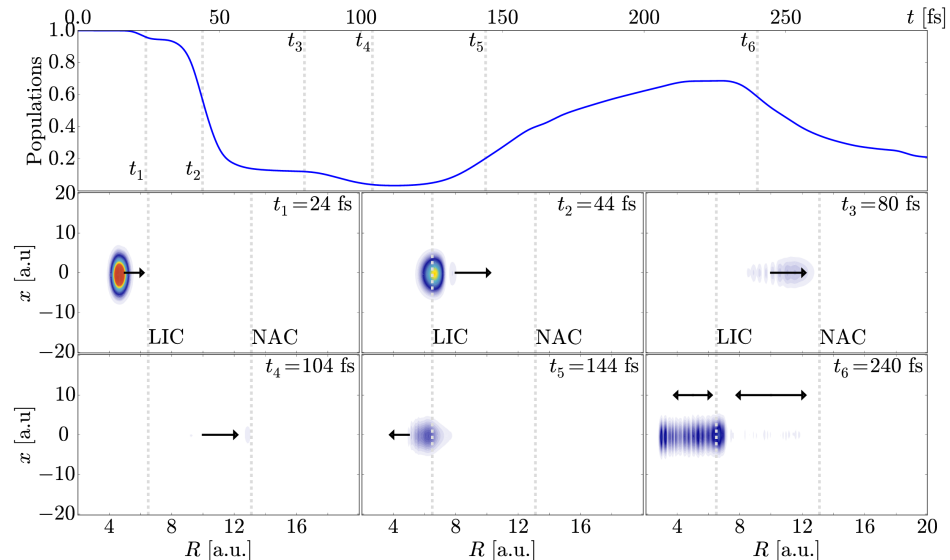


Figure 12.4: Same as Fig. 12.3 but for the population and time-dependent probability density of the $2^1\Sigma$ energy surface (initially populated at $t = 0$. Snapshots are taken at the same times as in Fig. 12.3 for comparison.

of the dissociation yield represents a tug of war between the LIC and the NAC effects. The closer proximity of the LIC to the NAC makes the NAC physics dominant, but still there is an interfering LIC contribution, which is less effective for smaller ω_c values.

To understand the inner workings of the cavity photodynamics of LiF, the case with a cavity frequency $\omega_c = 2.47$ eV is chosen to analyze it. At this initial total energy the dissociation

process comes through the population transfer from the upper e-PES to the lower g-PES. Then, the time dependent populations in these two states as well as the evolution of the probability densities for the corresponding g- and e-wave packets are plotted in Fig. 12.3 and figure 12.4, respectively.

The initial unentangled photonic-nuclear e-wave packet at $t = 0$ in $2^1\Sigma$ is approximately a direct product of two Gaussians of different widths. Its compact form is quite robust during dissociation (see Fig. 12.4). However, the underlying dynamics is better understood following the g-wave packet density in Fig. 12.3. Firstly, at $t = 24$ fs the g-wave packet splits in three portions along the x (radiation mode) coordinate. In fact, this splitting happens to occur below 1 fs [143]. The interaction term $\chi\omega_c\sqrt{2\hbar}\mu_{ij}(R)x$ causes transitions, so to speak, between vibronic states in both the molecular (through $\mu_{eg}(R)$) and the HO subsystems (through x). According to Fig. 9.6a, the dipole moment $\mu_{eg}(R)$ is not zero in LiF for $R > R_{eq}$ ($R_{eq} \sim 3$ a.u. is the equilibrium distance), so that transitions between the upper (e) and lower (g) HO states take place promptly. According to HO dipole selection rules its ground state $\psi_{n'=0}^e$ makes a sudden and dominant transition to $\psi_{n''=1}^g$ in the lower HO potential (hence the g-wave packet is created with a single node at the beginning). Further, since whereas the diagonal dipole moment μ_{ee} is almost negligible in $R_{eq} < R < 12$ a.u., the diagonal dipole moment μ_{gg} is not (see Fig. 9.6a). Indeed, its magnitude is larger than the transition dipole moment μ_{eg} in the same region. This means that the interaction term $\chi\omega_c\sqrt{2\hbar}\mu_{gg}(R)x$ also produces intra-state HO transitions within the g-state, from the previously populated $n'' = 1$ to $n'' = 0$ and mainly $n'' = 2$ [143], which generates a two-node g-wave packet extended in the x coordinate whose shape remains robust during its propagation in the confined zone $0 < R < R_{LIC}$, the inner region of the dressed potential $E_-(R)$ (Fig. 12.1). These e – g transitions at short $R < R_{LIC}$ are always present because the cavity interaction is always switched on but it is feeble because is quite out of resonance (the detuning is zero only at the position of the LIC).

The cavity interaction depletes the upper state population when the e-wave packet reaches the LIC, located at $R = 6.5$ a.u. for $\omega_c = 2.47$ eV. At this internuclear distance the transition dipole moment μ_{eg} is much more effective and the e-wave packet passing through the LIC produces a one-node g-wave packet in the lower PES which propagates with an inherited momentum. While this newly LIC-created wave function approaches the NAC region, the two-node g-wave packet has almost completed a vibrational cycle (approximately $\tau = 56$ fs) from $t = 24$ to $t = 80$ fs, inside the dressed $1^1\Sigma$ state. Similarly, the one-node g-wave packet bounces back and forth confined in the region $R_{LIC} < R < R_{NAC}$ with a period $\tau \sim 200$ fs.

The second enhancement of the ground state population is due to the NAC at $R = 13.1$ a.u.. Between $t = 80$ fs and $t = 104$ fs the remaining e-wave packet almost disappears because its density is fully transferred to the g-state at $t = 104$ fs (see time t_4 in Fig. 12.3 and Fig. 12.4). This latter portion of g-wave packet finally leads to dissociation. The middle one-node g-wave packet, after reflection from the $1^1\Sigma$ turning point near the NAC, approaches the LIC at $t \sim 144$ fs. Again, the efficient LIC drives a large portion (~ 0.6) of the one-node g-wave packet back to the upper e-PES, where a nodeless and extended e-wave packet emerges with its inherited momentum. In other words, from $t = 144$ to $t = 240$ fs the initial e-wave packet is partially reconstructed thanks to the LIC. Therefore, from this time onward, the full mechanism is again repeated, but with a smaller initial population. These cyclic mechanism explain the main features present in the populations in Fig. 12.2(a).

Note that the wave packet dynamics in Fig. 12.3 does not preserve a parity symmetry $x \rightarrow -x$ for the densities. This is because the PES for the ground state contains the light-matter interaction term and the non-zero negative value of μ_{gg} for R (see Fig. 9.6a) produces an additional linear potential in the x direction. From the time-dependent densities, it is clear the presence of LIC or that the dynamics evolves into the effective dressed states by the light. Moreover, the two-node g-wavepacket confined at short $0 < R < R_{LIC}$ shows different reflections and vibrational periods for each chosen cavity mode frequency ω_c . For instance, for $\omega_c = 3.1$ eV this portion of the g-wave packet is reflected at $R \sim 4$ a.u.; for $\omega_c = 2.47$ the turning point is at $R \sim 5$ a.u. (see Fig. 12.3; and for $\omega_c = 2.09, 1.76$ and 1.24 eV this inner g-wave packet travels up to $R \sim 6, 7$ and 8 a.u., respectively, and then is reflected back. This is an indication of the existence of a movable LIC between virtual dressed PES.

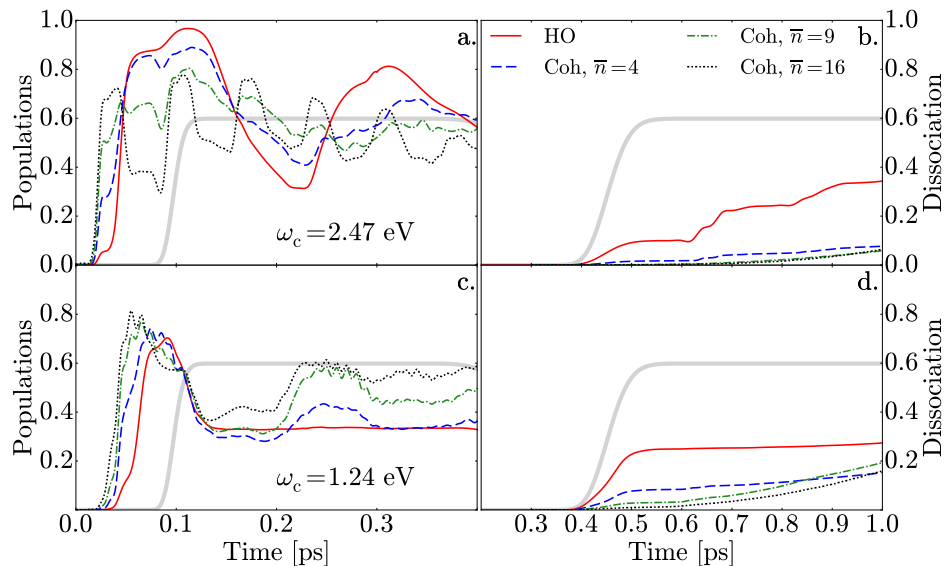


Figure 12.5: (Left panels) Time-dependent population corresponding to the adiabatic ground state $1^1\Sigma$ for the molecule LiF initially fully excited in the $2^1\Sigma$ and coupled to the radiation present in a cavity in the form of a coherent state $|\alpha\rangle$, with different average number of photons $\bar{n} = |\alpha|^2 = 4$ (blue dashed line), 9 (green dotted-dashed line) and 16 (black dotted line). Probabilities are included for two different cavity mode frequencies $\omega_c = 2.47$ eV (a) and $\omega_c = 1.24$ eV (c), with $\chi = 0.05$. The probabilities for the undressed dynamics (grey thick line) and for the photodynamics with a Fock vacuum state (red solid line) are also included as a reference. (Right Panels) Total dissociation probability (represented by the flux escaping asymptotically above the dissociation threshold of the ground state $1^1\Sigma$), for the cavity mode frequencies $\omega_c = 2.17$ eV (b) and $\omega_c = 1.24$ eV (d), associated to the probabilities in (a) and (c), respectively.

12.1.2 PHOTODYNAMICS WITH COHERENT STATES

Now it is assumed that the optical cavity is filled with a coherent radiation. The coherent state of light in the position space representation is given by Eq. (7.37). Here, the complex number that characterizes the coherent state is given by $\alpha = |\alpha|e^{i\pi/4}$, which is related to the average number of photons in the cavity through $\bar{n} = |\alpha|^2$. Additionally, different values for the average number of photons are chose, namely, $\bar{n} = 4, 9$ and 16 . In contrast to the case of Fock states, the initial total wave packet is the direct product $\chi_{v=0}^g(R) \times \psi_\alpha(x)$. Then the choice for \bar{n} and the cavity mode frequency ω_c determine the initial location and momentum of the coherent state, which is readily represented in our radiation grid with $x \in [-50, 50]$ a.u. The box for the molecular and SPF for this case is the same chosen is the Fock case. The box for the radiation mode is larger due to for larger values of \bar{n} , the average energy, $\bar{E} = \sum_{n=0} P_n(\bar{n})E_n(\omega_c)$ is also larger, and the longer the oscillation amplitude in the HO potential.

Fig. 12.5 shows the time-dependent g -state populations and the dissociation yields with radiation represented as a coherent state for two cavity mode frequencies $\omega_c = 1.24$ and 2.47 eV, both with three different average number of photons ($\bar{n} = 4, 9$ and 16). For $\bar{n} = 4$, according to P_n , the main Fock components in the coherent state extend from $n = 0$ to $n = 9$ with a maximum in $n = 4$. This means that the coherent state initially moves within the HO potential with an average total energy higher to that of the vacuum Fock state. For $\omega_c = 2.47$ eV and $\bar{n} = 4$ the behavior of the g -population with $\bar{n} = 4$ is similar to that of the Fock vacuum state. Actually, the coherent state is a displaced vacuum state, $|\alpha\rangle = D(\alpha)|0\rangle$, with the same width. Nonetheless, some differences can be appreciated. At the short time range 20–50 fs the g -population develops a hump not present in the HO Fock case (see Fig. 12.5) that increases further for $\bar{n} = 9$ and 16 . This g -population enhancement is caused by the larger effective dipole transition in the HO mode along x . The coherent state is not an stationary state and it oscillates (preserving its shape) with a large amplitude between the turning points of the upper

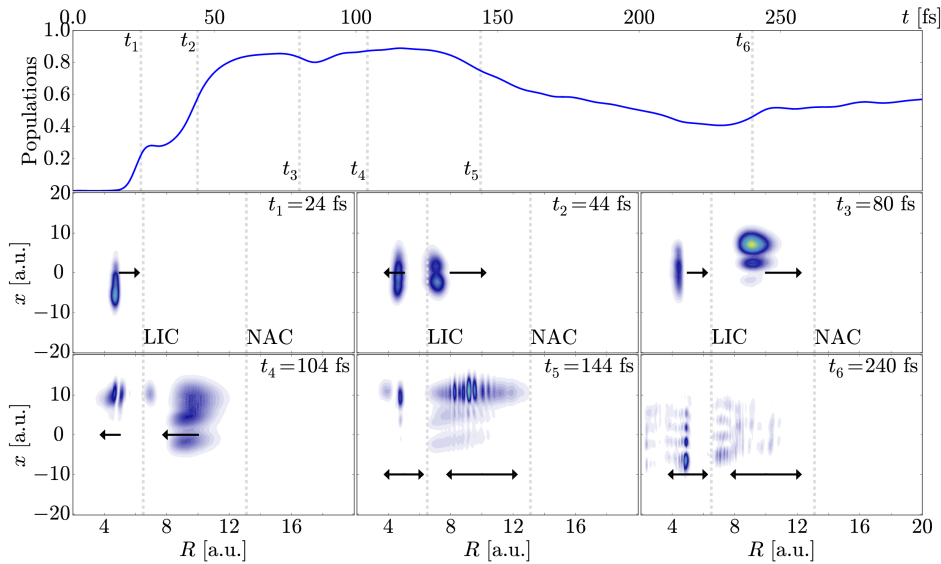


Figure 12.6: Snapshots of the time-dependent evolution for the probability density of the entangled radiation-molecule wave packet moving in the potential $1^1\Sigma$ energy surface composed by the molecular **PEC** of the electronic $1^1\Sigma$ state and the radiation of a HO with its corresponding interaction term (see Eq. (12.4)). The plot corresponds to a cavity mode frequency $\omega_c = 2.47$ eV, interaction factor $\chi = 0.05$ and the radiation is set up initially as a coherent state $|\alpha\rangle$ with an average number of photons $\bar{n} = 4$ and angular phase $\psi = \pi/4$. The times t_i for the snapshots are connected with different features present in the population of the $1^1\Sigma$ state (upper panel). Arrows indicate the direction of motion of the wave packet and its size is related to the magnitude of its momentum. Vertical lines within the snapshots indicate the internuclear distance $R = 6.5$ a.u. for the location of **LIC** and the internuclear distance $R = 13.1$ a.u. for the **NAC**.

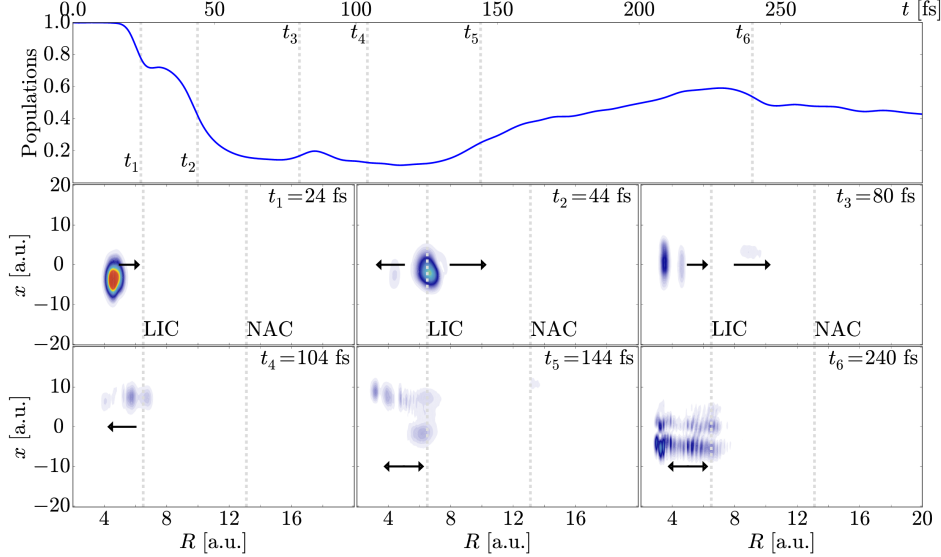


Figure 12.7: Same as Fig. 12.6 but for the population and time-dependent probability density of the $2^1\Sigma$ energy surface (initially populated at $t = 0$ with the radiation state as a coherent state). Snapshots are taken at the same times as in Fig. 12.6 for comparison.

HO potential at the average energy $\bar{E}(\bar{n})$, as it was explained in Section 7.2.3.2. This oscillation has a period $T = 2\pi/\omega_c$ and its amplitude is larger for increasing \bar{n} . These long excursions of the coherent state to large values of x makes that the effective dipole matrix elements between the moving coherent state and the HO Fock states of the g-state be more effective than between Fock states. This is reflected in the higher population transfer, even in the off-resonant region

$0 < R < R_{LIC}$ and also at R_{LIC} . This higher population transfer must be appreciated in the g-wave packet density (more intense than in the Fock state case). In the case $\omega_c = 2.47$ eV and $\bar{n} = 4$, see the first snapshot at time $t = 24$ fs included in Fig. 12.6. This piece of g-wave packet has no node structures, given that the coherent state is a superposition of Fock states and this tends to wash out any sharp node corresponding to particular HO transitions.

It must be noted that densities for $\omega_c = 2.47$ eV in Figs. 12.6 and 12.7 are frames at a fixed time, but these densities move upward-downward in the x direction, with a period $T = 1.67$ fs. For $\bar{n} = 4$ the coherent state is initially centered at $x \sim 6$ a.u. and with a positive momentum $\langle p \rangle_\alpha$, then it reaches the right turning point where the dipole is maximum. There are no less than 20 oscillation cycles of the coherent state to reinforce the dipole transitions before the e-wave packet reaches the LIC. Also, at $t = 44$ fs (see Fig. 12.7) a weak signal appears traveling in opposite direction to the e-wave packet moving across the LIC. It comes through the off-resonant cavity dipole transition, from the population of the g-state already trapped in $0 < R < R_{LIC}$ ($t = 44$ fs in Fig. 12.7). This piece of e-wave packet moves in the upper e-PES with a different momentum than the g-wave packet moving in $0 < R < R_{LIC}$ at $t = 44 - 80$ fs. At $t = 80$ fs the traveling piece of g-wave packet within the interval $0 < R < R_{LIC}$ partially transfers to the e-state, thus producing two fringes of delayed e-wave packets with slightly different momentum that eventually will interfere. The LIC is so effective with coherent states that the e-wave packet is almost emptied in the region $R < R_{NAC}$ and little density survives to arrive at the NAC (see $t = 80$ fs in Fig. 12.7). This is why the dissociation yield in Fig. 12.5 for any coherent state is much reduced with respect to the Fock case. Also, a large portion of the g-density confined in $R_{LIC} < R < R_{NAC}$ is transfer back to the e-state between 144 and 240 fs. Finally at $t = 240$ fs the e-wave packet, partially reconstructed with large interference structures, restarts the whole mechanism.

For $\bar{n} = 16$ the dynamical oscillatory pattern for the populations in Fig. 12.5 changes abruptly with a series a periodic structures separated by $\tau \sim 70$ fs. In this case, it takes ~ 34 fs for the e-wave packet to reach the LIC, time at which the g-state population shows its first maximum peak. However, in this occasion the e-wave packet do not cross the LIC, but it is reflected back for $R < R_{LIC}$. Due to the large enhancement of the dipole moment for the coherent states and even more for large \bar{n} , the g-population in exchanged with the e-state until the latter reaches the inner turning point where the $\mu_{eg} \sim 0$. When the upper e-wave packet arrives at the equilibrium distance R_{eq} , a new cycle repeats. Consequently, the sequence of peaks in Fig. 12.5 indicates the periodical arrival of the e-wave packet to the LIC from R_{eq} , and the full dynamics is confined in $0 < R < R_{LIC}$, with the NAC playing no role. This mechanism is confirmed by changing the cavity mode frequency to $\omega_c = 1.24$ (see Fig. 12.5, a case for which the LIC is located at $R_{LIC} = 8.5$ a.u.). In this case the period for the confined motion in $0 < R < R_{LIC}$ is longer, $\tau = 180$ fs, with the maximum humps indicating that the e-wave packet approaches the LIC, makes the transition, and it is reflected back.

12.1.3 PHOTODYNAMICS WITH SQUEEZED-COHERENT STATES

The squeezed coherent state in the position representation is given by Eq. (7.44). As it was explained in Chapter 7, the squeezed state is characterized by the complex variable $\xi = r e^{i\theta}$, where r is the squeezing parameter and $e^{i\theta}$ the squeezing phase. The angular difference has been fixed to $\psi - \theta/2 = 2\pi/5$. Remembering one of the properties of a squeezed state, one of the two variances increases and as a consequence the other decreases. This effect is appreciated if the state in Eq. (7.44) is propagated in time (see Fig. 7.2 for an illustrative picture). At the time of maximum expansion, the spatial allocation of the squeezed state may require the use of large grids $x \in [-70 : 70]$, specially for large \bar{n} , and the other parameters were kept as in the case of Fock state. The average number of photons for a squeezed coherent state is given by $\bar{n} = |\alpha|^2 + \sinh^2 r$. The squeezing parameter has been chosen as $r = 2$ and $|\alpha|^2 = 4$ and 9. In these cases, the squeezing character dominates over the coherent one in the contribution to \bar{n} .

Fig. 12.8 shows the time evolution of the g-populations and dissociation probabilities for two cavity mode frequencies, $\omega_c = 2.47$ and 1.24 eV. The pattern of oscillations in the g-populations for both $|\alpha|^2 = 4$ and $|\alpha|^2 = 9$ are similar between them but also comparable to

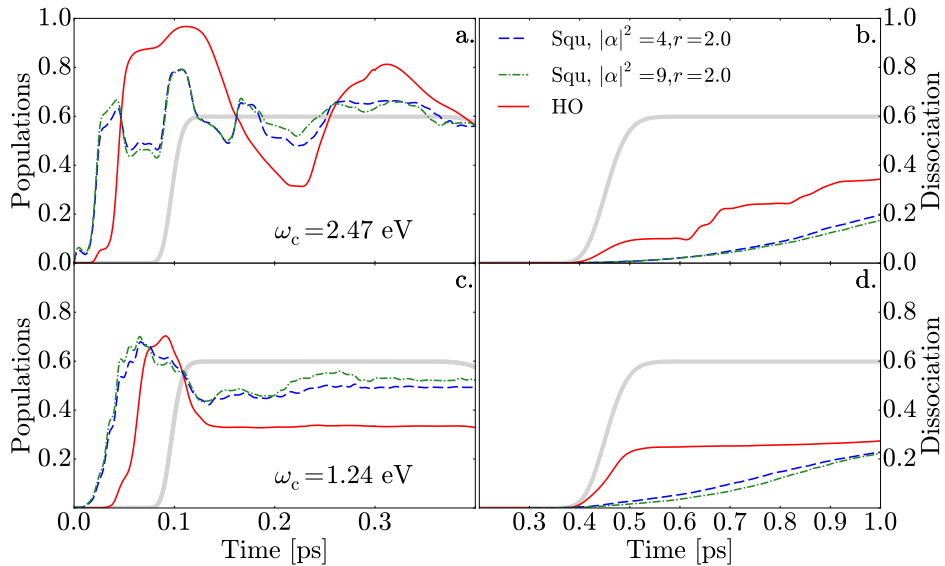


Figure 12.8: (Left panels) Time-dependent population corresponding to the adiabatic ground state $1^1\Sigma$ for the molecule LiF initially fully excited in the $2^1\Sigma$ and coupled with the radiation present in a cavity in the form of an squeezed coherent state $|\alpha, \xi\rangle$, with two different values of $|\alpha|^2=4$ (blue dashed line) and $|\alpha|^2 = 9$ (green dotted-dashed line), squeezing parameter $r = 2$ and angular phase angle $\psi - \theta/2 = 2\pi/5$, are included for two different cavity mode frequencies $\omega_c = 2.47$ eV (a) and $\omega_c = 1.24$ eV (c). The probabilities for the undressed dynamics (grey thick line) and for the photodynamics with an initial Fock vacuum state (red solid line) are also included as a reference. (Right Panels) Total dissociation probability (represented by the flux escaping asymptotically above the dissociation threshold of the ground state $1^1\Sigma$), for the cavity mode frequencies $\omega_c = 2.47$ eV (b) and $\omega_c = 1.24$ eV (d), associated to the probabilities in (a) and (c), respectively.

the g-populations for a coherent state with the largest value $\bar{n} = |\alpha|^2 = 16$. From the coherent radiation case, increasing of the dipole moment as \bar{n} increases was the responsible for these rapid oscillations with a short period of 70 fs. The cause is that the transition dipole moments for the squeezed state are larger than for the coherent state. The squeezed coherent state for $\omega_c = 2.47$ eV, $|\alpha|^2 = 4$ and $r = 2$ breaths twice the coherent oscillatory period $T = 1.67$ fs. If one calculates the time dependent dipole moment by

$$D(t) = \int dx \psi_{n''=1}^g(x) \times \psi_{\alpha, \xi}(x, t), \quad (12.9)$$

between the Fock state $|1\rangle$ and the evolving squeezed coherent state $|\alpha, \xi\rangle$ one finds a maximum magnitude of 2.45 a.u., while the same calculation for a moving coherent state provides 1.70 a.u. Consequently, it means that the squeezing introduces large effective dipole couplings even with smaller values of $|\alpha|$. Thus the cavity couples the two states mainly in the internuclear region $0 < R < R_{\text{LIC}}$ and the **LIC** is again more crucial than the **NAC** in the dynamics. The off-resonant cavity interaction in $R_e < R < R_{\text{LIC}}$ and the **LIC** itself depopulates the e-state (see Figs. 12.9 and 12.10 for $t = 5 - 43$ fs). The e-wave packet is almost no longer present in the region $R_{\text{LIC}} < R < R_{\text{NAC}}$, and thus there is little dissociation. It transfers its population at the **LIC** to the g-state at $t \sim 43$ fs and the latter remains mostly confined in that region. On the other side, the density in the region $0 < R < R_{\text{LIC}}$ is also confined but it is continuously exchanged between the g- and the e-state, which results in oscillating populations, with a period corresponding to one cycle of vibration of the g-wave packet in this inner zone. It must be also noted that the oscillatory (with breathing) motion along the cavity mode coordinate x provokes a larger spreading and self-interferences in the wave packets. This spreading along x (similar to the coherent state), which is not present in the Fock case, makes that g/e-wave packets visit a more extensive landscape of the **PES**. As it is mentioned above, both **PES** are not symmetric with respect to parity ($x \rightarrow -x$) due to the presence of diagonal dipole moments. Its effect is appreciated in the Fock case ($t = 144$ fs in Fig. 12.3 where the g-wave packet in

$R_{\text{LIC}} < R < R_{\text{NAC}}$ is biased toward positive x) in the coherent case ($t = 144$ fs in Fig. 12.6) and in the squeezed state (see $t = 80$ fs in Fig. 12.9).

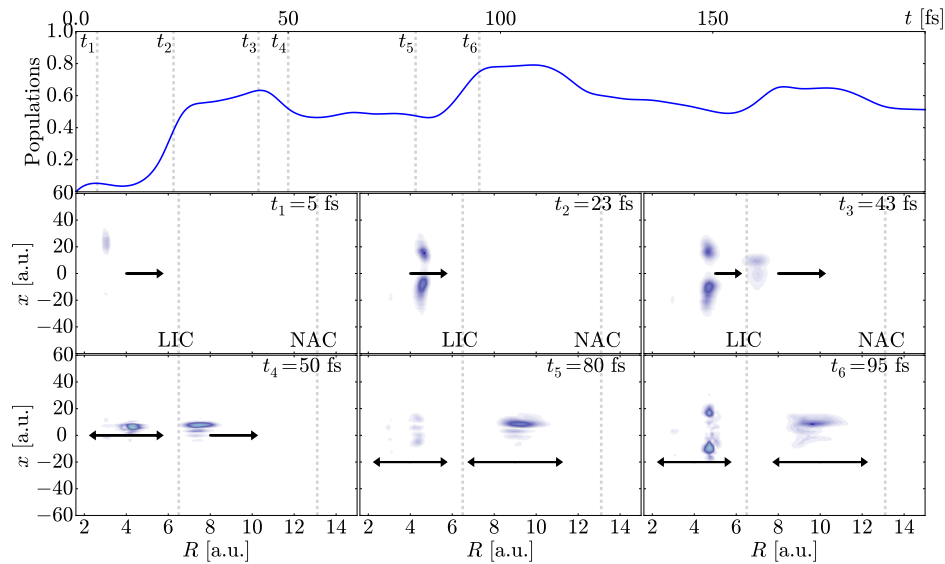


Figure 12.9: Snapshots of the time-dependent evolution for the probability density of the entangled radiation-molecule wave packet moving in the potential $1^1\Sigma$ energy surface composed by the molecular PEC of the electronic $1^1\Sigma$ state and the radiation of a HO with its corresponding interaction term (see Eq. (12.4)). The plot corresponds to a cavity mode frequency $\omega_c = 2.47$ eV, interaction factor $\chi = 0.05$ and the radiation is set up initially as a squeezed coherent state $|\alpha, \xi\rangle$ with an average number of photons $\bar{n} = 4$ and coherent and squeezing phase $\psi - \theta = 2\pi/5$, and squeezing parameter $r = 2$. The times t_i for the snapshots are connected with different features present in the population of the $1^1\Sigma$ state (upper panel). Arrows indicate the direction of motion of the wave packet and its size is related to the magnitude of its momentum. Vertical lines within the snapshots indicate the internuclear distance $R = 6.5$ a.u. for the location of LIC and the internuclear distance $R = 13.1$ a.u. for the NAC.

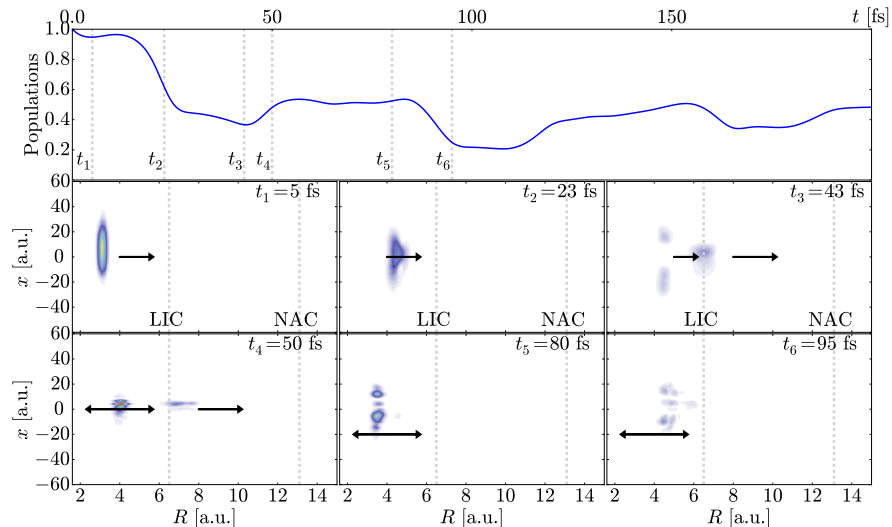


Figure 12.10: Same as Fig. 12.9 but for the population and time-dependent probability density of the $2^1\Sigma$ state (initially populated at $t = 0$ with the radiation state as a squeeze coherent state) in the $2^1\Sigma$ potential energy surface. Snapshots are taken at the same times as in Fig. 12.9 for comparison.

12.2 UNCOVERING LIGHT INDUCED CROSSINGS IN MOLECULES IMMERSED IN OPTICAL CAVITIES USING PUMP-PROBE LASER SCHEMES

As shown in the previous section, the field-free dynamics of a molecular system can be affected if this interacts with a quantized field. Now the perspective aims at the proposal of an experiment in which the fingerprints of the **LIC** in molecules produced because of the cavity light interaction could be detected experimentally. The proposal consists of a UV pump-IR probe laser scheme, a LiF molecular beam prepared as a supersonic jet traveling in the LAB x -axis, an optical cavity with reflective walls in the LAB y -direction and kinetic fragment detectors located in the LAB z -direction.

In addition to the $^1\Sigma$ electronic states calculated of LiF molecule, the first excited electronic state of $^1\Pi$ symmetry is calculated with the corresponding new transition dipole moments (see [Section 9.2](#)). Through this fully dissociative $^1\Pi$ state, it is expected to detect the fingerprints of **LIC**. The though experiment can be performed using an ultrashort intense XUV z -polarized pump laser that promptly excites a beam of LiF molecules from the ground $^1\Sigma$ state to the excited $2^1\Sigma$ state, just before entering the cavity in a crossed particle-light beam arrangement. After that, the beam of excited LiF* molecules passes through the optical cavity prepared with an enclosed quantum radiation with a chosen cavity frequency mode ω_c and a chosen cavity mode z -polarization, such that only those molecules aligned along the z -direction of both the pumping laser and cavity polarization are considered, which ensures electronic $\Sigma - \Sigma$ transitions due to the pump and the optical cavity. A few femtoseconds later a second ultrashort IR probe laser pulse with xy -polarization crosses the molecular beam of LiF* within the optical cavity in such a way that the laser only induces $\Sigma - \Pi$ transitions on those molecules already aligned in the z -direction. Those fragments dissociating in the z -direction perpendicular to the probe polarization axis are recorded by external kinematic detectors.

In this scheme, for a fixed-in-space molecule oriented parallel to the cavity polarization but perpendicular to the laser probe polarization axis will dissociate through both final $^1\Sigma$ (in the adiabatic picture) and $1^1\Pi$ molecular channels, which are energy-degenerated at $R \rightarrow \infty$. Both fragmentation channels produce fragments released in the same z direction getting out from the cavity and they eventually reach the detectors. However, a first proposal in order to discriminate the fragmentation signals coming from the Σ and Π channels is to measure the Σ fragmentation yield obtained when the probe laser field is not present and to subtract the Π fragmentation yield. Another more reasonable route is by choosing different central frequencies ω for the probe pulse (from IR to UV), so that the resulting dissociating wave packet in the $1^1\Pi$ state may have a kinetic energy release well separated from that of the $^1\Sigma$ dissociation, whose fragmentation energy is preserved after the prompt pump laser pulse. It is assumed that the detectors are able to measure kinetic energy release of arriving fragments.

12.2.1 DYNAMICS IN THE Σ STATES

This section explains the field-free evolution of the system when the LiF molecule is submitted to a quantized field and it is not affected by any other external force. As in the previous section, it is assumed for simplicity that LiF molecules within the cavity are oriented along the polarization axis of the cavity radiation field, so that only $\Sigma - \Sigma$ radiative transitions are allowed. In order to follow the ideas exposed above, a sudden FC excitation from the $^1\Sigma$ state to the $2^1\Sigma$ state is assumed. In this way, the initial unentangled photonic-nuclear e-wave packet at $t = 0$ in $2^1\Sigma$ is the direct product of the vibrational ground state of the $^1\Sigma$ electronic state and the ground state of the harmonic oscillator that represents the quantum field of the cavity. Additionally, the parameters to perform the **MCTDH** propagation are the following. The number of **SPF** used in the calculations was $n_R = n_x = 15$ to represent both the molecular state in the nuclear box and the radiation state in the radiation box. Similarly, the number of primitive basis is $N_R = 1169$ for the molecular vibrational mode and $N_x = 201$ for the radiation mode.

Fig. 12.11 shows the populations for the dynamics without the intervention of the probe laser field, using two cavity frequencies: $\omega_c = 2.91$ eV (red line) and $\omega_c = 2.09$ eV (blue line). In the case of $\omega_c = 2.91$ eV, the $\Sigma - \Sigma$ exchange of population occurs at $t \approx 40$ fs, when the initially populated $2^1\Sigma$ wave packet reaches the **LIC** located at $R_{\text{LIC}} = 6.0$ a.u. Around $t = 90$ fs the states transfer population due to the **NAC**, and beyond 140 fs, another population exchange happens to occur because part of the wavepacket turns around and again crosses the **LIC**. A similar dynamics occurs for $\omega_c = 2.09$ eV. However, in this case, the initial wavepacket reaches later the **LIC**, at $t \approx 50$ fs, since for the frequency mode 2.09 eV the **LIC** is now located at $R_{\text{LIC}} = 7.0$ a.u. Similarly, around $t = 90$ fs the states exchange their population due to the presence of the **NAC** at $R_{\text{NAC}} \sim 13$ a.u. and beyond $t = 200$ fs, another population transfer occurs because the wavepacket crosses again the **LIC**. According to Eq. (12.4), the transition coupling term between the two electronic states is proportional to the cavity frequency ω_c and the x -coordinate that represents the cavity mode. Hence, if the cavity frequency is large, the population exchange through **LIC** should increase. However, Fig. 12.11 shows the opposite behaviour. The transfer of population is larger, both in the **LIC** and **NAC** regions, when the cavity frequency is smaller. To explain this unusual effect one has to visualize the evolutions of the complete entangled wavepacket. Since the transition coupling term also depends upon the x -coordinate, is it important to know the spatial extension of radiation states along this coordinate. Eigenstates of HO with large natural frequency ω_c are more compact in space than those with smaller ω_c . This could make that the population transfer enhances more with a smaller cavity frequency, due to the larger extension of harmonic oscillator states.

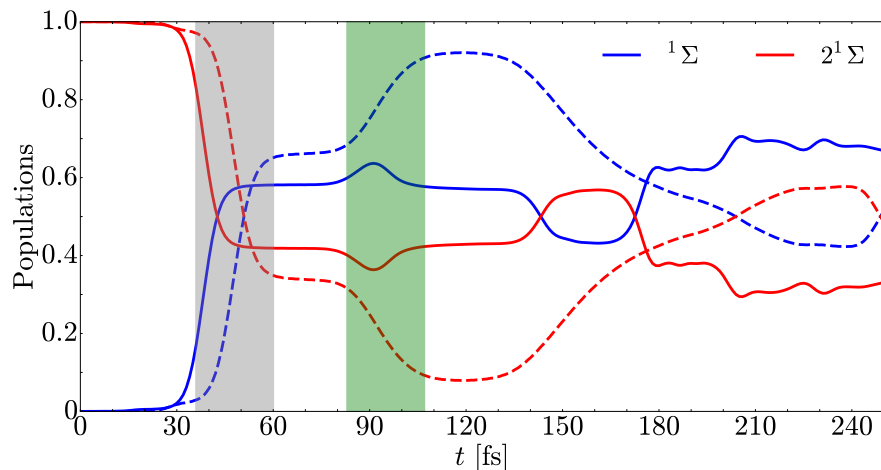


Figure 12.11: Time-dependent population corresponding to the adiabatic ground state $1^1\Sigma$ and the lowest excited state $2^1\Sigma$ for the molecule LiF initially fully excited in the $2^1\Sigma$ and coupled with the radiation present in a cavity in the form of the Fock vacuum state $|0\rangle$. Probabilities are included for two different cavity mode frequencies $\omega_c = 2.91$ eV (solid lines), $\omega_c = 2.09$ eV (dashed lines), with $\chi = 0.01$. Shaded regions correspond to the **LIC** region (grey) and **NAC** region (green).

Another point to consider in the dynamics without probe laser is to find out the vibrational energy distribution within the ground state $1^1\Sigma$ once the e -wave packet has crossed the **LIC**. Vibrational energy distribution is important because it is the first step to choose a frequency for the probe laser pulse, that will be used later. Fig. 12.12 shows the vibrational energy distribution of the adiabatic ground state $1^1\Sigma$ for two different cavity frequencies ($\omega_c = 2.91$ and $\omega_c = 2.09$ eV) and for two different propagation times. In the Fig. 12.12 the lines correspond to the time when the e -wave packet has crossed completely the **LIC**. From here it is possible to infer two different aspects. The first is related with the two high peaks around 4.2 eV and 5.1 eV, which means that the closer the **LIC** is to the **NAC**, highly energy lying vibrational states become populated in $1^1\Sigma$ state. It is worth mentioning that the lowest dissociation limit of LiF is 5.86 eV. On the other hand, the small peaks located at 1.2 and 2.8 eV, come from those dipole transitions discussed in Section 12.1. These transitions can be seen in Figs. 12.3 and 12.6 for a vacuum and coherent state, respectively.

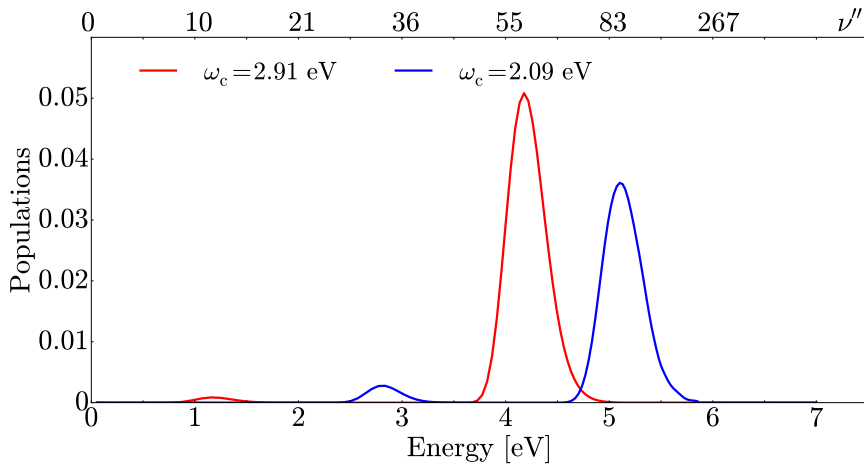


Figure 12.12: Vibrational energy distribution of the adiabatic ground state $1^1\Sigma$ for the cavity frequencies $\omega_c = 2.91$ eV (red line) and $\omega_c = 2.09$ eV (blue line). The upper x-label corresponds to the vibrational number state of the $1^1\Sigma$ adiabatic state.

12.2.2 PUMP-PROBE DYNAMICS SCHEME IN TWO Σ AND ONE Π STATES

The three states considered here for LiF are: the ground state $1^1\Sigma$, and the two lowest excited states, $2^1\Sigma$ and $1^1\Pi$. Note that the two excited states are nearly (diabatically) degenerated except in the Frank-Condon region (see Fig. 9.5). The cavity interaction produces a **LIC** only between Σ states because it is assumed that the cavity polarization is parallel to the molecular axis. Taking the cavity frequencies, $\omega_c = 2.91$ eV and $\omega_c = 2.09$ eV, the position of the **LIC** are located at $R_{\text{LIC}} = 6.0$ a.u. and $R_{\text{LIC}} = 7.0$ a.u., respectively, i.e., where the internuclear distance at which the dressed states cross to each other. The prompt excitation of the pump XUV pulse projects the ground vibrational state of the $1^1\Sigma$ state onto the $2^1\Sigma$ excited state. Then the excited molecule enters the cavity, thus creating an evolving light-matter wave packet. If dynamics only focusses on the molecular potentials, the well-justified Frank-Condon principle produces a wave packet with average energy around 7 eV, so that the kinetic energy release of fragments dissociating through the $1^1\Sigma$ channel is around 1 eV. In contrast, the IR-UV probe laser is tunable and it can excite the molecule to the $1^1\Pi$ state below 7 eV or further up in energy above 7 eV so that fragments dissociating from the $1^1\Pi$ channel show a kinetic energy excess quite distinguishable from that in the $1^1\Sigma$ channel.

This pump-cavity-probe sequence with *i*) $1^1\Sigma \rightarrow 2^1\Sigma$ pump transition, then *ii*) cavity interaction within the Σ manifold and *iii*) subsequent $\{1, 2\}^1\Sigma \rightarrow 1^1\Pi$ transitions, respectively, is justified due the strength of dipole couplings in LiF (see Fig. 9.6). The magnitudes of the $1^1\Sigma \rightarrow 1^1\Pi$ and $2^1\Sigma \rightarrow 1^1\Pi$ dipolar couplings are much smaller than the $1^1\Sigma \rightarrow 2^1\Sigma$ dipolar coupling. This leads to the approximation of neglecting the $\Sigma - \Pi$ transition due to the cavity interaction (and fragmentation for molecules oriented perpendicular to the cavity polarization axis), i.e., a dressed picture involving Σ and Π states and multiple **LIC** is neglected, if present. Nevertheless, this small fragmentation would not be detected by the experimental arrangement, although it may slightly reduce the whole signal. Dipolar couplings in Fig. 9.6 also indicate that the dominant transition at short internuclear distances is between the $1^1\Sigma$ ground state and the $1^1\Pi$ state. This means that the production of fragmentation along the Π channel requires a prior cavity-mediated transfer from the excited $2^1\Sigma$ state to the ground $1^1\Sigma$ state. Note that if the pump laser is switched off and/or the cavity is removed, LiF remains in the ground vibrational state of $1^1\Sigma$ state and, in spite of the dominant dipolar coupling $1^1\Sigma - 1^1\Pi$, both the cavity and the IR probe laser are unable to excite the molecule to drive it up to dissociation. Thus the optical cavity is the mediator to populate the ground state (provided a previous pump excitation) from which the $1^1\Pi$ channel is excited.

To asses all previous ideas in order to detect experimentally the **LIC**, dynamics calculations are performed using **MCTDH**. A high intense probe laser field is introduced in the cavity

scheme with a controllable time delay τ with respect to the pump excitation (assumed to occur at $t = 0$). Fig. 12.13 includes the classical field for the probe laser pulse, characterized with a ultrashort duration $T = 35$ fs, a high intensity of $I = 7.89 \times 10^{14}$ W/cm², and a IR central frequency of $\omega = 1$ eV. Note that the delay τ is defined with respect to the center of the pulse. Extensive calculations scanning the dynamics using this laser probe are performed with many different delays $\tau \in [20, 180]$ fs and recording populations, densities, etc., with special attention to the population transferred to the Π dissociative channel.

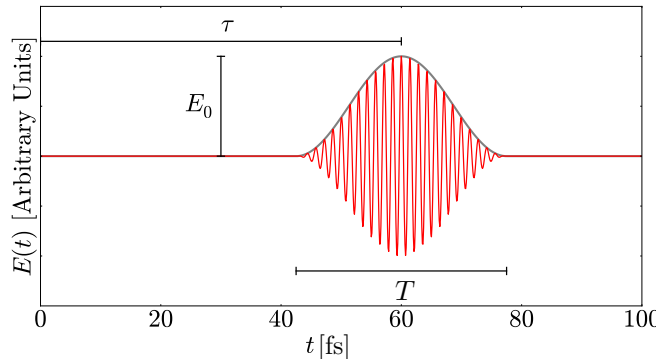


Figure 12.13: Parameters for the probe laser pulse $E(t)$ with polarization axis perpendicular to that of the cavity mode. The pulse parameters are intensity $I = 7.89 \times 10^{14}$ W/cm², duration $T = 35$ fs, a tunable time delay τ with respect to the pump laser excitation (set at $t = 0$) and a pulse central frequency $\omega = 1$ eV.

The final $^1\Pi$ population (formally $t \rightarrow \infty$) versus the pump-probe time delay τ for two different cavity frequencies is plotted in Fig. 12.14, where it is possible to appreciate that the fragmentation is enhanced at specific time delays. Vertical lines indicate the maxima and minima, which are defined in Table 12.2 for the two cavity frequencies used and the two IR probe laser field used in each case.

Table 12.2: Values of the probe pulse time delay t_0 (in fs) of maximums and minima of final population of the $^1\Pi$ excited state, according to Fig. 12.14.

	$\omega_c = 2.91$ eV		$\omega_c = 2.09$ eV	
	$\omega = 2.0$ eV	$\omega = 2.5$ eV	$\omega = 1.5$ eV	$\omega = 2.0$ eV
Maximums	48	45	57	38
	85	95	142	152
Minima	70		100	95

To clarify the situation, the spatial distribution of the Σ and Π wave packet densities at the for each time delay show in Table 12.2 is analyzed.

The snapshots in Fig. 12.15 clearly indicate that the Π wave packet generates from the $^1\Sigma$ ground state (see columns with the label t_2). In addition to excitations in the molecular mode, excitations in the cavity mode are appreciated when the $^2\Sigma$ wave packet crosses the LIC creating the $^1\Sigma$ wave packet, i. e., the wave packet goes from the ground vibrational state to the first vibrational state of the HO. The portion of $^1\Sigma$ wave packet leading to dissociation after the NAC passage does not interfere with the excitation to the $^1\Pi$ state due to the transition dipole moment in that region is practically zero. The portion that remains bound in the ground state, bounces back and forth approximately between the classical turning points of the dressed potential. When this wavepacket passes through the LIC region the transition to the $^1\Pi$ dissociating channel is notoriously enhanced. This would give direct experimental evidence of the generation of a LIC position in a molecule induced by a cavity interaction. The periodicity

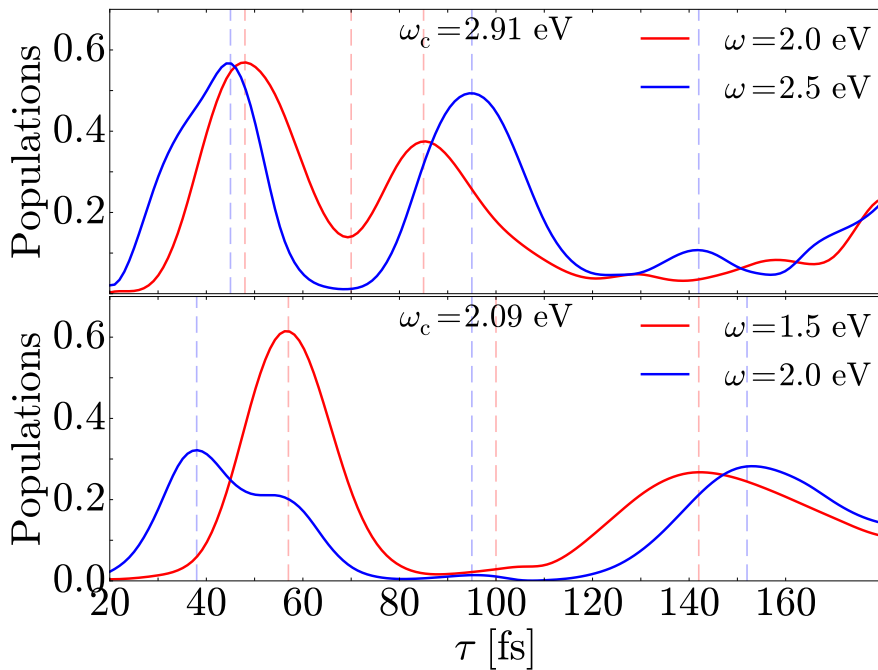


Figure 12.14: Final population of the ${}^1\Pi$ excited state as a function of the pump-probe delay t_0 for a cavity mode frequency $\omega_c = 2.91$ eV (upper panel) and $\omega_c = 2.09$ eV (lower panel) and different probe laser frequencies. Vertical lines indicate those delays at which the ${}^1\Pi$ population reaches a maximum or minimum.

in the ${}^1\Pi$ fragmentation signal versus time delay τ may be used in the R-localization of the molecular [LIC](#). The results can be reproduced and monitored with different cavity frequencies ω_c , which produce a different induced R-localization of the [LIC](#) (see [Fig. 12.14](#)).

In order to detect separately the dissociation fragments from the ${}^1\Pi$ and ${}^1\Sigma$ dissociation channels, the pulse central frequency for the probe IR pulse has to be chosen carefully. In [Fig. 12.15](#), a standard IR field for the probe with $\omega = 2.0$ eV is used. This means that the ${}^1\Pi$ and ${}^1\Sigma$ dissociation signals can be detected separately by the [KER](#), as it is possible to perceive in the first row of [Fig. 12.16](#). In this, the peaks that correspond to the ${}^1\Pi$ and ${}^1\Sigma$ dissociation channels are located around 0.33 eV and 1.14 eV, respectively, i. e., the peaks are completely separated and thus both fragments could be detected experimentally. According to [Fig. 12.12](#), the wavepacket in the ground state is centered in energy around 4.21 eV and adding the pulse central frequency of 2.0 eV gives as a result an average energy of 6.21 eV in the ${}^1\Pi$ state. Thus, taking into account the dissociation limit is 5.86 eV, the [KER](#) gives as a result 0.35 eV, which agrees with the [KER](#) calculated. The [KER](#) value of 1.14 eV for the ${}^1\Sigma$ dissociation channel is the energy value of the ${}^2{}^1\Sigma$ [PEC](#) at equilibrium.

If larger pulse central frequencies for the laser probe pulse are chosen, only the peak corresponding to the ${}^1\Pi$ dissociation channel moves to the right. However, one has to be careful to avoid a value for this frequency that overlaps the two peaks, due to it would be impossible to difference between the two fragments. Using a pulse central frequency $\omega = 2.5$ eV, it is possible to distinguish between the two fragments. [Fig. 12.17](#) shows the populations and snapshots of the wave packets and second row in [Fig. 12.16](#) shows the [KER](#) for this case. In this, the peaks corresponding to the ${}^1\Sigma$ and ${}^1\Pi$ channel have a little overlap around 1 eV, however, this does not avoid both fragments can be detected experimentally separately. Following the blue line in upper panel in [Fig. 12.14](#), it is important to note that the two peaks correspond to delays when the wave packets in the ${}^1\Sigma$ states are crossing the [LIC](#). In other words, an indication for the position and existence of the [LIC](#).

Previous examples were analyzed for a cavity frequency of $\omega_c = 2.91$ eV, i. e., $R_{\text{LIC}} = 6.0$ a.u., nonetheless, the [LIC](#) position can change according to the properties or size of the cavity. Hence,

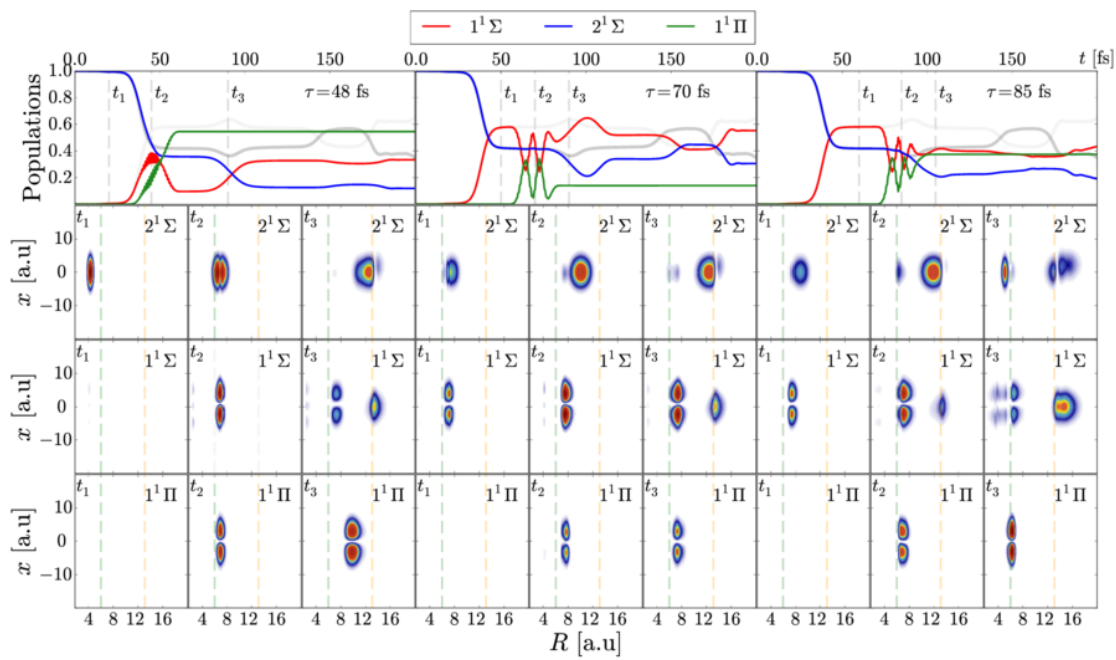


Figure 12.15: (First row) Populations for three different time delays ($\tau = 48, 70, 85$ fs) of the time-dependent evolution for the probability density of the entangled radiation-molecule wave packet moving in the three PES composed by the molecular PEC of the electronic states and the radiation of a HO with its corresponding interaction term (see Eq. (12.4)). The plot corresponds to a cavity mode frequency $\omega_c = 2.91$ eV, laser frequency $\omega = 2.0$ eV and interaction factor $\chi = 0.01$. (From second row) Snapshots of the probability density corresponding the initially excited $2^1\Sigma$ state, the $1^1\Sigma$ ground state and the excited $1^1\Pi$ state (from top to bottom). The snapshots are taken for the different pump-probe time delays τ quoted in Table 12.2, when the transfer to the Π state is maximum or minimum. The times t_i represented by the gray dashed lines in each time delay τ for the snapshots are connected with different features present in the population of all electronic states. Vertical lines within the snapshots indicate the internuclear distance $R_{\text{LIC}} = 6.0$ a.u. for the location of LIC and the internuclear distance $R_{\text{NAC}} = 13.1$ a.u. for the NAC.

changing the LIC position to $R_{\text{LIC}} = 7.0$ a.u. generates a cavity frequency of 2.09 eV. With this cavity frequency, dynamic calculations varying the probe pulse time delay are performed with pulse central frequencies $\omega = 1.5$ eV and $\omega = 2.0$ eV, (see Figs. 12.18 and 12.19, respectively).

Lower panel in Fig. 12.14 shows the final population of the $1^1\Pi$ excited state as a function of the pump-probe delay τ for a cavity mode frequency $\omega_c = 2.09$ eV. In this, the first and third vertical dashed lines, in each pulse central frequency, indicate the maxima exposed in Table 12.2, which, as in the case of $\omega_c = 2.91$ eV, correspond to time delays when the wave packets in the $1^1\Sigma$ states are crossing the LIC region. First dashed lines (blue and red at $\tau = 38$ fs and $\tau = 57$ fs, respectively) indicate that the $2^1\Sigma$ wave packet crosses the LIC and generates the $1^1\Sigma$ wave packet, even with cavity excitations (see second column in Figs. 12.18 and 12.19). Third dashed lines (red and blue at $\tau = 142$ fs and $\tau = 152$ fs, respectively) indicate that the $1^1\Sigma$ wavepacket, that is moving to the left, returns to the LIC position and creates a portion of $2^1\Sigma$ wavepacket (see eighth column in Figs. 12.18 and 12.19). On the other hand, when the final population of $1^1\Pi$ state is minimum (second dashed lines in lower panel of Fig. 12.14), dynamics is almost equal that in the case without a probe pulse. This can be seen in Figs. 12.18 and 12.19 comparing the grayscale lines with the red and blue lines for the time delays $\tau = 100$ fs and $\tau = 95$ fs. The reason why at this time delays the final population in the $1^1\Pi$ state is negligible is because the wavepacket goes further away in the R coordinate and as a consequent, the wavepacket, for those time delays, is located in the regions where the transition dipole is close to zero, which makes that the population transfer is very low.

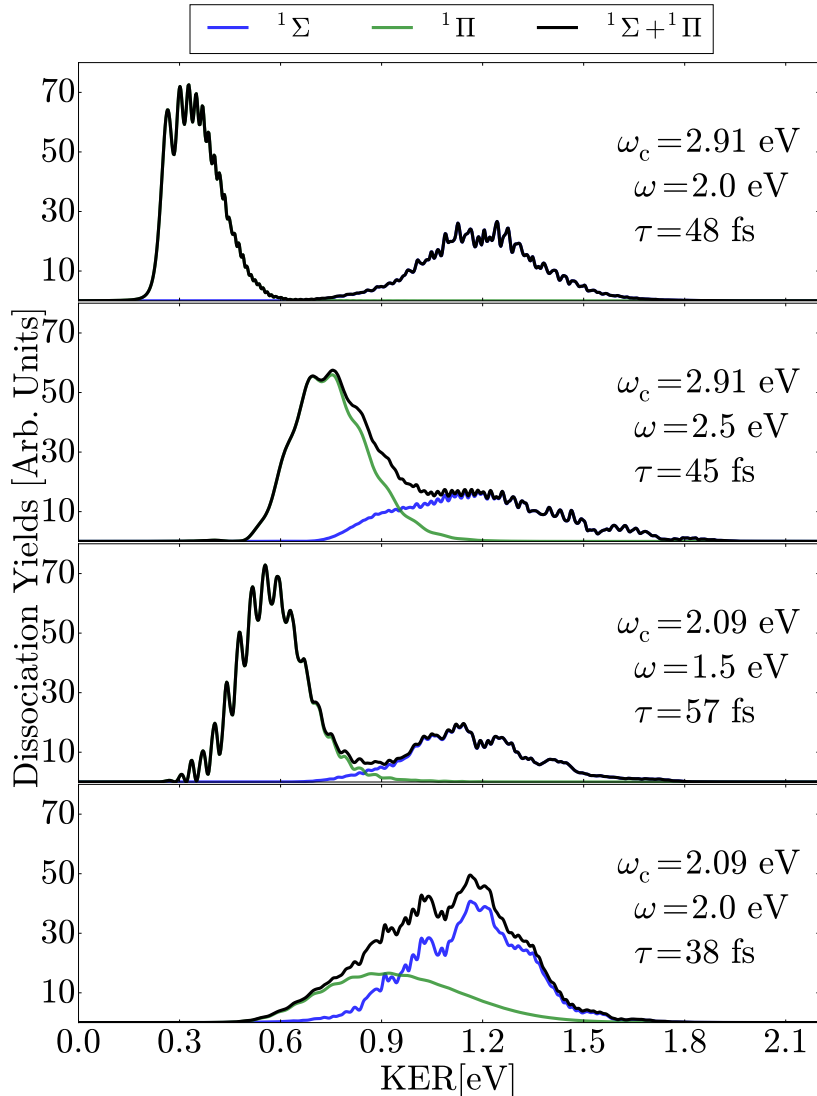


Figure 12.16: Dissociation yields of the adiabatic electronic states $1^1\Sigma$ and $1^1\Pi$ in terms of the **KER** for different cavity mode frequencies and different pulse central frequencies. Parameters and time delays are specified in each plot. Time delays correspond to the first maximum in each case according to Fig. 12.14.

Following the idea that in the case of $\omega_c = 2.91$ eV, to find evidences of the **LIC** position, the two lower panels in Fig. 12.16 show the **KER** calculated for the two pulses central frequencies used in this cavity frequency. In the case of the pulse central frequency $\omega = 1.5$ eV, it is possible to observe that both peaks can be distinguished. The first peak correspond to the **KER** in the $1^1\Pi$ dissociation channel located around 0.62 eV and the second to the $1^1\Sigma$ located at 1.14 eV approximately. According to Fig. 12.12, the wavepacket in the ground state is centered in energy around 5.1 eV and adding the pulse central frequency of 1.5 eV gives as a result an average energy of 6.6 eV in the $1^1\Pi$ state. Hence, according to the 5.86 eV for the dissociation limit, the **KER** gives as a result 0.74 eV, which agrees with the **KER** calculated. However, in the case of the pulse central frequency $\omega = 2.0$ eV, both peaks overlap in the complete **KER** and as a consequence, it is not possible to difference between the two dissociation channels. This is the proof that the pulse central frequency has to be chosen carefully and that experimental parameters are depending on each other, in order to obtain evidences of the existence of the **LIC** in the region where the cavity frequency is in resonance with the energy difference between the two $1^1\Sigma$ **PEC**.

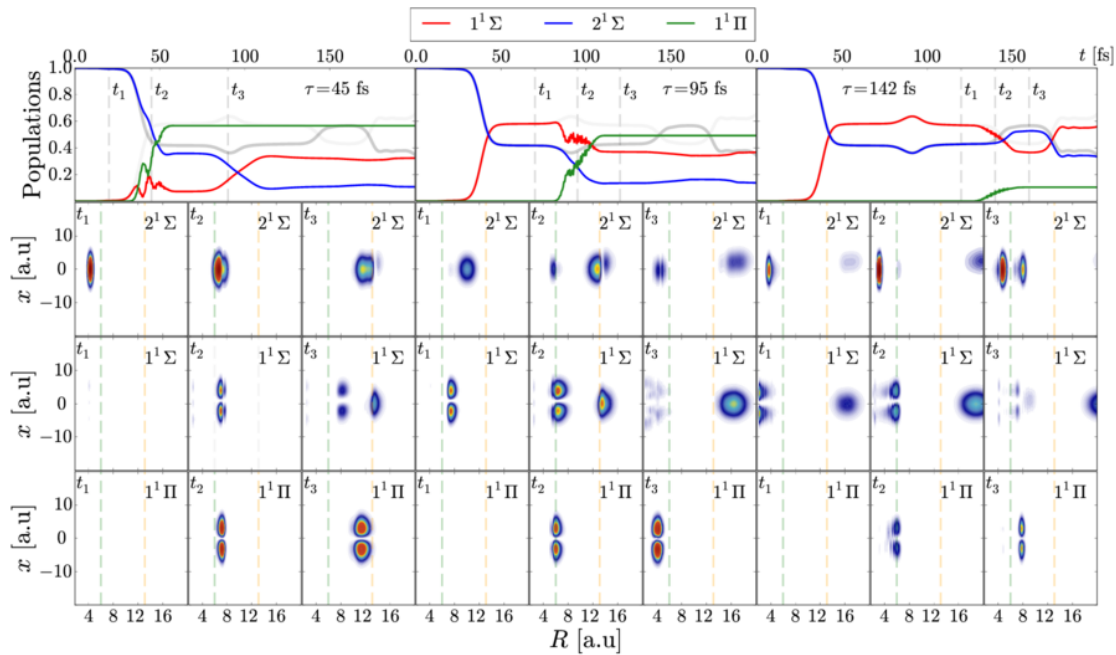


Figure 12.17: (First row) Populations for three different time delays ($\tau = 45, 95, 142$ fs) of the time-dependent evolution for the probability density of the entangled radiation-molecule wave packet moving in the three PES composed by the molecular PEC of the electronic states and the radiation of a HO with its corresponding interaction term (see Eq. (12.4)). The plot corresponds to a cavity mode frequency $\omega_c = 2.91$ eV, laser frequency $\omega = 2.5$ eV and interaction factor $\chi = 0.01$. (From second row) Snapshots of the probability density corresponding the initially excited $2^1\Sigma$ state, the $1^1\Sigma$ ground state and the excited $1^1\Pi$ state (from top to bottom). The snapshots are taken for the different pump-probe time delays τ quoted in Table 12.2, when the transfer to the Π state is maximum or minimum. The times t_i represented by the gray dashed lines in each time delay τ for the snapshots are connected with different features present in the population of all electronic states. Vertical lines within the snapshots indicate the internuclear distance $R_{\text{LIC}} = 6.0$ a.u. for the location of LIC and the internuclear distance $R_{\text{NAC}} = 13.1$ a.u. for the NAC.

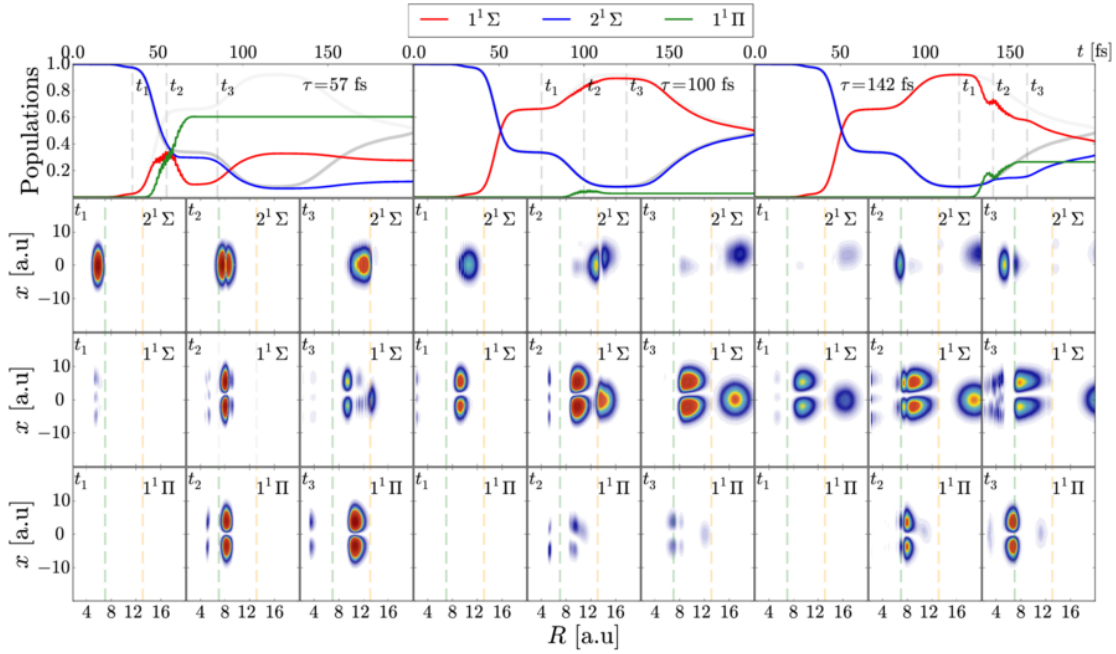


Figure 12.18: (First row) Populations for three different time delays ($\tau = 57, 100, 142$ fs) of the time-dependent evolution for the probability density of the entangled radiation-molecule wave packet moving in the three PES composed by the molecular PEC of the electronic states and the radiation of a HO with its corresponding interaction term (see Eq. (12.4)). The plot corresponds to a cavity mode frequency $\omega_c = 2.09$ eV, laser frequency $\omega = 1.5$ eV and interaction factor $\chi = 0.01$. (From second row) Snapshots of the probability density corresponding the initially excited $2^1\Sigma$ state, the $1^1\Sigma$ ground state and the excited $1^1\Pi$ state (from top to bottom). The snapshots are taken for the different pump-probe time delays τ quoted in Table 12.2, when the transfer to the Π state is maximum or minimum. The times t_i represented by the gray dashed lines in each time delay τ for the snapshots are connected with different features present in the population of all electronic states. Vertical lines within the snapshots indicate the internuclear distance $R_{\text{LIC}} = 7.0$ a.u. for the location of LIC and the internuclear distance $R_{\text{NAC}} = 13.1$ a.u. for the NAC.

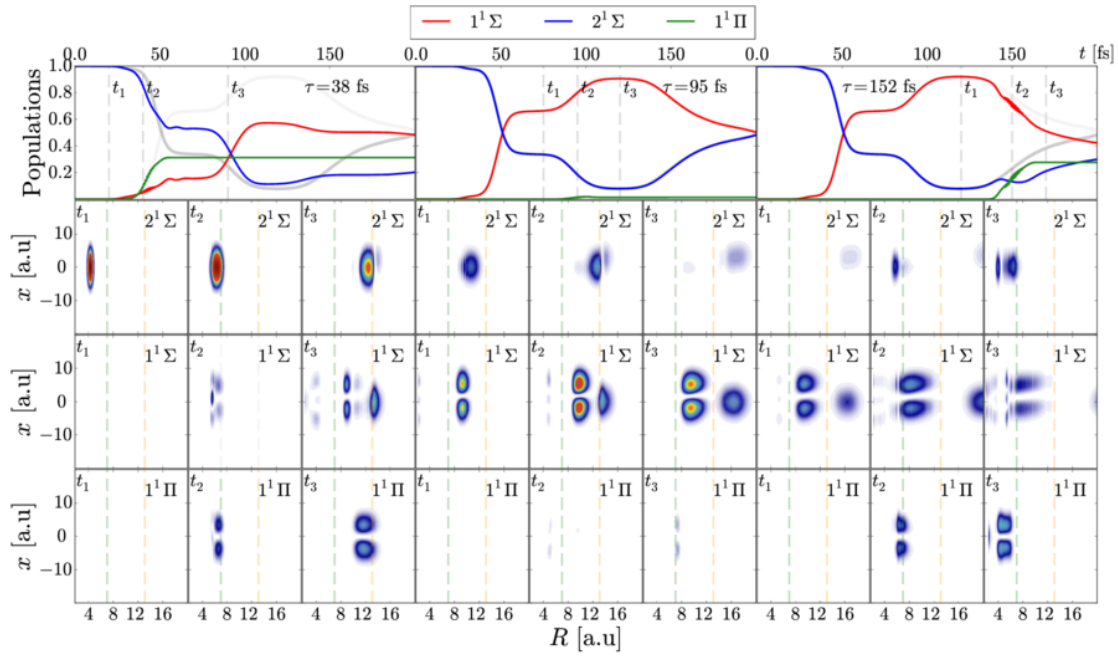


Figure 12.19: (First row) Populations for three different time delays ($\tau = 38, 95, 152$ fs) of the time-dependent evolution for the probability density of the entangled radiation-molecule wave packet moving in the three PES composed by the molecular PEC of the electronic states and the radiation of a HO with its corresponding interaction term (see Eq. (12.4)). The plot corresponds to a cavity mode frequency $\omega_c = 2.09$ eV, laser frequency $\omega = 2.0$ eV and interaction factor $\chi = 0.01$. (From second row) Snapshots of the probability density corresponding the initially excited $2^1\Sigma$ state, the $1^1\Sigma$ ground state and the excited $1^1\Pi$ state (from top to bottom). The snapshots are taken for the different pump-probe time delays τ quoted in Table 12.2, when the transfer to the Π state is maximum or minimum. The times t_i represented by the gray dashed lines in each time delay τ for the snapshots are connected with different features present in the population of all electronic states. Vertical lines within the snapshots indicate the internuclear distance $R_{\text{LIC}} = 7.0$ a.u. for the location of LIC and the internuclear distance $R_{\text{NAC}} = 13.1$ a.u. for the NAC.

CONCLUSIONS

The results found in this work can be split in two parts: *i*) light-matter interaction with classical electromagnetic fields and *ii*) light-matter interaction with quantized fields. Then, in the first part, different control scenarios of the photodissociation in simple molecules are presented during the proceedings of this thesis and calculated with the multiconfigurational time-dependent Hartree method (**MCTDH**). The study goes from the simplest diatomic molecule, H_2^+ , until the triatomic molecule CH_3 passing for other molecules like LiF , H_2O and CO_2 . In the case of the H_2 molecule, calculations for three-state ionization dynamics performed with the multiconfigurational time-dependent Hartree method (**MCTDH**) compared with those using a spectral method to solve the time dependent Schrödinger equation (**TDSE**) in terms of molecular vibronic eigenfunctions show the same results, which endorses the implementation of **MCTDH** including laser pulses. Similarly, for another diatomic molecule, lithium fluoride (LiF), both the electronic structure and non-adiabatic and diabatic two-state dynamics calculations were performed to analyze the effect of the avoided crossing between the two lowest $^1\Sigma$ electronic states (covalent-ionic diabatic crossing) on the photodissociation. In this part, the comparison between two diabatization methods and adiabatic dynamics plus non-adiabatic couplings is analyzed. The results indicate that although the solution to diabatize two electronic potential energy curves is not unique, the diabatization methods and the adiabatic dynamics provide similar results. Then the number of nuclear degrees of freedom is increased by moving to triatomic molecules. First, the photofragmentation dynamics of the simple water molecule H_2O and its isotope HOD was revisited by using the **MCTDH** method. Due to the mass difference, the OH and OD vibrations in HOD molecule behave as uncoupled local modes. These local modes were excited independently by a driving IR pulse in the $X^1\text{A}_1$ ground electronic state. This motion in local modes induces the molecule to fragment into one of the two arrangement channels ($\text{H}+\text{OD}$ or $\text{D}+\text{OH}$) after an excitation to the upper A^1B_1 electronic state due to a delayed UV laser pulse. It is shown that an initial IR-induced heating within the ground $X^1\text{A}_1$ electronic state becomes crucial to increase the branching ratio of the selected reaction channel, in cases in which forces in the ground and excited electronic states are non-bond selective. Moving to another triatomic molecule and motivated by recent experiments on the photofragmentation of carbon dioxide CO_2 after UV excitation in the region of 12 eV, both the electronic structure and the photodynamics of carbon dioxide in this high energy region was studied in detail. The importance of these studies are based on the fact that the experiments produced evidence of $\text{CO}+\text{O}(^1\text{S}, ^1\text{D})$ fragments as well as $\text{C}+\text{O}_2$ fragments. In the electronic structure detailed study, the introduction of a series of Rydberg states, in addition to valence states, causes notorious changes in the potential energy curves of CO_2 and a plethora of non-adiabatic curve crossings. The reduced 1D multistate model implemented show the importance of both Rydberg and valence states in the photodynamics of CO_2 and the results are compared with available experiments. In this work illustrates the importance of dealing with Rydberg and valence states simultaneously in the calculations of excited states in the CO_2 molecule. Finally, in this first part for tetraatomic molecules, the dynamics in the methyl radical CH_3 is carried out to study the multistate dynamics of photodissociation into $\text{H}+\text{CH}_2$, using a reduced 1D model within the manifold of the six lowest states of A' symmetry.

In the second part of this work, it is shown that the strong coupling in the light-matter interaction can be produced by confining a molecule (in this case LiF) within an optical cavity, so that the molecule interacts with the cavity quantum modes of light. In addition to the presence of a non-adiabatic crossing between the ionic and covalent $^1\Sigma$ potential energy curves in LiF , the quantized field produces a light induced crossing between the radiation-dressed potential energy curves. To show this and other effects produced by the interaction with quantized fields, three scenarios for the quantum radiation states are considered: Fock states, coherent states and squeezed coherent states as different expressions of quantum light. In other very recent studies it has been pointed out that there are no real radiation quantum

effects when using Fock states [137, 138] and that any special effect in the population dynamics or dissociation yields can be fully reproduced by using a semiclassical approach for the radiation-matter interaction, only just by fitting the correct intensity of the classical pulse to the constants of the interaction terms in the cavity-matter interaction. However, this is not a general case and the conditions under which a quantum field could be replaced by his counterpart classical field are still an open problem. Additionally, this work shows that the molecular cavity photodynamics of LiF may drastically change upon the quantum field present in the cavity. In addition, contrary to previous statements, these results indicate the fully quantum nature of the radiation cannot be reproduced whatsoever using a classical light. Finally but not less important, an experimental route is proposed to reveal the presence and position of light-induced crossings along the internuclear distance by analyzing photodissociation yields from a third $^1\Pi$ state using ultrashort lasers within a pump-probe scheme.

PART V

APPENDIX

A

CHARACTER TABLES OF THE POINT GROUPS

C_{2v} POINT GROUP

Table A.1: Character Table of C_{2v} Point Group.

C _{2v}	E	C ₂ (z)	σ _v (xz)	σ _v (yz)	Linear and Rotation functions	Quadratic functions
A ₁	1	1	1	1	<i>z</i>	<i>x</i> ² , <i>y</i> ² , <i>z</i> ²
A ₂	1	1	-1	-1	<i>R</i> _z	<i>xy</i>
B ₁	1	-1	1	-1	<i>x</i> , <i>R</i> _y	<i>xz</i>
B ₂	1	-1	-1	1	<i>y</i> , <i>R</i> _x	<i>yz</i>

Table A.2: Product Table for C_{2v} Point Group.

	A ₁	A ₂	B ₁	B ₂
A ₁	A ₁	A ₂	B ₁	B ₂
A ₂	A ₂	A ₁	B ₂	B ₁
B ₁	B ₁	B ₂	A ₁	A ₂
B ₂	B ₂	B ₁	A ₂	A ₁

C_s POINT GROUP

Table A.3: Character Table of C_s Point Group.

C _s	E	σ _h	Linear and Rotation functions	Quadratic functions
A'	1	1	<i>x</i> , <i>y</i> , <i>R</i> _z	<i>x</i> ² , <i>y</i> ² , <i>z</i> ² , <i>xy</i>
A''	1	-1	<i>z</i> , <i>R</i> _x , <i>R</i> _y	<i>yz</i> , <i>xz</i>

Table A.4: Product Table for C_s Point Group.

	A'	A''
A'	A'	A''
A''	A''	A'

BIBLIOGRAPHY

- [1] T. A. Welton, "Some observable effects of the quantum-mechanical fluctuations of the electromagnetic field," *Phys. Rev.*, vol. 74, pp. 1157–1167, 1948.
- [2] M. Scully and M. Zubairy, *Quantum Optics*. Cambridge University Press, 1997.
- [3] H. A. Bethe, "The electromagnetic shift of energy levels," *Phys. Rev.*, vol. 72, pp. 339–341, 1947.
- [4] W. E. Lamb and R. C. Retherford, "Fine structure of the hydrogen atom by a microwave method," *Phys. Rev.*, vol. 72, pp. 241–243, 1947.
- [5] H. B. G. Casimir and D. Polder, "The influence of retardation on the london-van der waals forces," *Phys. Rev.*, vol. 73, pp. 360–372, 1948.
- [6] M. Bordag, U. Mohideen, and V. Mostepanenko, "New developments in the casimir effect," *Physics Reports*, vol. 353, no. 1, pp. 1 – 205, 2001.
- [7] C. Gerry and P. Knight, *Introductory Quantum Optics*. Cambridge University Press, 2005.
- [8] M. Born and R. Oppenheimer, "Zur Quantentheorie der Moleküle," *Annalen der Physik*, vol. 389, no. 20, pp. 457–484, 1927.
- [9] T. Azumi and K. Matsuzaki, "What does the term "vibronic coupling" mean?," *Photochemistry and Photobiology*, vol. 25, no. 3, pp. 315–326, 1977.
- [10] C. J. Ballhausen and A. E. Hansen, "Electronic spectra," *Annual Review of Physical Chemistry*, vol. 23, no. 1, pp. 15–38, 1972.
- [11] M. Born and K. Huang, *Dynamical Theory of Crystal Lattices*. International series of monographs on physics, Clarendon Press, illustrated, reprint, revised ed., 1998.
- [12] L. J. Butler, "Chemical reaction dynamics beyond the Born-Oppenheimer approximation," *Annual Review of Physical Chemistry*, vol. 49, no. 1, pp. 125–171, 1998. PMID: 15012427.
- [13] J. Von Neumann and W. EP, "Über das verhalten von eigenwerten bei adiabatischen prozessen," *Phys. Zschr.*, vol. 30, pp. 467–470, 1929.
- [14] J. H. V. Vleck, "On the isotope corrections in molecular spectra," *The Journal of Chemical Physics*, vol. 4, no. 6, pp. 327–338, 1936.
- [15] V. A. Johnson, "Correction for nuclear motion in H_2^+ ," *Phys. Rev.*, vol. 60, pp. 373–377, 1941.
- [16] D. R. Hartree, "The wave mechanics of an atom with a non-Coulomb central field. Part I. Theory and methods," *Mathematical Proceedings of the Cambridge Philosophical Society*, vol. 24, pp. 89–110, 1928.
- [17] V. Fock, "Näherungsmethode zur Lösung des quantenmechanischen Mehrkörperproblems," *Zeitschrift für Physik*, vol. 61, no. 1, pp. 126–148, 1930.
- [18] J. C. Slater, "Note on Hartree's method," *Phys. Rev.*, vol. 35, pp. 210–211, 1930.
- [19] C. Cramer, *Essentials of Computational Chemistry: Theories and Models*. Wiley, 2013.
- [20] T. Helgaker, P. Jorgensen, and J. Olsen, *Molecular Electronic-Structure Theory*. Wiley, 2014.
- [21] F. Jensen, *Introduction to Computational Chemistry*. Wiley, 2013.
- [22] D. Feller, "Application of systematic sequences of wave functions to the water dimer," *The Journal of Chemical Physics*, vol. 96, no. 8, pp. 6104–6114, 1992.
- [23] K. A. Peterson, D. E. Woon, and T. H. Dunning, "Benchmark calculations with correlated molecular wave functions. IV. the classical barrier height of the $h+h_2 \rightarrow h_2+h$ reaction," *The Journal of Chemical Physics*, vol. 100, no. 10, pp. 7410–7415, 1994.
- [24] J. C. Slater, "Atomic shielding constants," *Phys. Rev.*, vol. 36, pp. 57–64, 1930.

- [25] M. J. Frisch, G. W. Trucks, H. B. Schlegel, G. E. Scuseria, M. A. Robb, J. R. Cheeseman, G. Scalmani, V. Barone, B. Mennucci, G. A. Petersson, H. Nakatsuji, M. Caricato, X. Li, H. P. Hratchian, A. F. Izmaylov, J. Bloino, G. Zheng, J. L. Sonnenberg, M. Hada, M. Ehara, K. Toyota, R. Fukuda, J. Hasegawa, M. Ishida, T. Nakajima, Y. Honda, O. Kitao, H. Nakai, T. Vreven, J. A. Montgomery, Jr., J. E. Peralta, F. Ogliaro, M. Bearpark, J. J. Heyd, E. Brothers, K. N. Kudin, V. N. Staroverov, R. Kobayashi, J. Normand, K. Raghavachari, A. Rendell, J. C. Burant, S. S. Iyengar, J. Tomasi, M. Cossi, N. Rega, J. M. Millam, M. Klene, J. E. Knox, J. B. Cross, V. Bakken, C. Adamo, J. Jaramillo, R. Gomperts, R. E. Stratmann, O. Yazyev, A. J. Austin, R. Cammi, C. Pomelli, J. W. Ochterski, R. L. Martin, K. Morokuma, V. G. Zakrzewski, G. A. Voth, P. Salvador, J. J. Dannenberg, S. Dapprich, A. D. Daniels, Ö. Farkas, J. B. Foresman, J. V. Ortiz, J. Cioslowski, and D. J. Fox, "Gaussian 09 Revision E.01." Gaussian Inc. Wallingford CT 2009.
- [26] H.-J. Werner, P. J. Knowles, G. Knizia, F. R. Manby, M. Schütz, *et al.*, "Molpro, version 2015.1, a package of ab initio programs," 2015. <http://www.molpro.net>.
- [27] T. H. Dunning and P. J. Hay, "Gaussian basis sets for molecular calculations," in *Methods of Electronic Structure Theory* (H. Schaefer, ed.), vol. 3 of *Modern Theoretical Chemistry*, ch. 1, Springer US, 1977.
- [28] T. H. Dunning, "Gaussian basis sets for use in correlated molecular calculations. I. The atoms boron through neon and hydrogen," *The Journal of Chemical Physics*, vol. 90, no. 2, pp. 1007–1023, 1989.
- [29] R. A. Kendall, T. H. D. Jr., and R. J. Harrison, "Electron affinities of the first–row atoms revisited. Systematic basis sets and wave functions," *The Journal of Chemical Physics*, vol. 96, no. 9, pp. 6796–6806, 1992.
- [30] D. E. Woon and T. H. D. Jr., "Gaussian basis sets for use in correlated molecular calculations. III. The atoms aluminum through argon," *The Journal of Chemical Physics*, vol. 98, no. 2, pp. 1358–1371, 1993.
- [31] D. E. Woon and T. H. D. Jr., "Gaussian basis sets for use in correlated molecular calculations. V. core–valence basis sets for boron through neon," *The Journal of Chemical Physics*, vol. 103, no. 11, pp. 4572–4585, 1995.
- [32] J. Cízek, "On the correlation problem in atomic and molecular systems. calculation of wavefunction components in Ursell–type expansion using quantum–field theoretical methods," *The Journal of Chemical Physics*, vol. 45, no. 11, pp. 4256–4266, 1966.
- [33] C. J. and P. J., "Correlation problems in atomic and molecular systems III. rederivation of the coupled–pair many–electron theory using the traditional quantum chemical methods," *International Journal of Quantum Chemistry*, vol. 5, no. 4, pp. 359–379, 1971.
- [34] A. Hurley, *Electron correlation in small molecules*. Theoretical chemistry, Academic Press, 1976.
- [35] P. R. Taylor, G. Bacsay, N. Hush, and A. Hurley, "The coupled–pair approximation in a basis of independent–pair natural orbitals," *Chemical Physics Letters*, vol. 41, no. 3, pp. 444 – 449, 1976.
- [36] C. T. Daniel and S. H. F., *An Introduction to Coupled Cluster Theory for Computational Chemists*, pp. 33–136. Wiley-Blackwell, 2007.
- [37] I. Levine, *Physical chemistry*. McGraw-Hill, 2008.
- [38] G. D. Purvis and R. J. Bartlett, "A full coupled–cluster singles and doubles model: The inclusion of disconnected triples," *The Journal of Chemical Physics*, vol. 76, no. 4, pp. 1910–1918, 1982.
- [39] J. Noga and R. J. Bartlett, "The full CCSDT model for molecular electronic structure," *The Journal of Chemical Physics*, vol. 86, no. 12, pp. 7041–7050, 1987.
- [40] G. E. Scuseria and H. F. Schaefer, "A new implementation of the full CCSDT model for molecular electronic structure," *Chemical Physics Letters*, vol. 152, no. 4, pp. 382 – 386, 1988.
- [41] Y. J. Bombelle, J. F. Stanton, M. Kállay, and J. Gauss, "Coupled–cluster methods including noniterative corrections for quadrupole excitations," *The Journal of Chemical Physics*, vol. 123, no. 5, p. 054101, 2005.
- [42] J. F. Stanton and R. J. Bartlett, "The equation of motion coupled–cluster method. A systematic biorthogonal approach to molecular excitation energies, transition probabilities, and excited state properties," *The Journal of Chemical Physics*, vol. 98, no. 9, pp. 7029–7039, 1993.
- [43] E. Schrödinger, "An undulatory theory of the mechanics of atoms and molecules," *Phys. Rev.*, vol. 28, pp. 1049–1070, 1926.
- [44] R. P. Feynman and A. R. Hibbs, *Quantum physics and path integrals*. McGraw-Hill, New York, 1965.
- [45] R. Feynman and A. Hibbs, *Quantum Mechanics and Path Integrals: Emended Edition*. Dover Publications, Incorporated, 2012.
- [46] D. Micha and I. Burghardt, *Quantum Dynamics of Complex Molecular Systems*. Springer Series in Chemical Physics, Springer Berlin Heidelberg, 2006.
- [47] P. A. M. Dirac, "A new notation for quantum mechanics," *Mathematical Proceedings of the Cambridge Philosophical Society*, vol. 35, no. 3, pp. 416–418, 1939.

- [48] J. Lill, G. Parker, and J. Light, "Discrete variable representations and sudden models in quantum scattering theory," *Chemical Physics Letters*, vol. 89, no. 6, pp. 483 – 489, 1982.
- [49] J. C. Light, I. P. Hamilton, and J. V. Lill, "Generalized discrete variable approximation in quantum mechanics," *The Journal of Chemical Physics*, vol. 82, no. 3, pp. 1400–1409, 1985.
- [50] D. Baye and P. H. Heenen, "Generalised meshes for quantum mechanical problems," *Journal of Physics A: Mathematical and General*, vol. 19, no. 11, p. 2041, 1986.
- [51] H. Meyer, F. Gatti, and G. Worth, *Multidimensional Quantum Dynamics: MCTDH Theory and Applications*. John Wiley & Sons, 2009.
- [52] F. Gatti, B. Lasorne, H. Meyer, and A. Nauts, *Applications of Quantum Dynamics in Chemistry*. Lecture Notes in Chemistry, Springer International Publishing, 2017.
- [53] P. A. M. Dirac, "Note on exchange phenomena in the thomas atom," *Mathematical Proceedings of the Cambridge Philosophical Society*, vol. 26, no. 3, pp. 376—385, 1930.
- [54] J. Frenkel, *Wave Mechanics: Elementary Theory*. Oxford Univ. Press, 1932.
- [55] M. Beck, A. Jäckle, G. Worth, and H.-D. Meyer, "The multiconfiguration time-dependent Hartree (MCTDH) method: a highly efficient algorithm for propagating wavepackets," *Physics Reports*, vol. 324, no. 1, pp. 1 – 105, 2000.
- [56] H.-D. Meyer, U. Manthe, and L. Cederbaum, "The multi-configurational time-dependent hartree approach," *Chemical Physics Letters*, vol. 165, no. 1, pp. 73 – 78, 1990.
- [57] L. Levin, W. Skomorowski, L. Rybak, R. Kosloff, C. P. Koch, and Z. Amitay, "Coherent control of bond making," *Phys. Rev. Lett.*, vol. 114, p. 233003, 2015.
- [58] G. A. Worth and L. S. Cederbaum, "Beyond born-oppenheimer: Molecular dynamics through a conical intersection," *Annual Review of Physical Chemistry*, vol. 55, no. 1, pp. 127–158, 2004.
- [59] W. Domcke, D. Yarkony, and H. Köppel, *Conical Intersections: Electronic Structure, Dynamics & Spectroscopy*. Advanced series in physical chemistry, World Scientific, 2004.
- [60] F. T. Smith, "Diabatic and adiabatic representations for atomic collision problems," *Phys. Rev.*, vol. 179, pp. 111–123, 1969.
- [61] A. Macías and A. Riera, "Ab initio quantum chemistry in the molecular model of atomic collisions," *Physics Reports*, vol. 90, no. 5, pp. 299 – 376, 1982.
- [62] M. Nisoli, S. Stagira, S. De Silvestri, O. Svelto, S. Sartania, Z. Cheng, M. Lenzner, C. Spielmann, and F. Krausz, "A novel-high energy pulse compression system: generation of multigigawatt sub-5-fs pulses," *Applied Physics B*, vol. 65, no. 2, pp. 189–196, 1997.
- [63] M. Schnürer, Z. Cheng, S. Sartania, M. Hentschel, G. Tempea, T. Brabec, and F. Krausz, "Guiding and high-harmonic generation of sub-10-fs pulses in hollow-core fibers at 10^{15} w/cm²," *Applied Physics B*, vol. 67, no. 2, pp. 263–266, 1998.
- [64] A. H. Zewail, "The nobel prize in chemistry 1999," *Nobel Prize*, Oct 1999.
- [65] B. Bransden and C. Joachain, *Quantum Mechanics*. Prentice Hall, 2000.
- [66] A. Palacios, J. L. Sanz-Vicario, and F. Martín, "Theoretical methods for attosecond electron and nuclear dynamics: applications to the h₂ molecule," *Journal of Physics B: Atomic, Molecular and Optical Physics*, vol. 48, no. 24, p. 242001, 2015.
- [67] K. Oughstun, *Electromagnetic and Optical Pulse Propagation 2: Temporal Pulse Dynamics in Dispersive, Attenuative Media*. Electromagnetic and Optical Pulse Propagation, Springer, 2009.
- [68] I. Bar, Y. Cohen, D. David, T. Arusi-Parpar, S. Rosenwaks, and J. J. Valentini, "Mode-selective bond fission: Comparison between the photodissociation of HOD (0,0,1) and HOD (1,0,0)," *The Journal of Chemical Physics*, vol. 95, pp. 3341–3346, 1991.
- [69] P. Brumer and M. Shapiro, "Control of unimolecular reactions using coherent light," *Chemical Physics Letters*, vol. 126, no. 6, pp. 541 – 546, 1986.
- [70] M. Shapiro, J. W. Hepburn, and P. Brumer, "Simplified laser control of unimolecular reactions: Simultaneous (ω_1, ω_3) excitation," *Chemical Physics Letters*, vol. 149, no. 5, pp. 451 – 454, 1988.
- [71] M. Shapiro and P. Brumer, *Quantum Control of Molecular Processes*. Wiley, 2012.
- [72] M. Shapiro and P. Brumer, "Weak field optimal control over product yields. the pump–dump scenario," *Chemical Physics Letters*, vol. 208, no. 3, pp. 193 – 196, 1993.
- [73] D. J. Tannor and S. A. Rice, "Control of selectivity of chemical reaction via control of wave packet evolution," *The Journal of Chemical Physics*, vol. 83, no. 10, pp. 5013–5018, 1985.

- [74] D. Tannor, *Introduction to Quantum Mechanics*. University Science Books, 2007.
- [75] D. Tannor, *Molecules in Laser Fields*. Taylor & Francis, 1993. ed. A.D. Bandrauk.
- [76] M. Shapiro and P. Brumer, "Laser control of product quantum state populations in unimolecular reactions," *The Journal of Chemical Physics*, vol. 84, no. 7, pp. 4103–4104, 1986.
- [77] L. Zhu, V. Kleiman, X. Li, S. P. Lu, K. Trentelman, and R. J. Gordon, "Coherent laser control of the product distribution obtained in the photoexcitation of HI," *Science*, vol. 270, no. 5233, pp. 77–80, 1995.
- [78] L. Zhu, K. Suto, J. A. Fiss, R. Wada, T. Seideman, and R. J. Gordon, "Effect of resonances on the coherent control of the photoionization and photodissociation of HI and DI," *Phys. Rev. Lett.*, vol. 79, pp. 4108–4111, 1997.
- [79] T. Baumert, B. Buehler, M. Grosser, R. Thalweiser, V. Weiss, E. Wiedenmann, and G. Gerber, "Femtosecond time-resolved wave packet motion in molecular multiphoton ionization and fragmentation," *The Journal of Physical Chemistry*, vol. 95, no. 21, pp. 8103–8110, 1991.
- [80] T. Baumert, M. Grosser, R. Thalweiser, and G. Gerber, "Femtosecond time-resolved molecular multiphoton ionization: The Na_2 system," *Phys. Rev. Lett.*, vol. 67, pp. 3753–3756, 1991.
- [81] D. J. Tannor, R. Kosloff, and S. A. Rice, "Coherent pulse sequence induced control of selectivity of reactions: Exact quantum mechanical calculations," *The Journal of Chemical Physics*, vol. 85, no. 10, pp. 5805–5820, 1986.
- [82] T. Seideman, M. Shapiro, and P. Brumer, "Coherent radiative control of unimolecular reactions: Selective bond breaking with picosecond pulses," *The Journal of Chemical Physics*, vol. 90, no. 12, pp. 7132–7136, 1989.
- [83] Z. Chen, P. Brumer, and M. Shapiro, "Coherent radiative control of molecular photodissociation via resonant two-photon versus two-photon interference," *Chemical Physics Letters*, vol. 198, no. 5, pp. 498 – 504, 1992.
- [84] V. Blanchet, C. Nicole, M.-A. Bouchene, and B. Girard, "Temporal coherent control in two-photon transitions: From optical interferences to quantum interferences," *Phys. Rev. Lett.*, vol. 78, pp. 2716–2719, 1997.
- [85] R. J. Glauber, "Coherent and Incoherent States of the Radiation Field," *Phys. Rev.*, vol. 131, pp. 2766–2788, 1963.
- [86] C. M. Caves, "Quantum-mechanical noise in an interferometer," *Phys. Rev. D*, vol. 23, pp. 1693–1708, 1981.
- [87] K. B. Møller, T. G. Jørgensen, and J. P. Dahl, "Displaced squeezed number states: Position space representation, inner product, and some applications," *Phys. Rev. A*, vol. 54, pp. 5378–5385, 1996.
- [88] I. I. Rabi, "Space quantization in a gyrating magnetic field," *Phys. Rev.*, vol. 51, pp. 652–654, 1937.
- [89] M. Kowalewski, K. Bennett, and S. Mukamel, "Non-adiabatic dynamics of molecules in optical cavities," *The Journal of Chemical Physics*, vol. 144, no. 5, p. 054309, 2016.
- [90] D. Walls and G. Milburn, *Quantum Optics*. SpringerLink: Springer e-Books, Springer Berlin Heidelberg, 2008.
- [91] F. Jahnke, *Quantum Optics with Semiconductor Nanostructures*. Woodhead Publishing Series in Electronic and Optical Materials, Elsevier Science, 2012.
- [92] K. Vahala, *Optical Microcavities*. Advanced series in applied physics, World Scientific, 2004.
- [93] G. J. Halász, M. Šindelka, N. Moiseyev, L. S. Cederbaum, and A. Vibók, "Light-induced conical intersections: topological phase, wave packet dynamics, and molecular alignment," *The Journal of Physical Chemistry A*, vol. 116, no. 11, pp. 2636–2643, 2012.
- [94] F. Martí, "Ionization and dissociation using b-splines: photoionization of the hydrogen molecule," *Journal of Physics B: Atomic, Molecular and Optical Physics*, vol. 32, no. 16, p. R197, 1999.
- [95] J. L. Sanz-Vicario, H. Bachau, and F. Martín, "Time-dependent theoretical description of molecular autoionization produced by femtosecond xuv laser pulses," *Phys. Rev. A*, vol. 73, p. 033410, 2006.
- [96] T. Sharp, "Potential-energy curves for molecular hydrogen and its ions," *Atomic Data and Nuclear Data Tables*, vol. 2, pp. 119 – 169, 1971.
- [97] W. Kolos and L. Wolniewicz, "Potential–energy curves for the $\text{X}^1\Sigma_g^+$, $\text{b}^3\Sigma_u^+$, and $\text{C}^1\Pi_u$ states of the hydrogen molecule," *The Journal of Chemical Physics*, vol. 43, no. 7, pp. 2429–2441, 1965.
- [98] P. M. Morse, "Diatomc molecules according to the wave mechanics. ii. vibrational levels," *Phys. Rev.*, vol. 34, pp. 57–64, 1929.
- [99] C. C. Marston and G. G. Balint–kurti, "The fourier grid hamiltonian method for bound state eigenvalues and eigenfunctions," *The Journal of Chemical Physics*, vol. 91, no. 6, pp. 3571–3576, 1989.
- [100] H.-J. Werner and W. Meyer, "MCSCF study of the avoided curve crossing of the two lowest $^1\Sigma^+$ states of LiF," *The Journal of Chemical Physics*, vol. 74, no. 10, pp. 5802–5807, 1981.
- [101] S. Scheit, Y. Arasaki, and K. Takatsuka, "Controlled dynamics at an avoided crossing interpreted in terms of dynamically fluctuating potential energy curves," *The Journal of Physical Chemistry A*, vol. 116, no. 11, pp. 2644–2653, 2012. PMID: 22087788.

- [102] T. J. Giese and D. M. York, "Complete basis set extrapolated potential energy, dipole, and polarizability surfaces of alkali halide ion-neutral weakly avoided crossings with and without applied electric fields," *The Journal of Chemical Physics*, vol. 120, no. 17, pp. 7939–7948, 2004.
- [103] M. Kowalewski, K. Bennett, and S. Mukamel, "Cavity femtochemistry: Manipulating nonadiabatic dynamics at avoided crossings," *The Journal of Physical Chemistry Letters*, vol. 7, no. 11, pp. 2050–2054, 2016. PMID: 27186666.
- [104] H. Hellmann, "Zur rolle der kinetischen elektronenenergie für die zwischenatomaren kräfte," *Zeitschrift für Physik*, vol. 85, no. 3, pp. 180–190, 1933.
- [105] R. P. Feynman, "Forces in molecules," *Phys. Rev.*, vol. 56, pp. 340–343, 1939.
- [106] U. V. Riss and H. D. Meyer, "Calculation of resonance energies and widths using the complex absorbing potential method," *Journal of Physics B: Atomic, Molecular and Optical Physics*, vol. 26, no. 23, p. 4503, 1993.
- [107] J. Zhang, D. G. Imre, and J. H. Frederick, "HOD spectroscopy and photodissociation dynamics: selectivity in hydroxyl/hydroxyl–d bond breaking," *The Journal of Physical Chemistry*, vol. 93, no. 5, pp. 1840–1851, 1989.
- [108] B. Amstrup and N. E. Henriksen, "Control of hod photodissociation dynamics via bond–selective infrared multiphoton excitation and a femtosecond ultraviolet laser pulse," *The Journal of Chemical Physics*, vol. 97, no. 11, pp. 8285–8295, 1992.
- [109] N. Elghobashi, P. Krause, J. Manz, and M. Oppel, "IR+UV laser pulse control of momenta directed to specific products: Quantum model simulations for $\text{HOD}^* \rightarrow \text{H}+\text{OD}$ versus $\text{HO}+\text{D}$," *Phys. Chem. Chem. Phys.*, vol. 5, pp. 4806–4813, 2003.
- [110] Z. Lu, Y. C. Chang, Y. Benitez, Z. Luo, A. B. Houria, T. Ayari, M. M. Al Mogren, M. Hochlaf, W. M. Jackson, and C. Y. Ng, "State-to-state vacuum ultraviolet photodissociation study of CO_2 on the formation of state-correlated $\text{CO}(\text{X}^1\Sigma^+; \nu)$ with $\text{O}(\text{^1D})$ and $\text{O}(\text{^1S})$ photoproducts at 11.95–12.22 eV," *Phys. Chem. Chem. Phys.*, vol. 17, pp. 11752–11762, 2015.
- [111] G. Worth, M. Beck, A. Jäckle, and H. Meyer, "The MCTDH package, version 8.4," 2007. <http://mctdh.uni-hd.de>.
- [112] V. Engel, R. Schinke, and V. Staemmler, "Photodissociation dynamics of H_2O and D_2O in the first absorption band: A complete ab initio treatment," *The Journal of Chemical Physics*, vol. 88, no. 1, pp. 129–148, 1988.
- [113] S. Meyer and V. Engel, "Vibrational revivals and the control of photochemical reactions," *The Journal of Physical Chemistry A*, vol. 101, no. 42, pp. 7749–7753, 1997.
- [114] R. L. Vander Wal and F. F. Crim, "Controlling the pathways in molecular decomposition: the vibrationally mediated photodissociation of water," *The Journal of Physical Chemistry*, vol. 93, no. 14, pp. 5331–5333, 1989.
- [115] R. L. V. Wal, J. L. Scott, and F. F. Crim, "Selectively breaking the O–H bond in HOD," *The Journal of Chemical Physics*, vol. 92, no. 1, pp. 803–805, 1990.
- [116] R. L. V. Wal, J. L. Scott, F. F. Crim, K. Weide, and R. Schinke, "An experimental and theoretical study of the bond selected photodissociation of HOD," *The Journal of Chemical Physics*, vol. 94, no. 5, pp. 3548–3555, 1991.
- [117] N. W. Winter, C. F. Bender, and W. A. Goddard, "Theoretical assignments of the low-lying electronic states of carbon dioxide," *Chemical Physics Letters*, vol. 20, no. 6, pp. 489 – 492, 1973.
- [118] W. B. England and W. C. Ermler, "Theoretical studies of atmospheric triatomic molecules. New *ab initio* results for the $^1\pi_g - ^1\delta_u$ vertical state ordering in CO_2 ," *The Journal of Chemical Physics*, vol. 70, no. 4, pp. 1711–1719, 1979.
- [119] H. Nakatsuji, "Cluster expansion of the wavefunction, valence and rydberg excitations, ionizations, and inner-valence ionizations of CO_2 and N_2O studied by the sac and sac ci theories," *Chemical Physics*, vol. 75, no. 3, pp. 425 – 441, 1983.
- [120] C. Cossart-Magos, M. Jungen, and F. Launay, "High resolution absorption spectrum of CO_2 between 10 and 14 eV," *Molecular Physics*, vol. 61, no. 5, pp. 1077–1117, 1987.
- [121] A. Spielfeldel, N. Feautrier, C. Cossart–Magos, G. Chambaud, P. Rosmus, H.-J. Werner, and P. Botschwina, "Bent valence excited states of CO_2 ," *The Journal of Chemical Physics*, vol. 97, no. 11, pp. 8382–8388, 1992.
- [122] R. J. Buenker, M. Honigmann, H.-P. Liebermann, and M. Kimura, "Theoretical study of the electronic structure of carbon dioxide: Bending potential curves and generalized oscillator strengths," *The Journal of Chemical Physics*, vol. 113, no. 3, pp. 1046–1054, 2000.
- [123] S. Y. Grebenschikov, "Photodissociation of carbon dioxide in singlet valence electronic states. i. six multiply intersecting ab initio potential energy surfaces," *The Journal of Chemical Physics*, vol. 138, no. 22, 2013.
- [124] I. Reineck, C. Nohre, R. Maripuu, P. Lodin, S. Al-Shamma, H. Veenhuizen, L. Karlsson, and K. Siegbahn, "High–resolution UV photoelectron spectrum of CO_2 ," *Chemical Physics*, vol. 78, no. 3, pp. 311 – 318, 1983.
- [125] R. N. Dixon, "The carbon monoxide flame bands," *Proceedings of the Royal Society of London A: Mathematical, Physical and Engineering Sciences*, vol. 275, no. 1362, pp. 431–446, 1963.

- [126] S. Y. Grebenschikov, "Photodissociation of carbon dioxide in singlet valence electronic states. ii. five state absorption spectrum and vibronic assignment," *The Journal of Chemical Physics*, vol. 138, no. 22, 2013.
- [127] S. Y. Grebenschikov, "Photochemistry of carbon dioxide from first principles: Application to photoabsorption of hot CO₂," *Journal of CO₂ Utilization*, vol. 15, pp. 32 – 40, 2016. Special Issue on the XIII International Conference on Carbon Dioxide Utilization (ICCDU-2015).
- [128] P.-O. Widmark, P.-Å. Malmqvist, and B. O. Roos, "Density matrix averaged atomic natural orbital (ano) basis sets for correlated molecular wave functions," *Theoretica chimica acta*, vol. 77, no. 5, pp. 291–306, 1990.
- [129] T. J. Lee and P. R. Taylor, "A diagnostic for determining the quality of single-reference electron correlation methods," *International Journal of Quantum Chemistry*, vol. 36, no. S23, pp. 199–207, 1989.
- [130] H.-J. Werner, P. J. Knowles, G. Knizia, F. R. Manby, and M. Schütz, "Molpro: a general purpose quantum chemistry program package," *WIREs Comput Mol Sci*, vol. 2, pp. 242–253, 2012.
- [131] G. Balerdi, J. Woodhouse, A. Zanchet, R. de Nalda, M. L. Senent, A. Garcia-Vela, and L. Banares, "Femtosecond predissociation dynamics of the methyl radical from the 3p_z Rydberg state," *Phys. Chem. Chem. Phys.*, vol. 18, pp. 110–118, 2016.
- [132] S. Marggi Poullain, D. V. Chicharro, A. Zanchet, M. G. Gonzalez, L. Rubio-Lago, M. L. Senent, A. Garcia-Vela, and L. Banares, "Imaging the photodissociation dynamics of the methyl radical from the 3s and 3p_z Rydberg states," *Phys. Chem. Chem. Phys.*, vol. 18, pp. 17054–17061, 2016.
- [133] H. Walther, B. T. H. Varcoe, B.-G. Englert, and T. Becker, "Cavity quantum electrodynamics," *Reports on Progress in Physics*, vol. 69, no. 5, p. 1325, 2006.
- [134] S. Haroche and J. M. Raimond, *Exploring the quantum: atoms, cavities, and photons*. Oxford: Oxford Univ. Press, 2006.
- [135] A. H. Zewail, *Femtochemistry: Ultrafast dynamics of the chemical bond: vol. I and II*. World Scientific, 1994.
- [136] M. Kowalewski and S. Mukamel, "Manipulating molecules with quantum light," *Proceedings of the National Academy of Sciences*, vol. 114, no. 13, pp. 3278–3280, 2017.
- [137] A. Csehi, G. J. Halász, L. S. Cederbaum, and A. Vibók, "Competition between Light-Induced and Intrinsic Nonadiabatic Phenomena in Diatomics," *The Journal of Physical Chemistry Letters*, vol. 8, no. 7, pp. 1624–1630, 2017. PMID: 28333471.
- [138] A. Csehi, G. J. Halász, L. S. Cederbaum, and A. Vibók, "Intrinsic and light-induced nonadiabatic phenomena in the NaI molecule," *Phys. Chem. Chem. Phys.*, vol. 19, pp. 19656–19664, 2017.
- [139] J. Galego, F. J. Garcia-Vidal, and J. Feist, "Cavity-induced modifications of molecular structure in the strong-coupling regime," *Phys. Rev. X*, vol. 5, p. 041022, 2015.
- [140] J. Galego, F. J. Garcia-Vidal, and J. Feist, "Many-molecule reaction triggered by a single photon in polaritonic chemistry," *Phys. Rev. Lett.*, vol. 119, p. 136001, Sep 2017.
- [141] F. Herrera and F. C. Spano, "Cavity-controlled chemistry in molecular ensembles," *Phys. Rev. Lett.*, vol. 116, p. 238301, Jun 2016.
- [142] J. Flick, M. Ruggenthaler, H. Appel, and A. Rubio, "Atoms and molecules in cavities, from weak to strong coupling in quantum-electrodynamics (qed) chemistry," *Proceedings of the National Academy of Sciences*, vol. 114, no. 12, pp. 3026–3034, 2017.
- [143] J. F. Triana, D. Peláez, and J. L. Sanz-Vicario, "Entangled photonic-nuclear molecular dynamics of lif in quantum optical cavities," *The Journal of Physical Chemistry A*, vol. 122, no. 8, pp. 2266–2278, 2018.